



ISSN 1816-112X

Science Citation Index Expanded,  
Materials Science Citation Index  
and ISI Alerting

## EDITORS-IN-CHIEF

### Asian Pacific, African and organizing Editor

S.L. Chan  
*The Hong Kong Polyt. Univ.,  
Hong Kong*

### American Editor

W.F. Chen  
*Univ. of Hawaii at Manoa, USA*

### European Editor

R. Zandonini  
*Trento Univ., Italy*

## INTERNATIONAL EDITORIAL BOARD

F.G. Albermani  
The Univ. of Queensland, Australia

I. Burgess  
Univ. of Sheffield, UK

F.S.K. Bijlaard  
Delft Univ. of Technology, The Netherlands

R. Bjorhovde  
The Bjorhovde Group, USA

M.A. Bradford  
The Univ. of New South Wales, Australia

D. Camotim  
Technical Univ. of Lisbon, Portugal

C.M. Chan  
Hong Kong Univ. of Science & Technology, Hong Kong

T.H.T. Chan  
Queensland Univ. of Technology, Australia

S.P. Chiew  
Nanyang Technological Univ., Singapore

W.K. Chow  
The Hong Kong Polyt. Univ., Hong Kong

K.F. Chung  
The Hong Kong Polyt. Univ., Hong Kong

G.G. Deierlein  
Stanford Univ., California, USA

L. Dezi  
Univ. of Ancona, Italy

D. Dubina  
The Politehnica Univ. of Timisoara, Romania

R. Greiner  
Technical Univ. of Graz, Austria

L. Gardner  
Imperial College of Science, Technology and  
Medicine, UK

L.H. Han  
Tsinghua Univ. China

S. Herion  
University of Karlsruhe, Germany

G.W.M. Ho  
Ove Arup & Partners Hong Kong Ltd., Hong Kong

B.A. Izzuddin  
Imperial College of Science, Technology and  
Medicine, UK

J.P. Jaspart  
Univ. of Liege, Belgium

S. A. Jayachandran  
IIT Madras, Chennai, India

S.E. Kim  
Sejong University, South Korea

S. Kitipornchai  
City Univ. of Hong Kong, Hong Kong

D. Lam  
Univ. of Bradford, UK

G.Q. Li  
Tongji Univ., China

J.Y.R. Liew  
National Univ. of Singapore, Singapore

E.M. Lui  
Syracuse Univ., USA

Y.L. Mo  
Univ. of Houston, USA

J.P. Muzeau  
CUST, Clermont Ferrand, France

D.A. Nethercot  
Imperial College of Science, Technology and  
Medicine, UK

Y.Q. Ni  
The Hong Kong Polyt. Univ., Hong Kong

D.J. Oehlers  
The Univ. of Adelaide, Australia

K. Rasmussen  
The Univ. of Sydney, Australia

J.M. Rotter  
The Univ. of Edinburgh, UK

C. Scawthorn  
Scawthorn Porter Associates, USA

P. Schaumann  
Univ. of Hannover, Germany

G.P. Shu  
Southeast Univ. China

L. Simões da Silva  
Department of Civil Engineering, University of  
Coimbra, Portugal

J.G. Teng  
The Hong Kong Polyt. Univ., Hong Kong

G.S. Tong  
Zhejiang Univ., China

K.C. Tsai  
National Taiwan Univ., Taiwan

C.M. Uang  
Univ. of California, USA

B. Uy  
University of Western Sydney, Australia

M. Veljkovic  
Univ. of Lulea, Sweden

F. Wald  
Czech Technical Univ. in Prague, Czech

Y.C. Wang  
The Univ. of Manchester, UK

Y.L. Xu  
The Hong Kong Polyt. Univ., Hong Kong

D. White  
Georgia Institute of Technology, USA

E. Yamaguchi  
Kyushu Institute of Technology, Japan

Y.B. Yang  
National Taiwan Univ., Taiwan

Y.Y. Yang  
China Academy of Building Research, Beijing,  
China

B. Young  
The Univ. of Hong Kong, Hong Kong

X.L. Zhao  
Monash Univ., Australia

Z.H. Zhou  
Alpha Consultant Ltd., Hong Kong

## General Information

### *Advanced Steel Construction, an international journal*

#### **Aims and scope**

The International Journal of Advanced Steel Construction provides a platform for the publication and rapid dissemination of original and up-to-date research and technological developments in steel construction, design and analysis. Scope of research papers published in this journal includes but is not limited to theoretical and experimental research on elements, assemblages, systems, material, design philosophy and codification, standards, fabrication, projects of innovative nature and computer techniques. The journal is specifically tailored to channel the exchange of technological know-how between researchers and practitioners. Contributions from all aspects related to the recent developments of advanced steel construction are welcome.

#### **Instructions to authors**

**Submission of the manuscript.** Authors may submit double-spaced manuscripts preferably in MS Word by emailing to one of the chief editors as follows for arrangement of review. Alternatively papers can be submitted on a diskette to one of the chief editors.

Asian Pacific, African and organizing editor : Professor S.L. Chan, Email: ceslchan@polyu.edu.hk  
American editor : Professor W.F. Chen, Email: waifah@hawaii.edu  
European editor : Professor R. Zandonini, Email: riccardo\_zandonini@ing.unitn.it

All manuscripts submitted to the journal are recommended to accompany with a list of four potential reviewers suggested by the author(s). This list should include the complete name, address, telephone and fax numbers, email address, and at least five keywords that identify the expertise of each reviewer. This scheme will improve the process of review.

#### **Style of manuscript**

**General.** Author(s) should provide full postal and email addresses and fax number for correspondence. The manuscript including abstract, keywords, references, figures and tables should be in English with pages numbered and typed with double line spacing on single side of A4 or letter-sized paper. The front page of the article should contain:

- a) a short title (reflecting the content of the paper);
- b) all the name(s) and postal and email addresses of author(s) specifying the author to whom correspondence and proofs should be sent;
- c) an abstract of 100-200 words; and
- d) 5 to 8 keywords.

The paper must contain an introduction and a conclusion. The length of paper should not exceed 25 journal pages (approximately 15,000 words equivalents).

**Tables and figures.** Tables and figures including photographs should be typed, numbered consecutively in Arabic numerals and with short titles. They should be referred in the text as Figure 1, Table 2, etc. Originally drawn figures and photographs should be provided in a form suitable for photographic reproduction and reduction in the journal.

**Mathematical expressions and units.** The Systeme Internationale (SI) should be followed whenever possible. The numbers identifying the displayed mathematical expression should be referred to in the text as Eq. (1), Eq. (2).

**References.** References to published literature should be referred in the text, in the order of citation with Arabic numerals, by the last name(s) of the author(s) (e.g. Zandonini and Zanon [3]) or if more than three authors (e.g. Zandonini et al. [4]). References should be in English with occasional allowance of 1-2 exceptional references in local languages and reflect the current state-of-technology. Journal titles should be abbreviated in the style of the Word List of Scientific Periodicals. References should be cited in the following style [1, 2, 3].

Journal: [1] Chen, W.F. and Kishi, N., "Semi-rigid Steel Beam-to-column Connections, Data Base and Modelling", Journal of Structural Engineering, ASCE, 1989, Vol. 115, No. 1, pp. 105-119.

Book: [2] Chan, S.L. and Chui, P.P.T., "Non-linear Static and Cyclic Analysis of Semi-rigid Steel Frames", Elsevier Science, 2000.

Proceedings: [3] Zandonini, R. and Zanon, P., "Experimental Analysis of Steel Beams with Semi-rigid Joints", Proceedings of International Conference on Advances in Steel Structures, Hong Kong, 1996, Vol. 1, pp. 356-364.

**Proofs.** Proof will be sent to the corresponding author to correct any typesetting errors. Alternations to the original manuscript at this stage will not be accepted. Proofs should be returned within 48 hours of receipt by Express Mail, Fax or Email.

**Copyright.** Submission of an article to "Advanced Steel Construction" implies that it presents the original and unpublished work, and not under consideration for publication nor published elsewhere. On acceptance of a manuscript submitted, the copyright thereof is transferred to the publisher by the Transfer of Copyright Agreement and upon the acceptance of publication for the papers, the corresponding author must sign the form for Transfer of Copyright.

**Permission.** Quoting from this journal is granted provided that the customary acknowledgement is given to the source.

**Page charge and Reprints.** There will be no page charges if the length of paper is within the limit of 25 journal pages. A total of 30 free offprints will be supplied free of charge to the corresponding author. Purchasing orders for additional offprints can be made on order forms which will be sent to the authors. These instructions can be obtained at the Hong Kong Institute of Steel Construction, Journal website: <http://www.hkisc.org>

The International Journal of Advanced Steel Construction is published quarterly by non-profit making learnt society, The Hong Kong Institute of Steel Construction, c/o Department of Civil & Structural Engineering, The Hong Kong Polytechnic University, Hung Hom, Kowloon, Hong Kong.

**Disclaimer.** No responsibility is assumed for any injury and / or damage to persons or property as a matter of products liability, negligence or otherwise, or from any use or operation of any methods, products, instructions or ideas contained in the material herein.

**Subscription inquiries and change of address.** Address all subscription inquiries and correspondence to Member Records, IJASC. Notify an address change as soon as possible. All communications should include both old and new addresses with zip codes and be accompanied by a mailing label from a recent issue. Allow six weeks for all changes to become effective.

#### **The Hong Kong Institute of Steel Construction**

HKISC

c/o Department of Civil and Structural Engineering,

The Hong Kong Polytechnic University,

Hunghom, Kowloon, Hong Kong, China.

Tel: 852- 2766 6047 Fax: 852- 2334 6389

Email: [ceslchan@polyu.edu.hk](mailto:ceslchan@polyu.edu.hk) Website: <http://www.hkisc.org/>

ISSN 1816-112X

Science Citation Index Expanded, Materials Science Citation Index and ISI Alerting

Copyright © 2012 by:

The Hong Kong Institute of Steel Construction.



ISSN 1816-112X

Science Citation Index Expanded,  
Materials Science Citation Index and  
ISI Alerting

#### EDITORS-IN-CHIEF

##### Asian Pacific, African and organizing Editor

S.L. Chan  
*The Hong Kong Polyt. Univ.,  
Hong Kong*  
Email: ceslchan@polyu.edu.hk

##### American Editor

W.F. Chen  
*Univ. of Hawaii at Manoa, USA*  
Email: waifah@hawaii.edu

##### European Editor

R. Zandonini  
*Trento Univ., Italy*  
Email: riccardo.zandonini@ing.unitn.it

# Advanced Steel Construction

*an international journal*

VOLUME 8 NUMBER 3

SEPTEMBER 2012

#### Technical Papers

- |   |     |
|---|-----|
| Restrained Buckling Behavior of Core Component in Buckling-Restrained Braces<br><i>J. Wu, R.J. Liang, C.L. Wang and H.B. Ge</i>   | 212 |
| An Experimental Study on Sandwich Composite Panel Infilled Steel Frames<br><i>Hetao Hou, Canxing Qiu, Jingfeng Wang and Guoqiang Li</i>                                     | 226 |
| Residual Web Bearing Capacity of Corroded Steel Beams<br><i>Yasser Sharifi</i>  | 242 |
| A Bifurcation Analysis of Space Structures by Using 3D Beam-Column Element Considering Finite Deformations and Bowing Effect<br><i>K.S. Lee and S.E. Han</i>                | 256 |
| Slim Buckling-Restrained Steel Plate Shear Wall and Simplified Model<br><i>Ye Lu and Guoqiang Li</i>  | 282 |
| Viscous Dissipative, Ductility-based and Elastic Bracing Design Solutions for An Indoor Sports Steel Building<br><i>Stefano Sorace, Gloria Terenzi and Gianluca Bertino</i> | 295 |

# RESTRAINED BUCKLING BEHAVIOR OF CORE COMPONENT IN BUCKLING-RESTRAINED BRACES

J. Wu<sup>1,2</sup>, R.J. Liang<sup>1</sup>, C.L. Wang<sup>2,3</sup> and H.B. Ge<sup>2,3\*</sup>

<sup>1</sup> Key Laboratory of Concrete and Prestressed Concrete Structures of the Ministry of Education, Southeast University, Sipailou 2, Nanjing 210096, China

<sup>2</sup> International Institute for Urban Systems Engineering, Southeast University, Sipailou 2, Nanjing 210096, China

<sup>3</sup> Department of Civil Engineering, Meijo University, Tempaku-ku, Nagoya 468-8502, Japan

\*(Corresponding author: E-mail: gehanbin@meijo-u.ac.jp)

Received: 30 May 2011; Revised: 27 July 2011; Accepted: 12 August 2011

---

**ABSTRACT:** In order to investigate the bending moment of the core plate as well as the contact force between the core plate and the restraining component of a Buckling-Restrained Brace member, focus is set to the multi-wave buckling behavior of the core plate under increasing axial load. Based on the equilibrium equation of a segment subjected to axial and lateral forces, equations are derived to describe the deflection curve, the distribution of the moment of the core plate and the contact force. Discussion about these equations reveals the process of multi-wave buckling of the core plate, which is different with that of a free buckling without the lateral restraining component. The core plate experiences point contact, line contact and new wave generation repeatedly, and the axial loads corresponding to different states are given. A calculation example illustrates that the derived equations agree with numerical results, and an experimental result is used to verify the equations.

**Keywords:** Buckling-restrained brace, Restrained buckling, Contact, Multi-wave buckling

---

## 1. INTRODUCTION

Buckling-Restrained Brace (BRB) is a kind of metal-yield energy-dissipation device. The core plate of a BRB, which sustains the axial tension and compression under strong earthquakes, is expected to yield before the main structural members. Because BRBs dissipate the energy inputted by the earthquake through the post-yield hysteretic behavior, structural seismic responses decrease and main structural members are kept away from severe damage. Due to the advantages of BRBs such as stable hysteretic characteristics, simplicity in installation and low cost, they have been applied extensively in many building structures as well as bridges in Japan, North American and China (Uang et al. [1], Lai and Tsai [2], Xie [3], Luo et al. [4], Chen et al. [5]).

As shown in Figure 1, a BRB mainly consists of the core plate, the unbonding material and the restraining component (Watanabe et al. [6]). The core plate, commonly made of the low yield metal with a rectangle or cross sectional shape, is designed to resist the axial force. The restraining component is designed to enhance the bending stiffness of the BRB and restrict the buckling amplitude of the core to prevent the BRB from overall buckling. Furthermore, the core plate is expected to yield in both compression and tension and exhibits the stable and repeatable elasto-plastic hysteretic behavior. As shown in Figure 1, the restraining component is manufactured with a steel tube filled with concrete or mortar. Between the core plate and the restraining component, there is an unbonding material to reduce the friction and eliminate the force transferred from the core plate to the restraining component when the BRB is subjected to the compressive force.

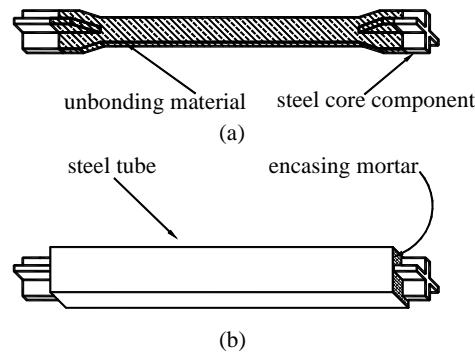


Figure 1. Concept of a Type of Buckling-Restrained Brace (Watanabe et al. [6])

Due to the confinement of the restraining component, the compressed core plate will generate high-order, slight-amplitude and multi-wave buckling shape, which is a kind of restrained buckling or constrained buckling. The buckling mode shape of a restrained buckling member cannot develop freely like Euler buckling because the existence of the restraining component, which lead to great changes of the behavior of the core plate (Guo and Ren [7]). Sridhara [8] proposed a compressive member embedded in a tube and derived the buckling load when the point contact occurs between the core plate and the tube, using the linear elastic small deflection theory and supposing that the deflection is infinity when the member buckles. Prasad [9] carried out a series of compression test of the typical sleeved member with fixed ends, and obtained the longitudinal force-displacement curve, which demonstrated a temporary drop in load when the core jumped from one mode to other. Domokos et al. [10] analyzed the force-displacement curve of the compressed elastic beam between the rigid, frictionless side-walls through theoretical formula, numerical analysis and tests. Ha [11] studied the rigid constrained buckling of the elastic column in a rigid tube when the point contact and line contact occur, using the calculation model like Domokos's [10]. Chai [12] carried out the theoretical analysis and experimental test on the post-buckling behavior of the compressed elastic column between two straight, rigid and frictionless side-walls in 1998, and obtained the similar force-displacement curve as given in the reference [10]. Shen and Deng [13-14] proposed the mechanical model when the line contact occurs between the core plate and the flexible outer tube.

Generally, a BRB member will break due to the low cycle fatigue of the core plate when subjected to the reversed cyclic loading with the large strain amplitude. It is obvious that the capacity of the low cycle fatigue is related to the maximum strain encountered during the loading procedure, such as the maximum compressive strain of the core plate, which is the combination of the average strain due to the axial force and the bending strain due to the curvature of the multi-wave buckling. The significant contact force and the consequent friction between the core plate and the restraining component take place when the core plate is subjected to the compression force. Consequently, the restraining component sustains part of the axial force. However, the contact and friction forces disappear because the buckled waves of the core plate under the tension are straightened. So, the compressive force of the core plate is greater than its tensile force with the same strain amplitude and the hysteric behavior of the BRB is asymmetric.

The low-cycle fatigue property and the hysteretic behavior are greatly influenced by the behavior of the core plate, indicating that the restrained buckling behavior of the core is an important problem in the researches of the BRB. Although the experiment demonstrated that the multi-wave buckling occurs in the core plate (Usami et al. [15]), the buckling mechanism of the core plate needs to be further investigated. Based on the compressive equilibrium equation of a member restrained by contact, this paper derives the deflection curve of the core plate, which is contacted with two rigid restraining components in point and in line, and reveals the process and mechanism of the multi-wave buckling of the core plate.

## 2. ASSUMPTIONS

When analyzing the behavior of a BRB member, it should be included in consideration of the geometric nonlinear effect caused by the buckling behavior of the core plate in compression, the contact nonlinear effect caused by contact restraint of the lateral restraining component, and the material nonlinear effect while the BRB develops post-yield strain. Therefore, the mechanical simulation of the BRB's core component is a complex nonlinear problem. On the basis of the actual conditions for a common BRB member, several assumptions are adopted in this paper as follows:

- 1) The bending deformation of the restraining component is neglected. Generally, the bending stiffness of the restraining component is much greater than that of the core plate. The lateral deformation of the restraining component caused by the contact forces is extremely slight, so that it can be ignored.
- 2) Two ends of the core plate do not rotate during the loading process. This is due to the large bending stiffness at the ends, which are usually enhanced with stiffeners in the vertical plane.
- 3) Two ends of the core plate are constantly close or contacted with one side of the restraining component. The original position of the core may be parallel to the restraining component, or a little deviate in the range of the clearance. However, when the core buckles in compression and subsequently contacts with the restraining component, the contact force in the middle makes both ends of the core contact with the opposite side of the restraining component. Obviously, only the symmetric buckling mode shape is considered in this assumption. The reference [10] implied that the duration of an antisymmetric buckling mode was very short so that the wave was unstable and would jump into higher modes randomly. In this paper, only symmetric buckling modes are considered.
- 4) The elastic modulus of the core plate remains constant. The modulus keeps constant before the core plate yields, and it decreases as the core experiences post-yielding, especially during the severe tension-compression cyclic loading with large inelastic strains. The difficulty of the inelastic buckling is that the modulus in the loading zone of a section may differ from that in the unloading zone, which causes the buckling load difficult to solve. However, according to the *Shanley concept*, the tangent modulus solution of inelastic buckling load is the lower limit and close to the experimental results. It implies that as inelastic buckling is under consideration, the elastic modulus in corresponding equations can be simply replaced by the tangent modulus to obtain a reasonable solution.
- 5) The axial deformation of the core in compression is neglected. The length of the compressed core plate will decrease due to the bending caused by buckling and the deformation caused by the axial force. For a BRB member, the clearance between the core plate and the restraining component, which is the maximum amplitude for the buckling deformation, is very small, so that the bending-caused deformation is slight and negligible. The compressed deformation caused by the axial force is also very small and can be ignored.
- 6) The friction between the core plate and the restraining component is neglected. Due to the lateral deformation of the core plate and consequently contact forces between the core plate and the restraining component, the friction forces arise inevitably as the core plate buckles under compression. However, the magnitude of the friction forces is relatively small compared with the axial force the BRB member sustained, and the existence of the friction will make the problem complex. In order to simplify the derived equations, this study does not consider the friction effects.

### 3. DEFLECTION SHAPE OF CORE COMPONENT DURING BUCKLING PROCESS

#### 3.1 Deflection Equation under Axial and Lateral Forces

According to the assumptions (1) to (3), a BRB in its initial state is sketched in Figure 2(a), where  $L$ ,  $E$  and  $I$  are the length, elastic modulus and moment of inertia of the core plate, respectively, and  $2y_0$  is the clearance between the core plate and the far-side restraining component. As presented in Figure 2(b), when the increasing axial compression force  $P$  reaches to the Euler force  $P_E$  of the slender core plate with the  $L$  length, it buckles and makes critical contact with the far-side restraining component. The Euler force is given as follows:

$$P_E = \frac{4\pi^2 EI}{L^2} \tag{1}$$

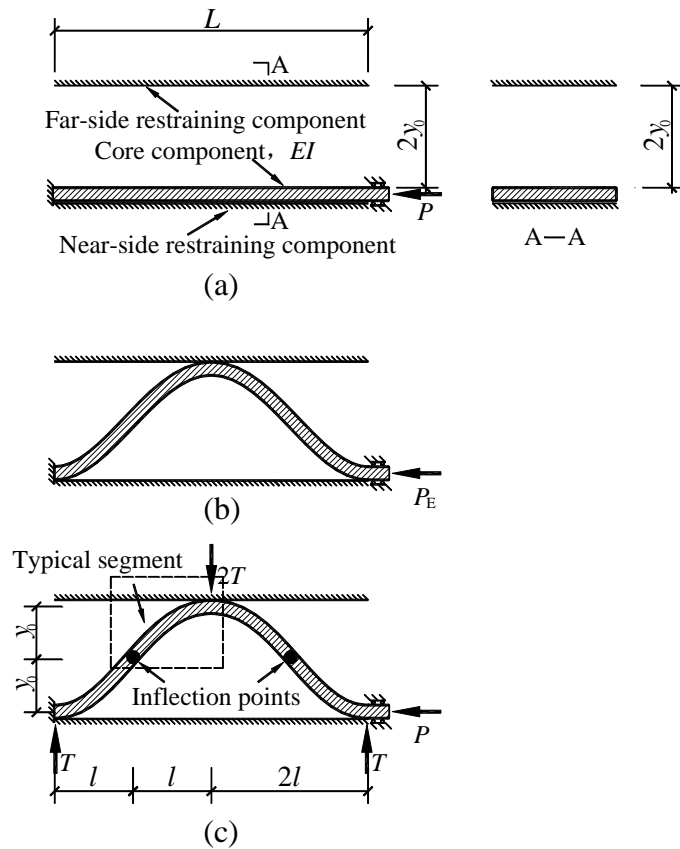


Figure 2. Buckling Process of Core Component

The deflection of the core plate tends to be developed with the increase of the axial force  $P$ , but the amplitude of the deformation is suppressed by the lateral restraining component. Therefore, the contact force generates between the core plate and the restraining component. As given in Figure 2(c),  $T$  is the shear force in the free segment between two contact points, and the distance between the two adjacent contact points is defined as  $2l$ . Considering the symmetry, any segment between the inflection point and the contact point is identical, and one is illustrated in Figure 3. Obviously, the segment under the combination of the axial force  $P$  and the contact force  $T$  satisfies:

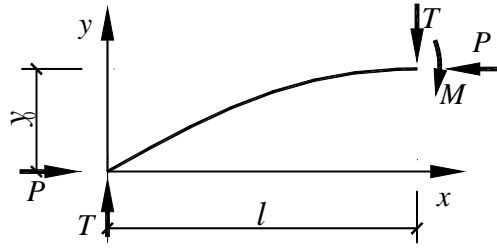


Figure 3. Calculating Diagram of Segment under Axial and Contact Forces

$$Py - Tx + EI \frac{d^2 y}{dx^2} = 0 \quad (2)$$

According to the boundary conditions  $(x = 0, y = 0)$  and  $(x = l, y = y_0)$ , the deflection equation of this member can be obtained as:

$$y = \frac{\sin\left(\alpha \frac{x}{l}\right)(Py_0 - Tl)}{P \sin \alpha} + \frac{T}{P}x \quad (3)$$

where  $\alpha$  is the dimensionless nominal axial force relative to the Euler buckling load:

$$\alpha = \frac{\pi}{2} \sqrt{\frac{P}{P_E}} \quad (4)$$

Specially, in the state of critical point contact, there are  $T = 0$  and  $\alpha = \pi/2$ , which lead to the deflection equation of this situation as:

$$y = y_0 \sin\left(\frac{\pi x}{2l}\right) \quad (5)$$

### 3.1 The Point Contact Situation

According to the symmetry of the core plate about the middle contact point, there is:

$$y'|_{x=l} = 0 \quad (6)$$

Substituting condition (6) into Eq. 3 gives half of the contact force in the middle contact point,

$$T = \frac{Py_0}{\alpha - \tan(\alpha)} \frac{\alpha}{l} \quad (7)$$

The deflection curve of the segment can be derived by substituting Eq. 7 into Eq. 3. That is,

$$y = y_0 \frac{1}{\tan \alpha - \alpha} \left( \frac{\sin\left(\alpha \frac{x}{l}\right)}{\cos \alpha} - \alpha \frac{x}{l} \right) \tag{8}$$

At the same time, the moment of the segment under this condition can be derived as follows:

$$M = Py - Tx = -EI \frac{d^2y}{dx^2} = Py_0 \frac{1}{\sin(\alpha) - \alpha \cos(\alpha)} \sin\left(\alpha \frac{x}{l}\right) \tag{9}$$

Figures 4 and 5 compare the deflection and moment curves of the core segment when  $\alpha/\pi$  is 0.5, 0.6, 0.7, 0.8, 0.9 and 1.0, respectively. As shown in these figures, the core segment and the restraining component always keep the state of the point contact in the above loading range. The increase of the axial force changes the deflection shape gradually, and makes the deflection curve plump and close to the restraining component around the contact point. Moreover, the position of the maximum moment moves from the contact point to the midpoint of this segment. When  $\alpha = \pi$  and  $P = 4P_E$ , the moment or the curvature of the core segment at the contact point decreases to 0, indicating that the condition  $\alpha = \pi$  is the end of the point contact state as well as the beginning of the line contact state, as given in the reference [13]. In other words, the point contact between the core plate and the restraining component occurs when  $0.5\pi < \alpha < \pi$ .

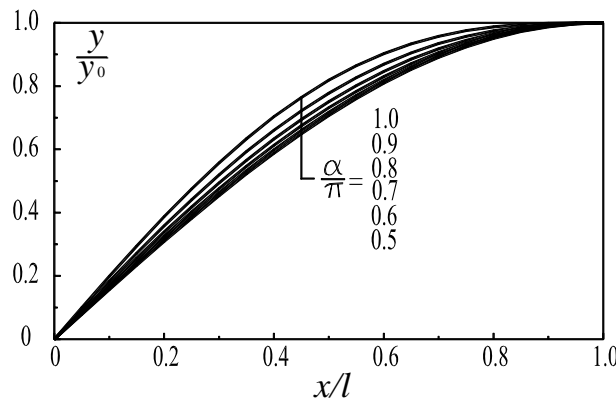


Figure 4. Deflection Curves under Different Axial Forces

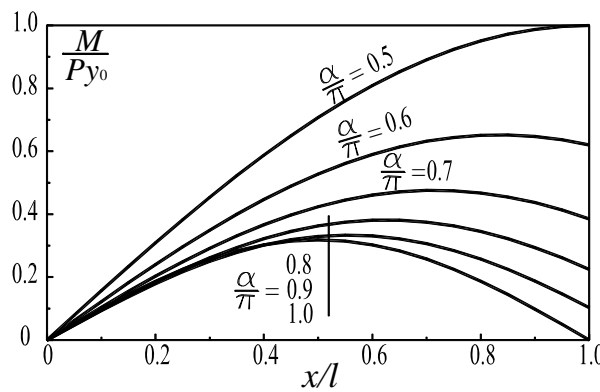


Figure 5. Moment Curves under Different Axial Forces

It is obvious that the difference between the restrained buckling and the free buckling can be investigated in the above derivation. As  $P = 4P_E$ , the segment buckles at the second order buckling mode for the free buckling, where the deflection curve performs two complete waves; while in the restrained buckling, there is only one complete wave under this load, because the contact force, which can be regarded as an intermediate action of the slender segment, enhances the lateral supporting stiffness to the core segment.

### 3.2 State of Line Contact

After the situation of  $\alpha = \pi$ , the increase of the axial force  $P$  tends to curve the segment plumper, resulting in the line contact between the segment and the restraining component. The free length of the segment that does not contact with the restraint,  $2l$ , tends to be reduced, and the corresponding Euler buckling load of the free segment is:

$$P_E' = \frac{\pi^2 EI}{4l^2} \quad (10)$$

Note that the free length in this situation is smaller than that in the point contact state. At this situation, only two concentrated contact forces exist at the two ends of contacted line, while in the rest part of the line there is no distributed contact force because the deflection curve is flat. The deflection equation of the free segment is the same as that in the end of point contact state except for the difference in the length of free segment. Owing to  $\alpha = \pi$ , the deflection equation at this point is:

$$y = y_0 \left[ \frac{1}{\pi} \sin\left(\pi \frac{x}{l}\right) + \frac{x}{l} \right] \quad (11)$$

In the situation of line contact, when investigating the nominal axial force  $\alpha$  with Eq. 4, the  $P_E$  should be replaced with  $P_E'$ , that is,

$$\alpha = \frac{\pi}{2} \sqrt{\frac{P}{P_E'}} \quad (12)$$

According to that  $\alpha = \pi$ , the half of the free length,  $l$  can be obtained by combining the Eq. 10 and Eq. 12, that is,

$$l = \pi \sqrt{\frac{EI}{P}} \quad (13)$$

The deflection curve of the core plate in this situation is shown in Figure 6.

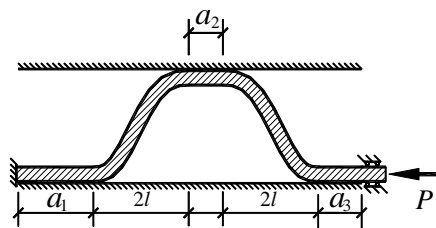


Figure 6. Illustration of State of Line Contact

### 3.3 Generation of New Wave

In Figure 6,  $a_1$ ,  $a_2$  and  $a_3$  are the lengths of the line contact segments. Note that the sum of the contacted lengths may be distributed arbitrary in these three segments. That is to mean, in some cases,  $a_1$  may be the largest one among the three, while in other cases that is  $a_2$  or  $a_3$ . The reason of this phenomenon lies in the total strain energy stored in the core plate. Given the same total length and shape of the free segments, the strain energy remains constant in spite of how the segments are distributed in longitude. As the axial force increases, the contact lines extend while each free part behaves like an independent segment with fixed ends without intermediate actions. If the contacted line extends sufficiently to occur a new buckling, the new waveform will be generated.

Obviously, in the event that all of the contacted line concentrates on one segment, this segment holds the maximum length to generate a potential buckling. Without loss of generality, all contact lengths are assumed to be concentrated to  $a_1$ , while  $a_2 = a_3 = 0$ , as shown in Figure 7(a). According to the above discussion, at the critical state of the new buckling, the length of the contacted line is controlled as follow:

$$P = \frac{4\pi^2 EI}{a_1^2} \quad (14)$$

While according to the 5th assumption, the total length of the core plate remains constant, that is

$$a_1 = L - 4l = L - 4\pi \sqrt{\frac{EI}{P}} \quad (15)$$

Substituting Eq. 15 into Eq. 14, while the second wave generates, the axial force is:

$$P = 36 \frac{\pi^2 EI}{L^2} = 9P_E \quad (16)$$

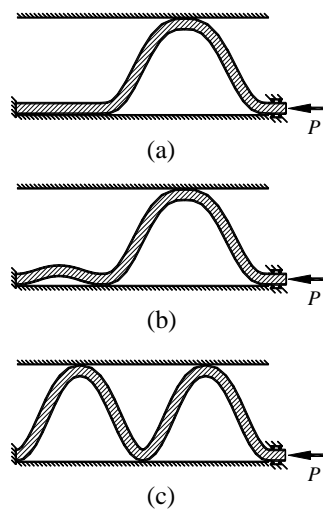


Figure 7. Process of New Wave Generation

Substituting Eq. 16 into Eq. 13 and Eq. 15, respectively, half the length of the free segment and the length of contact line can be derived as follows:

$$l = \frac{1}{6}L, \quad a_1 = \frac{1}{3}L \quad (17)$$

According to Eq. 17, the deflection curve of the core plate behaves asymmetric at the moment of the new wave generating. One part of the core plate is in the point contact situation with contact forces at the ends, while the other part is in the neutral equilibrium state of the beginning of a new buckling, as shown in Figure 7(b). However, this status is not stable because of the high potential energy, resulting in a quick alteration to a symmetrical contact state with two waves, which occupies lower energy, as shown in Figure 7(c). In this situation, there are  $l = L/8$  and  $P = 36\pi^2 EI/L^2$ . Substituting these parameters into Eq. 12 gives the nominal axial load of this state, that is,

$$\alpha = \frac{3}{4}\pi \quad (18)$$

As the above nominal axial force satisfies the condition  $0.5\pi < \alpha < \pi$ , it indicates that the core plate switches to a point contact state as soon as the new wave occurs. After that, an increase of the axial force will drive the core behaving as two separate segments, each of which is as that described in Figure 2(a), and with the length of  $L/2$ . At the same time, the nominal axial force  $\alpha$  increases to  $\pi$ , then the line contact will occur and a new wave will be generated subsequently.

### 3.4 Multi-wave Buckling

As discussed above, the point contact, line contact and new wave generation occur repeatedly under the increasing axial compression force for the restrained core component. If  $n$  waves have been generated for the core, each wave will develop as a separate segment with the length of  $L/n$ . According to the condition  $\alpha = \pi$ , the axial force at the end moment of point contact situation is:

$$P = 4P_E' = (2n)^2 P_E \quad (19)$$

Similarly, at the moment of generating a new wave, considering the length consistent condition of the core plate, that is, the summation of the contacted length and the waved-segment lengths equals to the original length, there is,

$$a_1 = L - 4n\pi \sqrt{\frac{EI}{P}} \quad (20)$$

Substituting Eq. 20 into Eq. 14, gives the axial force as the  $n + 1$ th wave generates

$$P = (2n + 1)^2 P_E \quad (21)$$

In the process of the axial force increasing, the value of the dimensionless nominal axial force relative to the free length of the current wave,  $\alpha$ , always keeps between  $\pi/2$  and  $\pi$ . The relationship between  $\alpha$  and the actual axial forces is shown in Figure 8. In this figure, the curved lines, which are very close to slash lines in Figure 8, represent the slow alterations of the deflection shapes in their current waveforms, while the horizontal lines represent the gradual increases of the contacted lengths, and the vertical lines represent the sudden increases of the number of waves. As a result, a point contact between the core plate and the restraining component occurs and continues when the axial force increases from  $(2n - 1)^2 P_E$  to  $(2n)^2 P_E$ , and the line contact between them

occurs and continues when the axial force increases from  $(2n)^2 P_E$  to  $(2n+1)^2 P_E$ .

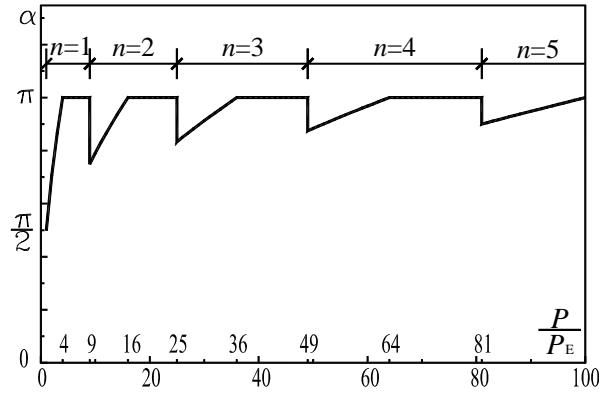


Figure 8. Relationship between  $\alpha$  and Axial Force

### 3.5 Contact Force

As illustrated in Figure 2(c), the contact force resisted by the core plate depends on the shear force of the curved segment,  $T$ . In case of the point contact between the core plate and the restraining component, the core plate can be regarded as  $n$  identical waves, each of which with the length of  $L/n$ , thus

$$l = \frac{L}{4n} \quad (22)$$

Applying Eq. 22 in Eq. 7, the shear force of the free segment is:

$$T = \frac{Py_0}{\sqrt{\frac{PL^2}{16n^2EI} - \tan\left(\sqrt{\frac{PL^2}{16n^2EI}}\right)}} \sqrt{\frac{P}{EI}} \quad (23)$$

And in case of line contact, applying  $\alpha = \pi$  and  $l = \pi\sqrt{\frac{EI}{P}}$  in Eq. 7, the shear force of the free segment can be derived as,

$$T = \frac{Py_0}{\pi} \sqrt{\frac{P}{EI}} \quad (24)$$

Several conclusions can be drawn by investigating the Eq. 23 and Eq. 24. The contact force is proportional to the clearance between the core plate and the restraining component. On the other hand, the contact force is monotonic increasing about the axial force applied to the core plate, and monotonic decreasing about the bending stiffness of the core plate. That is, the contact force will increase as the clearance increases, or as the axial force increases, or on the other hand as the bending stiffness of the core plate decreases. These findings are meaningful to design a BRB member, because the contact force is the main reason that causes the friction between the core plate and the restraining, while the friction, which causing the restraining component to resisting the axial force, leads to larger compressive yield capacity than predicted. For example, in order to minish the friction, a reasonable solution can be obtained by detailing the clearance as small as possible, or strengthening the bending stiffness of the core plate.

#### 4. NUMERICAL EXAMPLE

A core plate, with the width and the thickness of 0.1m and 0.01m respectively, is encased between two rigid, frictionless restraining components, with the clearance of 0.02m. The original location of the core plate satisfies the 3<sup>rd</sup> assumption mentioned above. The elastic modulus of the material is  $E = 2 \times 10^5 \text{ N/mm}^2$ , and the Euler buckling load is  $P_E = 65.797 \text{ kN}$ .

Figure 9 illustrates the maximum moment of the core plate calculated by Eq. 9 with the increasing of the axial force. The shear forces of the free segment calculated by Eqs. 23 or 24 are presented in Figure 10.

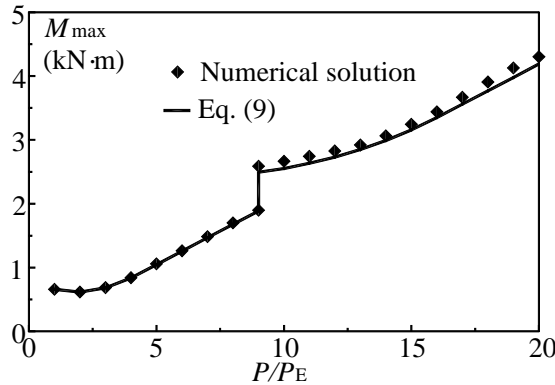


Figure 9. Relationship between Maximum Moment of Core and Axial Force

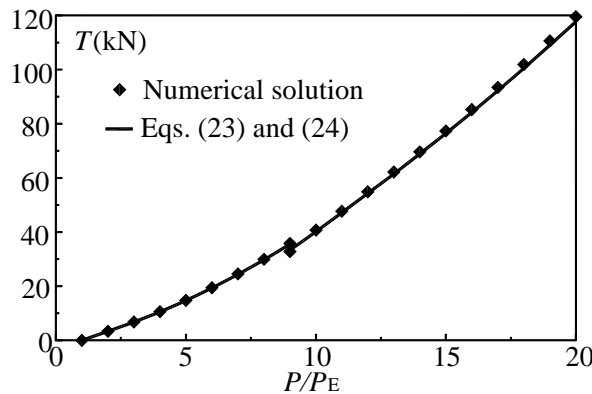


Figure 10. Relationship between Contact Force and Axial Force

As shown in Figures 9 and 10, an abrupt shift occurs both to the maximum moment and the contact force at  $P/P_E = 9$ . This phenomenon is caused by the mode shape jumping of the core plate from one to two waves at this load level.

A corresponding numerical model is established using the program ANSYS. The core plate and the rigid restraining components are modeled using the Beam189 element. They are divided into 60 elements along the longitude and covered with Conta176 and Targe170 elements, respectively. One end of the core is fixed, and the other end is clamped and subjected to an increasing axial force. The maximum moments of the core and the shear forces of the free segment under different axial force levels are also plotted in Figures 9 and 10, respectively, describing the consistency with the theoretical results. From the figures, the maximum error between the maximum moments calculated by the proposed equations and the numerical results is 4.3%, while that of the shear force is 1.4%. These disparities may be due to the error introduced in the nonlinear iteration of the numerical simulation, as well as the shortening of the core plate in longitude, which is neglected in this paper.

## 5. EXPERIMENTAL VERIFICATION

A sandwich BRB specimen is experimentally studied to verify the theoretical derivation. The core component of the specimen is a steel plate with the thickness of 10 mm, the width of 100 mm, and the length of the yielding segment  $L$  of 1075 mm. The measured elastic modulus of the steel is  $2.04 \times 10^5 \text{ N/mm}^2$ . The restraining component is composed of two cover plates with the thicknesses of 14mm connected by high-strength bolts through two side plates with the thicknesses of 12 mm. The core plate is covered with 1-mm-thick butyl rubber tapes as the unbonding material to reduce the friction force between the core and restraining components. The schematic diagram of this specimen is shown in Figure 11.

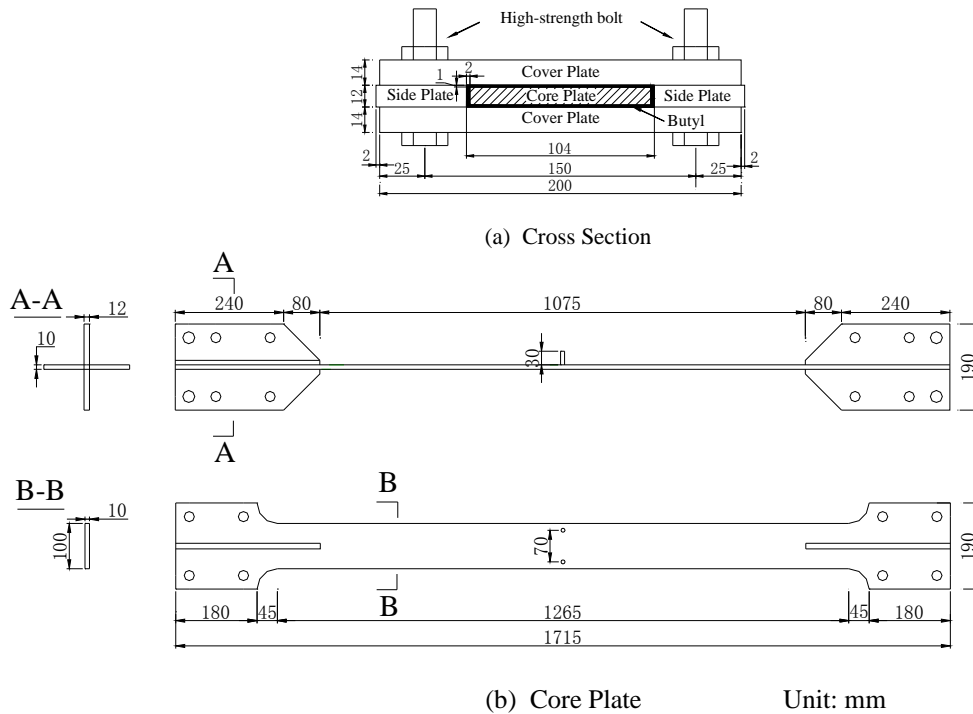


Figure 11. Schematic Diagram of BRB Specimen

When the core plate is under the compressive loading, the multi-wave buckling occurs. The unbonding material is pressed upon the restraining components and the final buckling shape is printed on the butyl rubber tape. A low-cycle static loading test with the strain amplitude of 2% is conducted, and the hysteretic curve is plotted in Figure 12. As shown in this curve, the tangent modulus after yielding,  $E'_t$ , can be measured as  $3.34 \times 10^3 \text{ N/mm}^2$ , and the maximum compressive loading  $P$  is 393 kN. According to the 4<sup>th</sup> assumption, the tangent modulus,  $E'_t$ , is used in Eq. 1 as  $E$ , so that  $P_E$  is calculated as 0.95 kN and  $P/P_E$  is equal to 413, which is between  $(2 \times 10)^2$  and  $(2 \times 10 + 1)^2$ . It indicates that the number of the final buckling wave is 10.

After the test, the unbonding material attached on the surface of the restraining component can reflect the multi-wave buckling shape clearly. As presented in Figure 13, the number of the final buckling wave is 10. It demonstrates that the theoretical result is identical with the test one.

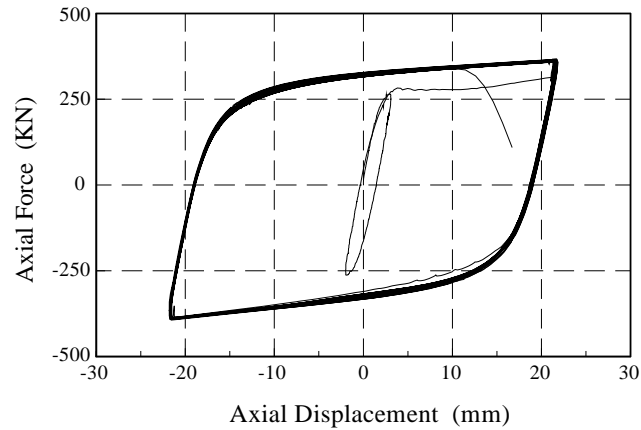


Figure 12. Hysteretic Curve of the BRB

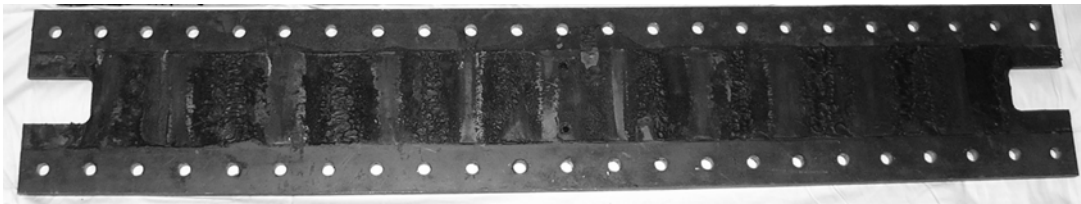


Figure 13. The Buckling Wave Print at the Cover Plate

## 6. CONCLUSIONS

Based on mechanical characteristics of the BRB member, some reasonable assumptions are introduced to establish the equilibrium equation of a free segment of the core under the combination of the axial compression and lateral contact forces. The equations used to describe the deflection curve, the moment distribution and the contact force of the core in the state of the point contact and the line contact, are derived. The discussion about the derived equations reveals the process and mechanism of the multi-wave buckling behavior under the increasing axial force. Some conclusions are summarized as follows:

- 1) The feature of a restrained buckling is different with that of a free buckling because the contact force acts like an intermediate support of the slender member, which strengthens the lateral stiffness of the member.
- 2) As the axial force increasing, the point contact and the line contact occur alternately. When the length of the contacted line accumulates enough to generate a new wave, a jump will occur to a higher order point contact state.
- 3) In the line contact state, the lengths of the contact lines may distribute arbitrarily in longitude. However, if they are concentrated to one segment, the new wave will be generated most easily.
- 4) As the axial force increasing, the point contact will occur while the axial force satisfies the condition  $P/P_E \in ((2n-1)^2, (2n)^2)$ . In this situation, the free segment maintains its equilibrium by changing its deflection curve. On the other hand, the line contact will occur as  $P/P_E \in ((2n)^2, (2n+1)^2)$ , during which the equilibrium is guaranteed by decreasing the length of the free segment and increasing the length of the contact lines.

5) The contact force is proportional to the clearance between the core and the restraining component. It is also influenced by the axial force it sustained and the bending stiffness of the core plate.

## ACKNOWLEDGEMENT

The authors would like to acknowledge financial supports from the National Natural Science Foundation (50878055, 51008077) and the Priority Academic Program Development of Jiangsu Higher Education Institutions.

## REFERENCES

- [1] Uang, C.M., Nakashima, M. and Tsai, K.C., "Research and Application of Buckling-Restrained Braced Frames", *International Journal of Steel Structures*, 2004, Vol. 4, No. 4, pp. 301-313.
- [2] Lai, J.W. and Tsai, K.C., "Research and Application of Buckling Restrained Braces in Taiwan", *ANCER Annual Meeting*, Hawaii, USA, 2004.
- [3] Xie, Q., "State of the Art of Buckling-Restrained Braces in Asia", *Journal of Constructional Steel Research*, 2005, Vol. 61, No. 6, pp. 727-748.
- [4] Luo, X.Q., Ge, H.B. and Usami, T., "Dynamic Numerical Simulation of Steel Frame-Typed Piers Installed with SMA Damping Devices Based on Multi-linear One Dimensional Constitutive Model", *International Journal of Advanced Steel Construction*, 2010, Vol. 6, No. 2, pp. 722-741.
- [5] Chen, Z.Y., Ge, H.B. and Usami, T., "Analysis and Design of Steel Bridge Structures with Energy Absorption Members", *International Journal of Advanced Steel Construction*, 2008, Vol. 4, No. 3, pp. 173-183.
- [6] Watanabe, A., Hitomi, Y., Saeki, E., et al., "Properties of Brace Encased in Buckling-restraining Concrete and Steel Tube", *Proceedings of 9<sup>th</sup> World Conference on Earthquake Engineering*, Tokyo-Kyoto, Japan, 1988, Vol. 4, pp. 719-724.
- [7] Guo, Y.T. and Ren, W.M., "Some Advances in Confined Buckling", *Advances in Mechanics*, 2004, Vol. 34, No. 1, pp. 41-52 (in Chinese).
- [8] Sridhara, B.N., "Sleeved Compression Member", USA: 5175972, 1993.
- [9] Prasad, B.K., "Experimental Investigation of Sleeved Column", *Proceedings of the 33<sup>rd</sup> AIAA/ASCE Structures, Structural Dynamics and Materials Conference*, Dallas, USA, 1992, pp. 991-999.
- [10] Domokos, G., Holmes, P. and Royce, B., "Constrained Euler Buckling", *Journal of Nonlinear Science*, 1997, Vol. 7, No. 3, pp. 281-314.
- [11] Ha, M.Q., "Study on the Mechanical Performances and Applications of Conventional and Innovative Buckling Restrained Braces", *Tongji University*, 2004 (in Chinese).
- [12] Chai, H., "The Post-buckling Response of a Bi-laterally Constrained Column", *Journal of the Mechanics and Physics of Solids*, 1998, Vol. 46, No. 7, pp. 1151-1181.
- [13] Shen, B. and Deng, C.G., "Continuous Transition from Point Contact to Line Contact between the Axially Compressed Inner Core and the Flexible Sleeve in a Sleeved Column", *Engineering Mechanics*, 2007, Vol. 24, No. 2, pp. 154-160 (in Chinese).
- [14] Shen, B. and Deng, C.G., "Buckling Analysis of an Axially Compressed Strut Constrained by a Flexible Sleeve", *Mechanics in Engineering*, 2006, Vol. 28, No. 5, pp. 43-46 (in Chinese).
- [15] Usami, T., Lu, Z.H. and Ge, H.B., "A Seismic Upgrading Method for Steel Arch Bridges Using Buckling-restrained Braces", *Earthquake Engineering and Structural Dynamics*, 2005, Vol. 34, No. 4-5, pp. 471-496.

# AN EXPERIMENTAL STUDY ON SANDWICH COMPOSITE PANEL INFILLED STEEL FRAMES

Hetao Hou <sup>1,2,3\*</sup>, Canxing Qiu <sup>1</sup>, Jingfeng Wang <sup>4</sup> and GuoQiang Li <sup>3</sup>

<sup>1</sup> Associate Professor, School of Civil Engineering, Shandong University, Jinan, China

<sup>2</sup> Postdoctor, Laiwu Steel Group Limited, Laiwu, Shandong, China

<sup>3</sup> Professor, School of Civil Engineering, Tongji University, Shanghai, China

<sup>4</sup> Associate Professor, School of Civil Engineering, Hefei University of Technology, Hefei, China

\*(Corresponding author: E-mail: houhetao@163.com)

Received: 31 May 2011; Revised: 28 August 2011; Accepted: 23 September 2011

---

**ABSTRACT:** Cyclic loading tests on eight full-scale one storey, one-bay test specimens were carried out to study the hysteretic behavior of steel frames infilled with sandwich composite panels. Six main influential parameters, including panel thickness, panel type, panel position, column orientation, beam-to-column connection type and connecting method of panel to steel frame are considered. Based on the experimental phenomena, seismic behaviors of specimens were reflected by hysteresis loops, skeleton curves, curves of strength degradation, curves of stiffness degradation, ductility coefficient and equivalent damping coefficient. Test results show that the failure modes of panels and steel frames are concrete spalling around the embedded parts, weld fracture, and local buckling of beam, respectively. The integrity of the panel is better than the traditional walls. The success of connection between panel and steel frame is significant to the mutual work of the two parts. Both of increasing the panel thickness and strengthening the connection can improve the seismic behavior of structure. At the end of the paper, seismic design recommendations based on the analysis of ductility index and energy dissipation of the structures are presented.

**Keywords:** Composite panels, Steel frames, Hysteretic behavior, Low cyclic loading tests

---

## 1. INTRODUCTION

Generally, the infilled walls in frame structures are intended to serve as internal partitions or external claddings. Therefore, the structures are always designed without taking account of the infilled walls in the overall behavior of the building. Nevertheless, although infilled walls are considered as non-structural parts in a frame, they have been widely recognized that the existence of infills within the interior of the buildings considerably improve their lateral stiffness, ultimate strength and energy dissipation capacity against earthquakes. In many cases of infilled frames with traditional walls made of concrete or bricks, much research have been carried out for analysis and design of these infilled frames when subjected to in-plane forces.

Polyakov [1,2] carried out parameter analysis of 65 large-scale infilled steel frames. The parameters included masonry units, mortar, method of loading, and wall openings. Besides individual panels, a three-story, three-bay frame of one-quarter scale was also tested. In the paper, Polyakov obtained the conclusion that the multistory-multibay infilled frame behaved as a group of individually braced frames, but not as a single monolith. The braced frame model was also confirmed by Papia et al. [3] and Cavaleri et al. [4] who defined a diagonal pin-jointed strut being able to represent the horizontal force-interstorey displacement cyclic law of the actual masonry infill. The proposed technique, unlike the previous empirical approaches, involves the axial stiffness of the columns of the frame more than their flexural stiffness. As a support of the analytical discussion, an experimental investigation involving single storey-single bay infilled reinforced concrete was carried out. The experimental results were taken into account to improve the proposed model.

Holmes [5] suggested a simple procedure for calculating the ultimate load and lateral displacement of steel frames with brickwork or concrete infilling. In the analytical model, the wall panel was replaced by an equivalent strut, the cross sectional area of which was obtained as  $td/3$ , by assuming that the reaction between the steel frame and infilling varies linearly along the frame beam. A comparison is then made with thirteen test results. The simplified equivalent strut for concrete block masonry walls was further studied (Khalid et al. [6]). In his paper, several quasi-static experiments on infilled frames were conducted. The specimens were quarter-scale semi-rigidly connected steel frames infilled with non-integral unreinforced concrete block masonry walls. Three primary parameters were investigated, including number of bays, material properties of the concrete blocks and the mortar joint, and type of infill openings. A varied cross-sectional area of equivalent strut model was proposed and furthermore, a model for the hysteresis loop was formulated.

Other researchers (Liauw and Kwan [7,8]) studied the non-linear behavior of a pair of four-storey single-span infilled frame both experimentally and analytically. For the non-integral infilled frames, it showed that the strength of non-integral infilled frames depended on the bending strength of the frame; while for the integral infilled frames, in which the infill and the frame are bonded or connected together, the effects of the connectors were investigated in relation to the stiffness and strength of the infilled frames.

Moghadam [9] conducted an intensive research on the seismic behavior of infilled frames and the research results included many aspects, such as the crack strength determination of infilled steel frames (Moghadam et al. [10]), the impact of repair and retrofit on in-plane behavior of masonry infilled steel frames (Moghadam [11]), seismic strengthening of masonry infilled structures (Moghadam and Mahmoodi [12]), mathematical functions to evaluate stress of infilled frames (Mahmoodi and Moghadam [13]), discrete element method in the nonlinear analysis of masonry-infilled steel frames with opening (Mohammadi et al. [14]).

Saari et al. [15] reported the seismic behavior of headed shear stud connectors for use in steel frames with partially restrained connectors and reinforced concrete infill walls. An experimental program was developed to quantify the strength and deformation capacities of shear studs for use in S-RCW infill system, and several design equations were verified. The study on the headed stud connectors lead to a further research carried out by Tong et al. [16], who studied the experimental and cyclic behavior of a composite structural system consisting of partially-restrained steel frames with reinforced concrete infill walls. The study showed that the system had the potential to offer strength appropriate for resisting the forces from earthquakes and stiffness adequate for controlling drift for low- to moderate-rise buildings located in earthquake-prone regions.

Despite the large amount of the previously mentioned literatures, it is evident that limited researches (Wright and Gallocher [17], Hanaor [18], Matteis and Landolfo [19]) are concerned about the sandwich composite panels. The sandwich composite panel was used because of its advantages of high ratio of strength to weight, good fire resisting performance, and excellent heat preservation capacity. The objective of this paper is to report an experimental investigation on steel frames infilled with sandwich composite panels.

## 2. EXPERIMENTAL RESEARCH

### 2.1 Description of specimens

In this experiment, eight specimens were manufactured and tested to investigate the performance of infilled frames under earthquake-type loading. The test frame was a full-scale one-bay, one-storey steel frame. The columns for specimen were H-shaped steel sections of a cross-section HW250×250×9×14mm, the beams were H-shaped steel sections of a cross-section HN250×125×6×9mm. The parameters varied in these experiments included the following: (1) panel thickness; (2) panel type; (3) panel position; (4) column orientation; (5) joint of steel frame; (6) connecting method between steel frame and panel. The characteristics of the test specimens are summarized in Table 1, with a schematic test setup shown in Figure 1. S1 was selected as reference specimen, while other specimens were designed according to the parameters. Geometrical dimensions of all specimens were selected to be the same. Properties of the test frames are shown in Figure 2. Connection between the frame and the infill was achieved by using a steel plate that was welded on the column flange, and a bolt that was drawn into the embedded part in the panel, as shown in Figure 2(a). Table 2 summarizes the results of the material tests of the steel coupons used in the specimens. The average compressive strength of concrete cubes (150mm×150mm×150mm) was tested as 26.5N/mm<sup>2</sup>, and the elastic modulus was given as  $3.1 \times 10^4$  N/mm<sup>2</sup>.

Table 1. Characteristics of Specimens

Specimen	Panel thickness (mm)	Panel type	Panel position	Column orientation	Frame joint	Connecting method
S1	140	SC <sup>a</sup>	Infilled	Strong	Welded flange-Bolted web	Column
S2	140	CL <sup>b</sup>	Infilled	Strong	Welded flange-Bolted web	Column
S3	170	SC	Infilled	Strong	Welded flange-Bolted web	Column
S4	140	SC	Infilled	Strong	Welded flange-Bolted web	Beam
S5	140	SC	Out-hanged	Strong	Welded flange-Bolted web	Column
S6	140	SC	Infilled	Strong	End-plate connection	Column
S7	140	SC	Infilled	Strong	Welded flange-Bolted web	Column & Beam
S8	140	SC	Infilled	Weak	Welded flange-Bolted web	Column

Notes: a—Sandwich composite panel, b—Composite light-weight panel

Table 2. Properties of Specimens

Specimen number	Thickness (mm)	Yield stress(N/mm <sup>2</sup> )	Ultimate stress(N/mm <sup>2</sup> )	Elastic modulus(N/mm <sup>2</sup> )	Elongation at fracture (%)
Beam flange	9	261.5	400.5	1.97×10 <sup>5</sup>	16
Beam web	6	271.3	430.5	2.05×10 <sup>5</sup>	19
Column flange	14	240.0	370.6	1.90×10 <sup>5</sup>	14
Column web	9	258.6	390.5	1.97×10 <sup>5</sup>	18
Connecting plate	10	249.3	380.4	1.95×10 <sup>5</sup>	15
Endplate	25	260.5	400.5	1.97×10 <sup>5</sup>	16

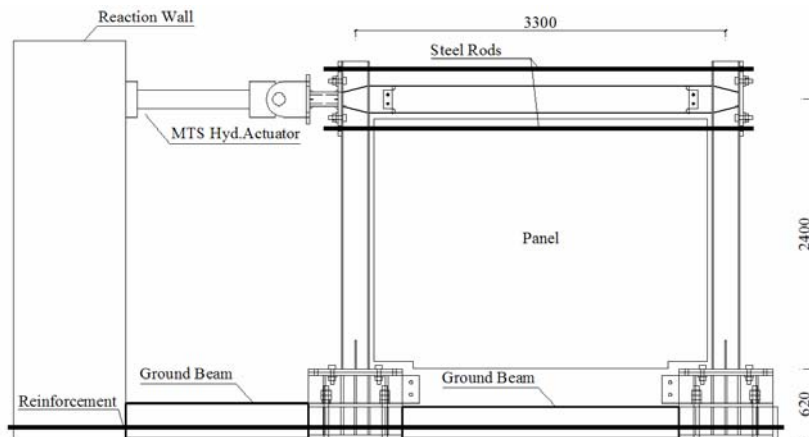
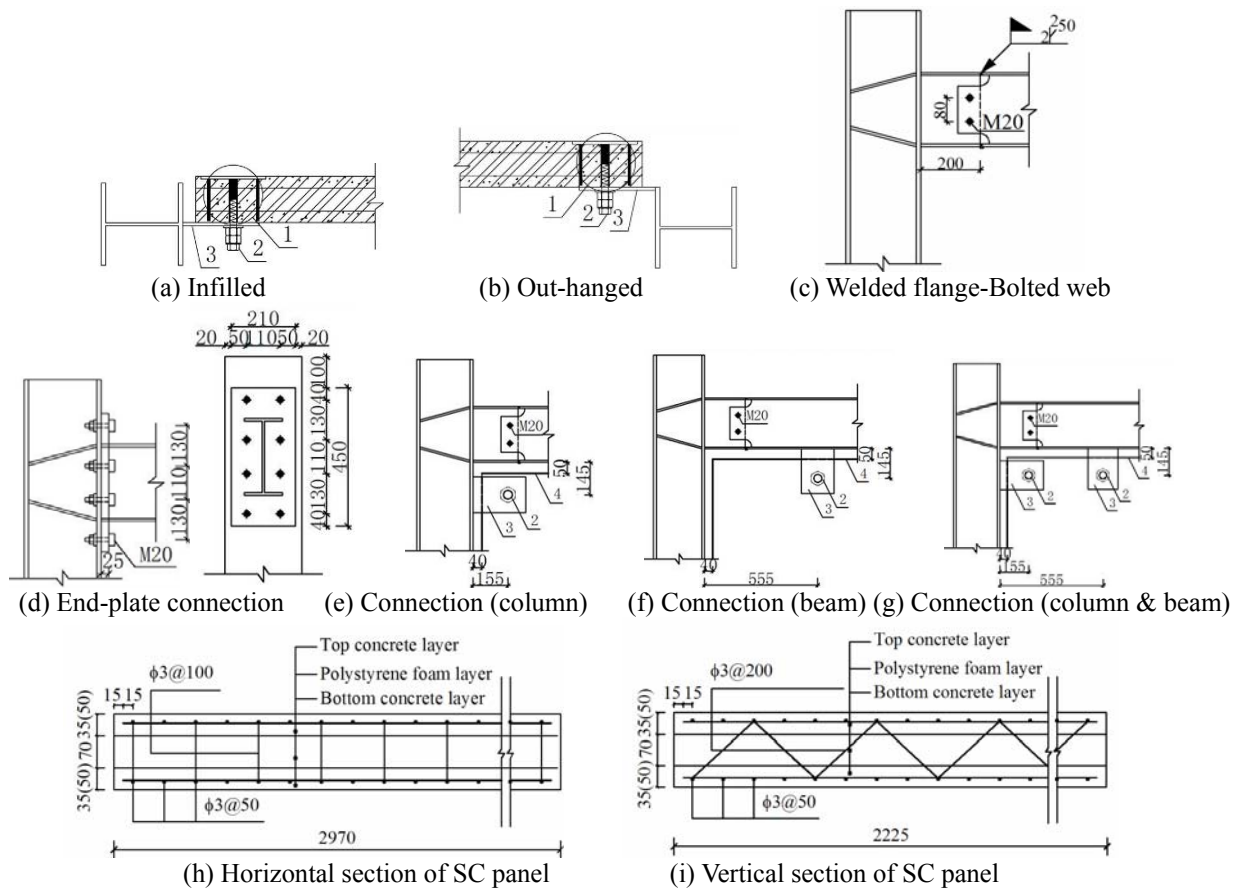


Figure 1. Test Setup (Dimensions in mm)



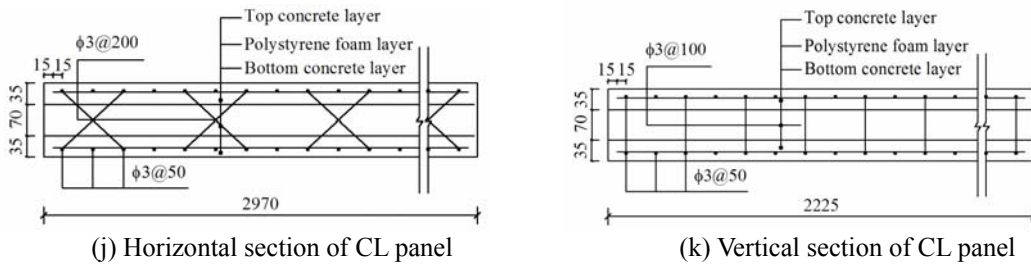


Figure 2. Characteristics of the Test Frames

1—Embedded part; 2—Bolt (M20); 3—Connecting plate (-220x160x10); 4—Panel edge

## 2.2 Experimental Setup and Testing Procedure

In order to investigate the effect of reversed cyclic lateral load on specimens, a closed-loop servo-hydraulic system was used to load the specimens by imposing cyclic static displacements in the plane of the wall at the center line of the beam. No axial load was applied to any of the specimens. The schematic of test setup and loading system is shown in Figure 1. The testing system consisted of reaction wall, ground beam, loading equipment and data acquisition system. The specimens were instrumented with LVDTs (linear variable differential transformers) to measure in-plane displacements and out-of-plane displacements. During the tests, story displacements and the lateral loads were monitored. After each cycle, new initiated cracks and crack propagation were marked on the specimens and failure mechanisms were observed.

The testing procedure of the experimentation, shown in Figure 3, was based on the ATC-24 [20] guidelines for cyclic testing of steel structures. The loading history was divided into two parts: elastic cycles and inelastic cycles. Firstly, the elastic cycles were imposed on the specimens by displacement control at levels of  $0.25 \Delta_y$ ,  $0.5 \Delta_y$  and  $0.7 \Delta_y$ , where  $\Delta_y$  is the evaluated lateral yielding displacement corresponding to the lateral yielding load  $P_y$ . In this paper,  $\Delta_y$  is taken as 9.6mm approximately based on the numerical analysis results. Two cycles were conducted at each of the lateral displacement of  $0.25 \Delta_y$ ,  $0.5 \Delta_y$  and  $0.7 \Delta_y$ . In further cycles, the inelastic cycles were applied to lateral displacement levels of  $1.0 \Delta_y$ ,  $1.5 \Delta_y$ ,  $2.0 \Delta_y$ ,  $3.0 \Delta_y$ ,  $5.0 \Delta_y$ , and  $7.0 \Delta_y$ . Three cycles were imposed at displacement levels of  $1.0 \Delta_y$ ,  $1.5 \Delta_y$ , and  $2.0 \Delta_y$ ; while two cycles were imposed at the other displacement levels listed above. The magnitude of the displacement increased gradually until any of the following phenomenon occurred: (1) severe local buckling of beams or columns; (2) shearing of bolts; (3) large deformation or deflection of members; (4) corner crushing of panels; (5) throughout cracks on the surface of panels.

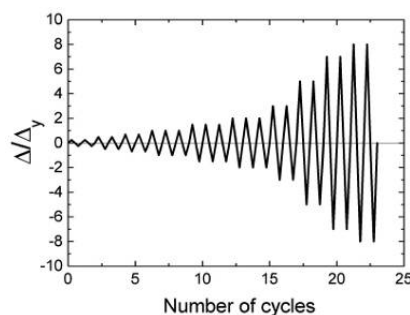


Figure 3. Testing Procedure

### 2.3 Instrumentation

Each beam end displacement was automatically recorded by a hydraulic actuator acting on each beam end. In addition, seven linear variable displacement transducers (LVDTs) were mounted to measure the middle displacement of column and panel, slip displacement of column bottom, and side-sway of the specimens. The layout of the LVDTs is illustrated in Figure 4.

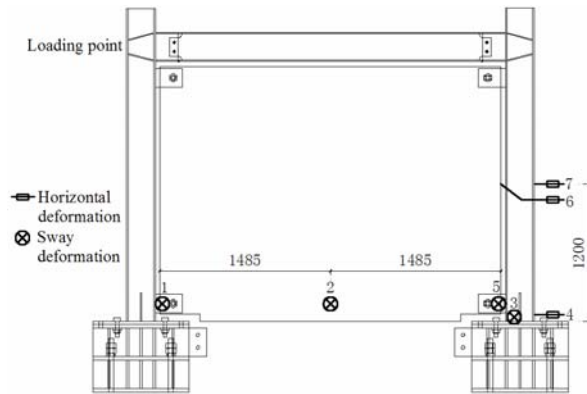


Figure 4. Layout of LVDTs (Unit: mm)

For the test specimens, a total of fifty-nine strain gauges were employed in each specimen excepted S6 in which six additional strain gauges were employed to measure the end plate strain. Strain gauges were used to monitor the strains in the flanges and webs of beam and column, and strain rosettes were applied to calculate the principle strain of steel connecting plate and panel. All the test results were recorded by Portable Data Collection System (Japan-TDS303). The layout of strain gauges is illustrated in Figure 5.

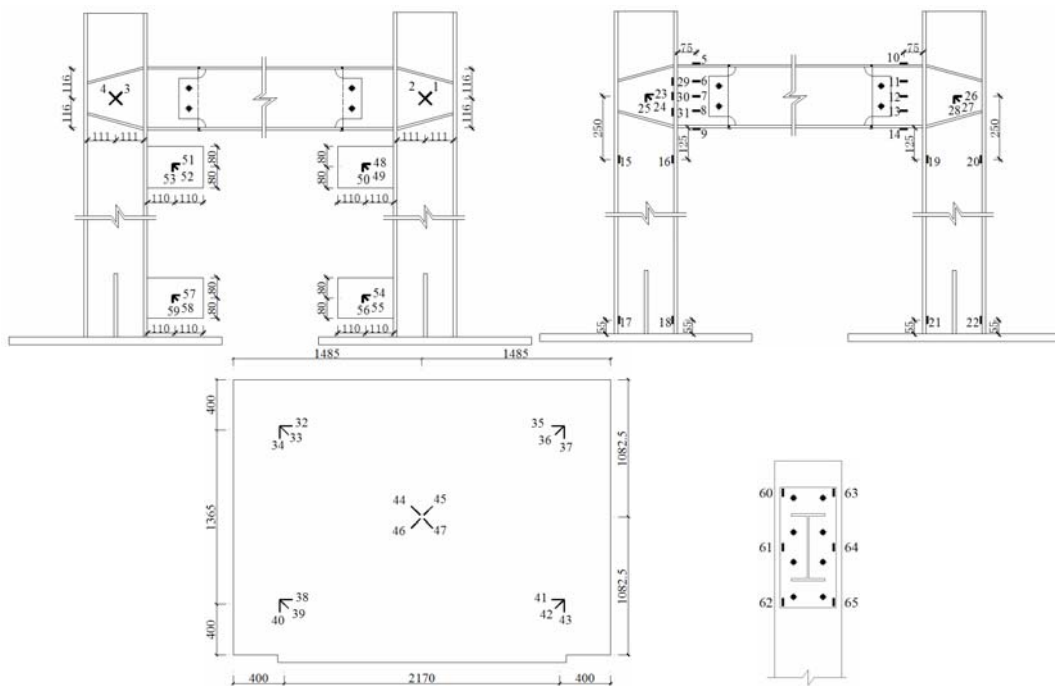


Figure 5. Layout of Strain Gauges (Unit:mm)

### 3. EXPERIMENTAL RESULTS

#### 3.1 Failure modes

The main experimental procedure of S1 subjected to cyclic displacement load is described below: when the displacement of beam end reached 1.6mm at the first cycle of  $0.5\Delta_y$ , short small cracks appeared on the panel surface around the right-bottom and left-top embedded parts; when the displacement reached -2.4mm at the second cycle, a 25cm long vertical small crack was found in the middle part of panel surface. During the loading cycle of  $2.0\Delta_y$ , with the displacement increased to -9.6mm at the first cycle, the crack in the middle part of panel surface propagated to the top; meanwhile some 15 cm long cracks appeared on the panel surface around the left-bottom and right-bottom embedded parts, when the displacement reached -4.8mm at the first cycle and 8.4mm at the second cycle, respectively. At the second cycle of  $3.0\Delta_y$ , the specimen made a rattling sound, which may be caused by the friction between connecting plate and bolt. When the displacement rose to -22mm at the first cycle of  $5\Delta_y$ , concrete spalling was found around the right-top and right-bottom embedded parts; and the spalling lasted to the end of the loading procedure. At the second cycle of  $7\Delta_y$ , local buckling of bottom flange near weld occurred when the displacement reached to 48mm, and with the displacement increased to -67.2mm, accompanied by loud popping noises, the right weld fractured at the bottom flange. At this moment, severe concrete spalling was found around the embedded parts, moreover, many cracks appeared on the panel surface. Due to the experimental phenomenon, shown in Figure 6(a~g), testing procedure was terminated.

The other seven specimens showed similar damaging progress, including appearance and propagation of cracks, spalling of concrete around the embedded parts, local buckling of beam flange, and weld fracture. It should be noted that weld fracture did not occur in Specimen 7; nevertheless bolt shearing was found when the displacement reached to -43mm at the first cycle of  $5\Delta_y$ , which is shown in Figure 6(h).

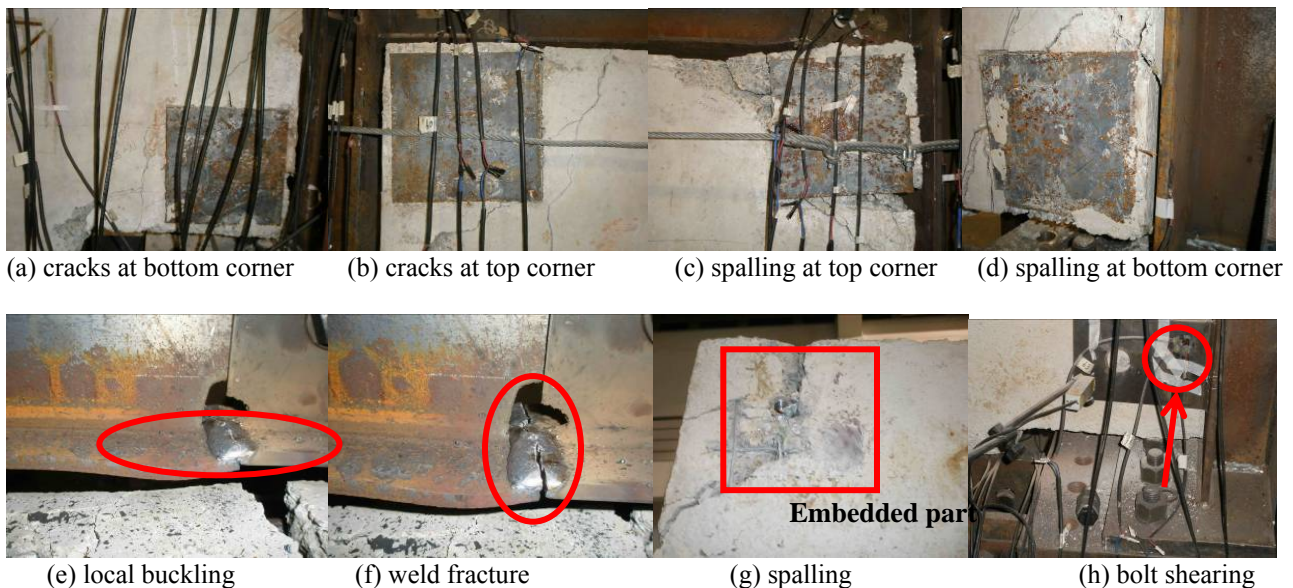


Figure 6. Failure Pattern of Specimen

As can be seen from the experiment phenomenon, specimens tended to make rattling sound during the initial loading process, which attributed to the hole diameter(40mm) of connecting plate was greater than that of bolt(20mm). When the specimen was subjected to a horizontal load, the bolt slipped in the hole; however, the limited space ( $\pm 10\text{mm}$ ) restricted the relative slide between the connecting plate and bolt, hence interaction between panel and steel frame was achieved in state when the lateral displacement of specimen reached a high level. Now that mutual interaction was built, the steel frame resisted the load in cooperation with panel, so the initial lateral strength and initial lateral stiffness were raised, however, as to the quantitative analysis; the conducted experiment in this paper gives the results later. With the increasing of load, diagonal cracks around the embedded parts appeared on the surface of panel, and then long cracks were observed in the middle of panel. The observation was markedly different from the mentioned literatures, in which the infill panel, such as brick infill, masonry infill, and clay tile infill, generated large diagonal cracks across the panel. Therefore it shows that, as a precast concrete member, the composite panels exhibit a better integration than traditional walls. When the displacement increased from moderate level to high level, cracks around the embedded parts tend to dilate; namely cracks widen from cyclic loading along crack surfaces. As soon as cracks appeared, the forces transmitted from steel frame to panel were concentrated on the cracked region, followed by concrete spalling with the ongoing displacement. While for the rest part of panel, not only do no more new cracks appear, but also old cracks ceased to dilate. In the experiment, neither the connecting plate nor the embedded parts failed to keep working. These results showed that adequate detailing and proper construction of connection between steel frame and panel was achieved. It is important to note that the integral behavior of infilled frame depends on the success of connections of panels to the steel frames. S7, in which eight connecting plates were used, exhibited an obvious different behavior among all specimens. On the one hand, one of the bolts were sheared off during the loading process, which may be explained as: the infilled panel were so highly strengthened that the bolts which were allowed to slip slightly failed to resist the shearing force transmitted from the steel frame. On the other hand, the doubled bolts ( $8/4=2$ ) assured a much more effective cooperation between panel and steel frame, hence the panel made greater contribution to undertake the lateral force, consequently, neither the weld fractured nor the beam flange buckled.

### 3.2 Lateral load ( $P$ ) Versus Displacement Curves ( $\Delta$ )

The  $P$ - $\Delta$  hysteresis loops of the specimens are shown in Figure 7, in which  $P$  is the load applied to the beam end and  $\Delta$  is the corresponding displacement of the beam end. It is found that, in general, the hysteresis loops exhibit pinched behavior, which is quite typical for infills. The pinching behavior can be mainly explained by concrete spalling around the embedded parts. With an increase in beam end displacement, the lateral stiffness of specimen was observed to degrade. The stiffness degradation is attributed partly to plastic deformation of the steel frame but primarily to deactivation of panel. As mentioned previously, when the lateral displacement was so large that concrete spalling was found around the embedded parts, which led to the connection between panel and steel frame transmit mutual forces partially. Since the panel gradually quit working, the specimen shows a much lower lateral stiffness. By comparing S1 and S3, we find a thicker panel led to a fuller hysteresis loop, which means better energy dissipation ability. Meanwhile, a comparison is made between specimen 1 and specimen 4, the fuller hysteresis loop of specimen 1 gives the conclusion that column connection is more effective to integrate the steel frame and the infilled panel.

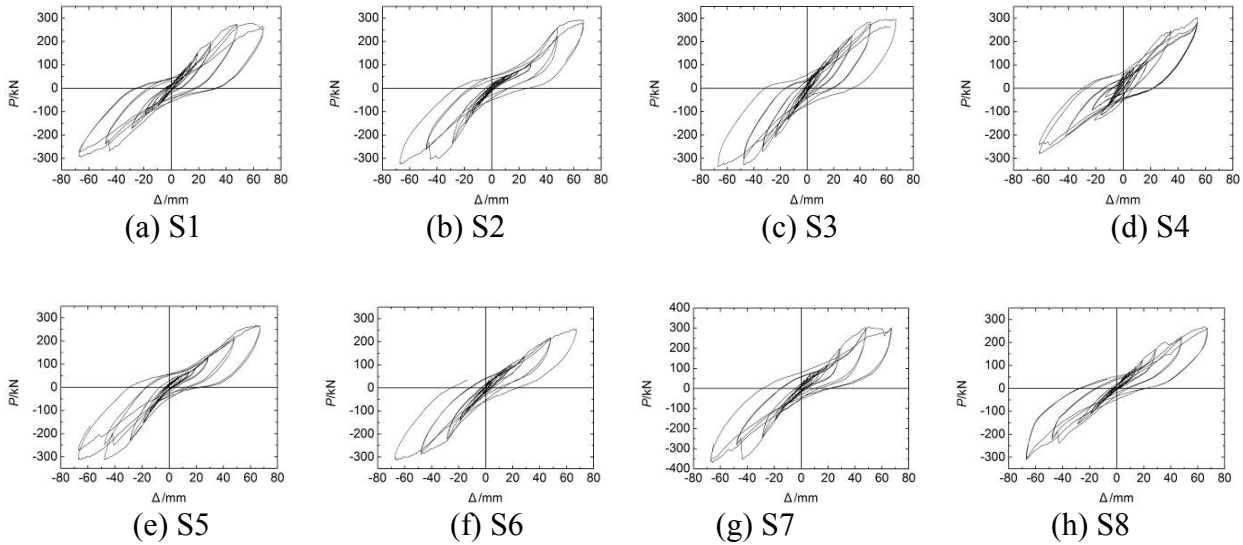


Figure 7. Load-displacement Hysteretic Loops

### 3.3 P-Δ Envelope Curves

According to the P-Δ hysteresis curves in Figure 7, the envelope curves, as illustrated in Figure 8, are constructed by connecting the peak value in each loading cycle. The characteristic points of envelope curve are determined by using the given method in Figure 9, in which the ultimate load is defined as  $P_u = 0.85P_{max}$ , and the corresponding displacement is  $\Delta_u$ , characteristic points of each specimen are listed in Table 3. In Figure 8, the envelope curves include two main portions. The positive loading portion shows no obvious degradation of the specimen strength, furthermore, the specimen strength even keep increasing till the end of experiment. It shows that although member damage occurred, such as weld fractured, beam buckled and concrete spalled, the specimen maintained bearing capacity, which were achieved by the success of connection between the frame and panel. As can be seen from Table 3, the ultimate displacement for each specimen is 48mm, and the yielding displacement is 5/12~5/8 of the ultimate displacement. One may conclude the following: (1) enhanced connection between the frame and the panel improved the maximum bearing capacity and ultimate capacity; (2) compared with infilled panel, out-hanged panel made few contributions to the lateral strength of the specimen, and the reduction is about 25%.

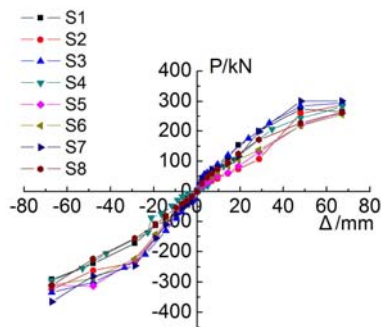


Figure 8. Skeleton Curves of Specimens

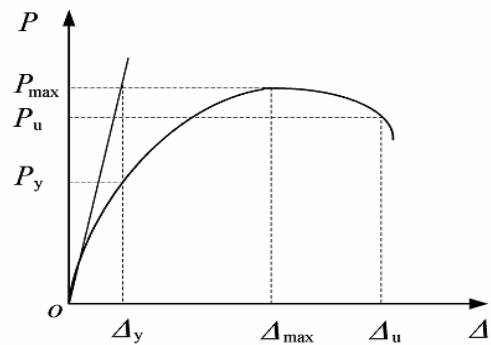


Figure 9. Determination of Feature Points

Table 3. Characteristic Points of Skeleton Curves of Specimens

Specimen	Yielding point		Maximum point		Ultimate point	
	$\Delta_y$ (mm)	$P_y$ (kN)	$\Delta_{max}$ (mm)	$P_{max}$ (kN)	$\Delta_u$ (mm)	$P_u$ (kN)
S1	20.2	158.3	48	274.8	64.7	233.6
S2	29.0	235.9	48	288.3	63.1	245.1
S3	27.7	227.1	48	295.3	72.6	251.0
S4	21.3	129.3	48	243.3	67.2	206.8
S5	26.2	117.8	48	219.8	73.4	186.8
S6	26.7	205.9	48	288.4	58.6	245.1
S7	25.6	171.4	48	300.5	58.6	255.4
S8	20.4	130.1	48	226.4	55.3	192.4

### 3.4 Strength Degradation

The strength of test specimen degrades with increasing cycles of reverse loads. The characteristic of the strength degradation can be evaluated by the strength degradation coefficient ( $\lambda_j$ ) at the same load. The strength degradation coefficient at the same load is expressed as:

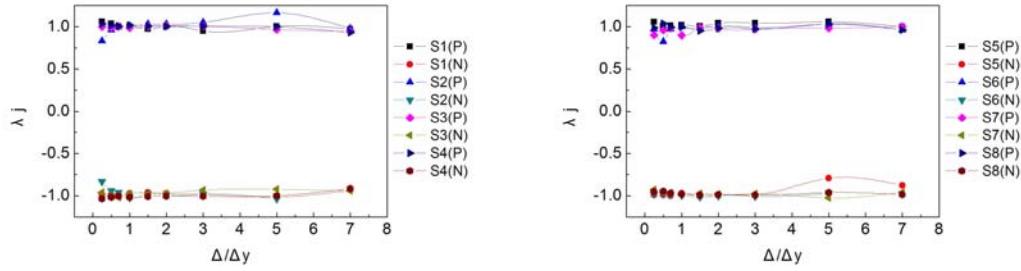
$$\lambda_j = \frac{P_j^i}{P_j^1} \quad (1)$$

Where  $P_j^i$  and  $\Delta/\Delta_y$  are respectively the maximum loads under the  $i$ th and first loading cycles when the relative beam end displacement ( $\Delta/\Delta_y$ ) equals  $j$ . The  $\lambda_j - \Delta/\Delta_y$  relationship of the specimens is shown in Figure 10(a). In Figure 10(a), P and N respectively mean positive direction and negative direction respectively. We can obtain the conclusion that the strength degradation coefficient at the same load showed no obvious degradation trend.

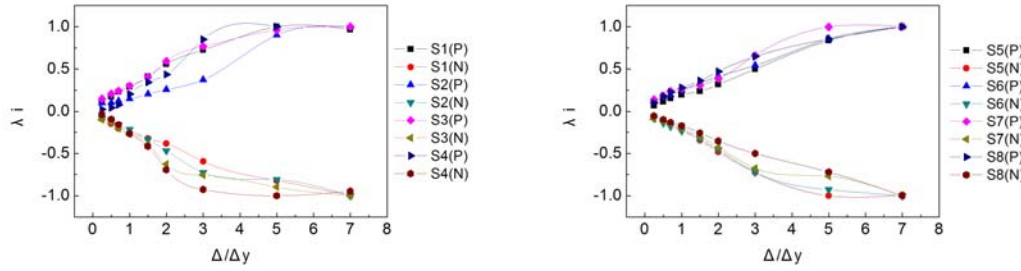
In order to evaluate the total strength degradation characteristic of the specimens during the loading procedure, the strength degradation coefficient at the total loads ( $\lambda_i$ ) was introduced. The strength degradation coefficient at the total load is expressed as:

$$\lambda_i = \frac{P_i}{P_{max}} \quad (2)$$

Where  $P_i$  is the maximum load under the  $i$ th loading cycles when the relative beam end displacement ( $\Delta/\Delta_y$ ) equals  $j$ ; and  $P_{max}$  is the maximum load in the whole loading procedure. Figure 10(b) exhibits the  $\lambda_i - \Delta/\Delta_y$  relationship of the specimens. The test results demonstrate that before the relative beam end displacement  $\Delta/\Delta_y \leq 3$ ,  $\lambda_i$  increases gradually with an increase of  $\Delta/\Delta_y$ ; when  $\Delta/\Delta_y > 3$ ,  $\lambda_i$  varies differently for each specimen with the increasing of the displacement, but the amplitude of variation is slight. This phenomenon shows that at the ultimate limit state the strength reduced slightly, namely the specimen still hold bearing capacity although the displacement was large.



(a) Strength Degradation Curves at the Same Load(S1-S4) (b) Strength Degradation Curves at the Same Load(S5-S8)



(c) Strength Degradation Curves at the Total Load(S1-S4) (d) Strength Degradation Curves at the Total Load(S5-S8)

Figure 10. Curves of Strength Degradation of the Specimens (P-positive, N-negative)

### 3.5 Stiffness Degradation

In order to reflect the stiffness degradation of specimens under cyclic loading, the stiffness of specimens can be evaluated by the index-cyclic stiffness (Tang [21]), which can be expressed as follows:

$$K_j = \frac{\sum_{i=1}^n P_j^i}{\sum_{i=1}^n u_j^i} \tag{3}$$

Where  $K_j$  is cyclic stiffness,  $P_j^i$  and  $u_j^i$  are the maximum beam load and the corresponding displacement, respectively, under the  $i$ th loading cycle when the relative beam displacement ( $\Delta/\Delta_y$ ) equals  $j$ , and  $n$  is the number of cycles when the deformation is controlled as  $u_j$ .

It can be concluded that the initial lateral stiffness of specimen ranged from  $1.1 \times 10^4$  kN/m to  $1.9 \times 10^4$  kN/m. With a slight increasing of displacement, the lateral stiffness decreased sharply, and the drastic descending trend extended to the relative displacement  $\Delta/\Delta_y = 1$ . At the following portion,  $K_j$  decreased slowly and steadily, reached the final value of  $4 \times 10^3$  kN/m, which is about 1/4~1/3 of the initial value. The following observation can be made by comparison: (1) the lateral stiffness can be enhanced by increasing the panel thickness and connection number; (2) the contribution of infilled panel is greater than out hanged panel; (3) the beam-to-column connection type of steel frame affected the lateral stiffness mildly.

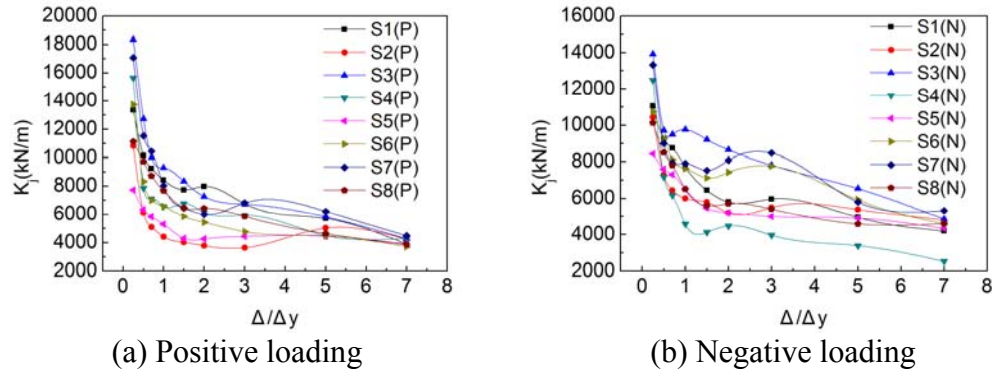


Figure 11. Curves of Stiffness Degradation of the Specimens (P-positive N-negative)

### 3.6 Ductility Coefficient

In the seismic analysis of structural engineering, ductility is a pivotal parameter to take into consideration. In the present paper, the displacement ductility coefficient and angular ductility coefficient are used to take account of the ductility of the infilled steel frame subjected to seismic loading. The displacement ductility coefficient  $\mu$  is defined as the ratio between the ultimate displacement ( $\Delta_u$ ) and the yielding displacement ( $\Delta_y$ ), which can be expressed as  $\mu = \Delta_u / \Delta_y$ ; The angular displacement ductility coefficient  $\mu_\theta$  is defined as the ratio between the ultimate angular displacement ( $\theta_u$ ) and the yielding angular displacement ( $\theta_y$ ), which can be expressed as  $\mu_\theta = \theta_u / \theta_y$ , where  $\theta_u = \arctan(\Delta_u / H)$ ,  $\theta_y = \arctan(\Delta_y / H)$ ,  $H$  is the column height and measured from the bottom to the center line of beam. Table 4 summarizes the displacement ductility coefficient and angular ductility coefficient of the test specimens. The Chinese Design Specification (GB50011-2010) [22] gives the detail ductility regulation for the moderate-high rise steel structures: the elastic layer angular displacement [ $\theta_e$ ]= $1/300 \approx 0.0033 \text{ rad} = 3.3 \text{ mrad}$ , and the elastic-plastic layer angular [ $\theta_p$ ]= $1/50 = 0.02 \text{ rad}$ . From Table 4, it can be found that the displacement ductility coefficient of the test specimens  $\mu = 2.18 \sim 3.20$ , the elastic yielding angular ductility coefficient  $\theta_y = 2.53 \sim 3.63 [\theta_e]$ , and the elastic-plastic angular ductility coefficient  $\theta_u = 1.15 \sim 1.53 [\theta_p]$ . The comparison made between the test specimen and the steel structure can lead to the conclusion that the infilled steel frame exhibits excellent ductility and thus measure up to the requirement of the structural seismic design for Chinese Specification.

Table 4. Ductility Coefficient of Specimens

Specimen	Yielding displacement $\Delta_y$ (mm)	Ultimate displacement $\Delta_u$ (mm)	Yielding angular displacement $\theta_y$ (mrad)	Ultimate angular displacement $\theta_u$ (mrad)	Displacement ductility coefficient $\mu$	Angular displacement ductility coefficient $\mu_\theta$
1	20.20	64.70	8.42	26.96	3.20	3.20
2	29.00	63.10	12.08	26.29	2.18	2.18
3	27.70	72.60	11.54	30.25	2.62	2.62
4	21.30	67.20	8.88	28.00	3.15	3.15
5	26.20	73.40	10.92	30.58	2.80	2.80
6	26.70	58.60	11.13	24.42	2.19	2.19
7	25.60	58.60	10.67	24.42	2.29	2.29
8	20.40	55.30	8.50	23.04	2.71	2.71

### 3.7 Energy Dissipation Capacity

The equivalent damping coefficient ( $\xi_e$ ) is adopted to analyze the energy dissipation capacity of the infilled steel frame. According to the simplified lateral load ( $P$ )-displacement ( $\Delta$ ) relationship shown in Figure 12,  $\xi_e$  can be calculated by Eq. 4. In Figure 12,  $S_{ABC}$  and  $S_{CDA}$  are areas enclosed by curves ABC and CDA, respectively, and  $S_{OBE}$  and  $S_{ODF}$  are areas within triangles OBE and ODF, respectively.

$$\xi_e = \frac{1}{2\pi} \frac{S_{ABC} + S_{CDA}}{S_{OBE} + S_{ODF}} \tag{4}$$

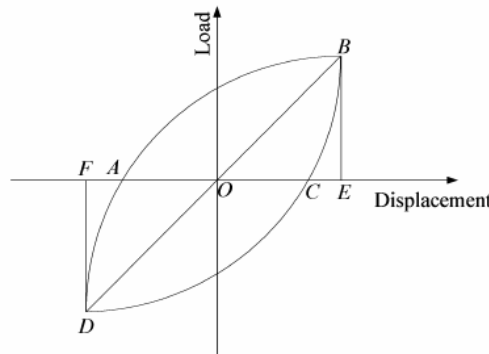


Figure 12. Determination for Energy Dissipated Coefficient

The dissipated energy capability  $E$  of each hysteretic loop is also used to evaluate the energy dissipation capacity, and  $E$  is expressed as:

$$E = \frac{S_{ABC} + S_{CDA}}{S_{OBE} + S_{ODF}} = 2\pi \cdot \xi_e \tag{5}$$

Figure 13 and Table 5 indicate that: (1) Generally, S3 and S7 exhibit better energy dissipation capacity than the other specimens, which confirms the conclusion that panel thickness and connection types are most influential factors to infilled frames; (2) The  $\xi_e - \Delta/\Delta_y$  relationship includes two main portions. Initially,  $\xi_e$  drops with increasing displacement, which is attributed to the dramatic decreasing of the lateral stiffness; however, in the second stage, when  $\Delta/\Delta_y \geq 2$ ,  $\xi_e$  increases with increasing displacement, which can be explained as: the severely damaged panel is gradually quitting action at this moment, and the curve reflects the plastic formation of steel frame. (3) At the yielding state,  $\xi_e$  is between 0.04 and 0.1; at the maximum state,  $\xi_e$  ranges from 0.12 to 0.14; at the final or ultimate state,  $\xi_e$  is about 0.13~0.16.

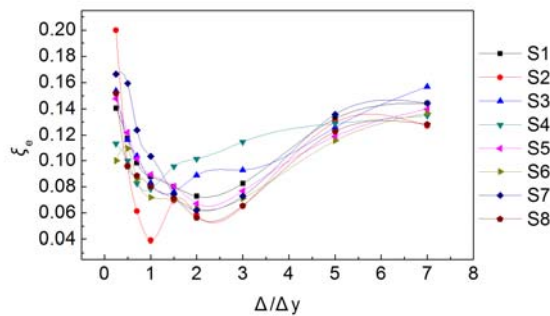


Figure 13. Relationship between  $\xi_e$  and Displacement

Table 5. Energy Dissipated Coefficients of Specimens

Specimen	S1		S2		S3		S4	
Status	Max.	ultimate	max.	ultimate	max.	ultimate	max.	ultimate
Displacement $\Delta/\Delta_y$	5.0	7.0	5.0	7.0	5.0	8.0	5.0	7.0
Total dissipated energy ( $N \cdot m$ )	10225	16984	9316	16402	11566	20853	9894	13638
Equivalent damping coefficient $\xi_e$	0.132	0.144	0.13	0.129	0.126	0.157	0.129	0.135
Dissipated energy capability $E$	0.832	0.906	0.815	0.797	0.791	0.986	0.809	0.847

Specimen	S5		S6		S7		S8	
Status	Max.	ultimate	Max.	ultimate	Max.	ultimate	Max.	ultimate
Displacement $\Delta/\Delta_y$	5.0	8.0	5.0	7.0	5.0	7.0	5.0	7.0
Total dissipated energy ( $N \cdot m$ )	9338	16872	8717	16317	11765	20257	8193	15542
Equivalent damping coefficient $\xi_e$	0.119	0.14	0.116	0.137	0.136	0.144	0.123	0.128
Dissipated energy capability $E$	0.748	0.878	0.727	0.859	0.853	0.906	0.771	0.804

#### 4. CONCLUSIONS

The following conclusions can be obtained from the observations and analysis on the conducted experiments of eight composite panels infilled steel frames:

- (1) The main failure modes of composite panel infilled steel frames include the concrete spalling around the embedded parts, the local buckling of beam flange and weld fracture of beam. Compared with traditional panels and walls, composite panels in the present paper, as precast concrete members, exhibit a better integration.
- (2) The integral behavior of infilled frame depends on the success of connections of panels to the steel frames. The connection type presented in the paper assured an effective connection between panels and frames.
- (3) Both of increasing panel thickness and connection number enhances the lateral stiffness and lateral strength of the infilled frames, while panel position and beam-to-column connection type affect the infilled frame slightly. Generally, the initial lateral stiffness of infilled frames range from  $1.1 \times 10^4 \text{ kN/m}$  to  $1.9 \times 10^4 \text{ kN/m}$ , and the final value is about 1/4~1/3 of the initial value.
- (4) The displacement ductility coefficient of the test specimens  $\mu = 2.18 \sim 3.20$ , the elastic yielding angular ductility coefficient  $\theta_y = 2.53 \sim 3.63 [\theta_e]$ , and the elastic-plastic angular ductility coefficient  $\theta_u = 1.15 \sim 1.53 [\theta_p]$ . The comparison made between the test specimen and the steel structure can lead to the conclusion that the infilled steel frame exhibits excellent ductility and thus measure up to the requirement of the structural seismic design for Chinese Specification.
- (5) At the yielding state, the equivalent damping coefficient  $\xi_e$  is between 0.04 and 0.1; at the maximum state,  $\xi_e$  ranges from 0.12 to 0.14; at the final or ultimate state,  $\xi_e$  is about 0.13~0.16.

## ACKNOWLEDGEMENT

This paper was supported by the National Key Technology R&D Program (Grant No. 2006BAJ04A02-06), Shandong Provincial Natural Science Foundation, China (Grant No. ZR2011EEM023), China Postdoctoral Science Foundation funded project (Grant No. 20090450736), Shanghai Postdoctoral Sustentation Fund (Grant No. 09R21415800) and Shandong Postdoctoral Science Foundation (Grant No. 200902004).

## REFERENCES

- [1] Polyakov, S.V., "On the Interaction between Masonry Filler Walls and Enclosing Frame when Loaded in the Plane of the Wall", Translations in Earthquake Engineering, Earthquake Engineering Research Institute, San Francisco, 1960, pp. 36-42.
- [2] Polyakov, S.V., "Masonry in Framed Buildings", G.L. Cairns, Translator, National Lending Library for Science and Technology, Boston Spa, Yorkshire, U.K., 1963.
- [3] Papia, M., Cavaleri, L. and Fossetti, M., "Infilled Frames: Developments in the Evaluation of the Stiffening Effects of Infills", Structural Engineering and Mechanics, 2003, Vol. 16, No. 6, pp. 675-693.
- [4] Cavaleri, L., Fossetti, M. and Papia, M., "Infilled Frames: Developments in the Evaluation of Cyclic Behaviour under Lateral Load", Structural Engineering and Mechanics, 2005, Vol. 21, No. 4, pp. 469-494.
- [5] Holmes, H., "Steel Frames with Brickwork and Concrete Infilling", Proceeding of Institution of Civil Engineers, 1961, pp. 473-478.
- [6] Mosalam, Khalid M., White, Richard N. and Gergely, Peter, "Static Response of Infilled Frames Using Quasi-static Experimentation", Journal of Structural Engineering, 1997, Vol. 123, No. 11, pp. 1462-1469.
- [7] Kwan, K.H. and Liauw, T.C., "Nonlinear Analysis of Integral Infilled Frames", Engineering Structure, 1984, Vol. 6, pp. 223-231.
- [8] Liauw, T.C. and Kwan, K.H., "Nonlinear Behavior of Non-integral Infilled Frames", Comput. & Structures, 1984, Vol. 18, No. 3, pp. 551-560.
- [9] Moghadam, H.A., "Seismic Behavior of Infilled Frames", Ph.D. Thesis, Imperial College, University of London, 1988.
- [10] Moghadam, H.A., Mohammadi, M.Gh. and Ghaemian, M., "Experimental and Analytical Investigation into Crack Strength Determination of Infilled Steel Frames", Journal of Constructional Steel Research, 2006, Vol. 62, No. 12, pp. 1341-1352.
- [11] Moghadam, H.A., "Lateral Load Behavior of Masonry Infilled Steel Frames with Repair and Retrofit", Journal of structural engineering, 2004, Vol. 130, No. 1, pp. 55-63.
- [12] Moghadam, H.A., and Mahmoodi, A., "Seismic Strengthening of Masonry Infilled Structures", Proceedings of the 10th European Conference on Earthquake Engineering, 1994, pp. 2293-7.
- [13] Mohammadi, M. and Moghadam, H.A., "Mathematical Functions to Evaluate Stress of Infilled Frames", Proceedings of the 1st Iranian National Conference of Civil Engineering, 2004.
- [14] Mohebkah, Amin, Tasnimi, A.A. and Moghadam, H.A., "Nonlinear Analysis of Masonry-infilled Steel Frames with Opening using Discrete Element Method", Journal of Constructional Steel Research, 2008, Vol. 64, No. 12, pp. 1463-1472.
- [15] Saari, William K., Hajjar, Jerome F., Schultz, Arturo E. and Shield, Carol K., "Behavior of Shear Studs in Steel Frames with Reinforced Concrete Infill Walls", Journal of Constructional Steel Research, 2004, Vol. 60, No. 10, pp. 1453-1480.

- [16] Tong, X.D., Hajjar, Jerome F., Schultz, Arturo E. and Shield, Carol K., “Cyclic Behavior of Steel Frame Structures with Composite Reinforced Concrete Infill Walls and Partially-restrained Connections”, *Journal of Constructional Steel Research*, 2005, Vol. 61, No. 4, pp. 531-552.
- [17] Wright, H.D. and Gallocher, S.C., “The Behavior of Composite Walling under Construction and Service Loading”, *Journal of Constructional Steel Research*, 1995, Vol. 35, No. 3, pp. 257-273.
- [18] Hanaor, Ariel., “Experimental Investigation of Composite Shear Panels under Cyclic Loading”, *Journal of Constructional Steel Research*, 2005, Vol. 61, No. 3, pp. 345-369.
- [19] De Matteis, Gianfranco, Landolfo, Raffaele, “Modelling of Lightweight Sandwich Shear Diaphragms for Dynamic Analyses”, *Journal of Constructional Steel Research*, 2000, Vol. 53, No. 1, pp. 33-61.
- [20] ATC-24, “Guidelines for Cyclic Seismic Testing of Components of Steel Structures”, Redwood City (CA): Applied Technology Council, 1992.
- [21] Tang, J.R., “Seismic Resistance of Joints in Reinforced Concrete Frames”, Nanjing (China): Southeast University Press, 1989.
- [22] GB50011-2010, “Specification of Structural Seismic Design”, Beijing, China Building Industry Press, 2010. [in Chinese]

# RESIDUAL WEB BEARING CAPACITY OF CORRODED STEEL BEAMS

Yasser Sharifi

*Department of Civil Engineering*

*Vali-e-Asr University of Rafsanjan, Rafsanjan, Iran*

*\*(Corresponding author: E-mail: y.sharifi@vru.ac.ir and yasser\_sharifi@yahoo.com)*

*Received: 3 June 2011; Revised: 7 August 2011; Accepted: 11 August 2011*

---

**ABSTRACT:** Corrosion is one of the most pervasive types of structural problem experienced by steel girder structures especially in corrosive environments. Each of the damage modes, if not properly monitored and rectified, can potentially lead to catastrophic failure or unanticipated out-of-service time. The purpose of this paper is to propose a simple methodology to assess the residual strength capacity of steel girders under the degradations of corrosion. Two credible models have been developed for corrosion damaged steel I-beams based on the actual thickness loss data which come from the already literatures. Finally, to show the application of the proposed methodology, the residual web bearing capacity of corroded steel beams was estimated. It was found that it is possible to establish the applicable diagrams and flowchart which demonstrate the residual web bearing capacity assessment of steel I-beams as those ages.

**Keywords:** Corrosion, Steel structures, Web bearing capacity, Corrosion damaged models, Thickness loss data

---

## 1. INTRODUCTION

Corrosion is the major cause of deterioration in steel structures. Results of this deterioration can range from progressive weakening of the steel structure over a long period of time to sudden collapse of the structure. The effects of corrosion damage vary with the type of structure, the location and extent of deterioration. It has been pointed out by Kayser [1] the most important form of corrosion is general loss of surface material. General corrosion accounts for the largest percentage of corrosion damage. Corrosion damage must be carefully appraised and evaluated. In some cases, immediate repair or closure is necessary while in other cases, the conditions created by corrosion can be tolerated. In all cases, however, the likely progression of corrosion must be considered (Kulicki et al. [2]). While loss of material due to corrosion reduces the section properties and hence the carrying capacity of a member, it can also change the mode of failure from one to another depending on the rate and place of corrosion. The analysis of existing structures may differ from the analysis of structures under design, especially if there is damage by corrosion. Some of the assumptions made in design may no longer be true and other failure mechanisms may become significant (Sharifi and Rahgozar [3-8]).

Steel structures such as ships, offshore platforms and land-based structures are prone to suffer various types of damage as they get older. Corrosion and fatigue cracking may be the two most important types of damage in aging structures (Paik et al. [9,10]). Nakai et al. [11] studied that Corrosion is an unavoidable phenomenon in steel structures and thickness loss of the structural members due to corrosion is a great concern when the integrity of structures is considered. Concepts of 'corrosion margin' and 'allowable corrosion level' have been introduced conventionally to cope with this problem. The corrosion margin is an additional thickness at the design stage and the allowable corrosion level is used as a guide to determine when to renew worn members at the maintenance stage. It has been pointed out by Czarnecki and Nowak [12] corrosion can lead to cracking (fracture), yielding or bucking of members. This can result in stress concentration, changes in geometric parameters, and a build-up of the corrosion products. These parameters are critical for the member's ability to resist load effects.

The effects of both uniform and pitting corrosion on load-carrying capacity and reliability of corrosion damaged steel box-girder bridges has been investigated by Sharifi and Paik [13,14] and Sharifi [15], respectively.

The effect of corrosion on structural strength is not yet clear. Further investigation is necessary to clarify how the corrosion affects strength of hold frames as beams. When beam strength is considered, (1) collapse strength (no buckling), (2) lateral-distortional buckling strength, (3) local buckling strength, (4) shear strength of web plates and (5) web crippling strength under concentrated loading etc. are important factors (Nethercot [16]).

It is possible to establish a relationship between the remaining capacities of various failure modes (moment, shear, lateral torsional buckling, bearing ...) and the loss of thickness for a given member. This approach can form the basis for establishing a quantitative relationship between the magnitude of corrosion defects and the corresponding remaining capacity. For a particular failure mode of a beam, if the percentage remaining capacity is plotted against the percentage loss of thickness, it will be obtained a curve that gives the relationship between them. The corrosion decay models, namely uniform and varying thickness loss models which are developed in this study will be used for the development of these curves. The results of this study can be used for a better prediction of the service life (remaining capacity) of deteriorating I-beams.

## **2. MECHANISM OF STEEL CORROSION**

In order to produce steel, iron ores must be processed. During the process of metal extraction, it consumes a large amount of energy to separate the metal from the ore. Large amounts of energy are consumed in the manufacturing of metals. This energy is essentially stored in the metal. Because of the fact that all configurations in nature tend to spontaneously change to lower states of energy, refined metal will deteriorate or corrode. For steel structures, such as exposed to water, oxygen and salt, the rate of corrosion will be considerably increased by the presence of salt from a marine environment or the use of deicing materials. In the natural environment, it has a tendency to oxidise to a form similar to its natural state under the influence of air and water. This deterioration process is known as corrosion. In a more precise, it is an electro-chemical reaction in which water with various pollutants in solution acts as the electrolyte. Corrosion of steel is an electro-chemical process in which iron, Fe, reacts with oxygen to form iron oxides. The familiar iron compounds are: Fe(OH)<sub>2</sub>, ferrous hydroxide; Fe(OH)<sub>3</sub>, ferric hydroxide; Fe<sub>2</sub>O<sub>3</sub>, iron oxide; and Fe<sub>3</sub>O<sub>4</sub>, magnetite. When steel is attacked under humid conditions in a clean rural atmosphere, the first oxidation product is ferrous ion in the lowest oxidation state, namely, Fe<sup>+2</sup>. because of the presence of air dissolved in moisture, the ferrous ion can react with it and precipitate ferrous hydroxide, Fe(OH)<sub>2</sub>, which can be quickly oxidised further to the ferric state, Fe<sup>+3</sup>, to give the gelatinous precipitate of ferric hydroxide (Fontana [17]).

## **3. FORMS OF CORROSION**

There are five main forms of corrosion which can affect a steel girder. The most prevalent form is a general loss of surface material: this condition will lead to the gradual thinning of members. General corrosion accounts for the largest percentage of corrosion damage. Pitting corrosion also involves loss of material at the surface. However, it is restricted to a very small area. Galvanic corrosion occurs when two dissimilar metals are electrochemically coupled. Such situations may occur at bolted or welded connections. Galvanic corrosion can be local, leading to pit formation. Crevice corrosion occurs in small confined areas, such as beneath peeling paint or between faying

surfaces. It is usually caused by a low concentration of dissolved oxygen in the moisture held within a crevice. Deep pits can also provide locations for crevice corrosion to occur. Stress corrosion occurs when metal is subjected to tensile stress in a corrosive environment (Fontana [17]).

#### 4. THE EFFECTS OF CORROSION ON STEEL STRUCTURES

The effects of corrosion vary with the type of structure and the location and extent of deterioration. Steel structures can be affected by corrosion in many ways. The main effects can be loss of material from the surface, which leads to thinner sections. Section loss due to uniform corrosion may take place over a large area of a structural member. The loss of material due to uniform corrosion results in the reduction of section properties of a member, such as cross sectional area, moment of inertia, section modulus, radius of gyration and etc., thus causing a reduction in the carrying capacity of the structure. The stiffness of members may also be reduced due to loss of material which may cause excessive deflection. At severe levels of corrosion, the ultimate capacity of a steel member may fall below the service loads. Also it should be pointed out that the mode of failure due to loss of material can be changed due to fact that the class of section can be altered. For example, a plastic section may become semi-compact section due to loss of material and local buckling may prevent the development of full plastic moment (Sharifi and Rahgozar [3-8]).

#### 5. CORRODED SAMPLES OF STEEL

Three identical universal mild steel I-beams ( $305 \times 165$  UB40 kg) were recovered from the site where all in a severely corroded condition (nearly 40 years old) as shown in Figure 1. The paint system had completely broken down with only remnants of the paint on the webs.

The thicknesses of these beams were measured by an instrument which was designed especially for this purpose. The instrument, which was used together with a depth gauge, is shown in Figure 2.



Figure 1. The Identical Corroded Universal Steel I-Beams

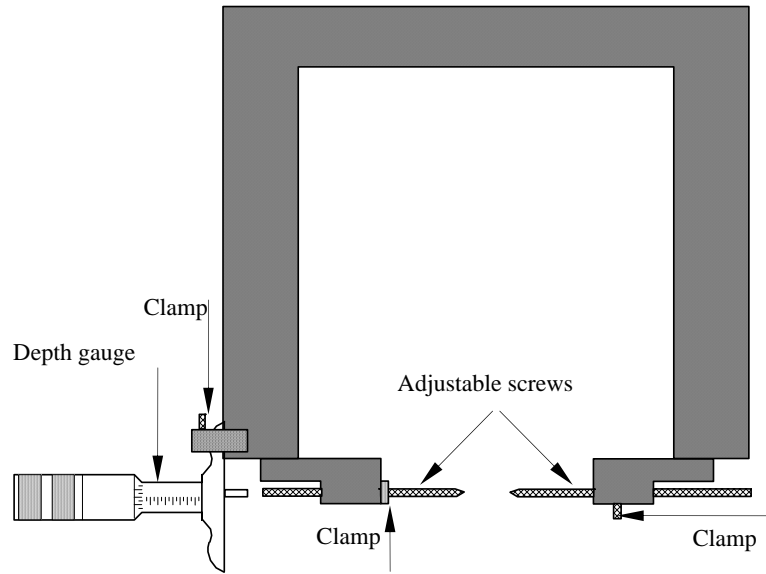


Figure 2. Instrument Used for Thickness Measurements of Sample Beams

As many readings as possible (up to 150 readings for each beam) were taken in order to increase the accuracy of the measurements. Average measurements of the thicknesses of each beam are shown in Table 1. The loss of thickness on average was more significant in the flanges than in the webs.

Table 1. Average Measured Thicknesses of Corroded Beams (Rahgozar [18])

Element	As new	Beam 1	Beam 2	Beam 3
Average thickness of top flange	10.20	7.45	7.81	7.23
Average thickness of bottom flange	10.20	5.62	5.85	4.84
Average thickness of top and bottom flanges	10.20	6.54	6.83	6.04
Average thickness loss of top and bottom flanges	0.00	3.66	3.37	4.16
Percentage average thickness loss of top and bottom flanges	0.00	35.9%	33.3%	40.8%
Average thickness of upper part of web ( $0.75h_w$ )	6.10	5.63	5.74	5.45
Average thickness of lower part of web ( $0.25h_w$ )	6.10	3.16	4.32	3.18
Average thickness of web	6.10	5.01	5.39	4.88
Average thickness loss of web (mm)	0.00	1.09	0.71	1.22
Percentage average thickness loss of web	0.00	17.8%	11.7%	20.0%

Note:  $h_w$  = depth of web, all measurements are in millimeters

## 6. ANALYSIS OF THE EFFECT OF CORROSION DAMAGE OF STEEL BEAMS

### 6.1 Corrosion Decay Models

Corrosion of steel occurs when the electrolytes are present on the surface, particularly in places where water and contaminants can accumulate. The places most commonly found with corrosion are the top surface of the bottom flange where water collects from dew or splash and on the web near the abutments and joints. It has been pointed out by Kayser and Nowak [19] that severe corrosion may take place at the bottom one quarter of the web. Therefore the top surface of the bottom flange and the bottom part of the web are the regions where severe corrosion may take place, as shown in Figures 3. Corrosion also takes place in the top flange and the top part of the web but the loss is much less as compared to that of the web's bottom part.

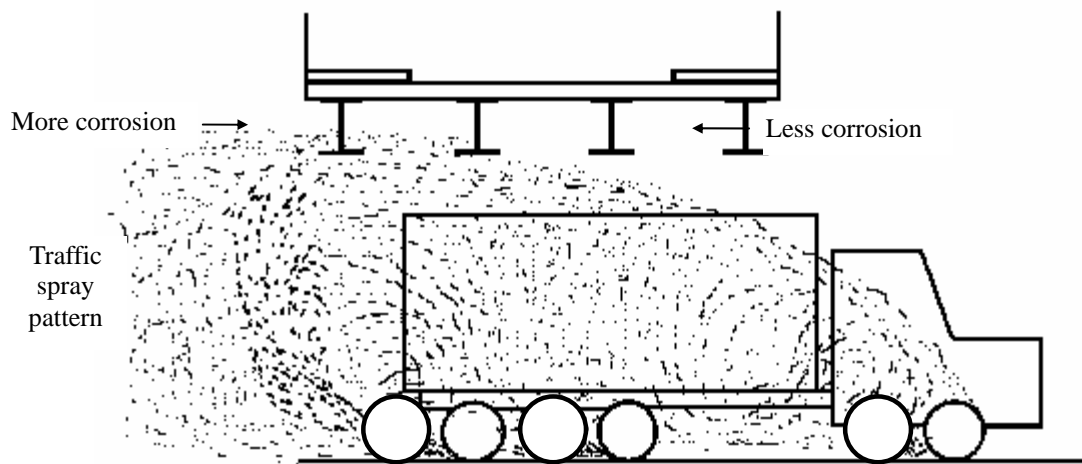
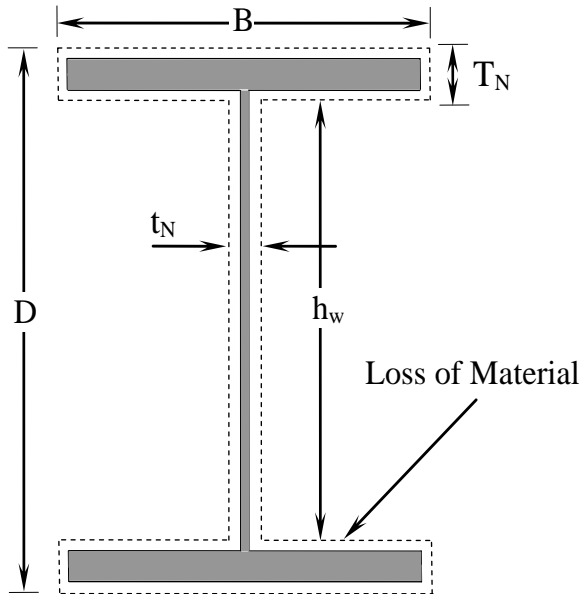


Figure 3(a) The Traffic Spray Accumulation on Girder Flanges and Webs



Figure 3(b). Typical Locations where Corrosion can occur on a Steel Girder Bridge

The development of corrosion decay models mainly requires the information on the locations where corrosion normally occurs and the types of corrosion damage of steel members. The most common form of corrosion damage of steel is general surface corrosion. The locations where corrosion occurs were discussed earlier. From these discussions, basic conclusions were made concerning the location of corrosion. Using this information, two corrosion decay models were considered by reducing the thickness of the sections. The two models which are shown in Figures 4 are as follow:



**Loss of Material**

Flanges  $\mu T_N$

Web  $\mu t_N$

Where  $T_N$  and  $t_N$  are the thicknesses of the flanges and web of as-new section,

$\mu = \%LFT/100 = \%LWT/100, \mu = \mu_F = \mu_W$

$\%LFT$  = Percentage loss of flange thickness

$\%LWT$  = Percentage loss of web thickness

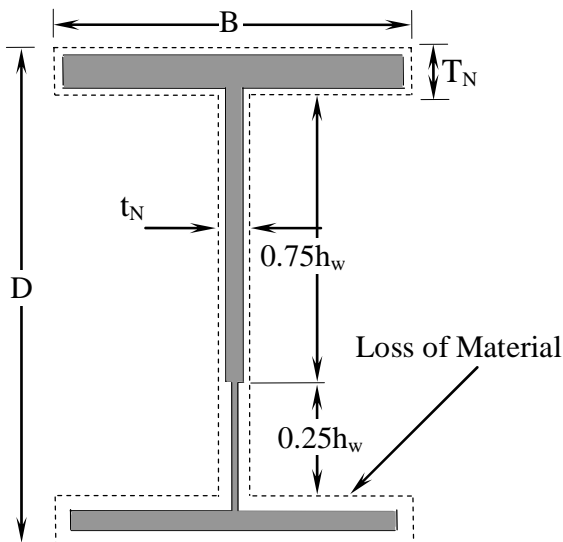
Figure 4(a). Uniform Thickness Loss in both Flanges and Web (Model 1)

Thickness of the top flange =  $T_N (1-\mu)$  (1a)

Thickness of the bottom flange =  $T_N (1-\mu)$  (1b)

Average thickness of the flanges,  $T_c = T_N (1-\mu)$  (1c)

Thickness of the web,  $t_c = t_N (1-\mu)$  (1d)



**Loss of Material**

Top flange  $0.7\mu T_N$

Upper part of the web  
( $0.75h_w$ )  $0.25\mu t_N$

Lower part of the web  
( $0.25h_w$ )  $1.25\mu t_N$

Bottom flange  $1.3\mu T_N$

where  $\mu = \%LFT / 100$

Figure 4(b). Varying Thickness Loss in both Flanges and Web (Model 2)

Figure 4. Corrosion Decay Models Simulated By Reducing the Thickness of Elements

Thickness of the top flange =  $T_N (1- 0.7\mu)$  (2a)

Thickness of the bottom flange =  $T_N (1- 1.3\mu)$  (2b)

Average thickness of the flanges  $T_c = T_N (1-\mu)$  (2c)

Thickness of the upper part of the web ( $0.75h_w$ ) =  $t_N (1- 0.25\mu)$  (2d)

Thickness of the lower part of the web ( $0.25h_w$ ) =  $t_N (1- 1.25\mu)$  (2e)

Average thickness of the web,  $t_c = t_N (1- 0.5\mu)$  (2f)

Where  $\mu = \mu_F = 2\mu_W$ .

In the case of model 2, the thickness loss of flanges and web were in similar proportion to the thickness loss of the samples of corrosion damaged beams obtained from a chemical plant (Table 1). The measured thicknesses of these beams are given in Table 1. It can be established from Table 1 that the thickness loss of the bottom flange of sample beams is approximately twice as that of the loss of the top flange. The thickness loss of the lower part of the web ( $0.25hw$ ) is nearly five times as that of the upper part of the web ( $0.75hw$ ). For two sample beams the average thickness loss of the web is approximately half of that of the average loss of the flanges. These ratios were used for the development of Model 2 (varying thickness loss model) as shown in Figure 4(b).

The thickness loss of the stiffeners of all the sample beams is very minimal, i.e. only about 10% of its original thickness. It is also observed that the percentage thickness loss of the stiffeners is nearly the same as that of the upper part of the web. Therefore, for the corrosion decay models, it was assumed that the loss of material in the stiffeners was in similar proportion to the thickness loss of the upper part of the web.

## 7. WEB BEARING CAPACITY

Plate elements (e.g. webs) are subjected to bearing stresses by concentrated loads or locally distributed edge loads (reactions from supports or other members) as shown in Figure 5. For example, a concentrated load applied to the top flange of a beam induces local bearing stresses in the web immediately beneath the load. When the load reaches its critical value, the web crushes (cripples) by combined compression and folding directly under the load.

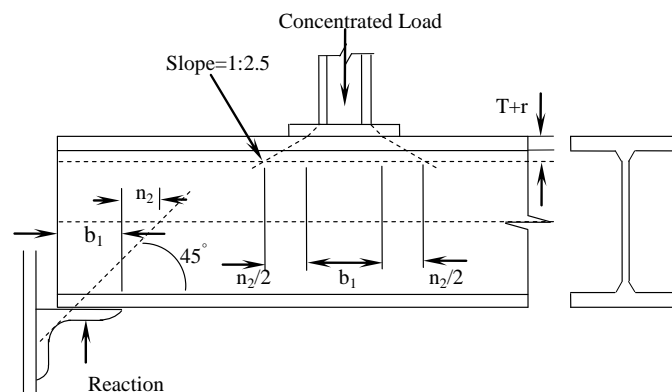


Figure 5. Effective Web Bearing Length to Resist Crushing

The ultimate bearing strength of a thick web depends on its design strength,  $p_y$ . although yielding first occurs under the centre of the bearing plate, general yielding does not takes place until the applied load is large enough to cases yielding of a web area defined by a dispersion of the applied load is large enough the flange. Even at this load the web does not collapse catastrophically, and some further yielding and redistribution is possible (Trahair et al. [20]).

Where point loads or reactions from supports or other members are applied to a beam as shown in Figure 5 then the web should be checked for bearing stresses. The web bearing strength,  $P_{wb}$ , is given by

$$P_{wb} = (b_1 + n_2) t p_y \quad (3)$$

where

$b_1$  is the stiff bearing length,

$n_2$  is the length obtained by the slope 1:2.5 dispersion through the flange and can be taken as follows :

$n_2 = 2 \times 2.5(T + r)$  for forces applied through a flange by loads or reactions in the length between the ends and

$n_2 = 2.5(T + r)$  for forces applied through a flange by loads or reactions at the ends,

$t$  is the thickness of the web and,

$p_y$  is the design strength of the web.

The code recommends that if the force applied through a flange by loads or reactions exceeds the local capacity of the web at its connection to the flange, then bearing stiffeners should be provided.

## 8. ASSESSMENT METHODS FOR EVALUATION THE RESIDUAL WEB BEARING CAPACITY

### 8.1 Simple Assessment Method Using the Developed Corrosion Decay Models

The web bearing strength,  $P_{wb}$ , of a section can be evaluated using the theory given in Section 7, in which the web bearing strength is given as follows:

$$P_{wb} = (b_1 + n_2) t p_y \quad (4)$$

Equation 4 may be written as:

$$P_{wb} = [b_1 + 2.5 c (T + r)] t p_y \quad (5)$$

where

$c = 2$  for forces applied through a flange by loads or reactions in the length between the ends, and  
 $c = 1$  for forces applied through a flange by loads or reactions at the ends.

The percentage residual web bearing capacity ( $\%RWBC$ ) of a corrosion damaged section can be presented the capacity of corrosion section ( $WBC_C$ ) to the capacity of the section in its new condition ( $WBC_N$ ). It can be expressed as:

$$\%RWBC = 100 (WBC_C / WBC_N) \quad (6)$$

Using Equation 5, the  $\%RWBC$  is obtained as:

$$\%RWBC = 100 \frac{t_C [b_1 + 2.5 c (T_C + r)]}{t_N [b_1 + 2.5 c (T_N + r)]} \quad (7)$$

The root radius,  $r$ , may be taken as constant throughout the service life of a beam. Equation 7 shows that the design strength has no effects on the  $\%RWBC$ . In order to obtain a minimum for the  $\%RWBC$ , it is necessary to identify the worst possible case, which can be taken as when  $b_1 = 0$ , i.e. stiff bearing plates are not provided. Substituting  $b_1 = 0$  into Equation 7 gives the  $\%RWBC$  as:

$$\%RWBC = 100 \frac{t_C (T_C + r)}{t_N (T_N + r)} \quad (8)$$

For uniform thickness loss model sections in which  $\mu = \mu_F = \mu_W$  where  $\mu = \%LFT / 100$ , if Equations

1a and 1b (for  $T_C$  and  $t_c$ ) are combined with Equation 8, the following relation is obtained for the %RWBC as:

$$\%RWBC = 100(1 - \mu) \frac{(1 - \mu) + \left(\frac{r}{T_N}\right)}{1 + (r/T_N)} \quad (9)$$

Equation 9 shows that when  $(r/T_N)$  decreases, the %RWBC also decreases. Hence, the minimum of %RWBC can be obtained when the value of  $(r/T_N)$  is the minimum. By analysing the available I-sections for UK steel manufactured, the minimum of  $(r/T_N)$  was obtained as 0.5 for section UB29 (457×191 UB 98). Now, substituting the minimum of  $(r/T_N)$  into Equation 9 gives the minimum of %RWBC of uniform thickness loss model sections as:

$$\text{Min}(\%RWBC) = 100(1 - \mu) \left(1 - \frac{2}{3}\mu\right) \quad (10)$$

For varying thickness loss model sections in which  $\mu = \mu_F = 2\mu_w$ , combining Equation 2c, 2f (for  $T_C$  and  $t_c$ ) and 8 together with the minimum value of  $(r/T_N)$  gives the minimum of %RWBC as:

$$\text{Min}(\%RWBC) = 100(1 - \mu) \left(1 - \frac{4}{3}\mu\right) \quad (11)$$

Therefore, Equations 10 and 11 may be used as the minimum curves for estimating the percentage remaining web bearing capacity of corrosion damaged beams that are not provided with web bearing stiffeners. The evaluated equations (10, 11) have been shown in Figure 6 for uniform and varying corrosion decay models. These two equations, which are derived from the developed corrosion models, are named as simple.

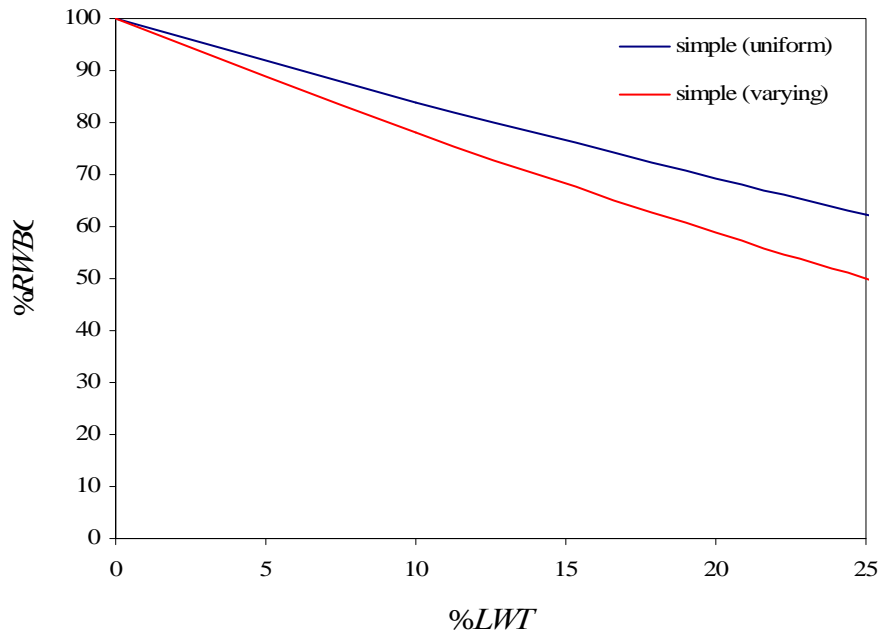


Figure 6. Minimum Curves of Simple Assessment Methods for Uniform and Varying Corrosion Models

### 8.2 Accurate Assessment Method

Here, it has been decided to employ this procedure for UK steel manufactured I-sections. The accurate assessment method involves analyzing all the I-sections (71 sections) manufactured in the UK. This will require a considerable amount of man hours and computer time to identify the section that gives the minimum curve. The aforementioned problem was minimized by using the following procedure that involves only about 25 sections and a computer programming. First, a family of sections (i.e. sections, which have the same serial size) was analyzed to observe their behavior regarding a particular failure mode and to identify the section that gives the minimum curve for the family. Considering the above observation, the sections with similar properties from each of the families were analyzed to identify the section that gives the minimum curve for all the sections. For simplicity, the results of the analysis are given in this study for only a few sections including the sections that have the maximum and minimum percentage residual capacity. The sections are numbered according to their position in the section table (e.g. *UB1*, *UB2*, etc.).

A family of sections with varying thickness loss was analyzed to study the behaviour of %*RWBC* of corrosion damaged sections that are not provided with web bearing stiffeners. The results and the detail of the family of sections are given in Figure 7.

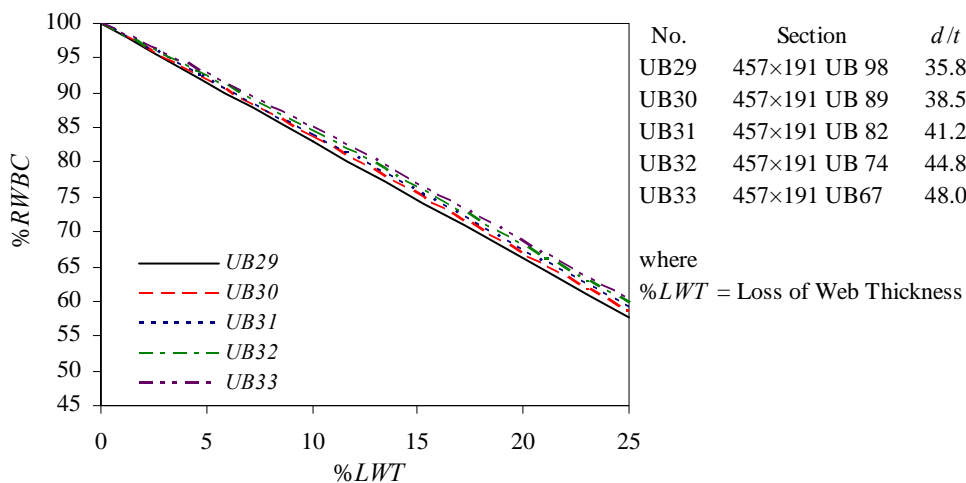


Figure 7. Behavior of %*RWBC* of a Family of Sections

It can be seen from Figure 7 that the section with the lowest value of *d/t* (*UB29*) gives the minimum curve for the %*RWBC* of the family of sections. Based on the above observation, sections that have the lowest value of *d/t* from each of the families were analyzed to obtain a minimum curve for the %*RWBC*. The results for five beams and the details of the sections are given in Figure 8.

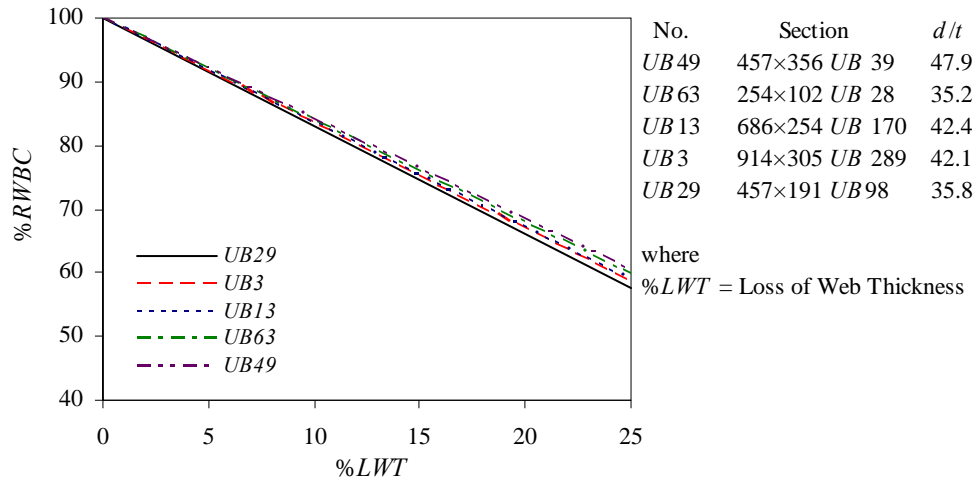


Figure 8. Behavior of %  $RWBC$  of Sections from Five Families

It is evident from Figure 8 that the section that has the lowest value of  $d/t$  ratio ( $UB29$ ) gives the minimum curve for the % $RWBC$  of the whole range of corrosion damaged beams that are not provided with web bearing stiffeners. The variation in the percentage remaining capacities between the maximum and minimum values of  $d/t$  ratio is small (less than 7% for web thickness loss of 25%).

## 9. MINIMUM CURVES

It was found in the analysis that the section with the lowest value of  $d/t$  ( $UB29$ ) gives the minimum curve for the % $RWBC$  of corrosion damaged sections that are not provided with web bearing stiffeners. The results of simple assessment have been compared with the minimum curves which are concluded from the accurate procedure in Figure 9 for uniform and varying thickness loss models.

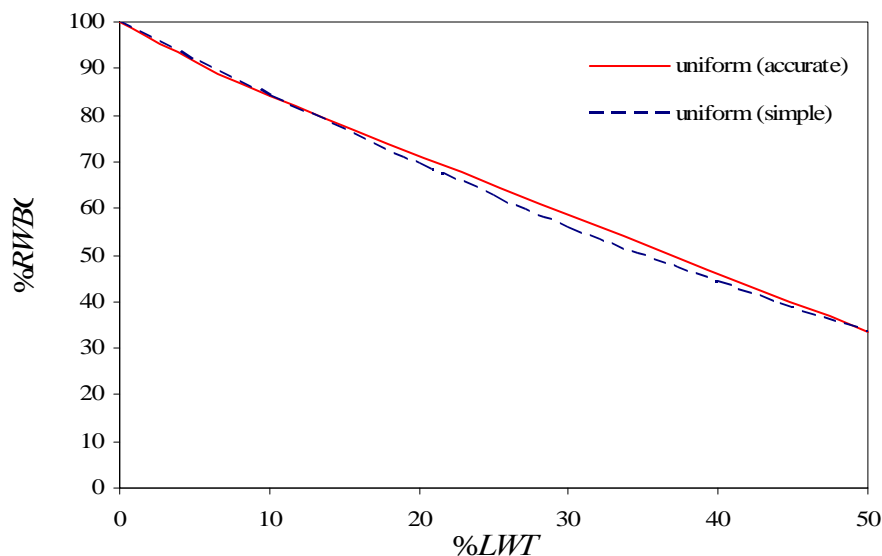


Figure 9(a). Minimum Curve to Estimate the % $RWBC$  of Corroded Steel I-Beam Due to Uniform Corrosion Models

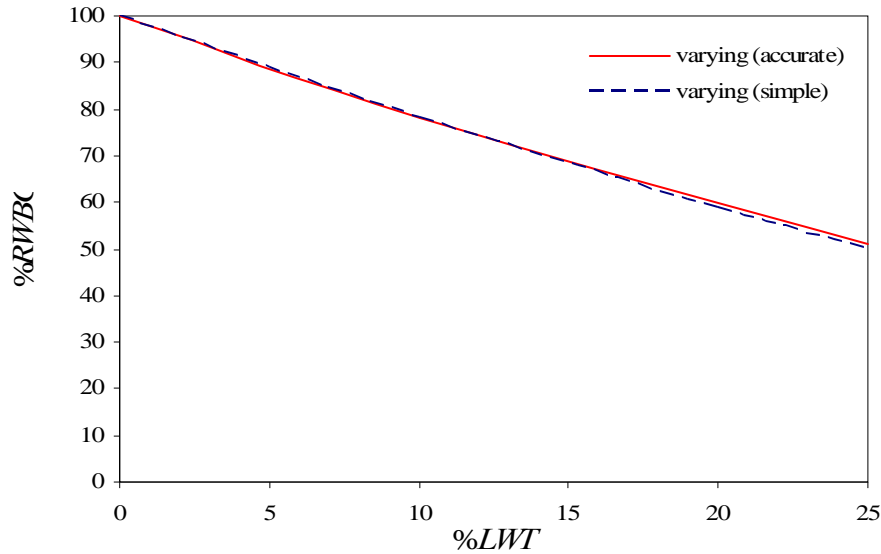


Figure 9(b). Minimum Curve to Estimate the %RWBC of Corroded Steel I-Beam Due to Varying Corrosion Models

From Figures 9 it is evident that the proposed simple method has a good agreement with the real load-carrying capacity (accurate method). Therefore, this procedure can be used to estimate the load-carrying capacity of corroded steel I-beams. Therefore, this procedure has been schematically shown in Figure 10. A practice engineer can evaluate the remaining web bearing capacity by using this flowchart.

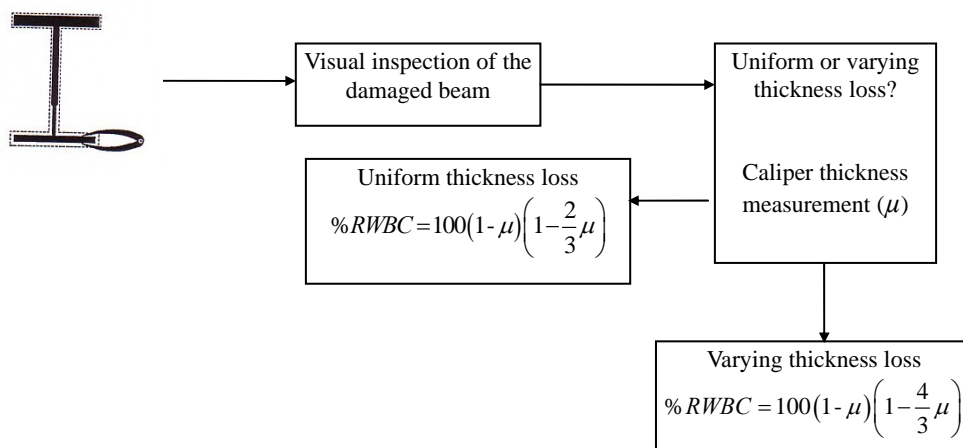


Figure 10. Procedures for Predicting the Remaining Web Bearing Capacity of a Corroded Steel Beam

### 10. CONCLUSIONS

It was shown by the accurate assessment method that, it is possible to obtain minimum curves that can be used to estimate the load-carrying capacities of corrosion damaged beams with considerable accuracy. Two credible corrosion models for steel I-beams sections have been developed based on the real corrosion loss data. By taking into account the effect of corrosion on the strength capacities (e.g., moment, shear, web bearing, ...) the minimum curves can be obtained. Here, the foregoing approach was employed in order to derive the residual web bearing capacity of corroded steel beams. Since there is a good agreement between the proposed (simple) and accurate assessment methods, the

validity of proposed analytical method (simple assessment method) is confirmed and these formulae may be used with the information on the loss of thicknesses of the section to estimate the percentage residual web bearing of corroded sections. The results of this research will help the practicing engineer to make a fast and reliable decision regarding the residual strength capacities of corrosion damaged I-beam.

## ACKNOWLEDGEMENT

The author is pleased to acknowledge the Vali-e-Asr University of Rafsanjan support.

## REFERENCES

- [1] Kayser, J. R., "The Effects of Corrosion on The Reliability of Steel Girder Bridges", PhD thesis, Department of Civil Engineering, University of Michigan, 1988.
- [2] Kulicki, J.M., Prucs, Z., Sorgenfrei, D.F. and Mertz, D.R., "Guidelines for Evaluating Corrosion Effects in Existing Steel Bridges", National Cooperative Highway Research Program, Report 333, Transportation Research Board, National Research Council, Washington, D.C; 1990.
- [3] Sharifi, Y. and Rahgozar, R., "Evaluation of the Remaining Shear Capacity in Corroded Steel I-Beams", International Journal of advanced Steel Construction, 2010, Vol. 6, No. 2, pp. 803-816.
- [4] Sharifi, Y. and Rahgozar, R., "Remaining Moment Capacity of Corroded Steel Beams", International Journal of Steel Structures, 2010, Vol. 10, No. 2, pp. 165-176.
- [5] Sharifi Y. and Rahgozar R., "Simple Assessment Method to Estimate the Remaining Moment Capacity of Corroded I-Beam Sections", Scientia Iranica Journal, 2010, Vol. 17, No. 2, pp. 161-167.
- [6] Sharifi Y. and Rahgozar R., "Evaluation of the Remaining Lateral Torsional Buckling Capacity in Corroded Steel Beams", Journal of Zhejiang University SCIENCE A, 2010, Vol. 11, No. 11, pp. 887-897.
- [7] Rahgozar R., Sharifi, Y. and Malekinejad, M., "Buckling Capacity of Uniformly Corroded Steel Members in terms of Exposure Time", Steel and Composite Structures, 2010, Vol. 10, No. 6, pp. 475-487.
- [8] Sharifi, Y. and Rahgozar, R., "Fatigue Notch Factor in Steel Bridges Due to Corrosion", Archives of Civil and Mechanical Engineering, 2009, Vol. IX, No. 4, pp. 75-83.
- [9] Paik, J.K., Lee, J.M. and Ko, M.J., "Ultimate Compressive Strength of Plate Elements with Pit Corrosion Wastage", Journal of Engineering Maritime Environment, 2003, Vol. 217, No. M4, pp. 185-200.
- [10] Paik, J.K., Lee, J.M. and Ko, M.J., "Ultimate Shear Strength of Plate Elements with Pit Corrosion Wastage", Thin-Walled Structures, 2004, Vol. 42, No. 8, pp. 1161-76.
- [11] Nakai, T., Matsushita, H. and Yamamoto, N., "Effect of Pitting Corrosion on the Ultimate Strength of Steel Plates Subjected to In-Plane Compression and Bending". Journal of Marine Science and Technology, 2006, Vol. 11, No. 1, pp. 52-64.
- [12] Czarnecki, A.A. and Nowak, A.S., "Time-Variant Reliability Profiles for Steel Girder Bridges", Structural Safety, 2008, Vol. 30, No. 49-64.
- [13] Sharifi, Y. and Paik, J.K., "Ultimate Strength Reliability Analysis of Corroded Steel-box Girder Bridges", Thin-Walled Structures, 2011, Vol. 49, No. 1, pp. 157-166.
- [14] Sharifi, Y. and Paik, J.K., "Environmental Effects on Ultimate Strength Reliability of Corroded Steel Box Girder Bridges", Structural Longevity, 2010, Vol. 18, No. 1, pp. 1-20.

- [15] Sharifi, Y. "Reliability of Deteriorating Steel Box-Girder Bridges under Pitting Corrosion", *International Journal of advanced Steel Construction*, 2011, Vol. 7, No. 3, pp. 220-238.
- [16] Nethercot, D. A., "Limit States Design of Structural Steelwork", 3rd ed. Spon Press, London, UK, 2001.
- [17] Fontana, M. G., "Corrosion Engineering", McGraw Hill Book Company, New York, Third Edition, 1987.
- [18] Rahgozar, R., "Remaining Capacity Assessment of Corrosion Damaged Beams using Minimum Curves", *Journal of Constructional Steel Research*, 2009, Vol. 65, pp. 299-307.
- [19] Kayser, J. R. and Nowak, A. S., "Capacity Loss Due to Corrosion in Steel-Girder Bridges", *Journal of Structural Engineering*, ASCE, 1989, 115, pp. 1525-1537.
- [20] Trahair, N. S., Bradford, M. A. and Nethercot D. A., "The Behavior and Design of Steel Structures to BS5950", Third Edition-British, London, Spon Press, Taylor & Francis Group, 2001.

# A BIFURCATION ANALYSIS OF SPACE STRUCTURES BY USING 3D BEAM-COLUMN ELEMENT CONSIDERING FINITE DEFORMATIONS AND BOWING EFFECT

K.S. Lee <sup>1,\*</sup> and S.E. Han <sup>2</sup>

<sup>1</sup> *Research Professor, Department of Civil & Environmental Engineering  
Korea Advanced Institute of Science and Technology, 373-1 Guseong-dong, Yuseong-gu, Daejeon, South Korea*

<sup>2</sup> *Professor, Department of Architectural Engineering, School of Architecture  
Inha University, 253 Yonghyundong, Nam-gu, Incheon, 402-751, South Korea*

*\*(Corresponding author: E-mail: kslee77@kaist.ac.kr)*

*Received: 22 September 2011; Revised: 19 December 2011; Accepted: 30 December 2011*

---

**ABSTRACT:** The present paper describes the space frame element and the fundamental strategies in computational elastic bifurcation theory of geometrically nonlinear, single load parameter conservative elastic spatial structures. A method for large deformation (rotation) analysis of space frame is based on an Eulerian formulation, which takes into consideration the effects of large joint rotations with finite deformation(rotation). The local member force-deformation relationships are based on the beam-column approach, and the change in member chord lengths caused by axial strain and flexural bowing are taken into account. And the derived geometric stiffness matrix is asymmetric because of the fact that finite rotations are not commutative under addition. To detect the singular point such as bifurcation point, an iterative pin-pointing algorithm is proposed. And the path switching mode for bifurcation path is based on the non-negative eigen-value and its corresponding eigen-vector. Some numerical examples for bifurcation analysis for a plane frame, plane circular arch and space dome structures are described.

**Keywords:** Elastic stability, Bifurcation, Space frame, Eulerian, Finite deformation

---

## 1. INTRODUCTION

This paper deals with the theoretical aspects of bifurcation buckling of space frame for the elastic stability. An arc-length method is used for the nonlinear post-buckling numerical strategies and 3D beam-column equations are adopted to investigate the numerical characteristics of bifurcation buckling which is the most important critical state of elastic stability of space frame for the space frame element.

The pioneering research work of Koiter [1] and Thompson and Hunt [2] focused on the general theory of elastic stability. Their studies were understood as the milestone work on the formulation of the basic theory of elastic stability theory and play an important role in establishing the theory of elastic stability problems, but there is a limitation to apply the higher order mathematical stability theories to the analytical methods such as finite element method.

Therefore, in recent years, it is applied to the actual problems of elastic stability by co-operating the arc length method [3-11] and the theory of nonlinear finite element method. Recently analytical theory of elastic stability including bifurcation analysis was introduced in references [9-11]. From the theory of elastic stability, buckling of elastic structure can be divided into snap-through, snap-back and bifurcation buckling, and commonly, bifurcation called as buckling of structures. The critical stability points in nonlinear elasticity may be classified into limit and bifurcation point. The snap through and snap back buckling has the characteristics of the limit point, and bifurcation has the characteristics of bifurcation point.

For limit point buckling, the path tracing scheme to successively compute the regular equilibrium points on the equilibrium path and the pinpointing scheme to precisely locate the singular equilibrium points are sufficient for the computational stability analysis. For bifurcation points, however, a specific procedure for path-switching is also necessary to detect the branching paths to be traced in the post buckling region. Generally, limit point buckling often occurred when the concentrated load is imposed at the apex of dome shaped shallow shell structure. And bifurcation buckling often occurred when the uniform loads of space structures subjected to compressive forces.

The indirect [3-5, 9-14] and direct methods [11,15-21] are proposed to detect the bifurcation point respectively. The detection of bifurcation point is determined by the detection parameter while equilibrium path is being traced with indirect method. With direct method, the extended system, which is a new set of equations added to the original set of nonlinear equilibrium equations, is solved to obtain both the critical point and its associated eigen-mode.

To search the complex equilibrium path of primary and bifurcation path of post buckling range, the space frame element should consider a finite rotation due to the geometric large deformation and elastic element force. Both a beam-column approach [22-26], based on the member basic force and deformation relationships, and a finite element approach [27-41] has been used in developing the nonlinear governing equations. The large-deformation geometrically nonlinear analysis is carried out by various methods of treatment of the non-vectorial nature of rotations, the selection of coordinate systems of the stress-strain tensor and the linearization of variational equations. Large rotations are usually represented by Euler's finite theory [27, 32] and applied to both beam-column [23-26] and finite element theory [27-33]. Agyris et al. [27-31] introduced so-called semi-tangential rotations to circumvent the non-vectorial or non-commutative behavior of successive finite rotations about fixed axes. An alternative way of deriving efficient non-linear finite element models is the co-rotational approach [34-40]. The main idea of this approach is to decompose the motion of the element into rigid body and pure deformational parts through the use of a reference system that continuously rotates and translates with the element. The procedure for the co-rotational approach is similar to the Eulerian finite rotation of a beam-column element. Most of these finite element nonlinear analysis techniques are based on assumed displacement fields and require a large number of elements to model a structure with large deformation. However it is known that an Eulerian formulated beam-column approach with bowing effect [24,25] can produce a sufficient solution with one element per member different from finite element formulations.

In this study, to identify the characteristics of critical point, which separated into the limit and bifurcation point, the indirect method was used to search the critical points through the calculation of parametric variable determined by the smallest eigen-value without considering the higher order terms in equilibrium equation. And unlike previous studies, which had used the smallest eigen-value only for the case of single bifurcation, in this study, the smallest eigen-value and corresponding eigen-vector are used to switch to the bifurcation path for single and multiple bifurcation analysis. And to perform the highly nonlinear post buckling analysis such as bifurcation, a space frame element that reflects the large deformation, rigid body motion and relative deformation are calculated according to the theory of Spiller [23] and Levy and Spiller [26] for Eulerian finite rotation of a 3D space frame. The elastic beam-column formulations of Kassimali and Abbasnia [24] are also adopted. The effects of axial force on the member bending moment (bowing effect) are included in the analysis. The asymmetric tangent stiffness matrix due to the finite rotation of space frame element, derived by Spiller [23] and Levy and Spiller [26], is used to include some symmetric and asymmetric buckling modes in physical situations. However, the effect of axial force on the member's torsional stiffness (Wagner effect) and warping effect are omitted for simplicity.

Finally, numerical examples for elastic bifurcation analyses were carried out for the proposed simple and efficient bifurcation algorithm with large deformation space frame element to demonstrate accuracy and efficiency.

## 2. THEORY OF ELASTIC STABILITY

The potential energy of structures can be written as follows

$$\mathbf{\Pi}(\mathbf{d}, \lambda) = \mathbf{U} + \mathbf{V} \quad (1)$$

$\mathbf{\Pi}$ : total potential energy,  $\mathbf{U}$ : strain energy,  $\mathbf{V}$ : external work,  
 $\mathbf{d}$ : displacement,  $\lambda$ : scalar load parameter

The variation of potential energy  $\delta\mathbf{\Pi}$  can be expressed from the Taylor expansion of Eq. 1 as follows

$$\delta\mathbf{\Pi}(d, \lambda) = \frac{\partial\mathbf{\Pi}}{\partial\mathbf{d}}\delta\mathbf{d} + \frac{1}{2}\delta\mathbf{d}^T \frac{\partial^2\mathbf{\Pi}}{\partial\mathbf{d}^2}\delta\mathbf{d} + \mathbf{O}(\delta\mathbf{d}^3) \quad (2)$$

From Eq. 2, by applying the well known equations for potential energy, a residual vector,  $\mathbf{g}(\mathbf{d}, \lambda) = \partial\mathbf{\Pi}/\partial\mathbf{d}$  and a tangent stiffness matrix,  $\mathbf{K}_t = \partial^2\mathbf{\Pi}/\partial\mathbf{d}^2$ , and omitting the higher order term, the Eq. 2 can be rewritten as follows

$$\delta\mathbf{\Pi}(\mathbf{d}, \lambda) = \mathbf{g}^T\delta\mathbf{d} + \frac{1}{2}\delta\mathbf{d}^T\mathbf{K}_t\delta\mathbf{d} \quad (3)$$

From the stationary condition of potential energy in equilibrium state, the equation of structure in equilibrium state can be represented as follows.

$$\mathbf{\Pi}_{,\delta\mathbf{d}} = \mathbf{g}(\mathbf{d}, \lambda) = \mathbf{F}(\mathbf{d}) - \lambda\mathbf{P} = 0 \quad (4)$$

In addition, the second term in Eq. 2 should be positive value according to the theory of stability in conservative system, and this condition can be expressed as follows in matrix form.

$$\mathbf{\Pi}_{,\delta\mathbf{d}^2} = \frac{1}{2}\delta\mathbf{d}^T\mathbf{K}_t\delta\mathbf{d} > 0 \quad (5)$$

It called as unstable state, if above equation is not positive value.

The state changes of stability point on equilibrium path,  $[\mathbf{d}, \lambda]$  represent the change of value Eq. 5  $\mathbf{\Pi}_{,\delta\mathbf{d}^2}$  from positive to negative.

And these state changes on equilibrium path called as critical state or critical point. In this paper, parameters  $l$  and  $*$  for the length of equilibrium path, represent the critical point, satisfying the following relationship.

$$(\mathbf{d}^*, \lambda^*) = (\mathbf{d}(l^*), \lambda(l^*)) \quad (6)$$

$$\mathbf{K}_t(\mathbf{d}^*, \lambda^*)\mathbf{x} = 0 \quad (7)$$

The definite definition for critical point of Eq. 7 can be obtained which satisfy the condition of  $\omega_j = 0$  in generalized eigen-value problem as follows.

$$|\mathbf{K}_t - \omega_j \mathbf{I}| \boldsymbol{\varphi}_j = 0 \quad (8)$$

Where  $\omega_j$  is j-th eigen-value in Eq. 8. Another expression for critical point in stability condition is represented by a determinant of tangent stiffness matrix which satisfying the necessary condition only as follows.

$$D = \det|\mathbf{K}_t| = 0 \quad (9)$$

We can obtain the expression for stable condition in equilibrium state, by using the value for eigen-value  $\omega_j$ . The system may remain in the stable state until the eigen-value  $\omega_j$  of N-DOF satisfy the following equation.

$$0 < \omega_1 \leq \omega_2 \leq \omega_3 \cdots \leq \omega_N \quad (10)$$

It reaches the critical or stability limit state when  $\omega_j$  may have the following values.

$$0 = \omega_1 = \omega_2 \cdots = \omega_k < \omega_{k+1} \cdots \leq \omega_N \quad (11)$$

The single critical condition,  $k = 1$  means that the minimum eigen-value satisfies zero value  $\omega_k = 0$  only. Where multiple critical condition,  $k > 1$  means multiple numbers of eigen-value are zero value simultaneously. In this study, we considered the single and multiple critical states for stability point.

The new equation for residual vector of Eq. 4 can be obtained from the Taylor series expansion about equilibrium state,  $[\mathbf{d}_0, \lambda_0]$  as follows.

$$\mathbf{g}(\mathbf{d}, \lambda) = \mathbf{g}(\mathbf{d}_0, \lambda_0) + \frac{\partial \mathbf{g}}{\partial \mathbf{d}_0} \Delta \mathbf{d} + \frac{\partial \mathbf{g}}{\partial \lambda_0} \Delta \lambda + O(\Delta \mathbf{d}^2, \Delta \lambda^2, \Delta \mathbf{d} \Delta \lambda) \quad (12)$$

If we assume the initial equilibrium state,  $\mathbf{g}(\mathbf{d}, \lambda) = \mathbf{g}(\mathbf{d}_0, \lambda_0) = 0$  and omitting the higher order term in Eq. 12, The new expression for Eq. 12 can be obtained as follows.

$$\frac{\partial \mathbf{g}}{\partial \mathbf{d}_0} \Delta \mathbf{d} + \frac{\partial \mathbf{g}}{\partial \lambda_0} \Delta \lambda = \mathbf{K}_t \Delta \mathbf{d} - \Delta \lambda \mathbf{P} = 0 \quad (13)$$

The critical point which represents the condition of change of state, stable to unstable or unstable to stable, the minimum eigen-value may be zero value,  $\omega_1 = 0$  on equilibrium path. And applying the corresponding minimum eigen-vector,  $\boldsymbol{\varphi}_1$  to Eq. 13, the new expression for Eq. 13 can be obtained as follows.

$$\Delta \mathbf{d}^T \mathbf{K}_t \boldsymbol{\varphi}_1 - \Delta \lambda \mathbf{P}^T \boldsymbol{\varphi}_1 = 0 \quad (14)$$

The left first tem of Eq. 14 can be omitted from the relationship of Eq. 7. Therefore, Eq. 14 can be rewritten as follows.

$$\Delta\lambda\mathbf{P}^T\boldsymbol{\varphi}_1 = 0 \quad (15)$$

The satisfactory condition of Eq. 15 can be classified as following two cases.

$$\mathbf{P}^T\boldsymbol{\varphi}_1 \neq 0, \Delta\lambda = 0 \quad \text{:Limit point} \quad (16-a)$$

$$\mathbf{P}^T\boldsymbol{\varphi}_1 = 0, \Delta\lambda \neq 0 \quad \text{:Bifurcation point} \quad (16-b)$$

As a result, Eqs. 16 and 17 represent the condition of separating the critical point by limit and bifurcation point. Therefore, we can divide the critical point of system by using the Eq. 16. If the bifurcation point is detected by using these equations, the post buckling equilibrium path is switched to the bifurcation of branching path in primary path by using following path switching algorithm.

### 3. SEARCH FOR EQUILIBRIUM PATH

The arc-length method can be considered as the most efficient numerical method to calculate the nonlinear equilibrium path. The general displacement or load incremental method using the Newton-Raphson method cannot exactly calculate the equilibrium path beyond an inflection point, such as limit point because of using only one parameter to control the analysis process. However the arc-length method can calculate the displacement and load parameter  $[\mathbf{d}, \lambda]$  simultaneously, by using the arc-length constraint which is a function of pre-defined arc-length parameter,  $\Delta l$ .

When using the arc-length method, the incremental displacement and load parameter  $[\Delta\mathbf{d}, \Delta\lambda]$  can be calculated by using the following simultaneous equations in predictor process.

$$\mathbf{K}_i\Delta\mathbf{d} - \Delta\lambda\mathbf{P} = 0 \quad (17)$$

$$\Delta\mathbf{d}^T\Delta\mathbf{d} - b\Delta\lambda^2\mathbf{P}^T\mathbf{P} = \Delta l^2 \quad (18)$$

$b$  : proportional constant,  $\Delta l$  : arc-length parameter

The arc-length method can be classified into a spherical and cylindrical arc-length method according to the value of proportional constant,  $b$  in Eq. 18. In this paper, the spherical arc-length method [3-5] is employed by using  $b = 1$ .

The Iterative displacement and load parameter  $[\delta\mathbf{d}, \delta\lambda]$  can be calculated by using following simultaneous equations which are linearized form of Eqs. 17 and 18, in corrector process.

$$\mathbf{K}_i\delta\mathbf{d} - \delta\lambda\mathbf{P} = \mathbf{g}(\mathbf{d}_i, \lambda_i) \quad (19)$$

$$\Delta\mathbf{d}^T\delta\mathbf{d} - b\Delta\lambda\delta\lambda\mathbf{P}^T\mathbf{P} = 0 \quad (20)$$

From the iterative corrector process, the converged equilibrium point on primary path can be solved by using the pre-defined arc-length parameter,  $\Delta l$  in predictor process. The incremental displacement and load parameter are updated by using the following equations.

$$\lambda_{i+1} = \lambda_0 + \Delta\lambda_{i+1} = \lambda_0 + \delta\lambda_{i+1} \quad (21)$$

$$\mathbf{d}_{i+1} = \mathbf{d}_0 + \Delta \mathbf{d}_{i+1} = \mathbf{d}_i + \eta_i \delta \mathbf{d}_i \quad (22)$$

$$\Delta \mathbf{d}_{i+1} = \Delta \mathbf{d}_i + \eta_i \delta \mathbf{d}_i \quad (23)$$

$$\eta_i = \rho \Delta l_i \quad (24)$$

In Eq. 23 and 24,  $\eta_i$  is proportional parameter to the tangent of equilibrium path, and  $\rho$  is proportional constant to the arc-length  $\Delta l$  which have the value  $0 < \rho \leq 1$ .

#### 4. DETECTION FOR CRITICAL POINT

In general, the buckling load may be determined by the value of eigen-value or determinant of tangent stiffness matrix in nonlinear buckling analysis process. The method described above is indirect method [3-5,9-14] for buckling analysis which is determined by a specific detecting parameter such as minimum eigen-value or arc-length  $\Delta l$ . However, opposed to the indirect method, direct method [11,15-21] uses the extended system to solve both the position of critical point and its associated eigen-mode directly. The extended system represents the condition for the occurrence of critical point.

In this paper, simple and efficient indirect method is used to solve the critical point. A value of arc-length  $\Delta l$  is used for the deterministic parameter of indirect method, whether critical point may be reached or not. The eigen-value of Eq. 8 is used to calculate the detecting parameter, arc-length  $\Delta l$ . If  $\Delta l$  is zero or nearly zero,  $\Delta l \cong 0$ , we determined that the system is unstable critical point. Whether the critical point is the limit or bifurcation point is determined by the conditional equation of Eqs. 16-a, 16-b.

The method of using the value of determinant is applicable to detect the critical point and state of primary path [10,13,14,19,20]. However it is not proper to use the determinant to calculate the arc-length parameter  $\Delta l$ . The reason is that the numerical error may occur to calculate the determinant of unstable tangent stiffness matrix. Therefore null value of the arc-length may be obtained, when the arc-length is close to zero value. The method of using the eigen-value enables us to calculate more accurate critical point and arc-length than to use the determinant, despite more calculations are needed.

The condition of structures can be determined by the value of eigen-value of tangent stiffness matrix. When a structure is unstable status of critical point such as bifurcation or limit point, the calculated eigen-value is shown as a null or negative value.

In equilibrium primary path, incremental length of primary path and structural stability has proportional relationship. When the structure is linear and stable, the large value of incremental length of primary path is possible. In other words, the corresponding large value of arc-length can be possible in this situation. And non-zero, relative large value of eigen-value would be obtained by using current tangent stiffness matrix. In contrast, near the critical point such as bifurcation or limit point, we should reduce the incremental length of primary path for the convergence by using smaller value of arc-length. And the condition of tangent stiffness matrix, eigen-value or determinant approaches to almost ill or negative at this point. In general, the more accurate eigen-value is appropriate than determinant.

The arc-length can be predefined as a fixed constant value, however this case is only valid for general nonlinear analysis or snap-through/snap-back buckling analysis. In bifurcation analysis, the pinpointing algorithm should be performed to detect the bifurcation point. Since the length of equilibrium path should be influenced by the value of eigen-value. And this can be done by relating the arc-length to the eigen-value efficiently. After that, the arc-length can be variable parameter for detecting and convergence according to the eigen-value. The predefined value arc-length is only required for initial reference value. Therefore the incremental length of primary path can be controlled by the arc-length.

Since, it is clear that the arc-length and eigen-value related dependently. When the arc-length is related to the eigen-value, the more accurate stability analysis is possible to detect the critical point. The arc-length control method with variable and parametric value is appropriate for the stability analysis. It can trace the complex shape of primary and bifurcated path.

Let the arc-length  $l_k$  up to the k-step of equilibrium path, and then the following equation can be derived from the Taylor expansion of the eigen-value  $\omega(l^*)$  at critical point  $l^*$ .

$$\omega(l^*) = \omega(l_k) + \dot{\omega}(l_k)\Delta l_k + \frac{1}{2}\ddot{\omega}(l_k)\Delta l_k^2 + \dots \tag{25}$$

The smallest non-negative eigen-value should be zero or nearly zero  $\omega_1(l^*) \cong 0$  at certain critical point.

In this study, by re-ordering the eigen-value [10] for each eigen-value, non-negative the zero or nearly zero-valued eigen-value is set to be the smallest eigen-value. And the corresponding eigen-vector is used to carry out the path switching to the bifurcation path.

The equation of arc-length at k-step,  $\Delta l_k$  can be described with the omitting of higher order term in Eq. 25 as following.

$$\Delta l_k = -\frac{\omega_1(l_k)}{\dot{\omega}_1(l_k)} \cong -\frac{\omega_1(l_k)\Delta l_{k-1}}{\omega_1(l_k) - \omega_1(l_{k-1})} \tag{26}$$

As it approaches the critical point, the arc-length is also close to zero,  $\Delta l_k \rightarrow 0$ . Therefore the following equation is used to determine the critical point.

$$\Delta l_k < \varepsilon \Delta l_1 \tag{27}$$

$\varepsilon$  : criterion for convergence(0.01)

Unlike previous studies of single bifurcation problems [3-5,11], Eq. 25 to Eq. 27 have been applied to the single and multiple bifurcation problems simultaneously in this study. The detection of bifurcation is performed by the value of arc-length of Eq. 27. The corresponding eigen-vector is used for the path switching algorithm in the following section.

## 5. PATH SWITCHING ALGORITHM

When the exact solution vector arrives near the bifurcation point on primary path, the initial approximate solution can be represented as the following equation by summing the approximate bifurcation mode  $\tilde{\mathbf{d}}_i$  to the exact solution of bifurcation point  $\mathbf{d}_{i-1}$ .

$$\mathbf{d}_i = \mathbf{d}_{i-1} + \eta_i \tilde{\mathbf{d}}_i \quad (28)$$

In above equation,  $\eta_i$  is the assumed constant for the bifurcation mode  $\tilde{\mathbf{d}}_i$  at i-th step. Unit value is applied to the value of  $\eta_i$  in this study. Crisfield [10] and Wriggers et al. [15] considered the higher order term to calculate the approximate bifurcation mode. However in this study, the smallest eigen vector [3-5,12-14,18] which corresponds to the re-ordered smallest eigen-value in previous section, is used for the bifurcation mode of Eq. 28 to both cases of single and multiple bifurcation problems. Additional variable is not required. Recently Fujii and Noguchi [20] studied the bifurcation problems without using the eigen vector.

After path switching to secondary bifurcation path, the structure may undergo new deformation mode comparable to perfect system of primary path. The identical numerical methods are used to trace the bifurcation path. There is no difference and also for the critical point in that path. The detection and path switching to another path may occur. The processes of path tracing and switching to secondary bifurcation path are illustrated in verification examples in following section.

In the bifurcation problems for space frame element, to detect and to switch to the bifurcation path, accurate eigen-value and corresponding eigen vector of tangent stiffness matrix are the most important factor. The simple but efficient algorithm of this study of bifurcation buckling analysis is sufficient to obtain the accurate solution of verification examples. The more important factor is the accurate element formulation. In this study, the exact element theory of large deformational Eulerian formulation of space frame element with bowing effect and asymmetric tangent stiffness which reflect the moment coupling effect is used to calculate the eigen-value and corresponding eigen-vector. The formulations of space frame element based on the beam-column equation are described in the following section.

## 6. ELASTIC SPACE FRAME ELEMENT

For the successful analysis of elastic stability problem, especially bifurcation, the accurate tangent stiffness matrix of structure is essential for corresponding eigen-value and eigen-vector. In this section, to this end, general theoretical formulations and computational algorithms have been developed for planer and space frames. One should include the formulation of a large deformational effect to analyze the post-buckling and bifurcation analysis of the space frame. Since, in this study, a method for large deformation analysis of space frame is based on an Eulerian formulation, which takes into consideration the effects of large joint rotations with finite rotation. The local member force-deformation relationships are based on the beam-column approach, and the change in member chord lengths caused by axial strain and flexural bowing are taken into account. And the derived geometric stiffness matrix is asymmetric because of the fact that finite rotations are not commutative under addition. However the coupling effect of the member axial-torsional and warping effects are omitted.

## 6.1 Eulerian Formulation for Finite Rotation

In the nonlinear analysis of space frames, the assumption that rotations of a body is additive has been widely adopted by researchers in updating the end rotations of frame elements at each incremental step. Such an assumption remains valid only for incremental steps with small rotations. For the cases with finite rotations, it is necessary to consider the non-commutative nature of rotations in three dimensions, such as post-buckling or bifurcation, which makes these space frames more difficult to analyze than trusses or plane frames in nonlinear analysis. In this paper, we used the previous work of Spiller [23] and Levy and Spiller [26] for the Eulerian finite rotation of 3D space frames, which is briefly described as follows.

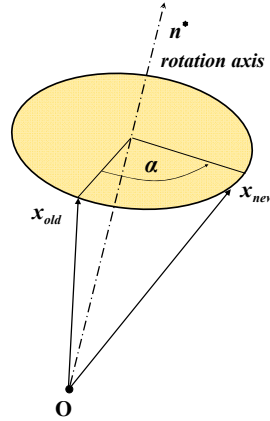


Figure 1. Rotation about an Axis

If an old position  $\mathbf{x}_{old}$  of a body is rotated to new position  $\mathbf{x}_{new}$ , Euler's Theorem of rigid body motions implies that any finite rotation (or sequence of rotations) can be described as a single rotation  $\alpha$  about some fixed axis described by a unit vector,  $\mathbf{n}^* = \{n_1^*, n_2^*, n_3^*\}$ , as shown in Figure 1. The new position vector  $\mathbf{x}_{new}$  is described by the old position vector  $\mathbf{x}_{old}$ , the rotation  $\alpha$  and the fixed axis unit vector  $\mathbf{n}^*$  as follows:

$$\mathbf{x}_{new} = \mathbf{x}_{old} - (1 - \cos \alpha) \{ \mathbf{x}_{old} - (\mathbf{x}_{old} \cdot \mathbf{n}^*) \mathbf{n}^* \} + \sin \alpha (\mathbf{n}^* \times \mathbf{x}_{old}) \quad (29)$$

We can obtain the following matrix representation of finite rotations.

$$\mathbf{x}_{new} = \tilde{\mathbf{R}} \mathbf{x}_{old} \quad (30)$$

$$\mathbf{x}_{old} = \mathbf{R} \mathbf{x}_{new} \quad (\mathbf{R} \tilde{\mathbf{R}} = \mathbf{I}) \quad (31)$$

where  $\mathbf{R}$  is the rotation matrix in terms of the  $\alpha$  and the components of  $\mathbf{n}^*$  as follows:

$$\tilde{\mathbf{R}} = \begin{bmatrix} \cos \alpha + \mu n_1^2 & -n_3 \sin \alpha + \mu n_1 n_2 & n_2 \sin \alpha + \mu n_1 n_3 \\ n_3 \sin \alpha + \mu n_1 n_2 & \cos \alpha + \mu n_2^2 & -n_1 \sin \alpha + \mu n_2 n_3 \\ -n_2 \sin \alpha + \mu n_1 n_3 & n_1 \sin \alpha + \mu n_2 n_3 & \cos \alpha + \mu n_3^2 \end{bmatrix} \quad (32)$$

with  $\mu = 1 - \cos \alpha$ .

Based on Euler's finite rotation formula, the rotation matrix is necessary to describe both joint rotations and member rigid body rotations. The matrix can be derived from the so-called Rodriguez rotation vector, a rotation about a fixed axis represented by a unit vector, and a scalar angle of rotation. Thus, a 3D rotation can be represented by a vector-like entity, but such entities cannot be added like vectors. Furthermore, it is assumed that these vector-like entities possess Taylor series expansions whose increments are the small rotation vectors of linear structural analysis [23, 26]. To separate the large rigid body deformation of a member from its relative deformation, which is assumed to be small, a Eulerian or local member coordinate system is used, as shown in Figure 2.

In Figure 2, the unit vector of the non-deformed member axis is  $\mathbf{n}_i$ , and the unit vector of the deformed member axis is  $\mathbf{n}'_i$ .

Furthermore, the unit vectors of the deformed member axis at joints 1 and 2,  $\mathbf{n}_1^*$  and  $\mathbf{n}_2^*$ , can be represented by Euler's joint rotation matrices,  $\mathbf{R}_1$  and  $\tilde{\mathbf{R}}_2$ . The unit vector of the non-deformed member axis,  $\mathbf{n}_i$ , can be represented as follows.

$$\mathbf{n}_1^* = \tilde{\mathbf{R}}_1 \mathbf{n}_i \tag{33}$$

$$\mathbf{n}_2^* = \tilde{\mathbf{R}}_2 \mathbf{n}_i \tag{34}$$

The rotation vector at joint 2,  $\theta_2$ , can be represented by the cross product of the member unit vector,  $\mathbf{n}_i$ , and the deformed member unit vector,  $\mathbf{n}_2^*$ , at joint 2 with properties as follows:

$$\theta_2 \cong \mathbf{n}_i \times \mathbf{n}_2^* \tag{35}$$

$$|\theta_2| = \cos^{-1}(\mathbf{n}_i \cdot \mathbf{n}_2^*) \tag{36}$$

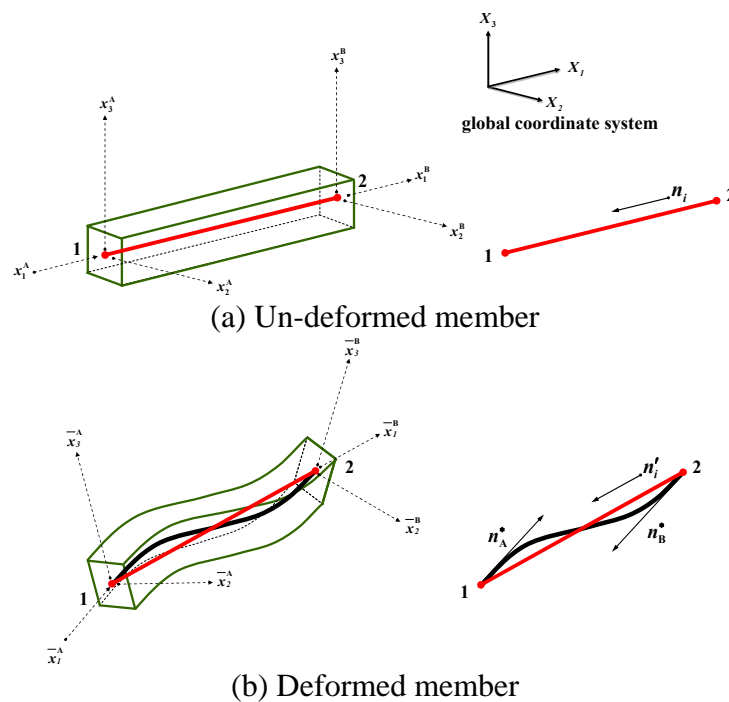


Figure 2. Relative member deformations

The end of member rotation vector for joint 1,  $\theta_1$ , is represented as follows:

$$\theta_1 = \theta_2 + \theta_{12} \tag{37}$$

where  $\theta_{12}$  is the rotation of joint 1 with respect to joint 2. This equation simply describes the vector form of the matrix product,  $\mathbf{R}\tilde{\mathbf{R}}_2$ .

From this simple and exact formulation of Euler's finite rotation [23, 26], we can calculate the exact member end rotations,  $\theta_1, \theta_2$  which separate the rigid body rotations. In the case of geometrically nonlinear large displacement analysis of space frame, the exact member rotational deformation is relatively small, because of its large rigid body rotation occurrence. The formulation of this study is valid for the elastic, elasto-plastic large deformation analysis of space frame element with beam-column equations. The accuracy and efficiency are demonstrated in verification examples lately.

### 6.2 Beam-column Equation

The member force of the space frame element shown in Figure 3 can be written by the 2D beam-column equations [22, 24, 25], which include the effect of member displacement upon the bending moment to the end. As a result, the member stiffness becomes a function of the axial load.

$$M_{1j} = \frac{EI_j}{L} (c_{1j}\theta_{1j} + c_{2j}\theta_{2j}) \quad (j = 2,3) \tag{38}$$

$$M_{2j} = \frac{EI_j}{L} (c_{2j}\theta_{1j} + c_{1j}\theta_{2j}) \quad (j = 2,3) \tag{39}$$

$$M_t = \frac{GJ}{L} \varphi_t \tag{40}$$

$$Q = EA \left( \frac{u}{L} - \sum_{j=2}^3 c_{bj} \right) \tag{41}$$

$$c_{bj} = b_{1j}(\theta_{1j} + \theta_{2j})^2 + b_{2j}(\theta_{1j} - \theta_{2j})^2 \tag{42}$$

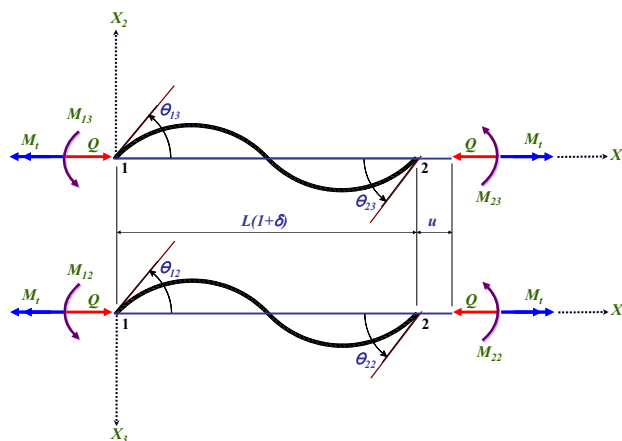


Figure 3. Relative Member Deformations and Corresponding Forces

In above equations,  $\theta_{1j}$  and  $\theta_{2j}$  are the relative member end rotations calculated by Eqs. 35 and 37, where  $\varphi_t$  is linear axial twist,  $u$  is axial displacement,  $A$  is the area of cross section,  $E$  is the modulus of elasticity,  $I_j$  is the moment of inertia about the  $X_j$ -axis,  $GJ$  is the torsional rigidity,  $c_{1j}$  and  $c_{2j}$  are the stability functions for bending about the  $X_j$ -axis,  $c_{bj}$  is the length correction factor caused by flexural deformation (bowing) about the  $X_j$ -axis, and  $b_{1j}$  and  $b_{2j}$  are the bowing functions of the axial force parameter  $q$ , defined as follows.

$$q = \frac{Q}{Q_{Euler}} = Q \frac{L^2}{\pi^2 EI_j} \quad (43)$$

The expression for the member axial force,  $Q$  in Eq. 41 contains bowing functions  $b_{1j}$  and  $b_{2j}$ , which are functions of the axial force parameter,  $q$ . Therefore, Eq. 41 is a nonlinear function. A computational difficulty arises in determining  $Q$  from the axial displacement,  $u$ . An iterative procedure must be employed to compute the axial force of a member and can be solved using the following process. Noting that  $q$  is the only unknown quantity in Eq. 41, let a new function,  $K(q)$ , be defined as follows:

$$K(q) = \frac{\pi^2}{\lambda^2} q + \sum_{j=2}^3 c_{bj} \frac{u}{L} = 0 \quad (44)$$

A new value of  $q_{i+1}$  is obtained from the first order Taylor series expansion,

$$q_{i+1} = q_i + \Delta q_i = q_i - \frac{K(q_i)}{K'(q_i)} \quad (45)$$

where  $K'(q)$  is the derivative of  $K(q)$  with respect to the axial force parameter,  $q$ , and represented as follows:

$$K'(q) = \frac{dK(q)}{dq} = \frac{\pi^2}{\lambda^2} + \sum_{n=2,3}^3 \frac{1}{\varepsilon_j} \{ b'_{1j} (\theta_{1j} + \theta_{2j})^2 + b'_{2j} (\theta_{1j} - \theta_{2j})^2 \} \quad (46)$$

where  $\lambda = L/\sqrt{I/A}$  and  $\varepsilon_j = I_j/I$ , in which  $I$  is an arbitrary reference moment of inertia and  $b'_{ij}$  is a differentiation of the bowing function with respect to  $q$ . An approximate solution to this equation for  $q_i$  is initially assumed, and the iteration is performed until  $|\Delta q_i|$  is sufficiently small. After determining the axial force  $Q$  by the iterative process, member end moments were computed from Eqs. 38-40. Detailed description of Eqs. 38-46 and the corresponding variables are explained in references [22,24,25].

### 6.3 Tangent Stiffness Matrix for Large Deformation

In this study, the beam-column approach in section 6.2 is applied to elastic post-buckling, bifurcation problems. The non-commutative nature of finite rotation in section 6.1 yields an asymmetric tangent stiffness matrix in both cases. The member force-deformation relationships may be rewritten as follows:

$$\bar{\mathbf{s}}^T = \{Q, M_t, M_{12}, M_{13}, M_{22}, M_{23}\} \quad (47)$$

$$\bar{\mathbf{u}}^T = \{u, \varphi_t, \theta_{12}, \theta_{13}, \theta_{22}, \theta_{23}\} \quad (48)$$

And the incremental form of the member equation is written as follows:

$$\Delta \bar{\mathbf{s}} = \mathbf{t} \Delta \bar{\mathbf{u}} \quad (49)$$

Where  $t$  is the element stiffness matrix according to the incremental member displacement  $\Delta \bar{\mathbf{u}}$  in the local coordinates, as shown previously in Eqs. 38-41. By using the incidence matrix  $\bar{\mathbf{B}}$ , the element nodal force and nodal displacement can be written as follows:

$$\bar{\mathbf{d}} = \bar{\mathbf{B}} \bar{\mathbf{u}} \quad (50)$$

$$\bar{\mathbf{f}} = \bar{\mathbf{B}} \bar{\mathbf{s}} \quad (51)$$

Conventionally, the element nodal force in global coordinates  $\mathbf{F}$  can be written from the rotation matrix  $\mathbf{R}$ :

$$\mathbf{F} = \mathbf{R} \bar{\mathbf{f}} = \mathbf{R} \bar{\mathbf{B}} \bar{\mathbf{s}} \quad (52)$$

Eq. 52 could be interpreted as a member equilibrium equation in a global coordinate system. The tangent stiffness matrix of the beam-column can be obtained from the differential form with respect to the incremental displacement [23,26]:

$$\begin{aligned} \Delta \mathbf{F} &= \Delta(\mathbf{R} \bar{\mathbf{B}} \bar{\mathbf{s}}) = \mathbf{R} \bar{\mathbf{B}} (\Delta \bar{\mathbf{s}}) + \mathbf{R} (\Delta \bar{\mathbf{B}}) \bar{\mathbf{s}} + (\Delta \mathbf{R}) \bar{\mathbf{B}} \bar{\mathbf{s}} \\ &= (\mathbf{K}_E + \mathbf{K}_G^S + \mathbf{K}_G^R) \delta \mathbf{d} \end{aligned} \quad (53)$$

The first term in Eq. 53 becomes the elastic stiffness matrix. The second and third terms become the geometric stiffness matrix.  $\mathbf{K}_G^S$  and  $\mathbf{K}_G^R$  indicate the stretching and rotational terms of the geometric stiffness. The rotational geometric stiffness matrix,  $\mathbf{K}_G^R$ , is asymmetric [23,26,39] due to the non-commutative nature of finite rotation.

Several formulations have been proposed in the literature [39, 41-44] to improve the shortcomings of the cubic element and the conventional stability-based beam-column element. The improved formulation of co-rotational cubic elements by Teh and Clarke [39] used the asymmetric tangent stiffness matrix and shows more accurate results. Liew et al. [44] used the symmetric portion of the induced moment matrix alone, which is referred to as the joint moment matrix and needs to be assembled to form the structure tangent stiffness matrix. However the derived comprehensive asymmetric geometric stiffness matrix of Eq. 53 in this study is responsible for the lateral-torsional buckling and some symmetric and asymmetric buckling modes in physical situations at the critical bifurcation point to obtain accurate results as in the case of Teh and Clarke [39]. By performing some numerical examples of following sections, we will show the accuracy and efficiency of proposed bifurcation algorithm and element theorem.

## 7. VERIFICATION EXAMPLES

In this section, the reported verification examples are analyzed by using the method of computational elastic bifurcation theory described above. Generally, the important research work of buckling classification of Thompson [2] is difficult to be applied to the actual problems, because which needs a diagonalized higher order derivative of energy function for classification criteria. However, by using the method of this study without considering higher order terms, eigen-value is used to classify the limit and bifurcation point buckling type, and is used to the path switching for primary and bifurcation path. Therefore the effectiveness and applicability of this study may be called as meaningful method. The following verification examples seem to be simple model, but they need amount of analytical efforts for numerical point of view.

### 7.1 Example 1 : Multiple Bifurcation of Trussed Star-dome

First verification example is the multiple bifurcation of trussed Star-dome [45]. After Hangai and Kawamata [45] reported the results, Star-dome became a representative verification example for buckling analysis which composed with trussed element. The reason that the trussed dome structure, Star-dome, is frequently used for the highly nonlinear buckling analysis is as follows. The truss element is most simple and easy to formulate in FEM analysis, the FE formulated nonlinear equilibrium equation of truss element shows the exact solution. And complex post buckling behaviors are presented relatively easy and clear with trussed element.

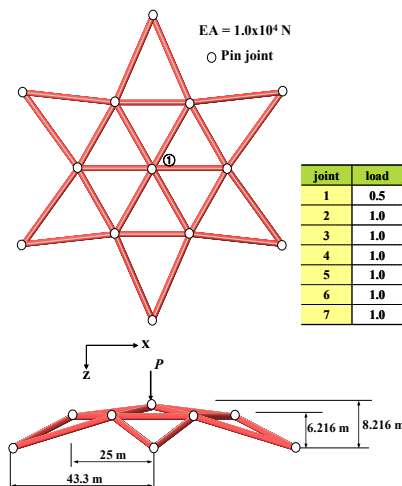


Figure 4. Star-dome : Geometry and Load Condition

To verify the accuracy and applicability, the post buckling bifurcation analysis is performed by using the proposed approach. Figure 4 illustrates the model for geometry and loading conditions. The boundary condition for Star-dome is pin support. Figure 5 illustrates the load-deflection curves for primary and bifurcation path at apex before first limit point. As shown in Figure 5, three bifurcation points are detected before the first limit point. In Figure 5, BP1, BP2, BP3 are bifurcation point and LP1 is limit point. Among bifurcation points, BP2, BP3 show the characteristics of multiple bifurcation point. The load parameters of each critical point in Figure 5, are described in Table 1 with the results of previous research works. The results buckling load parameters obtained using the proposed approaches are in good agreement with references [10,13]. In Table 2, the eigen-values and corresponding arc-lengths for each bifurcation and limit point are described.

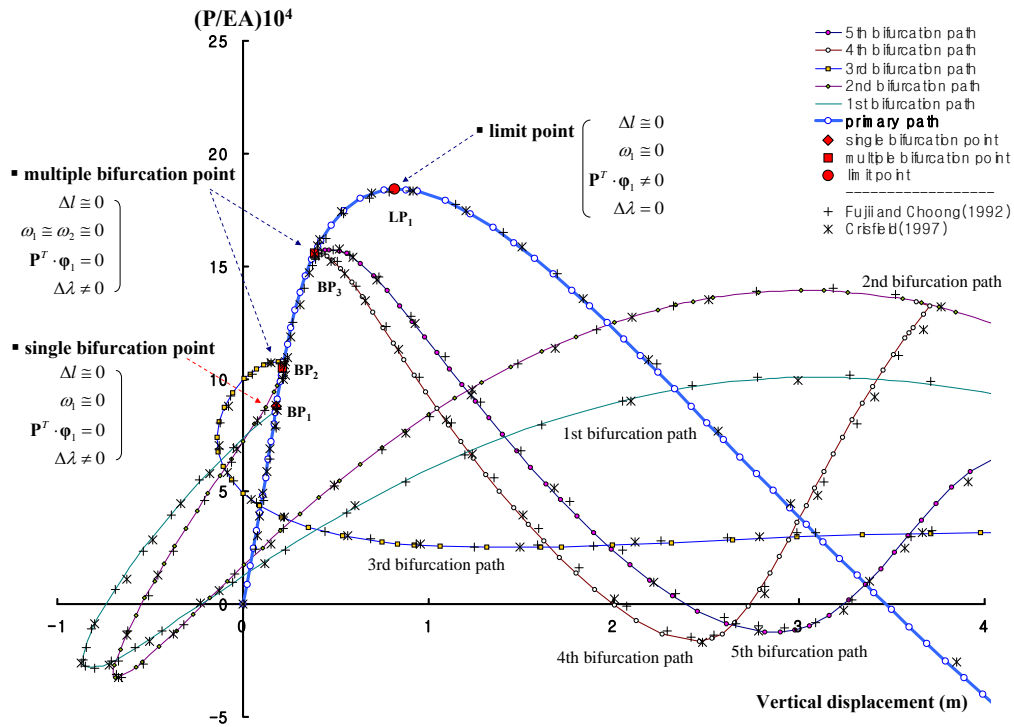


Figure 5. Star-dome: Primary and Bifurcation Paths, Deterministic Equation for Bifurcation Point

At critical points, BP1, BP2, BP3, LP1, the corresponding smallest non-negative eigen-values are nearly zero as described in Figure 5 and Table 2. We can distinguish the bifurcation and limit point by using Eq. 16. If  $\mathbf{P}^T \boldsymbol{\phi}_1 = 0$  and  $\Delta\lambda = 0$ , the point is bifurcation point. Otherwise  $\mathbf{P}^T \boldsymbol{\phi}_1 \neq 0$  and  $\Delta\lambda = 0$ , the point is limit point. As described in Figure 5 and Table 2, if multiple number of eigen-value is non-negative nearly zero or zero, the point is multiple bifurcation point. If single number of eigen-value is non-negative nearly zero or zero, the point is single bifurcation point. The deterministic parameter, arc-length calculated by using Eq. 26 is related the smallest non-negative eigen-value of Table 2. When the point is critical, the corresponding eigen-value and its arc-length present also critical value.

If the path switching is performed at particular bifurcation point, the corresponding smallest eigen-vector is used for the bifurcation mode in Eq. 28. Accurate representative bifurcation mode is satisfied by using the eigen vector only in this study. By using the algorithm of this study, just using the re-ordered the eigen-value for detection and corresponding eigen-vector for path switching, the resulting primary and bifurcation paths of this paper as described in Figure 5 are in good agreement with reference [10,13]. The additional process is minimized unlike reference [3,10,13]. The preparation of particular mode [3] or trial error [10] or combination of eigen-vector is not required.

Figure 6 illustrates the load-deflection curve of primary path and corresponding deformed shape of Star-dome after first limit point. It can be seen that there are eight limit points and fourteen bifurcation points in the primary path. The final resulting deformed shape at “⑩” is inversed configuration of initial shape. The load-deflection curve of primary path and its corresponding deformed shape is exactly symmetric about vertical axis. If some perturbations may be imposed to the system at each single or multiple bifurcation points, the structure may loose the symmetric and perfect status, and the system will branch to the bifurcation path.

Table 1. Load Parameters at Critical Points

	BP1	BP2	BP3	LP1
Present	8.700	10.282	15.662	18.420
Fujii and Choong[13]	8.689	10.267	15.606	-
Crisfield[10]	8.680	10.260	15.670	18.400

Table 2. Non-negative Smallest Eigen-value at Critical Points

no.	BP1(single)		BP2(multiple)		BP3(multiple)		LP1		
	eigen-value	arc length	eigen-value	arc length	eigen-value	arc length	eigen-value	arc length	
1	0.0063	1st	0.0123						1st bif. 2nd bif. 3rd bif. 4th bif. 5th bif.
2	1.7978								
3	1.7978								
4	5.6434								
5	5.6434								
6	10.0432								
7	12.9365								
8	235.8343								
9	235.8343								
10	397.4360								

Figures 7-11 illustrate the primary and bifurcation paths of load-deflection curves at each BP1, BP2, BP3 points in Figure 4. Each bifurcation paths are plotted inside the boundary of primary path. Any bifurcation paths do not deviate the boundary of primary path significantly. Because the motion of bifurcated system which loses the symmetry, will return to the primary path in to obtain the symmetry, the exact prediction of primary path is the most important factor of prerequisites in bifurcation analysis. And the bifurcation buckling may be understood as the unstable structural state losing symmetry and imperfection imposed system. The simple and efficient numerical process of this study enables the analysis of path tracing, detecting critical point and path switching with high accuracy.

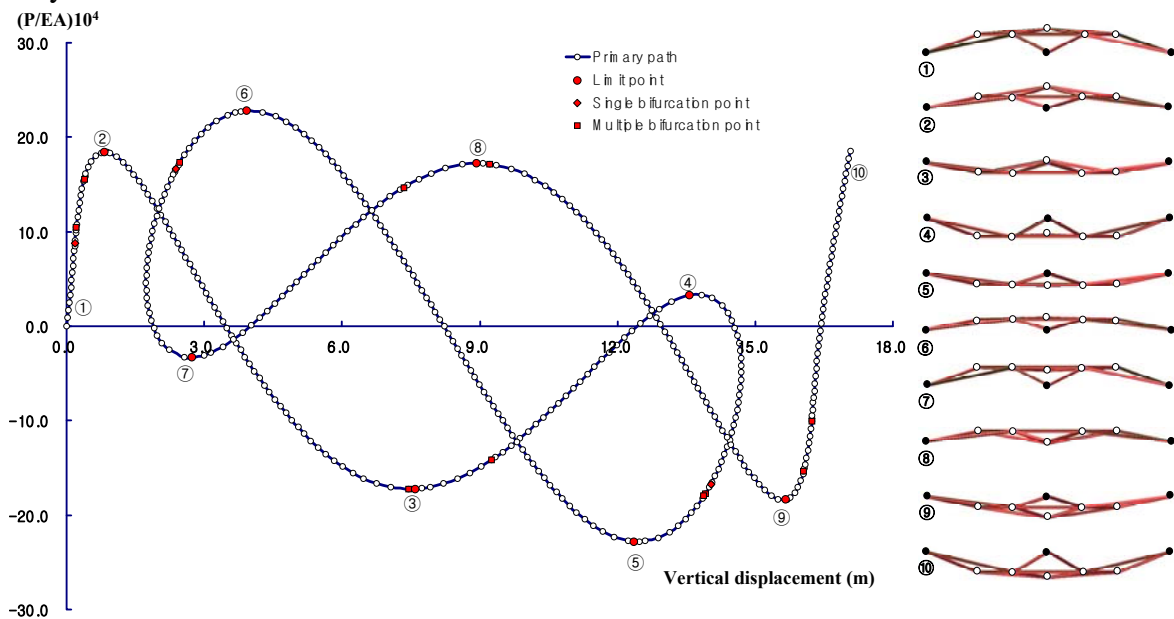


Figure 6. Star-dome : primary path and corresponding deformed shape at apex

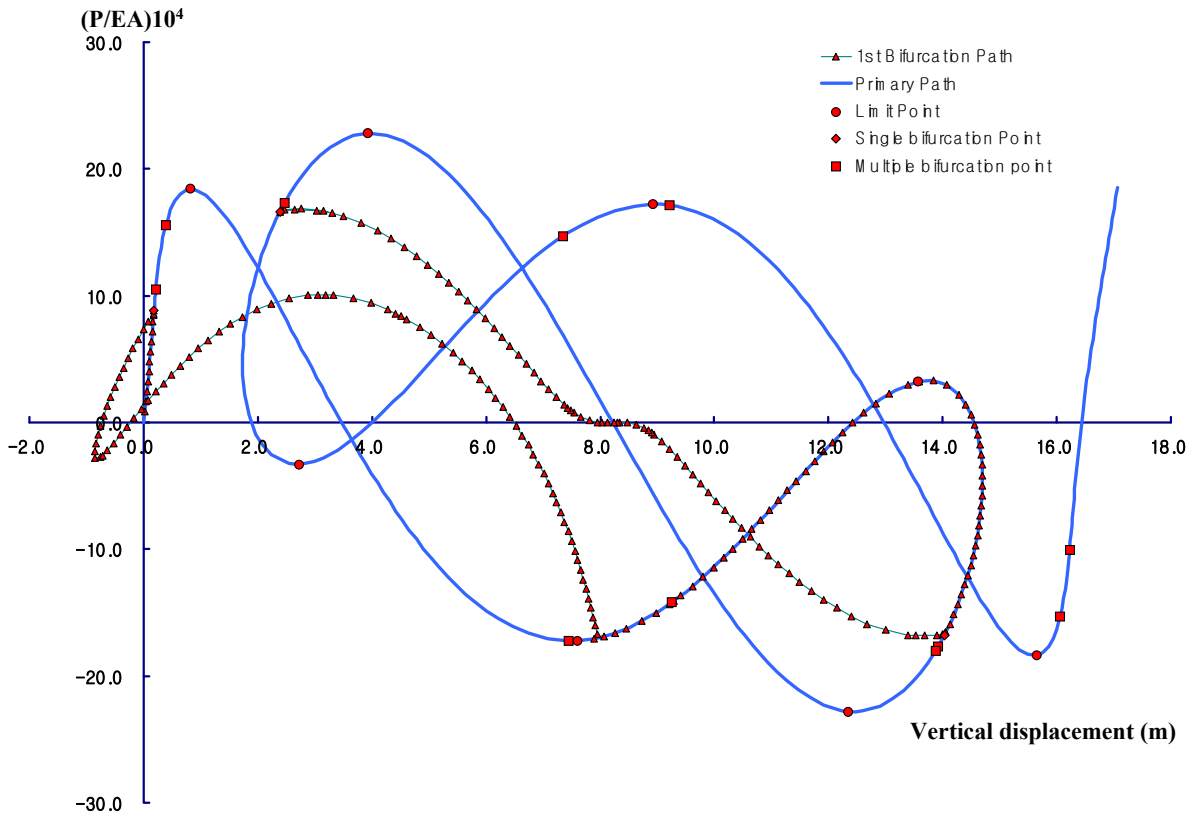


Figure 7. Star-dome : Primary and 1st Bifurcation Path at Apex

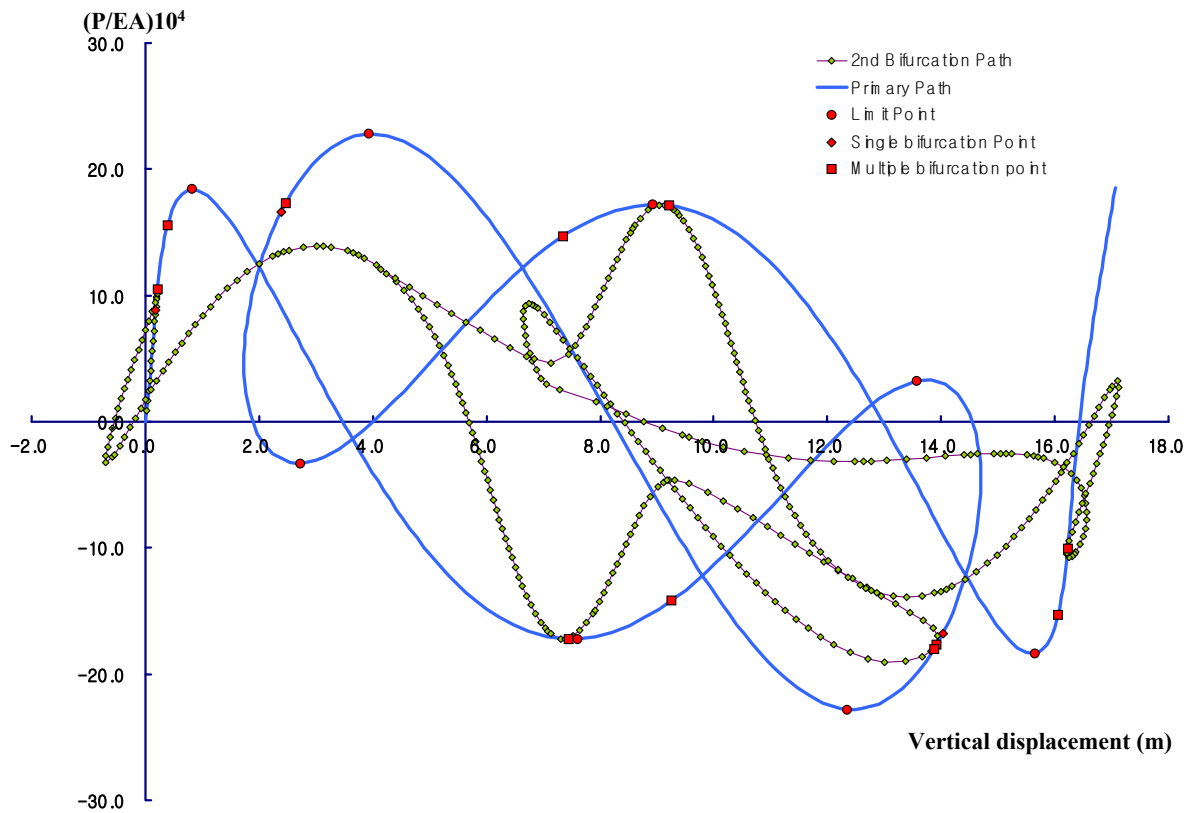


Figure 8. Star-dome : Primary and 2nd Bifurcation Path at Apex

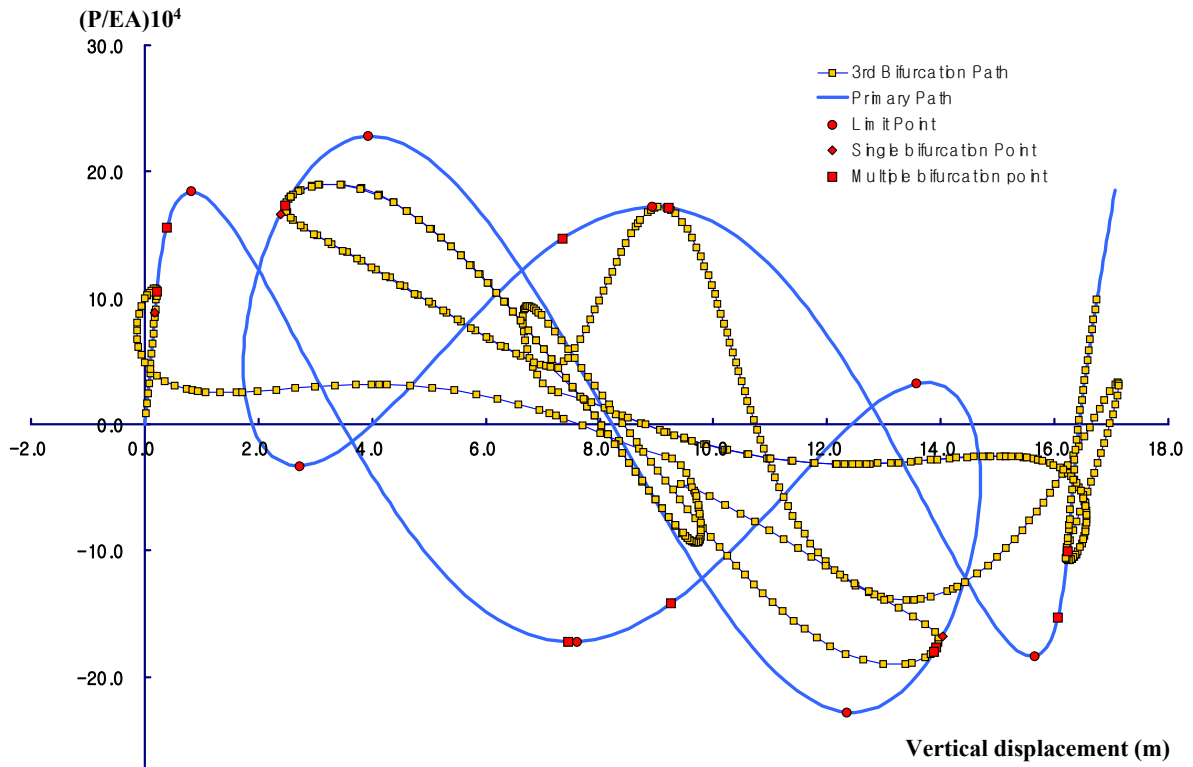


Figure 9. Star-dome : : Primary and 3rd Bifurcation Path at Apex

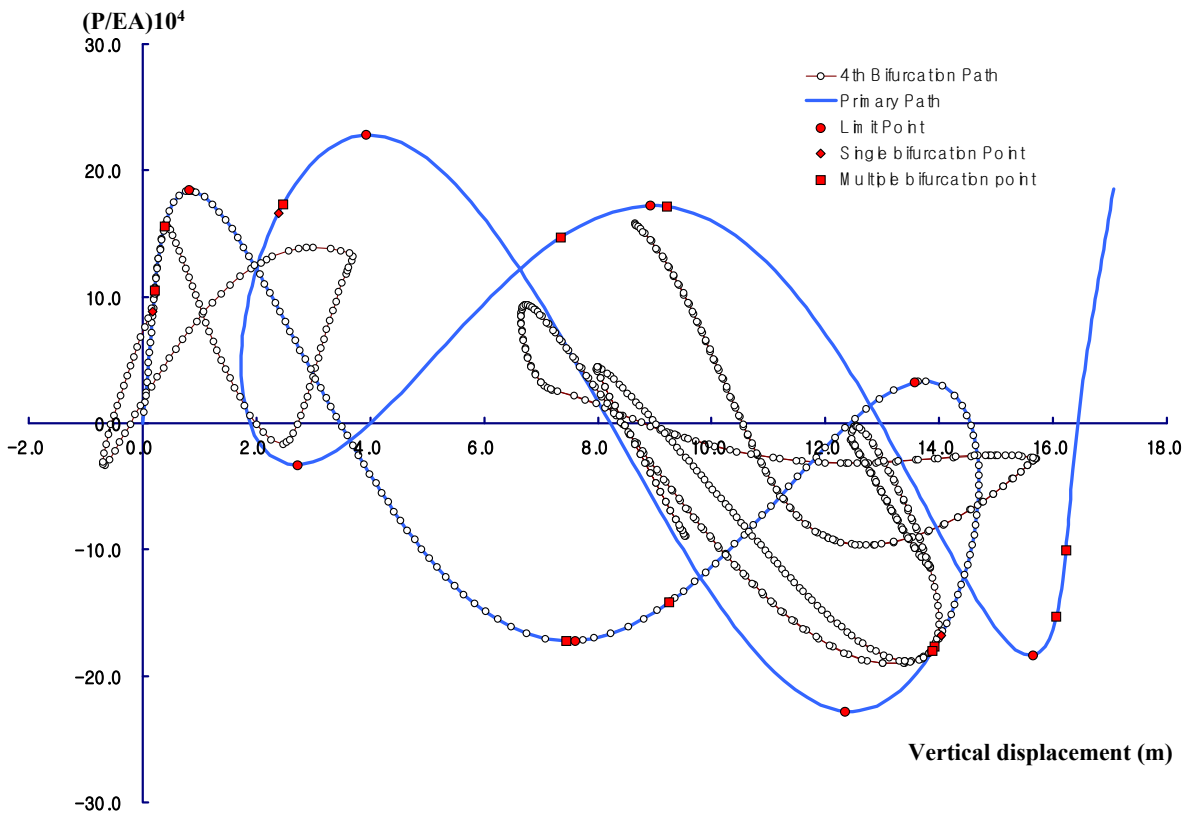


Figure 10. Star-dome : : Primary and 4th Bifurcation Path at Apex

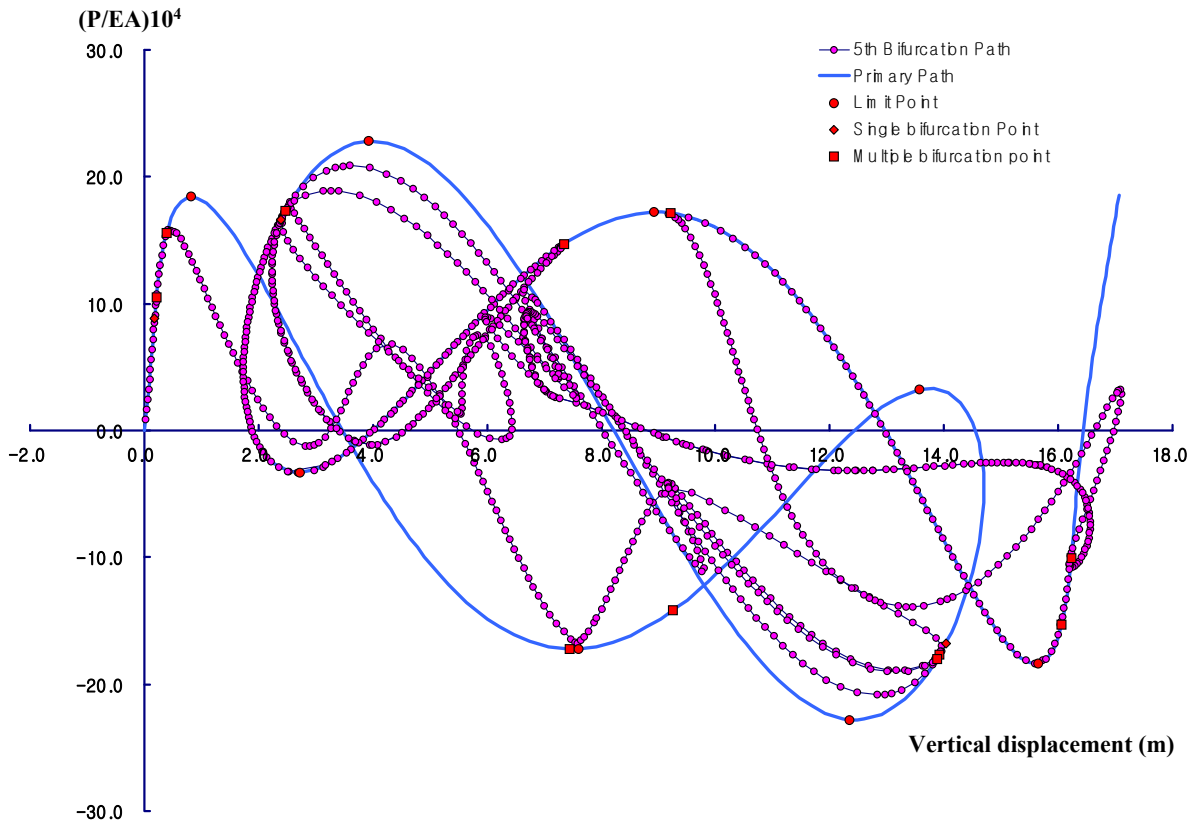


Figure 11. Star-dome : : Primary and 5th Bifurcation Path at Apex

## 7.2 Example 2 : Bifurcation of Plane arch with Geometric Imperfections

As shown in Figure 12, simple plane arch, which is modeled by 10 straight beam-column element of this study as the same of references [48], is analyzed to obtain the primary and bifurcation equilibrium path, and compared with previous reported results. The resulting equilibrium paths and limit points of two imperfections are illustrated in Figures 12 and 13. Figure 12 shows the load-deflection curves and deformed shape of this example which was analysis by Hosono [3] and Sabir and Lock [46]. Likewise the result of Star-dome model, the primary equilibrium path is the result of perfect and symmetric motion of system. However the deformed shape of bifurcation path, Figure 12, (b) represents the asymmetry and imperfect behavior. When geometrical imperfections are imposed to the system, the asymmetric motions occur and the resulting load-deflection curves are turned down before first bifurcation point BP1. Full load deflection curves are plotted in Figure 13.

Sabir and Lock [46] proposed the equilibrium primary and first bifurcation path by using FEM based displacement increment method. Hosono [3] analyzed the model by using beam element of Powell [47] and arc-length method. Previously, they reported only single, first bifurcation path which connect bifurcation point, BP1-BP4 in Figure 13. None reported second bifurcation path which connect bifurcation point, BP2-BP3. However the result of our bifurcation analysis, due to the correct bifurcation mode of eigen value analysis, which used the asymmetric tangent stiffness matrix of Eq. 57 and geometric large deformational formulation of Eulerian finite rotation, searched un-reported second bifurcation path successfully.

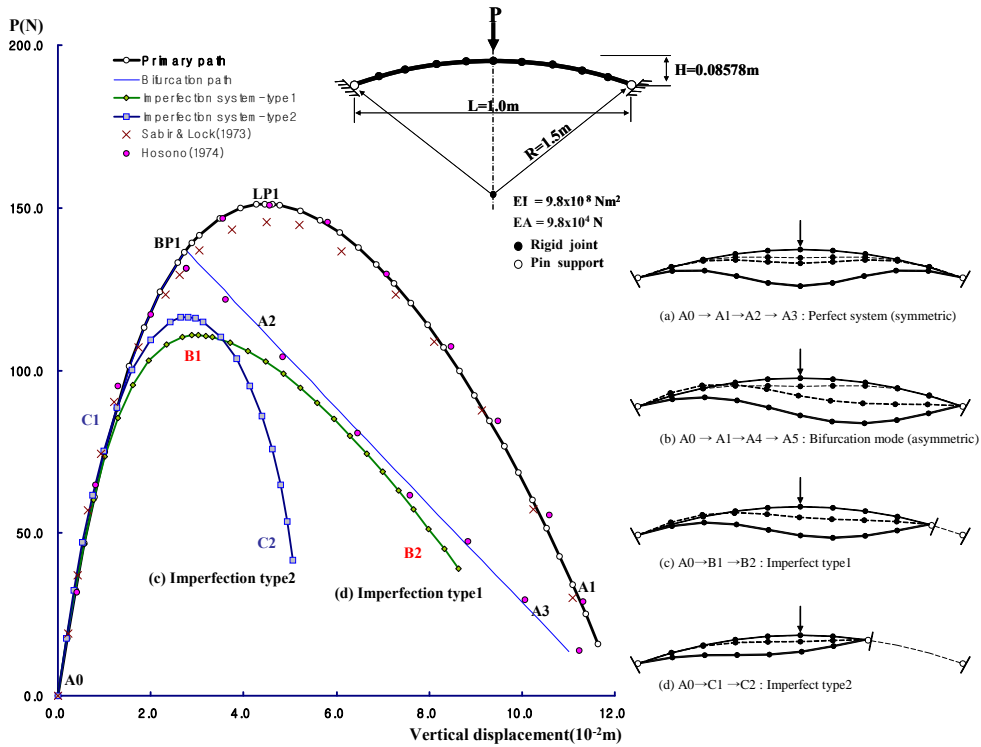


Figure 12. Plane Arch : Geometry, Load-deflection Curves and Corresponding Deformed Shape

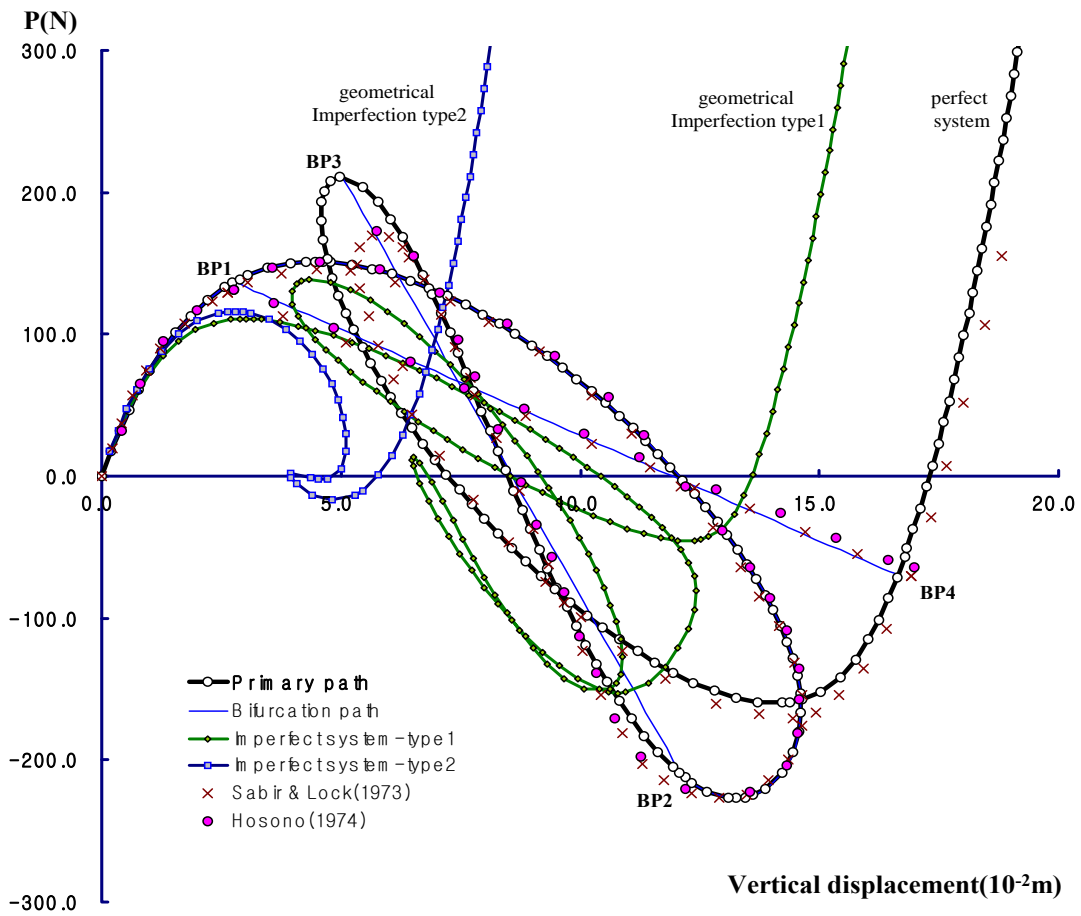


Figure 13. Plane Arch : Load-deflection Curves for each Loading Conditions

### 7.3 Example 3 : Bifurcation of Plane Frame

Fujii and Ramm [18] reported the equilibrium primary and three bifurcation paths previously. The result of bifurcation for plane frame, as shown in Figure 14, is compared with that of Fujii and Ramm [18]. As shown in Figure 14, the results of our studies are in good agreement with reported results for the shape of load-deflection curves with 5-element per member as the same as reference [18]. However there are some differences for the load parameters, because of the difference of adopted beam element theory. The Eulerian finite rotation formulation of our study enables the buckling analysis to be geometrically large deformational analysis exactly. As shown in Figure 14, three branched equilibrium bifurcation paths are returned to the symmetric primary path at bifurcation points, BP4, BP5 and BP6. These results explain the excellent performance of the theory of this paper for rigid body motion of large deformation in beam-column element theory and joint finite rotation. Eigen-modes obtained from asymmetric tangent stiffness are displaced in Figure 14, and are used for branch switch to bifurcation path. The overall processes of our studies for bifurcation analysis perform well without any difficulties.

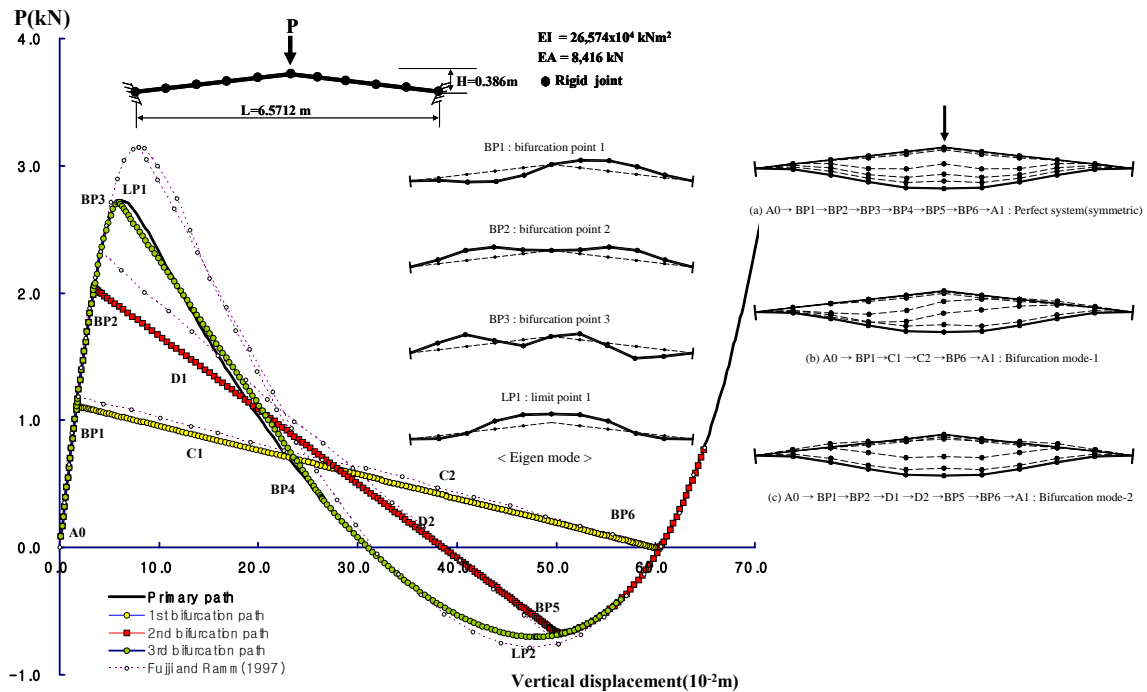


Figure 14. Plane Frame : Load-deflection Curves and Deformed Shape

### 7.4 Example 4 : Bifurcation of Space Dome

To verify the accuracy and applicability of the proposed beam-column element and stability theory to the 3D framed structure, space dome model, as shown in Figure 15, was performed. The loading case is divided as distributed and concentrated. Figure 16 illustrated the load-deflection curves for each loading condition as described in Figure 15. When the distributed loads are applied, the bifurcation buckling occurs. Otherwise the snap-through buckling may occur when the concentrated load is applied as shown in Figure 16. As described in references [24,48,50,51], the analysis is performed by 1 element per member. However Papadrakakis and Ghionis [49] performed this example with FE formulated 4 element/member. In general, the more number of elements per member is essential when FE beam element is used.

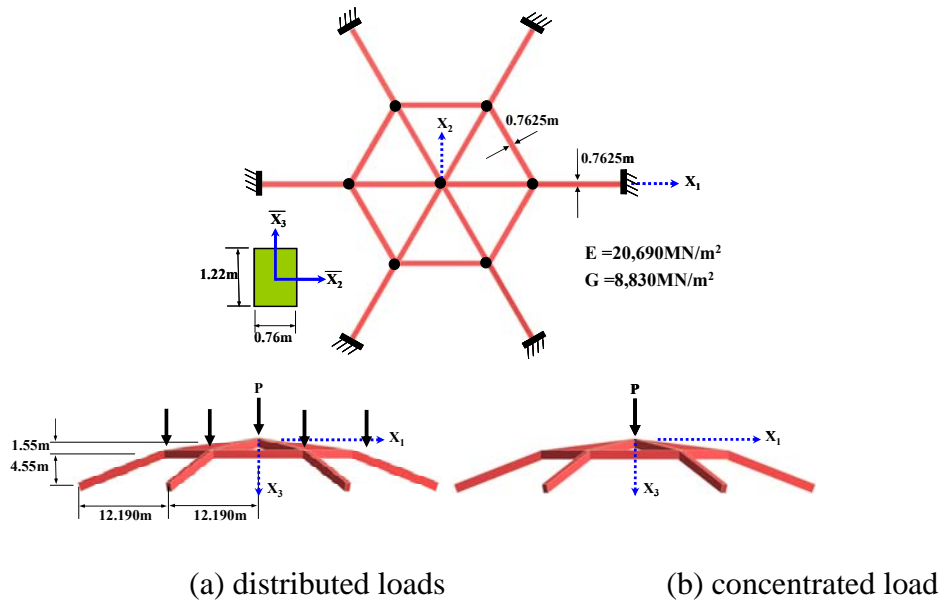


Figure 15. Space Dome: Geometry and Load Case

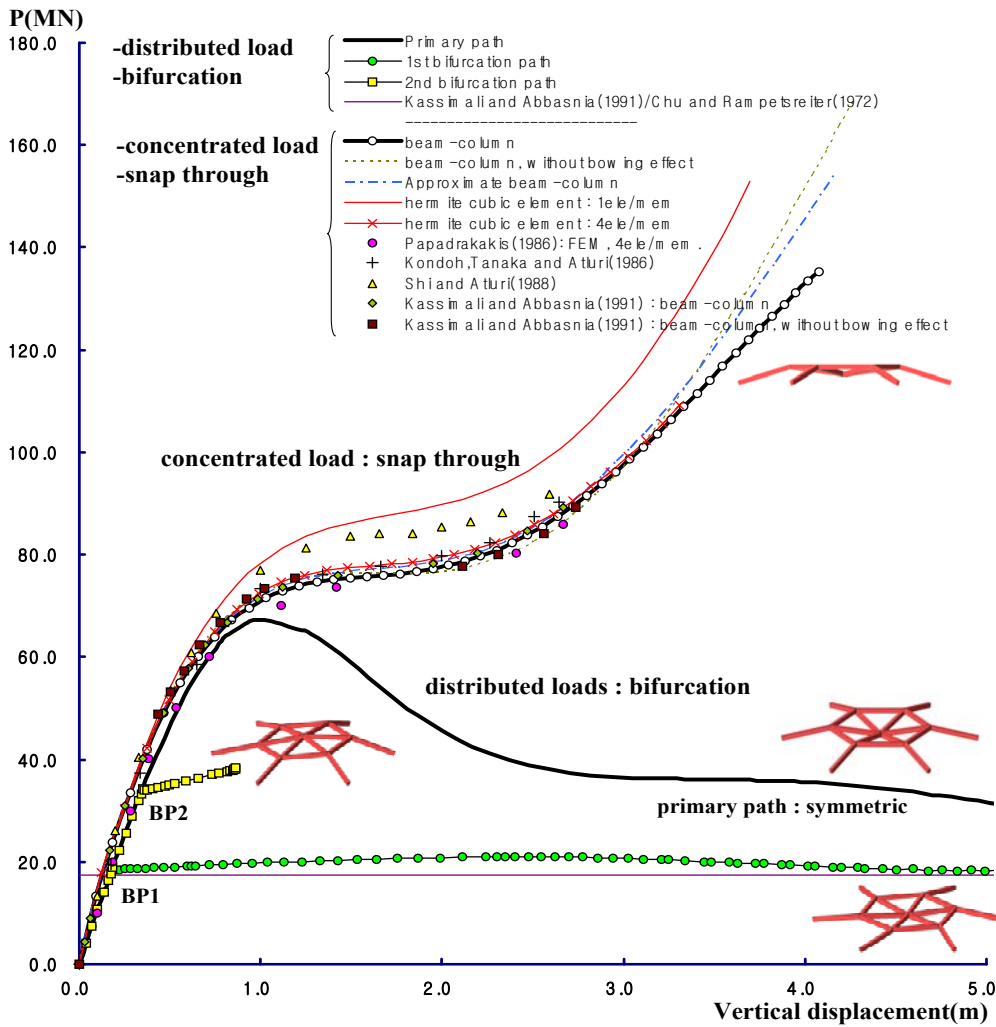


Figure 16. Space Dome: Load-deflection Curves

## 8. CONCLUSIONS

In this study, the bifurcation analysis for plane and space frame is performed by using the proposed numerical method and Eulerian formulated large deformational beam-column element theory. The simple and efficient indirect method is used to identify the characteristics of critical point through the calculation of parametric variables determined by the smallest eigen-value without considering the higher order terms in equilibrium equation. And these smallest eigen value and corresponding eigen vector are used to analysis both single and multiple bifurcation buckling cases. To account for the geometrical nonlinear of large deformational rigid body motion of space frame element for post buckling bifurcation analysis, Eulerian finite rotation and beam-column equations with bowing effect are developed based on previous proposed theories. As a result of adopted geometrically nonlinear element formulation, the tangent stiffness matrix is asymmetric [23, 26]. However the resulting eigen values and corresponding eigen modes based on the asymmetric tangent stiffness matrix do good performance for bifurcation analysis with efficient bifurcation theories of this study. The good agreement and superior performance of verification examples indicate that the adopted numerical method and element theory are worthy to consider for bifurcation and post buckling analysis.

In case concentrated load is applied, the resulting curves of this study by using 1 number of beam-column element with bowing effect and finite rotation shows good agreement with references. When the hermite cubic beam element is used, at least 4 FE element is required for the accuracy as in the case of Paradrakakis and Ghionis [49]. The approximate beam-column in Figure 16 represents the element formulation of using the approximate beam-column equation of Eqs. 47-50. In spite of approximated equations, the resulting curve of approximate beam-column element shows good performance compared with hermite cubic and beam-column element without bowing effect.

When the distributed loads are applied, Kassimali and Abbasnia [24] and Chu and Rampetsreiter [48] reported the buckling load value as 17.355 kN and 17.413 kN by using the eigen value analysis respectively with their symmetric tangent stiffness but the bifurcation path is not presented. In our study, the load parameter of first bifurcation point is 17.400 kN, therefore it can be seen that the first buckling load value of our study is in good agreement with references [48,24]. As shown in Figure 16, the nearly linear behavior is obtained until first limit point, LP1. The bifurcation point BP1 and BP2 are detected from the eigen value analysis with asymmetric tangent stiffness matrix of our study. The bifurcation modes in Figure 16 are conjugated with the deformed shape of structure. Therefore it can be understood that the motion of bifurcations are dependent with the bifurcation, eigen modes and tangent stiffness matrix. From the result of this example, it can be said that the large deformational Eulerian formulation of our study with asymmetric tangent stiffness may do good performance for 3D space frame to the highly nonlinear pre/post buckling analysis, path tracing, path switching, detection of critical points.

## ACKNOWLEDGEMENTS

This research was supported by a grant (code#'09 R&D A01) from Cutting-edge Urban Development Program funded by the Ministry of Land, Transport and Maritime Affairs of Korean government and also supported by INHA UNIVERSITY Research Grant.

## REFERENCES

- [1] Koiter, W.T., "On the Stability of Elastic Equilibrium", Thesis, Polytechnic Institute, Delft H.T., Paris, Amsterdam, 1945.
- [2] Thompson, J.M.T. and Hunt. G.W., "A General Theory of Elastic Stability", John Wiley & Sons, Chichester, UK, 1973.
- [3] Hosono, "The Analysis of Elastic Buckling Problem by using the Arc-length Method", Thesis, Tokyo University, 1974.
- [4] Riks, E., "An Incremental Approach to the Solution of Snapping and Buckling Problems", Intern. J. Solids Structures, 1979, Vol. 15, pp. 529-551.
- [5] Riks, E., "Some Computational Aspects of the Stability Analysis of Nonlinear Structures", Comput. Methods Appl. Mech. Engrg., 1984, Vol. 47, pp. 219-259.
- [6] Crisfield, M.A., "A Fast Incremental Iterative Solution Procedure that Handles 'snap through'", Computer & Structures, 1981, Vol. 13 pp. 55-62.
- [7] Ramm, E., "Strategies for Tracing the Non-linear Response near Limit Points", in Nonlinear Finite Element Analysis in Structural Mechanics, Wunderlich, W. et al. Eds., Springer-Verlag, Berlin, 1981, pp. 63-89.
- [8] Crisfield, M.A., "An Arc-length Method Including Line Searches and Accelerations", Int. J. Num. Meth. Eng., 1982, Vol. 19, pp. 1269-1289.
- [9] Crisfield, M.A. and Shi, J., "A Review of Solution Procedures and Path-following Techniques in Relation to the Non-linear Finite Element Analysis of Structures", Nonlinear Computational Mechanics: State of the Art, Edited by Wriggers, P. and Wagner, W. Eds., Springer-Verlag, Berlin, 1990, pp. 47-68.
- [10] Crisfield, M.A., "Nonlinear Finite Element Analysis of Solids and Structures", Vol. 2, Advanced Topics, John Wiley & Sons, 1997.
- [11] Choong, K.K. and Hangai, Y., "Review on Methods of Bifurcation Analysis for Geometrically Nonlinear Structures", Int. Assoc. Shells Spatial Struct. (Issue Dedicated to SEIKEN-IASS Symposium on Nonlinear Analysis and Design for Shell and Spatial Structures), 1993, Vol. 34, No. 2, pp. 133-149.
- [12] Wagner, W. and Wriggers, P., "A Simple Method for the Calculation of Postcritical Branches", Engng. Comput., 1988, Vol. 5, pp. 103-109.
- [13] Fujii, F. and Choong, K.K., "Branch-switching in Bifurcation of Structures", J. Struct. Eng., ASCE, 1992, Vol. 118, pp. 1578-1596.
- [14] Fujii, F. and Asada, K. "Branch-switching in Simple Spatial Bifurcation Models", SEIKEN-IASS Symp. on Nonlinear Analysis and Design for Shells and Spatial Structures, 1993, Tokyo, pp. 515-522.
- [15] Wriggers, P., Wagner, W. and Mische, C., "A Quadratically Convergent Procedure for the Calculation of Stability Points in Finite Element Analysis", Comput. Methods Appl. Mech. Engrg., 1988, Vol. 70, pp. 329-347.
- [16] Wriggers, P., and Simo, J.C. "A General Procedure for the Direct Computation of Turning and Bifurcation Points", Int. J. Numer. Meth. Engng, 1990, Vol. 30, pp. 155-176.
- [17] Chan, S.L., "A Non-linear Numerical Method for Accurate Determination of Limit and Bifurcation Points", Int. J. Numer. Meth. Engng., 1993, Vol. 36, pp. 2779-2790.
- [18] Fujii, F. and Ramm, E. "Computational Bifurcation Theory-path-tracing, Pinpointing and Path-switching", Engineering Structures, 1997, Vol. 19, pp. 385-392.
- [19] Fujii, F., Ikeda, K., Noguchi, H. and Okazawa, S., "Modified Stiffness Iteration to Pinpoint Multiple Bifurcation Points", Comput. Methods Appl. Mech. Engrg., 2001, Vol. 190 (18.19), pp. 2499-2522.
- [20] Fujii, F. and Noguchi, H., "Eigenvector-free Indicator, Pinpointing and Branch-switching for Bifurcation", Commun. Numer. Meth. Engng., 2003, Vol. 19, pp. 445-457.

- [21] Battini, J.M., Pacoste, C. and Eriksson, A., “Improved Minimal Augmentation Procedure for the Direct Computation of Critical Points”, *Comput. Methods Appl. Mech. Engrg.*, 2003, Vol. 192, pp. 2169–2185.
- [22] Oran, C., “Tangent Stiffness in Space Frame”, *J. Struc. Div., ASCE*, 1973, Vol. 99, No. 6, pp. 987-1001.
- [23] Spillers, W.R., “Geometric Stiffness Matrix for Space Frames”, *Computers & Structures*, 1990, Vol. 36, No. 1, pp. 29-37.
- [24] Kassimali, A. and Abbasnia, R., “Large deformation analysis of elastic space frames”, *J. Struct. Eng., ASCE*, 1991, Vol. 117, No. 7, pp. 2067-2087.
- [25] Abbasnia, R. and Kassimali, A., “Large Deformation Elastic-plastic Analysis of Space Frames”, *J. Construct. Steel Research*, 1995, Vol. 35, pp. 275-290.
- [26] Levy, R. and Spillers, W.R., “Analysis of Geometrically Nonlinear Structures, 2nd ed.”, *Kluwer Academic Publishers*, 2003.
- [27] Argyris, J., “An excursion into large rotations”, *Comput. Methods Appl. Mech. Engrg.*, 1982, Vol. 32, pp. 85–155.
- [28] Argyris, J.H., Dunne, P.C. and Scharpf, D.W., “On large displacement small strain analysis of structures with rotational degrees of freedom”, *Comput. Methods Appl. Mech. Engrg.*, 1978, Vol. 14, pp. 401-451.
- [29] Argyris, J.H., Balmer, H., Doltsinis, I.S.T., Dunne, P.C., Haase, M., Kleiber, M., Malejannakis G.A., Mlejnek, H.P., Muller, M. and Scharpf, D.W., “Finite element method-The natural approach”, *Comput. Methods Appl. Mech. Engrg.*, 1979, Vol. 17/18, pp. 1-106.
- [30] Argyris, J.H., Hilpert, O., Malejannakis, G.A. and Scharpf, D.W., “On the geometrical stiffness of a beam in space—A consistent v.w. approach”, *Comput. Methods Appl. Mech. Engrg.*, 1979, Vol. 20, pp. 105-131.
- [31] Argyris, J.H., Boni, B., Hindenlang, U. and Kleiber, M., “Finite element analysis of two and three dimensional elasto-plastic frames-the natural approach”, *Comput. Methods Appl. Mech. Engrg.*, 1982, Vol. 35, pp. 221-248.
- [32] Simo, J.C., “A finite strain beam formulation. Part I, The three-dimensional dynamic problem”, *Comput. Methods Appl. Mech. Engrg.*, 1985, Vol. 49, pp. 55–70.
- [33] Izzuddin, B.A. and Elnashai, A.S., “Eulerian formulation for large displacement analysis of space frames”, *J. Eng. Mech., ASCE*, 1993, Vol. 119, No. 3, pp. 549-569.
- [34] Meek, J.L. and Tan, H.S., “Geometrically Nonlinear Analysis of Space Frames by an Incremental Iterative Technique”, *Comput. Methods Appl. Mech. Engrg.*, 1984, Vol. 47, pp. 261-282.
- [35] Chan, S.L., “Geometric and Material Nonlinear Analysis of Beam-Columns and Frames Using the Minimum Residual Displacement Method”, *Int. J. Num. Meth. Eng.*, 1988, Vol. 26, No. 12, pp. 2657-2669.
- [36] Crisfield, M.A. and Cole, G., “Co-rotational Beam Elements for Two and Three-dimensional Nonlinear Analysis, *Discretisation Methods in Structural mechanics*”, ed. G. Kuhn & H. Mang, *Spring-Verlag*, 1989, pp. 115-124.
- [37] Crisfield, M.A., “A Consistent Co-rotational Formulation for Nonlinear Three Dimensional Beam Elements”, *Comput. Methods Appl. Mech. Engrg.*, 1990, Vol. 81, pp. 131-150.
- [38] Nour-Omid, B. and Rankin, C.C., “Finite Rotation Analysis and Consistent Linearization using Projectors”, *Comput. Methods Appl. Mech. Eng.*, 1991, Vol. 93, pp. 353-384.
- [39] Teh, L.H. and Clarke, M.J., “Co-rotational and Lagrangian Formulations of Elastic Three-dimensional Beam Finite Elements”, *J. Construct. Steel Research*, 1998, Vol. 48, pp. 23–44.
- [40] Battini, J.M. and Pacoste, C., “Co-rotational Beam Elements with Warping Effects in Instability Problems”, *Comput. Methods Appl. Mech. Engrg.*, 2002, Vol. 191, pp. 1755–1789.

- [41] Chan, S.L. and Zhou, Z.H., "Pointwise Equilibrium Polynomial Element for Nonlinear Analysis of Frames", *J. Struct. Eng.*, ASCE, 1994, Vol. 120, pp. 1703–1717.
- [42] Izzuddin, B.A., "Quartic Formulation for Elastic Beam-columns Subject to Thermal Effects", *J. Eng. Mech.*, ASCE, 1996, Vol. 122, pp. 861–71.
- [43] Chan, S.L. and Zhou, Z.H., "Nonlinear Integrated Design and Analysis of Skeletal Structures by 1 Element Per Member", *Engineering Structures*, 2000, Vol. 22, pp. 246–57.
- [44] Liew, J.Y.R., Chen, H., Shanmugam, N.E. and Chen, W.F., "Improved Nonlinear Plastic Hinge Analysis of Space Frame Structures", *Engineering Structures*, 2000, Vol. 22, pp. 1324-1338.
- [45] Hangai, E. and Kawamata, S., "Perturbation Method in the Analysis of Geometrically Nonlinear and Stability Problems", *Advances in Computational Methods in Structural Mechanics and Design*, UAH Press, 1972, pp. 473-489.
- [46] Sabir, A.B., and Lock, A.C., "Large Deflection, Geometrically Nonlinear Finite Element Analysis of Circular Arches", *Int. J. Mech. Sci.* 1973, Vol. 15, pp. 37-47.
- [47] Powell, G.H., "Theory of Nonlinear Elastic Structures", *J. Struct. Div. ASCE*, 1969, Vol. 95, No. 12, pp.2687-2701.
- [48] Chu, K.H., and Rampetsreiter, R.H., "Large Deflection Buckling of Space Frames", *J. Struct. Div.*, ASCE, Vol. 98, No. 12, pp. 2701-2722, 1972
- [49] Papadrakakis, M. and Ghionis, P., "Conjugate Gradient Algorithms in Nonlinear Structural Analysis Problems", *Comput. Methods Appl. Mech. Engrg.*, 1986, Vol. 59, No. 1, pp. 11-27.
- [50] Kondoh, K. and Atluri, S.N., "Simplified Finite Element Method for Large Deformation, Post-Buckling Analysis of Large Frame Structures, Using Explicitly Derived Tangent Stiffness Matrices", *Int. J. Num. Meth. Eng.*, 1986, Vol. 3, No. 1, pp. 69-90.
- [51] Shi, G. and Atluri, S.N., "Elasto-plastic Large Deformation Analysis of Space-frames : A Plastic-hinge and Stress-based Explicit Derivation of Tangent Stiffness", *Int. J. Num. Meth. Eng.*, 1988, Vol. 26, pp. 589-615.

# STRENGTH AND DUCTILITY EVALUATION METHOD FOR STEEL BRIDGE PIER FRAMES CONSIDERING EFFECT OF SHEAR FAILURE

L. Kang<sup>1</sup> and H.B. Ge<sup>2,\*</sup>

<sup>1</sup>Post Doctoral Researcher, Dept. of Civil Engineering, Meijo University, Nagoya, 468-8502, Japan  
E-mail: connielan@tom.com

<sup>2</sup>Professor, Dept. of Civil Engineering, Meijo University, Nagoya, 468-8502, Japan.  
\*(Corresponding author: E-mail: gehanbin@meijo-u.ac.jp)

Received: 25 August 2011; Revised: 4 October 2011; Accepted: 21 November 2011

---

**ABSTRACT:** This paper presents a practical evaluation method for predictions of strength and ductility capacity of steel bridge pier frames including effects of shear failure. The shearing behavior of structure is simulated by introducing membrane and truss elements at the mid-span of girder. In order to investigate the effects of shear failure on the strength and ductility capacity, a series of pushover analyses are carried out, comparisons between different methods are conducted and effects of sensitive parameters are discussed. From these investigations and discussions, the availability of the shear ductility prediction method proposed in this study is verified, especially for the unstiffened cases with large web width-thickness ratio of girder. Furthermore, a boundary between bending and shear failure modes is obtained based on discussions.

**Keywords:** Steel bridge pier frame, Shear failure, Bending failure, Ductility capacity, Membrane element, Web width-thickness ratio of beam

---

## 1. INTRODUCTION

Steel bridge piers suffered severe seismic damage during the Hyogoken-Nanbu earthquake, on January 17th, 1995. Some of steel bridge piers' failure during this earthquake mainly resulted from the shear local buckling, as shown in Figure 1. Severe shear damage in such structures caused considerable disruption to the relief work. This resulted in a consensus to be reached that the seismic capacity, especially the ductility, of such structures needs further and extensive investigation. Because no similar damage ever being reported in Japan before, shear failure, especially at the mid-span of girder, was not considered in seismic design prior to this earthquake. However, since then the necessity of accounting for the effect of shear failure in the phase of seismic design has been gradually realized. In the past years, the performance of bending failure has been deeply investigated [1-6]. For the shear failure of steel pier frames due to the shear local buckling, the experimental investigations have been conducted [7, 8], but the corresponding evaluation method is sparse and specific quantitative criterion to relate these failure modes to steel bridge piers is lacking. Besides, for steel bridge pier frames, both bending and shear failure verifications should be conducted in order to identify which type of failure will occur, especially during earthquake loading [9-11].

The shear failure of column-beam joint in building frames has been regarded as important damage mode [12, 13]. Because of the strengthening measures of pier-girder joint in steel bridge pier frames, large shear deformation may occur at the mid-span of girder [14]. Similar to the previous research [14-18], the strength and ductility should be considered and verified at the same time. A pushover analysis is terminated when any of the structure's failure criterion is satisfied and this state is taken as the ultimate state of the structure, based on which the ductility capacity of the structure can be determined. During the past years, there is a considerable amount of literatures on failure criterion. The bending failure criterion has been deeply studied in previous studies [1, 3-5, 19]. Besides, the shear failure criterion was studied [20, 21]. Although a simple analytical model

considering shear deformation was discussed by Chusilp and Usami [21], the complete pushover analysis including shear failure for steel bridge pier frames has not been conducted because of the limitation of previous simulation model. The effect of shear failure on the ductility capacity of structure has not been studied in the previous research. In recent years, with the development of computational technology, the strength and ductility including effect of shear deformation and failure can be calculated and predicted accurately and easily. In the previous studies [20, 21], parameter analysis of shear deformation has been done and these results can provide basis for the proposed study. The aim of this study is to provide an analytical model to check and verify the strength and ductility including bending and shear failure modes for steel bridge pier frames more effectively.

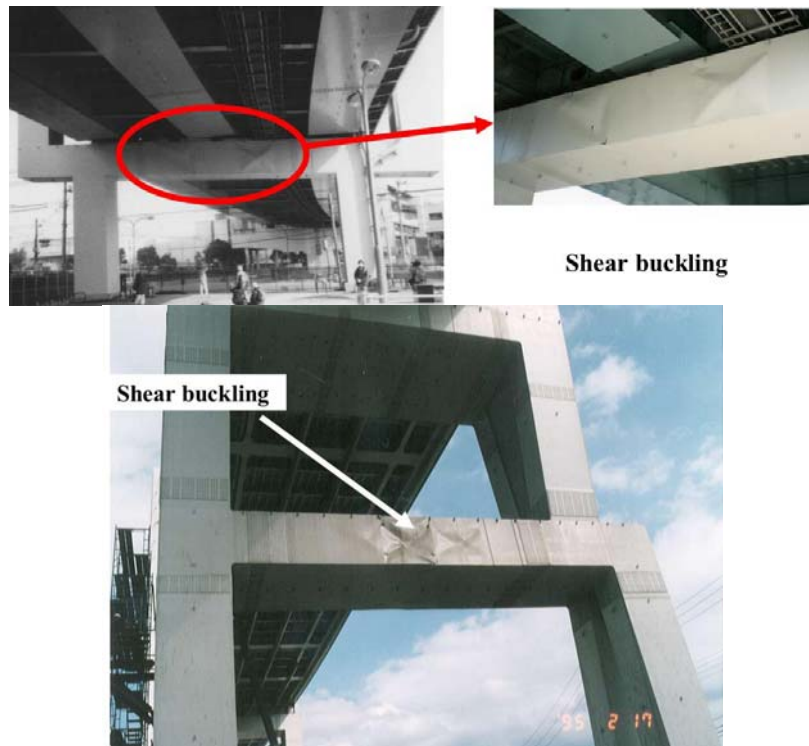


Figure 1. Examples of Shear Failure in Damaged Steel Bridge Pier Frames in the 1995 Kobe Earthquake

Because of the aforementioned lack of verification method about strength and ductility evaluation including shear failure in steel bridge pier frames, a hybrid model including beam, membrane and truss elements is proposed in this paper and a series of pushover analyses are carried out based on this model. First of all, a so-called MB model is established in section 2, in which the details including finite element model, dimensions, cross section, constraint between different elements and so on will be given. Secondly, the previous failure criteria are stated. Furthermore, comparisons between the proposed and previous models' results as well as sensitive parameter analysis are conducted. From the results and discussions, a boundary between bending and shear failure modes is obtained.

## 2. FINITE ELEMENT ANALYTICAL MODEL OF STEEL BRIDGE PIER FRAMES

In this study, the ABAQUS finite element software [22] was utilized to investigate the structural behavior of steel bridge pier frames. Two different finite element analytical models are established, which are BB and MB models, respectively, as shown in Figure 2. In which, the BB model only includes the beam element, and the MB model consists of the membrane and truss elements at the

mid-span of girder except for the beam element. In the previous study [5], the BB model was employed to evaluate the bending performance of steel structures. In both two models, the  $P-\Delta$  effect is taken into account, and the local buckling is ignored. For different models, the effect of shear behavior is taken into account in different ways. In the BB model, the shear deformation is included by using a type of beam element (i.e., B21) based on the Timoshenko beam theory, and the effect of shear failure is not considered. However, in the MB model, the shear deformation is also considered by introducing the membrane element at the mid-span of girder, which can take the effect of shear failure into account. The BB model only with the beam element can't take the effect of shear failure (as shown in Figure 1) into consideration, because the beam element can't accurately simulate the shear buckling occurring at the mid-span of girder. In this study, because the MB model with membrane element at the mid-span of girder can reveal the shear failure more comprehensively and correctly during pushover analysis, the MB model is employed to replace the traditional model (BB model), and the corresponding seismic verification method including the effect of shear failure by using this hybrid analytical model is developed and established.

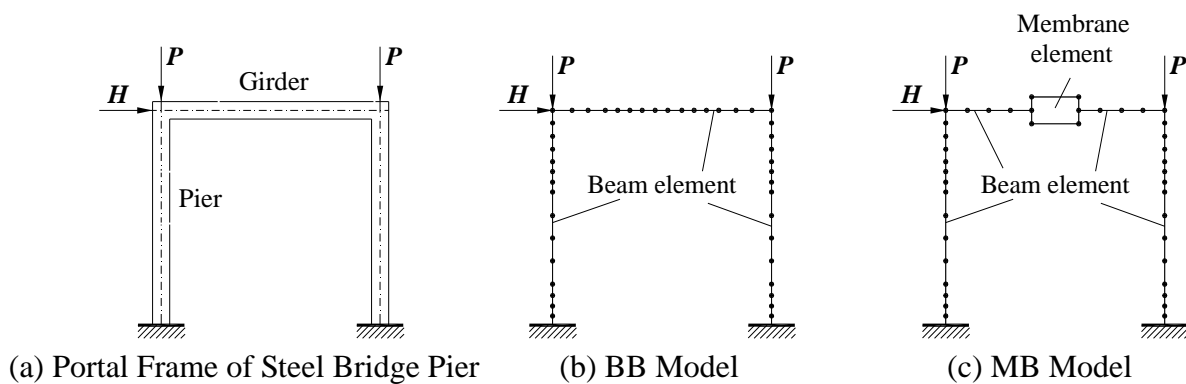


Figure 2. Steel Bridge Pier Frame

## 2.1 Analytical Model

### 2.1.1 The analytical model only including beam element (BB model)

The beam element (B21) in ABAQUS, which accounts for the shear deformation based on the Timoshenko beam theory, is utilized in this model, and each of girder and piers is divided into 15 beam elements [23]. Since this type of portal frame is commonly subjected to heavy loading, the plates at the pier-girder connections should be strengthened by doubling the plate thickness in order to avoid shear failure [14].

### 2.1.2 The finite element model with membrane element at the mid-span of girder (MB model)

In this analytical model, the beam element at the mid-span of girder is replaced by the membrane and truss elements. The four-node membrane element (M3D4) in ABAQUS, which has two degrees of freedom at each node, is adopted at the mid-span of girder, and in other parts of beam member the Timoshenko beam element is utilized (same to the BB model). Each pier member is divided into 15 beam elements [23]. The distance between the pier-girder joint and the membrane element is the length of 3 beam elements. Besides, same to the BB model, the plates at the pier-girder connections should be strengthened by doubling the plate thickness in order to avoid shear failure of joints [14]. The only difference between the BB model and MB model is the element type to model the mid-span girder. In order to predict the shear failure mode of steel bridge frame structure, the MB model consists of the membrane and truss elements except for the beam element, and it is then regarded as a hybrid model including three types of elements.

## 2.2 Dimensions of Analytical Model

In this study, a series of finite element analyses are carried out. As shown in Figure 3, the label of analyzed models (e.g., US35-70A and SS35-40B) is defined as follows. The first letter indicates the type of cross section, where “U” and “S” represent unstiffened box section and stiffened box section, respectively. The following letter S indicates steel bridge pier frame. Accordingly, “US” and “SS” refer to steel bridge pier frames with unstiffened steel box section and stiffened steel box section, respectively. The next two numbers denote the flange width-thickness ratio of column,  $R_f$ , and the web width-thickness ratio of beam,  $R_{wb}$ , respectively. They are 100 times larger than the actual value. The last letter (A or B) represents the beam length, where “A” means the length of beam is 8300 mm, and “B” indicates the length is 12450 mm. In other words, the values of  $l/h$  in two cases are 0.769 and 1.15, respectively. Additionally, for some unstiffened cases, in order to evaluate the effect of stiffened measure on the failure mode, stiffeners are employed and “-S” and “-2S” indicate one stiffener and two stiffeners to strengthen the unstiffened specimens, respectively. Some main parameters of finite element analysis are listed in Table 1. Equivalent web width-thickness ratios of beam  $R_{wb}$  of -S and -2S cross sections are given in Table 2. A total of 38 different cases are analyzed in this study.

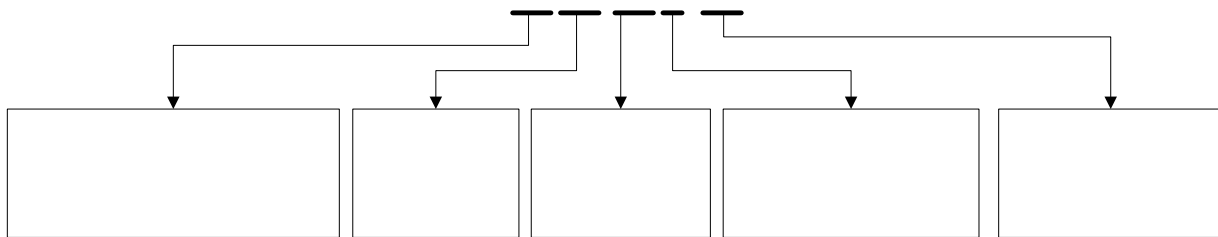


Figure 3. Label of Analytical Cases

Table 1. Main Parameters for Finite Element Analysis

Parameters	Range
Column height, $h$ (mm)	10800
Beam length, $l$ (mm)	8300,12450
Flange width-thickness ratio of column, $R_f$	0.35~0.45
Web width-thickness ratio of beam, $R_{wb}$	0.4~1.5
Yield stress of steel (MPa)	314
Stiffness ratio of column stiffener	3.0
Stiffness ratio of beam stiffener	1.0

Table 2. Web Width-thickness Ratio of Beam  $R_{wb}$  of -S and -2S Cross Sections

Specimens	US35-60A-S	US35-70A-S	US35-100A-S	US35-150A-S
$R_{wb}$	0.313	0.372	0.573	0.860
Specimens	US45-60A-S	US45-70A-S	US45-100A-S	US45-150A-S
$R_{wb}$	0.308	0.363	0.540	0.811
Specimens	US35-100A-2S	US35-150A-2S		
$R_{wb}$	0.591	0.549		

US35-

US:Unstiffened box section  
of steel bridge pier frame  
SS: Stiffened box section of

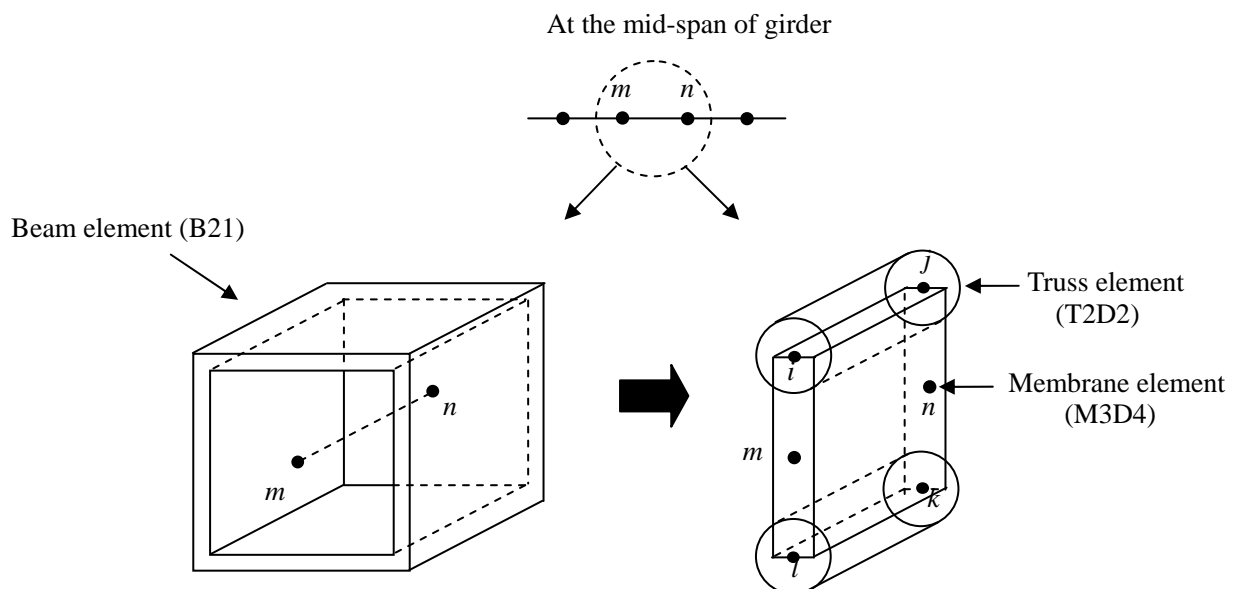
Flange width-  
thickness ratio  
of column

Web w  
thickne  
of beam

### 2.3 Cross Section of Steel Bridge Pier Frame

For the BB model, the beam element at the mid-span of girder is shown in Figure 4(a). In which,  $m$ ,  $n$  are the two nodes of beam element, and the cross section of pier and girder members are introduced by sectional properties and parameters. For the beam cross sections, the web plate of beam is unstiffened belonging to US model and the web plate of beam is stiffened belonging to SS model. A box section with longitudinal stiffeners (SS model) is one of the most common cross-sectional types used for thin-walled steel structures. In the analysis of such structures, the original stiffened section can certainly be used but, for simplification, an equivalent unstiffened section is introduced [5].

However, in the MB model, the beam element at the mid-span of girder is replaced by membrane and truss elements, as shown in Figure 4(b). It is well-known that shear local buckling may occur at the mid-span of girder. In order to accurately predict the shear failure of steel bridge pier frames, one membrane and two truss elements are introduced into the MB model. The analytical method may be suitable for simulating the in-plane deformation of pushover analysis because the out-of-plane deformation can't be taken into account in membrane element. In addition, the two truss elements are used to model the flange plate at the mid-span of girder because the flange works mainly in tension or compression modes. In the Figure 4(b),  $m$ ,  $n$  are the two nodes of side beam elements, and  $i, j, k, l$  are the four nodes of membrane element. Membrane and truss elements share the same nodes, in which  $i$  and  $j$  are two nodes of one truss element,  $l$  and  $k$  are two nodes of the other one. The thickness of membrane element is twice of the thickness of web plate based on equivalent cross section method. Cross section area of truss element is equal to that of flange plate of beam.



(a) Beam Element of BB Model

(b) Membrane and Truss Elements of MB Model

Figure 4. Difference between BB Model and MB Models

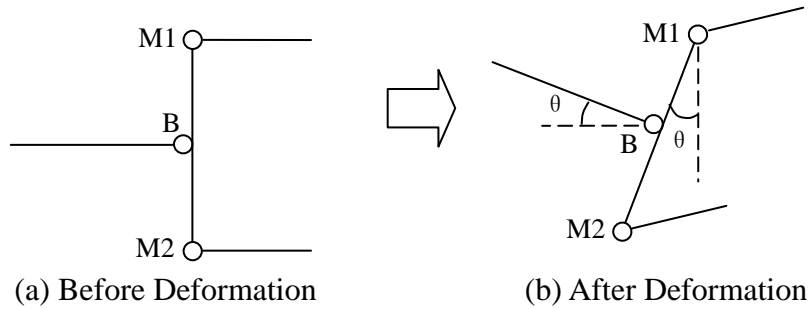


Figure 5. Connection between Membrane and Beam Elements

## 2.4 Constraint between Membrane and Beam Elements

In the proposed analytical model, the connection between membrane and beam elements is established based on the assumption of plane cross section. In Figure 5, B is the node of beam element, and M1 and M2 represent the nodes of membrane element. There are two following constraint conditions:

- (1) The length of the connection part (the length between nodes M1 and M2 in Figure 5), which connects membrane element with beam element, is constant;
- (2) At the connection part between membrane and beam elements, the rotation of beam element node B is equal to the rotations of the two nodes (M1 and M2) of membrane element.

The displacement relationship between beam and membrane elements can be expressed as follows:

$$u_M - u_B = (X_A - X_B)(\cos \theta - 1) - (Y_M - Y_B)\sin \theta \quad (1)$$

$$v_M - v_B = (X_M - X_B)\sin \theta + (Y_M - Y_B)(\cos \theta - 1) \quad (2)$$

in which,  $u$  and  $v$  denote the displacements of  $X$ -axis and  $Y$ -axis, respectively.  $X, Y$  represent the coordinate magnitudes of  $X$ -axis and  $Y$ -axis after deformation, respectively. The subscript  $M$  expresses that the variable belongs to membrane element, and the subscript  $B$  expresses that the variable belongs to beam element.  $\theta$  denotes the rotation of beam element node.

## 2.5 Weight of Upper Structure

In this study, the weight of upper structure is regarded as vertical loads applying on the steel bridge pier frame. Based on the seismic coefficient method [24], the weight of upper structure is calculated. Considering a certain safety coefficient (in this study, is 1.14, same to the reference [23]), the analytical model is subjected to the horizontal load  $H = 0.2P$  and the vertical loads of  $P$  at the top of the steel bridge pier frame. The weight of upper structure is obtained. The range of  $P/P_y$  is from 0.28 to 0.5.

## 3. FAILURE CRITERION

The pushover analysis involves applying monotonic lateral loads to approximately simulate the horizontal displacements of steel bridge pier frames. In somewhat different formats, the pushover analysis has been proposed and evaluated mainly as a demand prediction tool for concrete structures [25-27]. In recent work of the authors [23, 28], the pushover analysis has been proposed for steel frame structures serving for both the capacity evaluation and demand prediction. During

the pushover analysis, a proper failure criterion is necessary. For RC structures, the failure criterion is usually based on the rotational capacity of plastic hinges. However, the capacity of frame structures composed of thin-walled steel members is mainly controlled by local buckling. In this paper, a failure criterion including bending and shear failure modes is employed to evaluate bending and shear failure modes. Besides, the locations of failure verification, the damage degree and the effective failure length are described in the following sections.

### 3.1 Location of Failure Verification

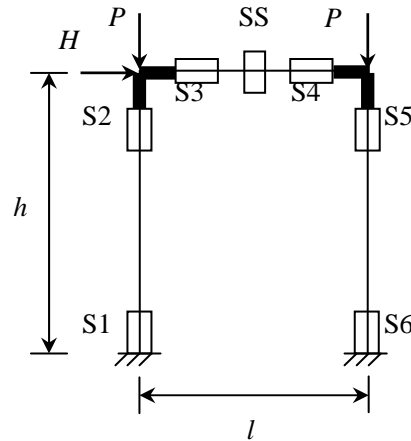


Figure 6. Location of Failure Verification

With the increase of loading, the failure verification locations become wider. Because the steel frame is under combined loading of bending and compression, the compression strain is raised [5]. To completely investigate the bending behavior of steel frames, six bending verification locations (S1~S6) are determined as shown in Figure 6, in which  $l$  is the length of girder,  $h$  is the height of pier,  $P$  and  $H$  are vertical and horizontal loads, respectively. Because the stiffness of the pier-girder joint is relatively large (as described in Sections 2.2 and 2.3), in this study, SS at the mid-span of girder is regarded as the shearing verification location, as shown in Figure 6.

### 3.2 Failure Verification

#### 3.2.1 Bending failure verification

In the proposed ductility evaluation method, the bending failure criterion can be described by a damage index  $D_{sb}$ , which is defined:

$$D_{sb} = \frac{\varepsilon_{a,s}}{\varepsilon_{u,s}} \quad (3)$$

when  $D_{sb}$  reaches 1.0, the bending ultimate state of structure is considered to be attained. Here,  $\varepsilon_{a,s}$  represents the average strain of the compressive flange (for the box section) over a certain effective failure length that will be discussed further below. The value  $\varepsilon_{u,s}$  denotes the failure strain and, to define it, the empirical formulas obtained from stub-column analyses are employed.

The empirical formulas of the failure strains were proposed for thin-walled steel stub columns with box sections that are subjected to compression and bending. The behavior of box-sectioned stub-columns with and without longitudinal stiffeners has been extensively investigated under combined compression and bending, and corresponding empirical equations for the failure strains were given as follows [5]:

For unstiffened box stub-columns:

$$\frac{\varepsilon_{u,s}}{\varepsilon_y} = \frac{0.108(1 - N/N_y)^{1.09}}{(R_f - 0.2)^{3.26}} + 3.58(1 - N/N_y)^{0.839} \leq 20.0 \quad (4)$$

For stiffened box stub-columns:

$$\frac{\varepsilon_{u,s}}{\varepsilon_y} = \frac{0.8(1 - N/N_y)^{0.94}}{(R_f \cdot \bar{\lambda}_s^{0.18} - 0.168)^{1.25}} + 2.78(1 - N/N_y)^{0.68} \leq 20.0 \quad (5)$$

in which,  $P$  = axial force;  $P_y$  = squash load;  $R_f$  = flange width-thickness ratio parameter; and  $\bar{\lambda}_s$  = stiffener's slenderness ratio parameter. The definitions of  $R_f$  and  $\bar{\lambda}_s$  can refer to the reference [19]. In this study,  $R_f = 0.3 \sim 0.7$ ,  $N/N_y = 0.0 \sim 0.5$ . When the axial force is a tension, it will be taken to be zero.

### 3.2.2 Shear failure verification

In the proposed ductility procedure, the shear failure criterion can be described by a damage index  $D_{ss}$ , which is defined:

$$D_{ss} = \frac{\gamma_s}{\gamma_{u,s}} \quad (6)$$

in which,  $\gamma_s$  is the shearing strain of membrane element,  $\gamma_{u,s}$  is the ultimate strain obtained by the equations (7) and (8). Simple formulas are proposed for estimating the ductility capacity of box girders with and without longitudinal web stiffeners as follows [21, 29]:

For unstiffened cross section:

$$\frac{\gamma_{u,s}}{\gamma_y} = \frac{0.142}{(R_{wb} - 0.18)^{4.0}} + 4.0 \leq 20.0 \quad (7)$$

For stiffened cross section:

$$\frac{\gamma_{u,s}}{\gamma_y} = 2.5 + \frac{0.5}{R_{wb}^{6.0}} \leq 20.0 \quad (8)$$

$R_{wb}$  is the web width-thickness ratio of box girders. The limit scope of the equation (8) is  $\gamma_{ws} \geq \gamma_{ws}^*$ ,  $1.0 \leq \alpha_{wb} \leq 2.0$ .  $\alpha_{wb}$  is the web length-width ratio of the girder. The details can refer to the references [21, 29].

### 3.3 Effective Failure Length

The effective failure length  $l_e$  of a box-sectioned member adopted in this method is assumed as  $l_e = \min\{0.7B, l_d\}$  where  $B$  is the flange width and  $l_d$  is the distance between two adjacent diaphragms [5]. For pipe section stub-columns in compression and bending, an empirical equation for the critical length (i.e., the length giving the lowest strength) was proposed by Gao et al. [3], and this length is found to be about half of the mode length of collapse in local buckling (i.e., the so-called elephant foot bulge) observed in long columns with pipe sections under cyclic lateral loading [30].

On this basis, a modified equation (approximately doubling the critical length equation of short cylinders) is employed to define the effective failure length of thin-walled pipe section structures, which is given by Zheng et al. [5]:

$$l_e = 1.2 \left( \frac{1}{R_t^{0.08}} - 1 \right) d \quad (9)$$

The critical parts could be in more than one place in a framing structure, and all of them should be checked. In a thin-walled steel structure, the excessive deformation tends to intensify in a local part and consequently the redistribution of the stress becomes unexpected. Thus, once the failure criterion at any one of the critical parts is satisfied, the ultimate state of such a structure is thought to be reached.

## 4. RESULTS AND DISCUSSIONS

The purpose of this study is to propose an improved analytical model and to evaluate the bending and shear failure modes of steel bridge pier frames by using the proposed model. Therefore, a hybrid model including membrane and truss elements at the mid-span of girder is developed. In this section, first of all, by the comparison of the results between MB and BB models, the reliability of the proposed model is verified. Next, by analyzing the parameters' effect, the relationship between structural parameters and shear failure of steel bridge pier frames is investigated. Finally, by utilizing the proposed method, the cases with stiffened and unstiffened plates are analyzed, and the influences of stiffened measure on the ductility evaluation and failure mode are investigated.

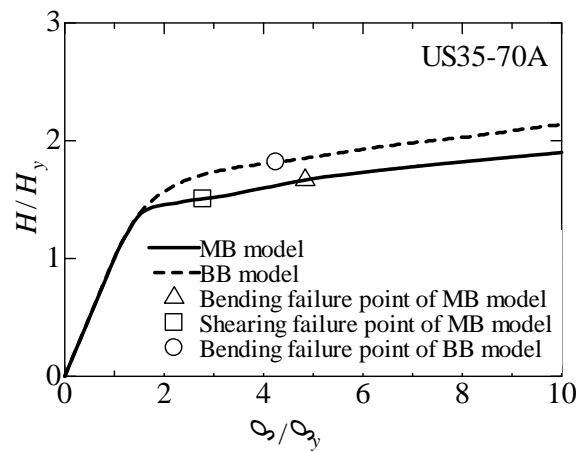
### 4.1 Comparison between MB and BB Models' Results

Table 3. Comparison of Different Models' Ductility Capacity

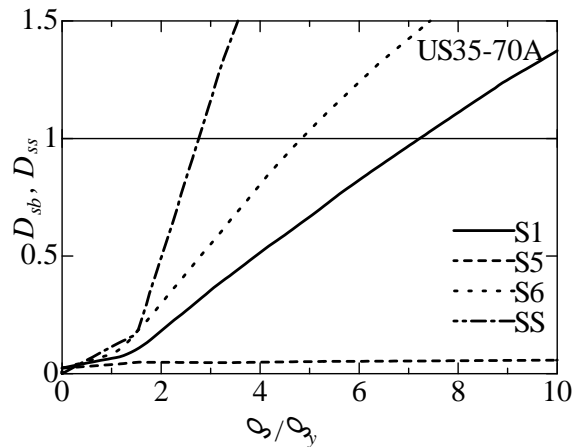
Specimens	BB model $\delta_{ub}/\delta_y$	MB model $\delta_{ub}/\delta_y$	MB model $\delta_{us}/\delta_y$	Specimens	BB model $\delta_{ub}/\delta_y$	MB model $\delta_{ub}/\delta_y$	MB model $\delta_{us}/\delta_y$
US35-40A	4.74	4.73	14.1	SS35-40A	3.28	3.96	8.67
US35-50A	4.65	4.71	6.14	SS35-50A	3.37	3.82	9.50
US35-60A	4.48	4.72	3.37	SS35-60A	3.22	3.52	7.13
US35-70A	4.25	4.84	2.78	SS35-70A	3.22	3.28	4.85
US35-100A	3.40	4.45	2.70	SS45-40A	2.48	2.53	6.07
US35-150A	3.42	4.95	2.01	SS45-50A	2.34	2.36	5.98
US45-40A	2.93	2.92	6.86	SS45-60A	2.34	2.34	4.85
US45-50A	2.81	2.93	4.02	SS45-70A	2.34	2.34	3.59
US45-60A	2.75	2.97	2.53	SS35-40B	3.99	3.96	
US45-70A	2.63	2.90	2.03	SS35-50B	3.55	3.55	18.97
US45-100A	2.50	2.89	1.90	SS35-60B	3.57	3.53	11.09
US45-150A	2.47	3.03	1.41	SS35-70B	3.53	3.49	7.92
US35-60A-S	4.53	4.50	27.9	SS45-40B	2.66	2.63	24.4
US35-70A-S	4.21	4.20	19.1	SS45-50B	2.57	2.55	14.7
US35-100A-S	3.42	3.94	7.65	SS45-60B	2.47	2.42	7.26
US35-150A-S	3.49	4.56	2.43	SS45-70B	2.43	2.42	4.97
US45-60A-S	2.74	2.74	12.9				
US45-70A-S	2.66	2.72	9.33				
US45-100A-S	2.47	2.61	5.72				
US45-150A-S	2.51	2.87	1.96				
US35-150A-2S		4.45	5.93				
US45-150A-2S		2.83	4.79				

Notes: Gray section means the minimum value between  $\delta_{ub}/\delta_y$  and  $\delta_{us}/\delta_y$  of MB model.

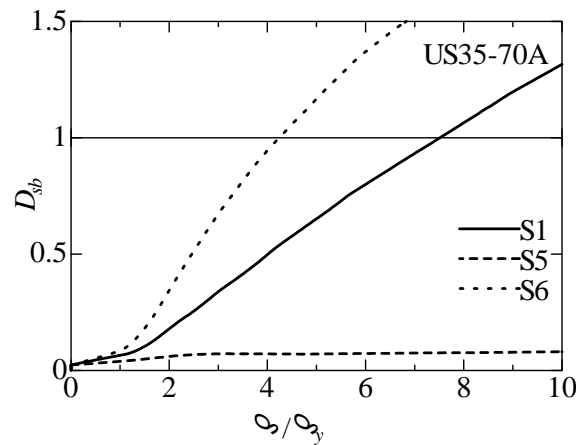
The computational results for the case of US35-70A by using MB and BB models are shown in Figure 7. Firstly, Figure 7(a) indicates the horizontal load versus horizontal displacement curves obtained from the MB and BB models. It demonstrates the relationship between  $H/H_y$  ( $H$  is the horizontal load,  $H_y$  is the horizontal yield load) and  $\delta/\delta_y$  ( $\delta$  is the horizontal displacement,  $\delta_y$  is the horizontal yield displacement) for the steel bridge pier frames. Secondly, Figure 7(b) illustrates the damage degree of steel frame versus horizontal displacement curves obtained from the finite element analysis of MB model. In Figure 7(b), the damage degrees of S2~S4 (S1~S6 are six locations of failure verification as shown in Figure 6) are relatively small, and then the magnitudes of S2~S4 are omitted in Figure 7(b). Lastly, Figure 7(c) demonstrates the damage degree versus horizontal displacement curves of the BB model. Table 3 reveals the ductility capacity of all the analytical examples obtained from finite element analyses of BB and MB models.  $\delta_{ub}/\delta_y$  and  $\delta_{us}/\delta_y$  represent the ratios of bending and shear ultimate-to-yield horizontal displacements, respectively. In this study, they are termed as the bending ductility and shear ductility, respectively.



(a) Horizontal Load-displacement Curves and Failure Points of MB and BB Models



(b) Damage degree of MB Model



(c) Damage Degree of BB Model

Figure 7. Horizontal Load Displacement Curves and Damage Degree of MB and BB Models

Based on the analytical results of US35-70A as shown in Figure 7, the web width-thickness ratio of beam is comparatively large, and shear failure is predicted to occur at the mid-span of girder. Figure 7(a) reveals that the shear failure occurs before bending failure during the pushover analysis of MB model, and the steel frame may encounter shear failure firstly. Besides, the horizontal displacements of the MB model in this study are larger than that of BB model obtained from the previous method, which is used to evaluate the bending performance. From the analytical responses of Figure 7(b), we can observe that the shear damage degree of SS increases more quickly than the bending damage degree of other locations. Individual differences in simulation results may reflect differences in analytical models, specifically in the damage degree and horizontal displacement. In conclusion, the previous method, which only consists of beam element, can't be employed to predict the shear failure of steel bridge pier frames.

Furthermore, some differences may exist in the load-displacement curves between MB and BB models as shown in Figure 7. On one hand, when the magnitude of  $\delta$  is near to  $1.7\delta_y$ , the strength of BB model increases continuously and smoothly, however, for MB model the same phenomenon does not exist. It demonstrates that the web plate at mid-span of MB model's girder has reached the ultimate shear state. Because the shear failure mainly results in the horizontal displacement of steel frames, the strength increase will be delayed. On the other hand, the bending failure points obtained from MB and BB models are different. The large width-thickness ratio parameter leads to the decrease of shearing strength, and meanwhile the bending plastic damage may be delayed during the bending verification procedure because of the relatively large bending plastic deformation capacity. Consequently, for the cases of shearing beam with large width-thickness ratio parameter, the prediction precision of its failure mode will be improved by using the proposed method in this study.

#### 4.2 Effect of Web Width-thickness Ratio of Beam $R_{wb}$

Relationships between horizontal displacement and web width-thickness ratio of beam,  $R_{wb}$ , are illustrated in Figure 8. The shear ductility capacity of steel bridge pier frames is evaluated, and can be expressed as  $\delta_{us}/\delta_y$ . The results of unstiffened and stiffened models are shown in Figure 8, from which it is observed that the shear ductility decreases with the increase of  $R_{wb}$ . The similar conclusion is obtained from the previous research [20, 21]. From the results of Figure 8, the shear ductility capacity of the examples with the flange width-thickness ratios of column  $R_f = 0.35$  is relatively larger compared with the examples with  $R_f = 0.45$ . Based on the stiffness matching theory, for these analytical examples, the web width-thickness ratio of beam corresponding to large flange

width-thickness ratio of column should be relatively large. Accordingly when the magnitude of model's  $R_f$  is equal to 0.45, its  $R_{wb}$  should be relatively large. In other words, when the web plate of beam is thick, the shear ductility capacity of steel bridge pier frames might be large. The similar conclusion has been demonstrated in the previous study [20].

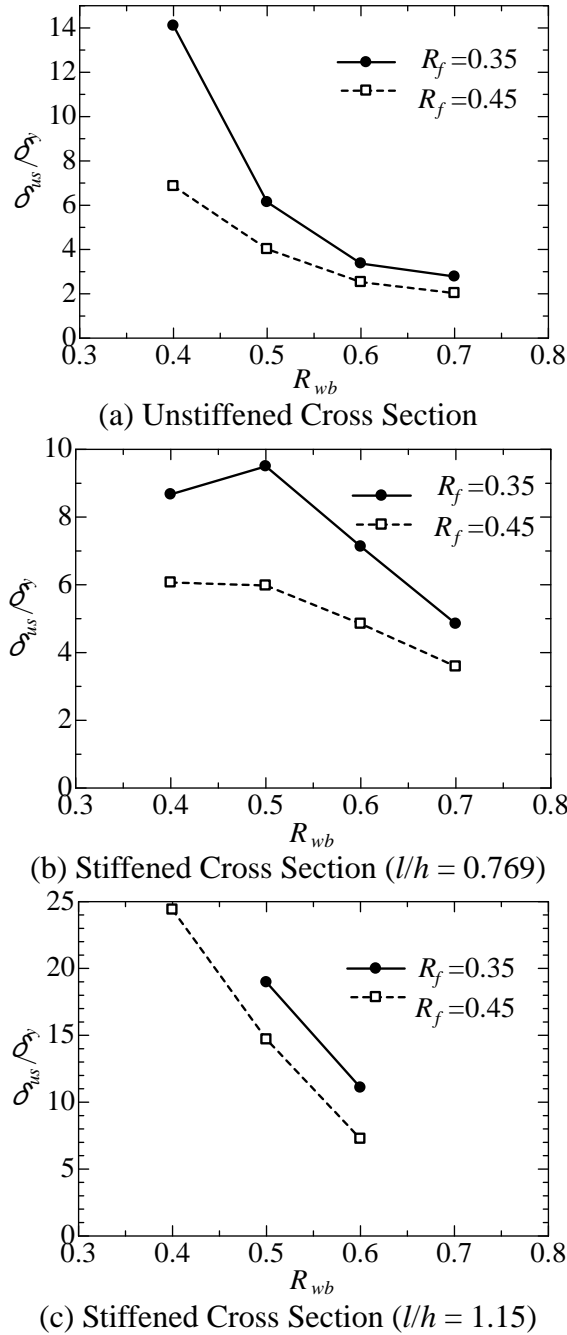
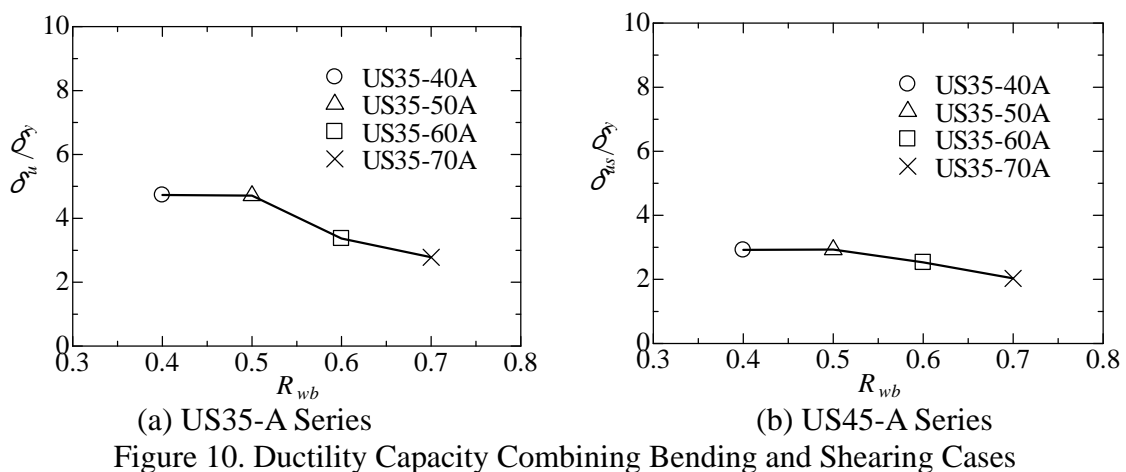
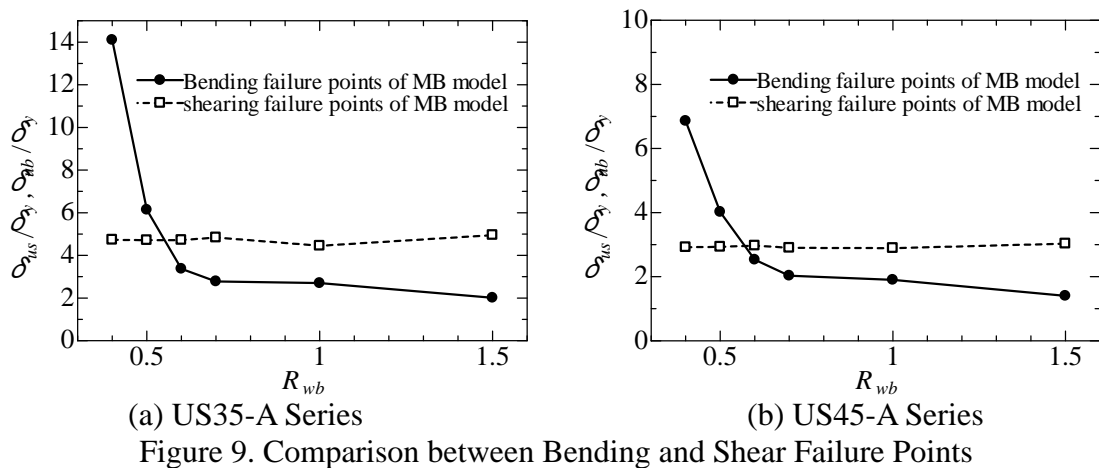


Figure 8. Effect of Web Width-thickness Ratio of Beam,  $R_{wb}$ , on Shear Ductility Capacity of Steel Frames

### 4.3 Comparison between Bending and Shear Failure Modes

The horizontal displacements versus web width-thickness ratio of beam  $R_{wb}$  curves are illustrated in Figure 9 obtained from the unstiffened cases. It is observed that the bending ductility of unstiffened structures decreases with the increase of  $R_{wb}$ , however, the shear ductility basically

retains constant with the increase of  $R_{wb}$ . When  $R_{wb}$  is larger than 0.6, although the ultimate bending displacement is near to the ultimate shear displacement, the first appearance of shear failure should not be ignored. In Figure 9, when  $R_{wb}$  is equal to 0.4 and 0.5, the bending failure occurs before the shear failure, but on the contrary when  $R_{wb}$  is equal to 0.6~1.5, the shear failure occurs before the bending failure. From the point of view of structural ductility, when  $R_{wb}$  is equal to 0.4 and 0.5, shear ductility is better than bending ductility, but when  $R_{wb}$  is equal to 0.6~1.5, the opposite is true. Figure 10 indicates the ultimate displacements  $\delta_u / \delta_y$  of steel bridge pier frames, which combines the bending and shear cases. In Figure 11, all of computational results are given in the same figure. The solid and black mark means bending failure, and the hollow and white one means shear failure. For the cases with stiffened cross section, the bending failure is dominant. On the other hand, for the cases with unstiffened cross section, the shear failure plays a critical role when  $R_{wb}$  is from 0.6 to 1.5. The above findings indicate that we can make a judgment between bending and shear failure modes by the magnitude of  $R_{wb}$ , and the approximate boundary of  $R_{wb}$  is 0.6. Generally a pier frame may be designed to avoid the occurrence of shear failure. Therefore, its  $R_{wb}$  should be less than 0.6. In this study, for some stiffened cases, the stiffener plates make the shear failure risk decrease, and for the unstiffened cases, maybe the shear failure occurs firstly when  $R_{wb}$  is greater than 0.6. Consequently, the unstiffened cases should be verified and analyzed, and some stiffened measures for avoiding occurrence of shear failure should be taken into account. The discussions will be carried out deeply in following section 4.4.



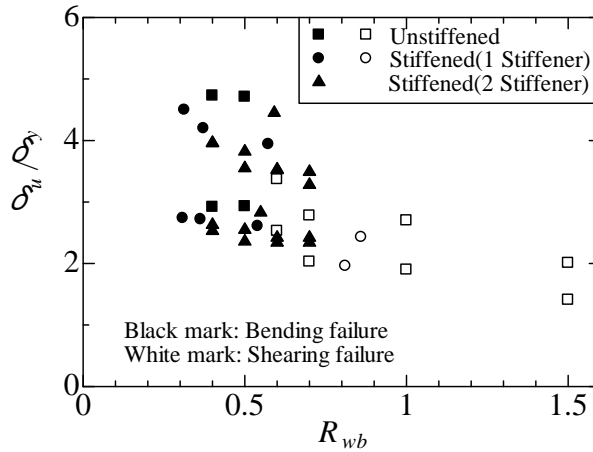


Figure 11. Relationship between Failure Modes (Bending and Shear Failure Modes) and Web Width-thickness Ratio of Beam  $R_{wb}$

4.4 Performance of Steel Frames with and without Stiffeners

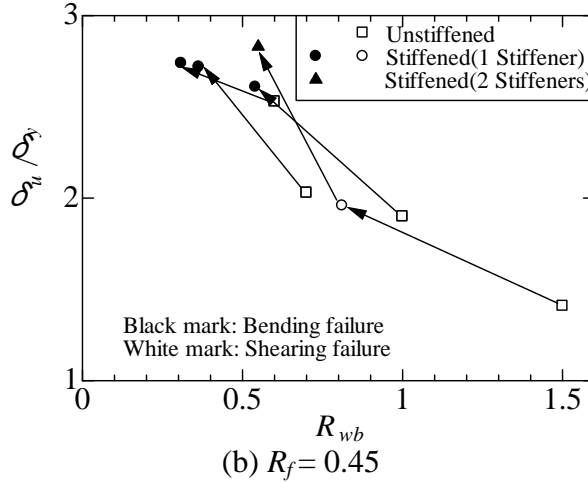
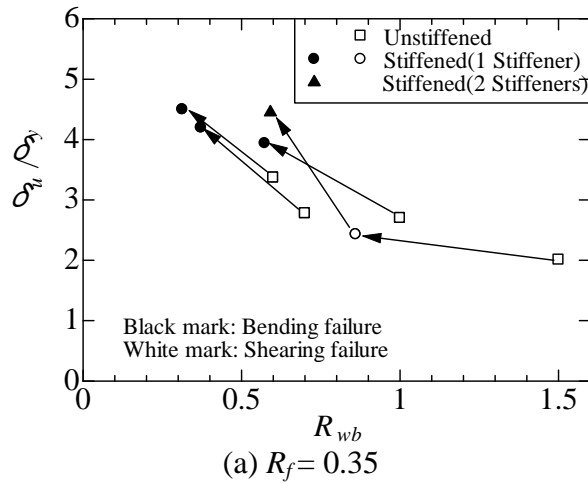


Figure 12. Effect of Stiffener Plate on Failure Modes

Ductility evaluation of US35-60A~150A and US45-60A~150A conducted above reveals that their shear failure is dominant, and some stiffener measures should be taken to avoid shear failure. In order to investigate the effect of stiffener measures on the failure mode for steel frames, the analytical cases with and without stiffeners are conducted. The ultimate displacements  $\delta_u / \delta_y$  versus web width-thickness ratio of beam  $R_{wb}$  curves are shown in Figure 12. The figure

illustrates how to improve ductility capacity, and how the failure mode translates from bending to shear failure by taking some stiffened measures. The flange width-thickness ratios  $R_f$  of column and beam are 0.35 and 0.45 in Figure 11(a) and Figure 12(b) (ductility capacity), respectively. The following demonstrates and explains these figures.

- (1) When the flange width-thickness ratio  $R_f$  of column is 0.35 and 0.45, the failure mode changes from shear to bending failure at  $R_{wb} = 0.6$ , for  $R_{wb} = 1.0, 0.7, 0.6$ , respectively. This discussion does not include the case of  $R_{wb} = 1.5$ , which has the thinnest web plate. Although for some stiffened cases in above analyses, shear failure will appear firstly when  $R_{wb} > 0.8$ ,  $R_{wb} = 0.6$  is regarded as the boundary from shear failure to bending failure, as described above.
- (2) When the flange width-thickness ratio  $R_f$  of column is 0.35, its ductility capacity is more better than the case of  $R_f=0.45$ . The main reason of this result is that bending failure is dominant if the flange width-thickness ratio is relatively small.

Next, for the cases with the thinnest web plate, every web plate has two stiffeners. The web width-thickness ratio of beam  $R_{wb} = 0.591$  ( $R_f=0.35$ ) and  $R_{wb} = 0.549$  ( $R_f=0.45$ ), respectively. These computational results are given in Figure 12. The model with two stiffeners has undergone bending failure. The ductility capacity has been improved greatly.

Different marks refer to different stiffened sections as shown in Figures. 11 and 12. From these results, shear failure is prone to occur when  $R_{wb} > 0.6$ . For this reason, in this study, the magnitude 0.6 of web width-thickness ratio of beam is regarded as the key parameter of identifying different failure types.

## 5. SUMMARY AND CONCLUSIONS

In this paper, a more accurate analytical method considering the effect of shear failure at the mid-span of girder was proposed to investigate the ductility performance of steel bridge pier frames. Different two simulation models, namely BB and MB models, were employed to evaluate the ductility and failure behavior of steel bridge pier frames. In the proposed MB model, membrane and truss elements were introduced. Moreover, comparisons between MB and BB models' results were carried out and parameter effect investigation was conducted. From the above discussions, we can draw the following conclusions:

- (1) Comparison between the previous BB model's and the proposed MB model's results has been conducted in this study. The deformation of MB model is larger than that of BB model. The traditional method using the BB model cannot accurately take shear failure at mid-span of girder into account. However, in some cases the effect of shear failure on ductility capacity of steel frames should not be ignored, especially for the cases with large web width-thickness ratio of beam.
- (2) Because shear failure is one of the main failure modes of the cases with unstiffened web plate of beam, the finite element analysis using the MB model is necessary. Compared with the BB model, the MB model can accurately predict the shear failure of steel bridge pier frames. When the bending failure is dominant, the proposed analysis method in this paper shows acceptable agreement with the previous method.
- (3) The stiffener of beam web plate can greatly improve ductility capability of structures.
- (4) The magnitude of beam web width-thickness ratio (0.6) is the key parameter of identifying different failure types (bending and shear failure modes).

- (5) The strength and ductility evaluation method of steel bridge pier frames can be effectively used to study the effects of various structural parameters which will be very useful in establishing design guidelines.

## ACKNOWLEDGMENT

The first author is the post doctor researcher of Meijo University at Nagoya, Japan, who is supported by the Daiko Foundation. The author would like to thank to the Daiko Foundation for their financial assistance.

## REFERENCES

- [1] Nishikawa, K., Yamamoto, S., Natori, T., Terao, O., Yasunami, H., Terada, M., "An Experimental Study on Improvement of Seismic Performance of Existing Steel Bridge Piers", *Journal of Structural Engineering, JSCE*, 1996, Vol. 42, No. A, pp. 975-986 (in Japanese).
- [2] White, D.W., Barth, K.E., "Strength and Ductility of Compact-flange I-girders in Negative Bending", *Journal of Constructional Steel Research*, 1998, Vol. 45, No. 3, pp. 241-280.
- [3] Gao, S., Usami, T., Ge, H.B., "Ductility of Steel Short Cylinders in Compression and Bending", *Journal of Engineering Mechanics, ASCE*, 1998, Vol. 124, No. 2, pp. 176-183.
- [4] Nishikawa, K., Murakoshi, J., Takahashi, M., Okamoto, T., Ikeda, S., Morishita, H., "Experimental Study on Strength and Ductility of Steel Portal Frame Pier", *Journal of Structural Engineering, JSCE*, 1999, Vol. 45, No. A, pp. 235-244 (in Japanese).
- [5] Zheng, Y., Usami, T., Ge, H.B., "Ductility Evaluation Procedure for Thin-walled Steel Structures", *Journal of Structural Engineering, ASCE*, 2000, Vol. 126, No. 11, pp. 1312-1319.
- [6] Susantha, K., Aoki, T., Kumano, T., Yamamoto, K., "Applicability of Low-yield-strength Steel for Ductility Improvement of Steel Bridge Piers", *Engineering Structures*, 2005, Vol. 27, No. 7, pp. 1064-1073.
- [7] Hirano, T., Nishioka, T., Takada, Y., Yoshikawa, N., Matsuda, Y., "Report on Shear Strength of Web Panel in Cross Beam of Rigid Framed Steel Pier", *Steel Construction Engineering, JSSC*, 2006, Vol. 14, No. 11, pp. 527-534 (in Japanese).
- [8] Miki, T., Yamada, O., Higuchi, N., "An Experimental Study on Elasto-plastic Behavior of Steel Web Plates under Cyclic Shearing Force", *Journal of Structural Engineering, JSCE*, 2007, Vol. 53, No. A, pp. 117-124 (in Japanese).
- [9] Shen, Z., Zhang, Q., "Interaction of Local and Overall Instability of Compressed Box Columns", *Journal of Structural Engineering, ASCE*, 1991, Vol. 117, No. 11, pp. 3337-3355.
- [10] Chan, S.L., Kitipornchai, S., Al-Bermani, F.G.A., "Elasto Plastic Analysis of Box Beam Columns Including Local Buckling Effects", *Journal of Structural Engineering, ASCE*, 1991, Vol. 117, No. 7, pp. 1946-1962.
- [11] Fukumoto, Y., Uenoya, M., Nakamura, M., Kobayashi, Y., "Strength and Ductility of Plate Girder Panels under Cyclic Shear", *Journal of Structural Engineering, JSCE*, 2000, Vol. 46, No. 1, pp. 143-150 (in Japanese).
- [12] Krawinkler, H., Popov, E.P., Bertero, V.V., "Shear Behavior of Steel Frame Joints", *Journal of the Structural Division, ASCE*, 1975, Vol. 101, No. 11, pp. 2317-2336.
- [13] Ghobarah, A., Said, A., "Shear Strengthening of Beam-column Joints", *Engineering Structures*, 2002, Vol. 24, No. 7, pp. 881-888.
- [14] Chen, Z.Y., Ge, H.B., Kasai, A., Usami, T., "Simplified Seismic Design Approach for Steel Portal Frame Piers with Hysteretic Dampers", *Earthquake Engineering & Structural Dynamics*, 2007, Vol. 36, No. 4, pp. 541-562.

- [15] Nakamura, H., "Formulae for Evaluating Shear-bending Buckling Strength of Steel Piers with Circular Cross Section and Applicability of the Numerical Buckling Analysis Method", Proceedings of Nonlinear Numerical Analysis and Seismic Design of Steel Bridge Piers, Japan, 1997, Vol. 1, pp. 37-42 (in Japanese).
- [16] Lee, S.C., "Strength of Plate Girder Web Panels under Pure Shear", Journal of Structural Engineering, ASCE, 1998, Vol. 124, No. 2, pp. 184-194.
- [17] Morishita, N., Mori, H., Maeno, H., Okamoto, T., Nanoka, T., Usami, T., "Seismic Design of Steel Bridge Pier Frames Considering Shear Local Buckling in Beam Member", Proceedings of the 6th Symposium on Ductility Design Method for Bridges, Tokyo, 2003, Vol. 1, pp. 293-298 (in Japanese).
- [18] Susantha, K.A.S., Aoki, T., Kumano, T., "Strength and Ductility Evaluation of Steel Bridge Piers with Linearly Tapered Plates", Journal of Constructional Steel Research, 2006, Vol. 62, No. 9, pp. 906-916.
- [19] Zheng, Y., Usami, T., Ge, H.B., "Ductility of Thin-walled Steel Box Stub-columns", Journal of Structural Engineering, ASCE, 2000, Vol. 126, No. 11, pp. 1304-1311.
- [20] Chusilp, P., Usami, T., "Strength and Ductility of Steel Box Girders under Cyclic Shear", Journal of Structural Engineering, ASCE, 2002, Vol. 128, No. 9, pp. 1130-1138.
- [21] Chusilp, P., Usami, T., "New Elastic Stability Formulas for Multiple-stiffened Shear Panels", Journal of Structural Engineering, ASCE, 2002, Vol. 128, No. 6, pp. 833-836.
- [22] ABAQUS, "ABAQUS/Analysis User's Manual-version 6.6", ABAQUS, Inc.: Pawtucket, RI, 2006.
- [23] Usami, T., Zheng, Y., Ge, H.B., "Seismic Design Method for Thin-walled Steel Frame Structures", Journal of Structural Engineering, ASCE, 2001, Vol. 127, No. 2, pp. 137-144.
- [24] JRA, "Specifications for Highway Bridges, Part V", Japanese Road Association, 1996 (in Japanese).
- [25] Saiidi, M., Sozen, M.A., "Simple Nonlinear Seismic Analysis of R/C Structures", Journal of the Structural Division, ASCE, 1981, Vol. 107, No. 5, pp. 937-953.
- [26] Collins, K.R., Wen, Y.K., Foutch, D.A., "Dual-level Sesmic Design: a Reliability-based Methodology", Earthquake Engineering & Structural Dynamics, 1996, Vol. 25, No. 12, pp. 1433-1467.
- [27] Bracci, J.M., Kunnath, S.K., Reinhorn, A.M., "Seismic Performance and Retrofit Evaluation of Reinforced Concrete Structures", Journal of Structural Engineering, ASCE, 1999, Vol. 123, No. 1, pp. 3-10.
- [28] Zheng, Y., Usami, T., Ge, H.B., "Seismic Response Predictions of Multi-span Steel Bridges through Pshover Aalysis", Earthquake Engineering & Structural Dynamics, 2003, Vol. 32, No. 8, pp. 1259-1274.
- [29] Chusilp, P., Usami, T., Ge, H.B., Maeno, H., Aoki, T., "Cyclic Sear Bhaviour of Seel Bx Grders: Eperiment and Aalysis", Earthquake Engineering & Structural Dynamics, 2002, Vol. 31, No. 11, pp. 1993-2014.
- [30] Gao, S., Usami, T., Ge, H.B., "Ductility Ealuation of Seel Bidge Pers with Ppe Sctions", Journal of Engineering Mechanics, ASCE, 1998, Vol. 124, No. 3, pp. 260-267.

# SLIM BUCKLING-RESTRAINED STEEL PLATE SHEAR WALL AND SIMPLIFIED MODEL

Ye Lu <sup>1,\*</sup> and Guoqiang Li <sup>2</sup>

<sup>1</sup> Doctor, Department of Structural Engineering, School of Civil Engineering  
Tongji University, Shanghai, China

<sup>2</sup> Professor, State Key Laboratory of Disaster Reduction of Civil Engineering  
Tongji University, Shanghai, China

\*(Corresponding author: E-mail: luyet@tongji.edu.cn)

Received: 28 July 2011; Revised: 26 August 2011; Accepted: 22 September 2011

---

**ABSTRACT:** As a promising lateral load resisting elements in new or retrofit construction of buildings, buckling-restrained steel plate shear wall (BRSW) clamed with concrete plates had gained a great deal of attention of researchers and engineers. However, almost all of BRSWs being studied and employed are in small height-to-width ratio. Actually, in some situations, slim BRSW may be more serviceable if there do not have enough space to put wide BRSWs. Moreover, a new type BRSW was proposed in this paper. Several experimental investigations had been conducted on this BRSW, including monotonic loading tests and cyclic loading tests on four sets of specimens with different height-to-width ratio from 2:1 to 4:1, as well as comparative tests on normal steel plate shear walls. The detailing of the walls was modified to improve their energy dissipation. A simplified equivalent cross-brace model was presented and verified by finite element analyses.

**Keywords:** Buckling-Restrained, Steel plate shear wall, Experimental study, Simplification model

---

## 1. INTRODUCTION

Buckling-restrained steel plate shear wall (BRSW) system is one of the most commonly used lateral-load resisting systems in high-rise buildings, consisting of a steel plate shear wall with reinforced concrete wall attached to each side by bolting (Figure 1). Zhao and Astaneh-Asl [2] proposed innovative BRSW system that in traditional system the reinforced concrete wall is in direct contact with the boundary steel columns and beams, as in innovative system, there is a gap in between. Their study showed innovative wall behaved in a more ductile manner than traditional one. Guo [3] presented ellipse hole on concrete slabs to ensure freely relative slide between steel plate and reinforced concrete slabs which can be free from being crashed and prevent the steel plate from buckling. Tsai [4] studied low yielding strength BRSW with height-to-width ratio 0.43. Berman et al. [5], Vian et al. [6], Tsai et al. [7] and Li et al. [8] found the connection of the infill panel to only the beams could reduce the force in columns and avoid damage on columns untimely.

Steel plate shear walls most widely used and studied are in small height-to-width ratio. But in some cases, there will not be enough space for a wide shear wall. Therefore, a slim shear wall (height / width >1) might be employed. Guo et al. [9] tested three BRSWs in size of 1100×1100mm (height / width = 1) with connections to only the beams, which exhibit excellent seismic behavior. More over, many experimental studies (Tsai et al. [7], Guo et al. [9], Gao [10]) showed steel plate and concrete panels at the corner were very easily to be crushed and cracked. Therefore, a new type BRSW called I-type BRSW was presented in this paper, as shown in Figure 2. In this paper, I-type BRSW was in large height-to-width ratio. Monotonic and cyclic loading tests had been conducted to reveal their seismic behaviors. At the end of the paper, simplified model was proposed for structural design.

## 2. EXPERIMENT SCHEME

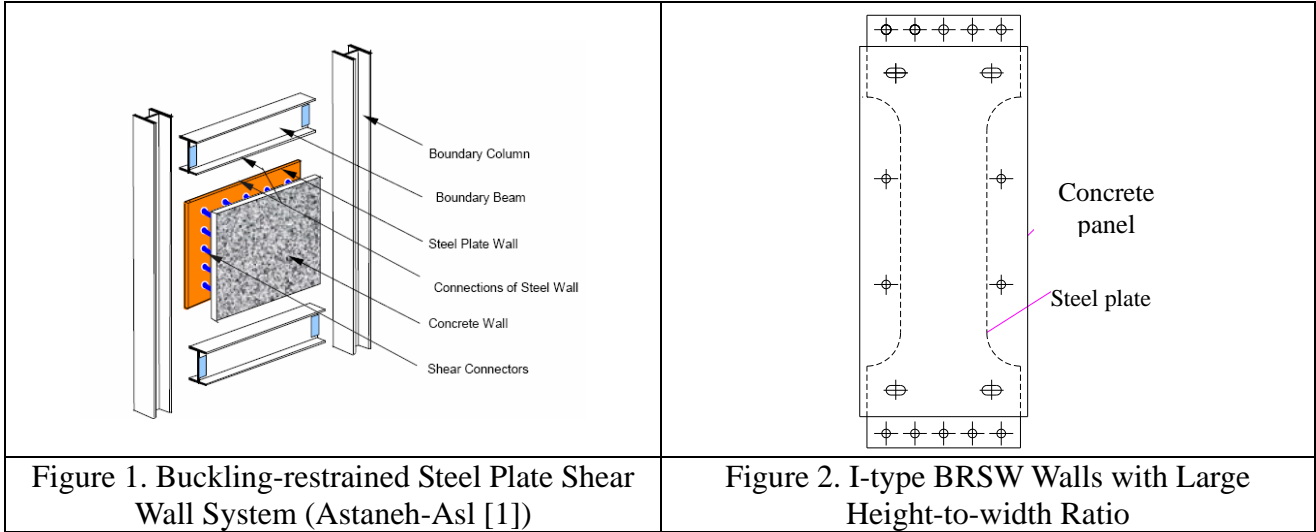


Figure 2 showed the configuration of I-type BRSW. The steel plate had reduced section at the middle in order to improve its energy dissipating performance and protect the root from fragile damage. The steel plate was bolted or welded only to upper and lower beams. The holes on steel plate to fix concrete panels were in ellipse shape to allow free relative displacement between steel plate and concrete panels. To reveal failure mechanics, ductility performance, hysteretic behavior and ultimate load-carrying capacity of this type BRSWs, monotonic and cyclic loading tests on four sets of specimens with different Height-to-Width ratio from 2:1 to 4:1 had been conducted in Structural Lab in Tongji University. For comparison, the tests on a set of normal SPSW specimens were also conducted.

### 2.1 Test Specimens

The specifications of 5 sets of specimens with 1/3-scale are shown in Table 1, and the meanings of the parameters in Table 1 are shown in Figure 3. Each set had two segments for monotonic and cyclic loading tests respectively. Set 1 were traditional SPSWs; Set 2 to Set 5 were BRSWs. To compare the performance of BRSWs and SPSWs, Set 4 had same size with Set 1. Set 2 and Set 3 had same size, but the later had one more column of fixing bolts, which was used to study the influence induced by different distance between restrained bolts.

Table 1. The Specifications of Specimens

	Specimens	Description	Test Type	$H$ (mm)	$B$ (mm)	$b$ (mm)	$h_s$ (mm)	$b_s$ (mm)	$H/B$	$H/b$	$h/b$
Set 1	I-180-1	Compared with Set 4	Mono	810	320	180	135	70	2.5	4.5	3
	I-180-2		Cyclic								
Set 2	IC-280A-1	BRSWs Set 3 have one more column bolts	Mono	810	440	280	125	80	1.85	3	2
	IC-280A-2		Cyclic								
Set 3	IC-280B-1	BRSWs Set 3 have one more column bolts	Mono	810	440	280	125	80	1.85	3	2
	IC-280B-2		Cyclic								
Set 4	IC-180-1	BRSWs Compared with Set 1	Mono	810	320	180	135	70	2.5	4.5	3
	IC-180-2		Cyclic								
Set 5	IC-140-1	BRSWs	Mono	810	300	140	125	80	2.7	5.8	4
	IC-140-2		Cyclic								

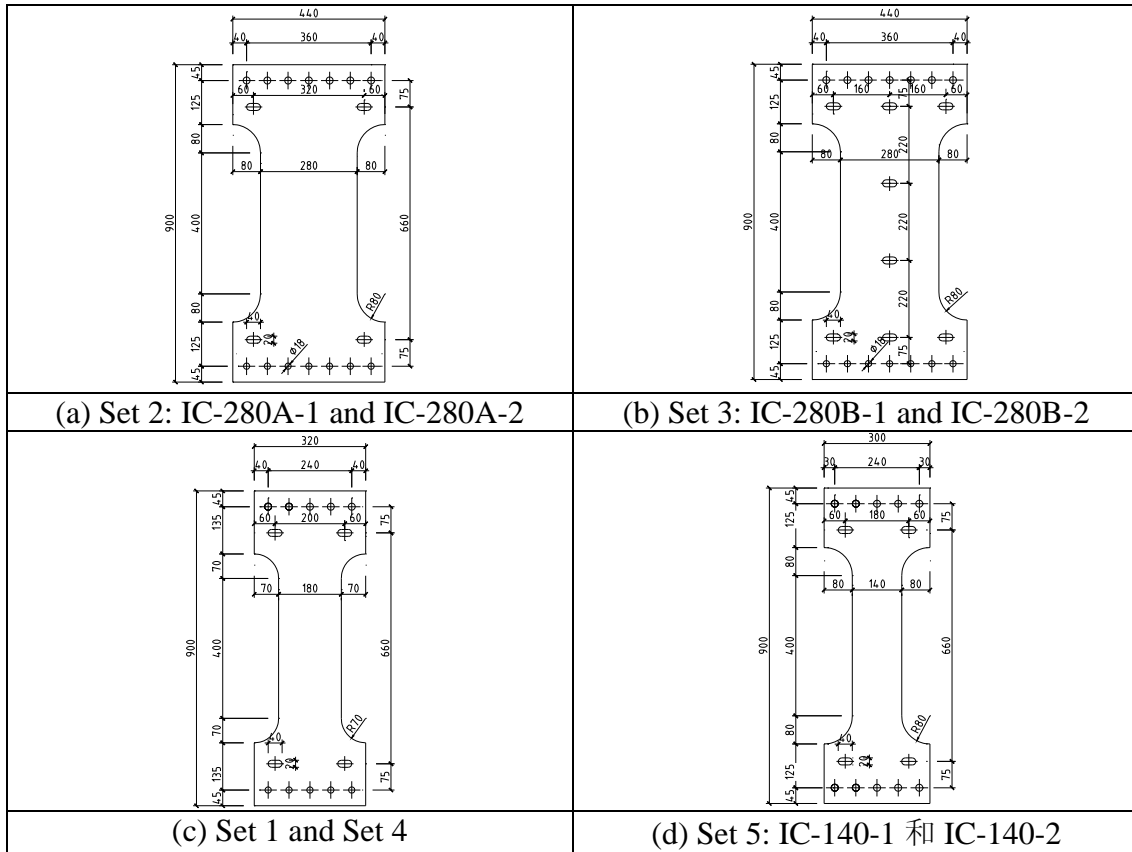


Figure 3. Steel Plate of Specimens

The specimens were made of steel plate with yielding strength of about 300 MPa and thickness of 3.5mm, and two concrete panels with nominal compressive strength  $f_c$  of 28 MPa and thickness of 35mm.

## 2.2 Test Set-up

The diagram of test set-up was shown in Figure 4. The beam and column were H-section with high stiffness to provide rigid boundary. All specimens were tested on the same frame.

Lateral load and following displacements were monitored and recorded during the test (Figure 4): in-place displacement at upper end of the wall by D1 and D2 displacement gauge; slippage of bottom fish plate by D3; displacement at the base of frame by D4; out-plane displacement of frame by D5, D6 and out-plane displacement of steel plate wall by D7~D10. Out-of-plane bracing located at the place of D5 and D6.

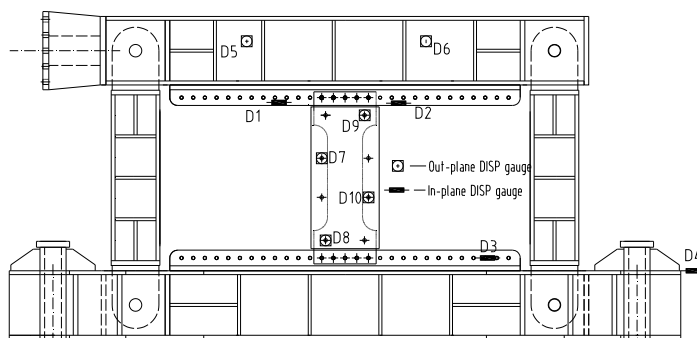


Figure 4. Test Set-up

Lateral force was applied at both end of upper beam by two single-acting jacks with maximum capacity of 20kN. No vertical load applied on wall. Lateral load were applied by deformation control. The maximum displacement of monotonic test was 45mm, which was about 1/20 of the height of the wall. The yielding displacement was the essential parameter for controlling the test. The maximum lateral displacement was 25mm, which was about 1/36 of the height of the wall.

### 3. BEHAVIORS OF SPECIMENS

SPSWs I-180-1 and I-180-2 buckled almost at the very early stage of test (Figure 5a). Out-of-plane deformation increased rapidly while load increased. Buckling deformation reached to 25mm corresponding to horizontal drift of only 10mm; as horizontal drift reached 20mm, out of plane displacement was nearly 35mm.

Owing to buckling restrained by precast concrete panel, out-plane deformation of BRSWs decreased considerably. For example, when lateral displacement reached 25mm, out-plane deformation of IC-280A-1 and IC-280B-1 is only 1mm and 2.5mm. Even when lateral displacements reached 50mm, the maximum out-plane deformation was only 4.019mm and 4.446mm.

Due to free deformation between concrete panels and steel plate, concrete panels had kept in well status during loading without serious cracking and deformation (Figure 6a). No fracture failure and obvious buckling occurred on steel plate (Figure 6). However, the steel plates weren't in such a fine flat like it before test, which showed that steel plate had experienced buckling during test. It was partly due to that the precast concrete panel is too thin and small to assure required flat during manufacture. In addition, fictional mark appeared on steel plate.



(a) Buckling at the beginning of loading



(b) Final out-plane deformation

Figure 5. I-180-1 and I-180-2

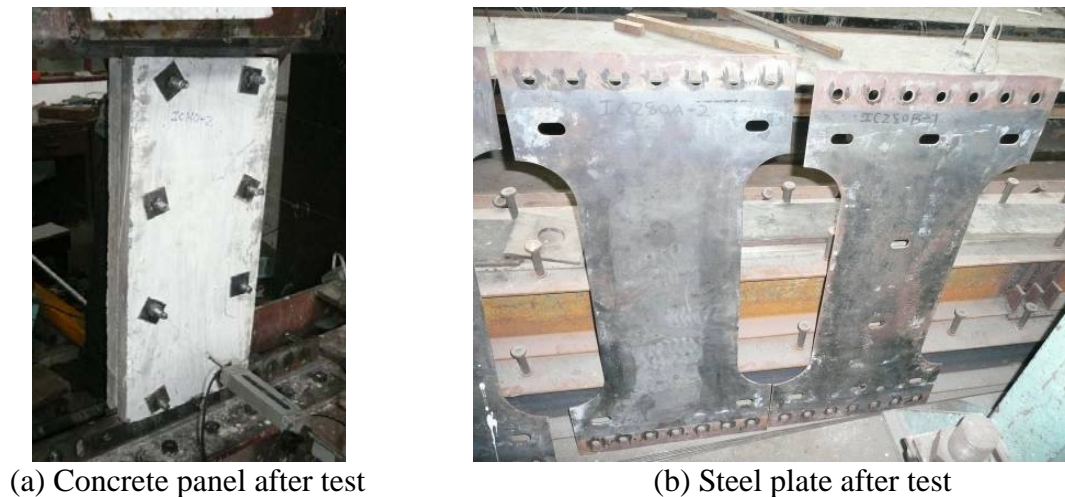


Figure 6. Concrete Panel and Steel Plate after Tested

#### 4. FINITE ELEMENT ANALYSIS

Finite element analysis using ANSYS program had been conducted in order to investigate the load bearing capacity and structural performance of I-type BRSWs. Boundary frame was ignored in order not to confuse with results of the wall. The steel plate was modeled by Shell 181 (Figure 7) which is a 4-nodes element with six degrees of freedom at each node: translations in the x, y, and z directions, and rotations about the x, y, and z axes. It is well-suited for linear, large rotation analysis of thin and moderately-thick shell structures. Two methods were presented to model buckling restrained effect provided by concrete panels.

Method 1: since concrete panels did not contribute strength and stiffness to BRSW system, and they only provided restrained on out-plane deformation of steel plate, no concrete elements were modeled in FE models. The buckling restrained function of concrete panels was simulated by simply defining out-plane deformation of steel plate as 0 (Figure 8).

Method 2: concrete panels were modeled by solid 65 and the nodes on the concrete panels were coupled with inner steel plate in the out-of-plane direction (z direction), at the positions with bolts.

Two methods were used to analyze the specimen IC-180-1 respectively. Comparison of Force-Displacement curves with test results (Figure 9) showed method 1 has better accurateness than method 2. Moreover, it was simpler. Therefore, in FE analysis, method 1 was adopted to simulate the function of concrete panels.

The lateral force acted at the top of plate. The bottom end of steel plate was fixed in 6 degrees of freedom. The up end of steel plate was fixed in 5 degrees of freedom. The X degree was free, but the nodes at up end edge were coupled with the node on which the force acted. The first elastic buckling mode was adopted as the imperfection shape of steel plate. Figure 10 showed stress distribution after yielding of the steel plate.

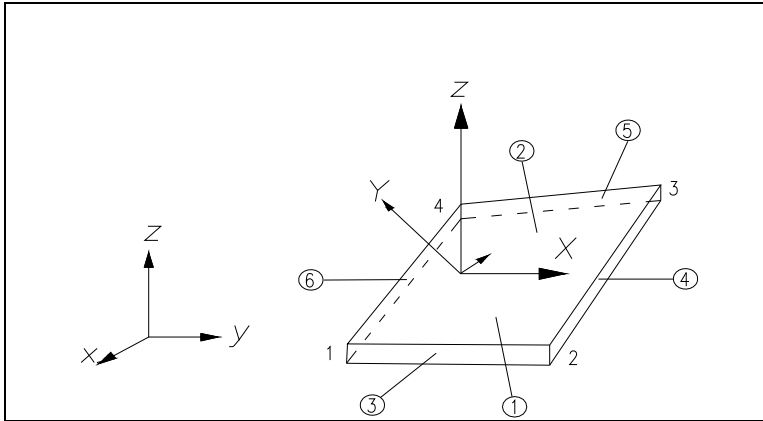


Figure 7. Shell 181 Element

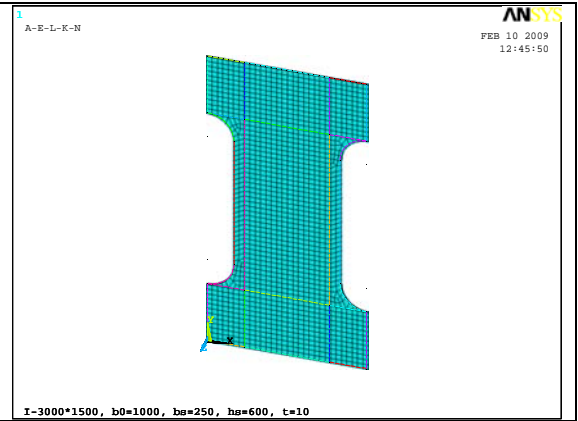


Figure 8. FE Element

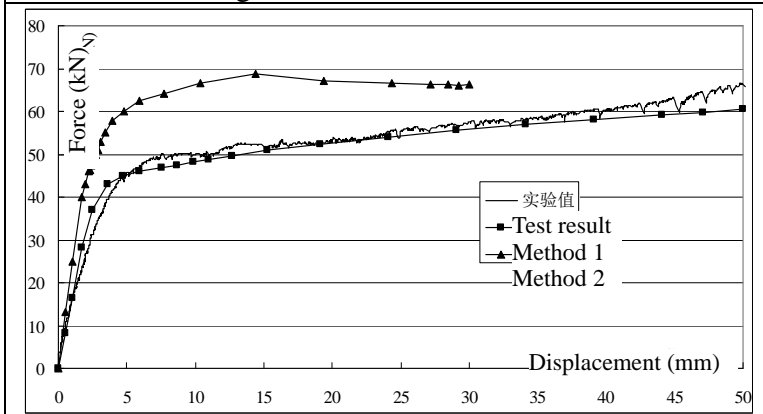


Figure 9. Comparison of Force-Displacement Curves

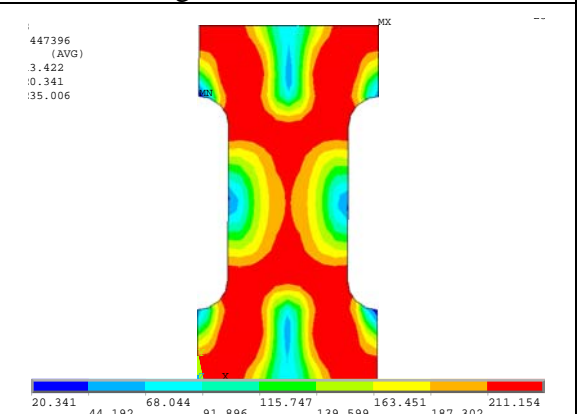


Figure 10. Stress Distribution after Yielding of the Steel Plate

## 5. ANALYSIS ON TEST RESULTS

### 5.1 Monotonic Test

Monotonic curves of all specimens are shown in Figure 7 and Table 2, compared with finite element curves obtained from ANSYS. Results obtained from test and FE analyses were coincident quite well, except of IC-140-1 in plastic range. The reason was that the concrete panels touched fish plate and increased loading capacity.

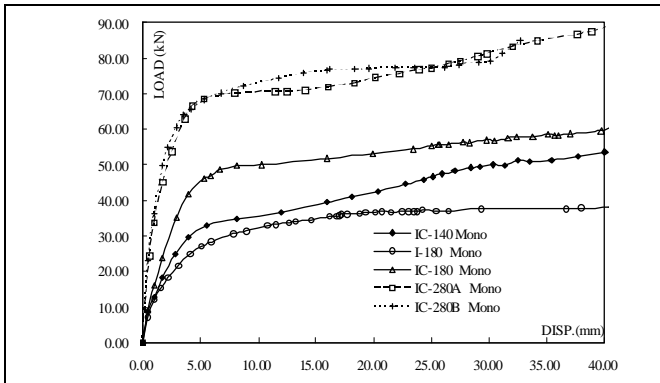


Figure 7. Monotonic Curves of All Specimens

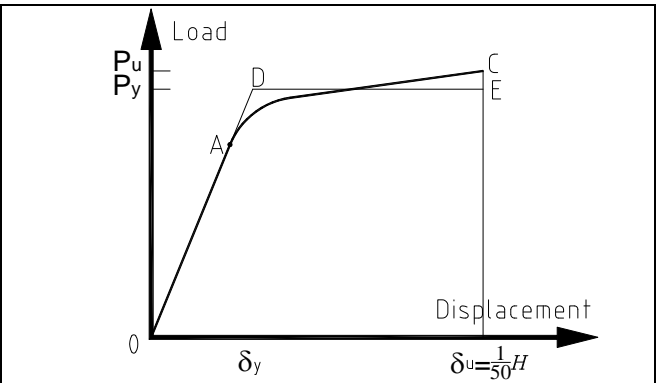


Figure 8. Determination of Yielding Point

Yielding points were determined by Energy-Equal Protocol as shown in Figure 8. Ultimate displacement  $\delta_u$  was defined as 1/50 of wall height, i.e. 16.2mm. Ultimate loading point C was determined by  $\delta_u$ . Prolong initial elastic curve OA to point D. Horizontal line DE crossed line  $C\delta_u$  at Point E. According to Energy-Equal Protocol, the area enclosed by OAC and X-axis should be equal to that enclosed by ODE and X-axis. Therefore, Point D can be determined, and it indicated nominal yielding strength  $P_y$  and yielding displacement  $\delta_y$ . Ductility coefficient  $\mu$  was the ratio between  $\delta_u$  and  $\delta_y$ .

Table 2. Parameters Comparison of Specimens

		Initial stiffness (kN/mm)	Nominal yielding point $P_y$ (kN)	Yielding displacement $\delta_y$ (mm)	Ultimate strength $P_u$ (kN)	Ductility coefficient
Set 1 I-180	FE analysis	11.06	29.92	2.71	32.94	5.98
	Test result	14.24	29.69	2.08	35.68	7.79
Set 2 IC-280A	FE analysis	32.80	72.85	2.22	78.39	7.30
	Test result	40.8	66.91	1.64	72.09	9.88
Set 3 IC-280B	FE analysis	32.80	72.85	2.22	78.39	7.30
	Test result	32.45	70.88	1.51	76.58	10.73
Set 4 IC-180	FE analysis	15.50	49.09	3.17	52.33	5.11
	Test result	20.80	46.61	2.24	51.92	7.23
Set 5 IC-140	FE analysis	10.77	27.94	2.59	30.56	6.25
	Test result	16.67	33.24	1.99	39.34	8.14

Compared Set 1 and Set 4, ultimate strength, yielding point and initial stiffness of the later increased obviously due to buckling restrained contributed by concrete panel.

The distance between restrained bolts would affect restrained effect from concrete panel, which can not be derived from FE analysis accurately. Compared Set 2 and Set 3, in plastic range, the curve of IC-280A-1 descended a little bit, which demonstrated slight buckling on steel plate. However, the buckling didn't develop too much. Yielding strength and ultimate strength of IC-280B-1 is greater than IC-280A-1, but not too much. Generally, the load versus displacement curves of specimens was similar to FE results.

Owing to the contribution of concrete panel, initial stiffness and ultimate strength obtained by test were higher than FE analysis.

## 5.2 Cyclic Loading Test

Cyclic loading curves are shown in Figure 9 and in well symmetric. The hysteresis curve of I-180-2 pinched seriously due to buckling (Figure 9a), which reflected bad energy dissipating performance. Compared with SPSW, the hysteresis curves of BRSWs were fairly wide (Figure 9 b, c, d), indicating good energy dissipating. However, after lateral displacement reached to 10mm, the curve of IC280-2 and IC180-2 appeared long yielding platform. Slight buckling of steel plate might be one of possible reasons. Meanwhile, during the course of test, the slippage of bolting connection of steel plate and beam, which exerted obvious sound, could reduce load bearing capacity. However, BRSWs still displayed good energy dissipating performance. In Figure 9c, IC280B-2 which had one more column of bolts showed higher load bearing capacity than IC280A-2, but the difference wasn't so much great.

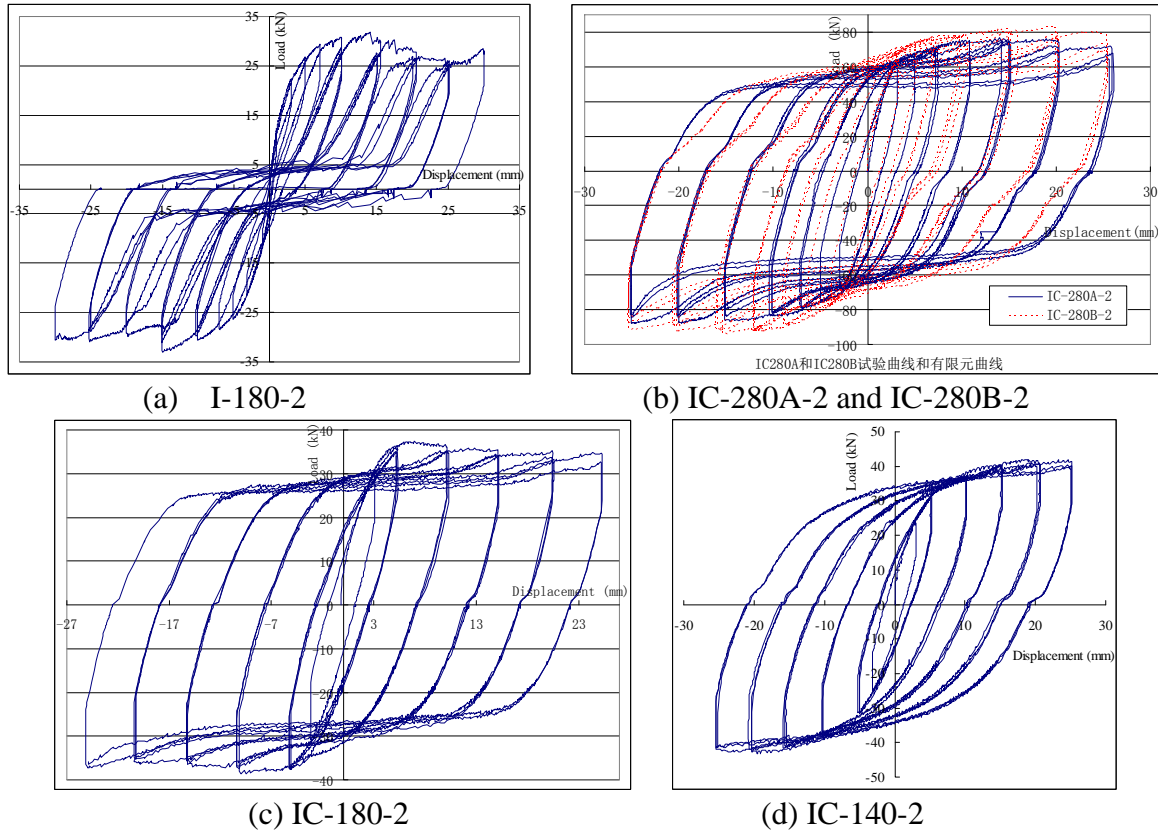


Figure 9. Cyclic Curves of All Specimens

In Figure 9d, the hysteresis curve of IC-140-2 was quite wide and there was no pinch and no yielding platform.

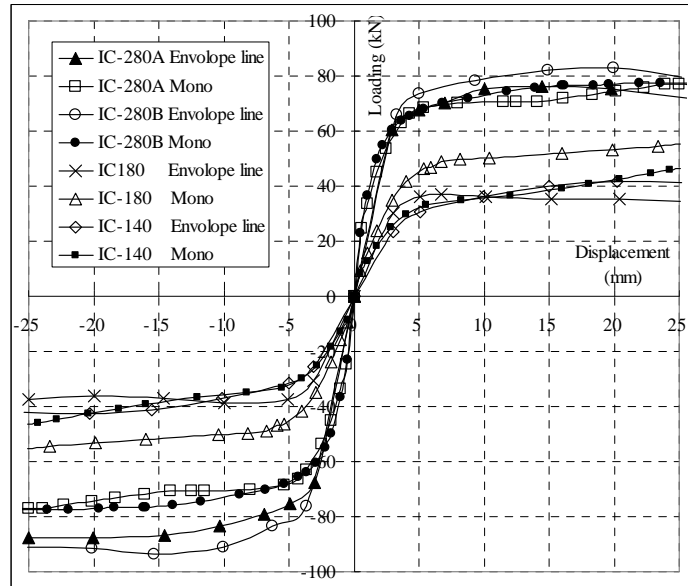


Figure 10. Comparison of Envelope Lines of Cyclic Loading and Monotonic Test Curves

Figure 10 showed comparison of envelope lines of cyclic loading and monotonic test curves respectively. All of the walls had stable load bearing capacity without abrupt increasing or decreasing. Except of IC180, envelope lines of cyclic test were quite close to that of monotonic test. Load bearing capacity in cyclic test of IC-180-2 was much less than that in monotonic test and even approached to the curves of IC140. Two reasons could explain this: 1) buckling

occurred in the test of IC-180-2 due to rough surface of concrete panel; 2) IC-180-2 was the last one to be tested, and the fish plate became very slippery because of friction by former tests. The slippage of base bolt was very serious, which decrease the load bearing capacity.

## 6. SIMPLIFIED MODEL

For convenience in engineer's application, some simplified models of steel plate shear walls were proposed before. Most of them were strip models, which were reasonable for the infill panel connected both to beams and columns, or a wide wall. For slim and two sides connecting I-type BRSWs studied in this paper, strip models were not appropriate.

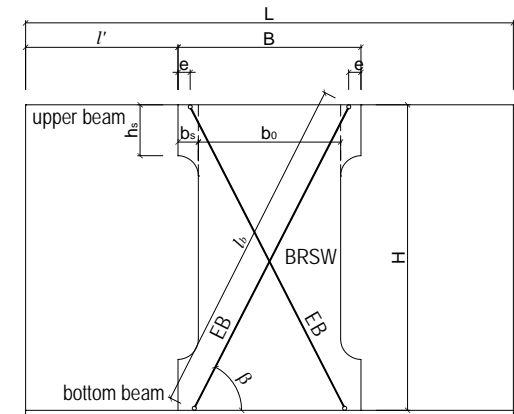
Zhang [11] adopted equivalent braces to represent the slit RC shear wall based on an equivalent lateral stiffness. Numerical results indicated that equivalent braces could be effectively utilized for the global static analyses of frame structures. Wang [12] applied equivalent eccentric cross braces model to simulate steel plate shear wall with vertical slits and received similar force and deformation of the structures.

Therefore, this paper adopted equivalent eccentric cross braces to simulate slim I-type BRSW. The principle was shown in Figure 11a. Since the steel plate was buckling restrained, it could bear pressure. Therefore, the simplified braces could bear tension and pressure. After critical parameters, such as cross sectional area, load bearing capacity of equivalent cross braces, as well as the eccentric distance  $e$  of the braces from the edge of BRSWs, were determined, engineers can build up design models in normal structural design software and get the internal forces of frame members.

Cross sectional area of brace can be determined by initial stiffness of BRSWs according to stiffness equivalent principle. According to Figure 11b, as lateral force  $F$  acting on the frame, the lateral drift  $\Delta_w$  will be:

$$\Delta_w = \frac{\Delta_b}{\cos \beta} = \frac{Fl_b}{2EA_b \cos^2 \beta} \quad (1)$$

Where  $A_b$  = the cross sectional area of brace;  $E$  = elasticity modulus;  $\Delta_b$ ,  $\beta$ ,  $l_b$ , are shown in Figure 11b.



(a) Principle of Equivalent Eccentric Cross Braces Model

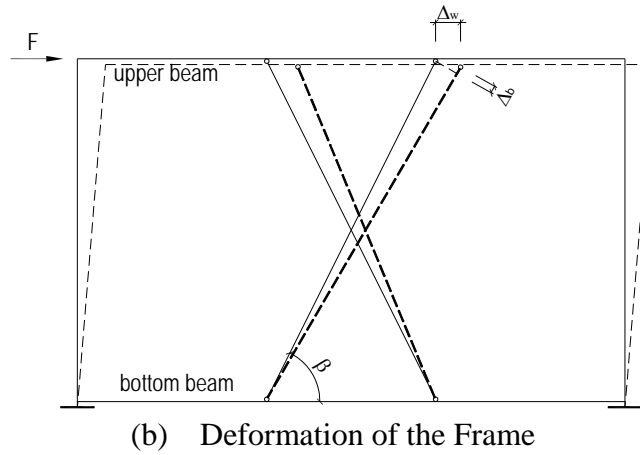


Figure 11. Equivalent Eccentric Cross Braces Model

With the stiffness equivalent principle, we have  $F=K \times \Delta_w$

Therefore, the cross sectional area of brace  $A_b$  should be:

$$A_b = \frac{Kl_b}{2E \cos^2 \beta} \tag{2}$$

Where  $K$ = initial stiffness of BRSWs.  $K$  could be determined by finite element analyses, or according to Lu. Y. [13], for I-type BRSWs, initial stiffness of BRSWs  $K$  could be derived by following formula:

$$K = \frac{1}{\Delta} = \frac{1}{\zeta + \delta} = \frac{G \times t \times b'_0}{H} + 12 \frac{EI}{H^3} = \frac{Et}{2.6 \frac{H}{\beta b_0} + (\frac{H}{\beta b_0})^3} \tag{3}$$

Where  $G$  = shear modulus of the steel plate,  $G=E/2(1+\nu)=\frac{E}{2.6}$ ;  $\nu$  = poison ratio of the steel plate;  $H, t$  = respectively, the height, thickness of the steel plate;  $I$  = inertia moment of the cross section of the steel plate.

$\beta$  was a parameter which has a relationship with the enlarged area of the end. According to large quantities analyses,  $\beta$  can be written in:

$$\beta = \frac{A + A_s}{0.95A} = 1.053 + \frac{4(h_s + b_s)b_s - \pi b_s^2}{Hb_0} \tag{4}$$

Where,  $A = H \times b_0$ ;  $A_s = 4 \times (h_s + b_s) \times b_s - \pi b_s^2$ , the enlarged area at the end of plate;  $h_s, b_s$ = enlarged dimension of the end, seen Figure 12b.

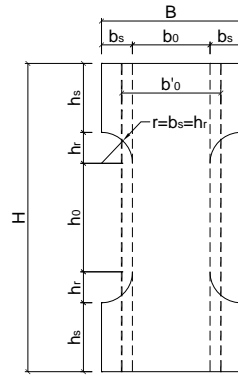


Figure 12. Revising of the Width for I-type Walls

To find the eccentric distance  $e$ , massive finite element analyses of BRSWs with various sizes had been conducted. The influences on  $e$  under different parameters had been studied, including width  $B$ , clear width  $b_0$ , height  $H$ , enlarged size  $b_s$  and  $h_s$ , distance to column  $l'$ , which indicated the location of the BRSW in the frame, as well as different connections of beams and columns, i.e. moment or simple connection. Numerical analysis showed the eccentric distance  $e$  only has relation with width  $B$  and  $l'$ . Therefore, empirical formula was supposed as:

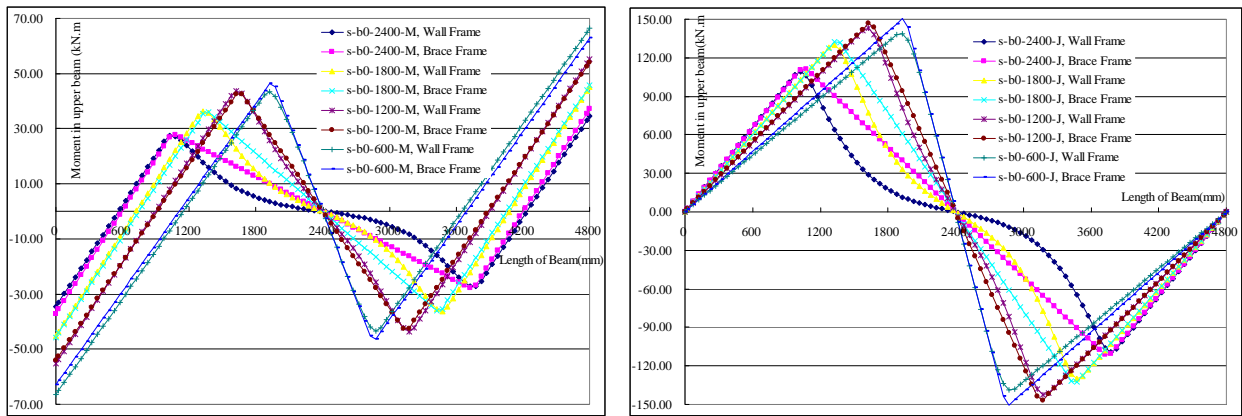
$$\begin{cases} e = 50\text{mm}, (l' \geq 700\text{mm}) \\ e = (2.93 \times 10^{-4} \times B - 0.1969)l' + 0.015B + 25, (l' > 700\text{mm}) \end{cases} \quad (5)$$

Table 3 showed the comparison of frame drift and maximum moment in beams between BRSWs and EB frames. The BRSWs located at the middle of frame. The beam section is H150×250×10×16, and the column section is H250×250×16×16. Length of beam  $L=4800\text{mm}$ , height of column and BRSWs  $H=3000\text{mm}$ , thickness of BRSWs = 10mm,  $h_s=600\text{mm}$ ,  $b_s=200\text{mm}$ . The clear width of wall  $b_0$  was various, and two kinds of connections of column to beam were considered, one was moment connection and the other was simple connection. Figure 13 demonstrated the distribution of moment in upper beam between original and simplified frames. Results showed the maximum moment in frames and frame drifts were very similar, both for two kinds of frames. However, as the height-to-width ratio of BRSWs decreased (the wall became wider), the moment curve displayed depressing phenomenon in the range of walls, which was due to that wide BRSWs could bear shear force with the beam. Although equivalent cross braces could not simulate this phenomenon, structural design are usually determined by maximum value of forces in structural members that the simplified model could have enough accurateness. Table 3 also showed  $b_0$  had no influence on the value of eccentric distance  $e$ . Additionally, analyses also showed the maximum value of moments in the beams of simple connection frames were larger than that in moment frames. However, if the walls were put continuously vertically, the moments in a beam caused by upper and lower BRSWs could counteract to each other. Only the top and bottom beams need special attention.

Table 3. Comparison of Drift and Moment between BRSWs and EB Frame

Frame	Connection of column to beam	$b_0$ (mm)	BRSWs frame		$e$ (mm)	EB frame		Error on moment	Error on drift
			Maximum moment in beams (kN·m)	Drift (mm)		Maximum moment in beams (kN·m)	Drift (mm)		
S-b0-600-M	moment	600	43.54	8.15	50	46.46	7.48	6.71	-8.22
S-b0-1200-M	moment	1200	43.83	5.48	50	42.5	5.41	-3.03	-1.28
S-b0-1800-M	moment	1800	36.38	3.74	50	35.95	3.83	-1.18	2.41

Frame	Connection of column to beam	$b_0$ (mm)	BRSWs frame		$e$ (mm)	EB frame		Error on moment	Error on drift
			Maximum moment in beams (kN·m)	Drift (mm)		Maximum moment in beams (kN·m)	Drift (mm)		
S-b0-2400-M	moment	2400	27.00	2.39	50	27.81	2.56	3.00	7.11
S-b0-600-J	simple	600	138.78	31.91	50	150.40	28.79	8.37	-9.78
S-b0-1200-J	simple	1200	143.05	21.72	50	146.63	21.34	2.50	-1.75
S-b0-1800-J	simple	1800	129.87	14.95	50	132.32	15.47	1.89	3.48
S-b0-2400-J	simple	2400	109.31	9.32	50	111.33	10.47	1.85	12.34



(a) Moment comparison in moment frames      (b) Moment comparison in simple connection frames

Figure 13. Comparison of Moment in Upper Beam between Frames with BRSWs and EB

## 7. CONCLUSION

The following concluding remarks may be drawn through this research:

- 1) Compared with normal steel plate shear walls, BRSW walls have stable and wide hysteresis curve, exhibiting good plastic deformation ability, and energy dissipating performance;
- 2) The growing circle bore to fix concrete panel could allow free deformation of steel plate during the course of loading and keep the concrete panel in sound condition. Therefore the concrete wall can have good performance as buckling restrained panel.
- 3) Bolting connector at the base of steel plate wall with beam is apt to slip, which could decrease load bearing capacity;
- 4) BRSW walls exhibited good mechanics performance, and no fracture failure occurred at the end of steel plate;
- 5) Simplified cross brace model were very convenient and had acceptable accurateness for the structural design of frame with BRSWs.

## ACKNOWLEDGEMENT

This paper is funded by the National Science Supported Plan (2012BAJ13B02).

## REFERENCES

- [1] Astaneh-Asl, A., "Seismic Behavior and Design of Composite Steel Plate Shear Walls", Steel TIPS Report, Structural Steel Educational Council, Moraga, Calif, 2002.
- [2] Zhao, Q.H. and Astaneh-Asl, A., "Cyclic Behavior of Traditional and Innovative Composite Shear Walls", *Journal of Structural Engineering*, ASCE, 2004, Vol. 130, No.2, pp. 271-285.
- [3] Guo, Y.L. and Dong Q.L., "Static Behavior of Buckling-Restrained Steel Plate Shear Walls", *Tall Buildings from Engineering to Sustainability*, ED: Cheung Y.K., Chau K.W., 2005, pp. 666-670.
- [4] Tsai, K.C., Lin, Y.C. and Lin, C.H., "Seismic Responses and Design of Steel Plate Shear Wall", *Proceedings of The Fourth Cross Strait & Hong Kong Conference on Steel Structures*, Shanghai, China, 2006, pp. 108-116. (in Chinese)
- [5] Berman, J. and Bruneau, M. "Plastic Analyses and Design of the Steel Plate Shear Walls", *Journal of Structural Engineering*, 2003, Vol. 129, No.11, pp. 1448-1456.
- [6] Vian, D. and Bruneau, M. "Steel Plate Shear Walls for Seismic Design and Retrofit of Building Structure", Technical Report MCEER-05-0010, Multidisciplinary Center for Earthquake Engineering Research, Buffalo, New York, 2005.
- [7] Tsai, K.C., Lin, C.H., Lin, Y.C., Hsieh, W.D and Qu, B. "Sub-structural Hybrid Tests of A Full Scale 2-story Steel Plate Shear Wall", Technical Report NCREE-06-017, National Center for Research on Earthquake Engineering, Taipei, Taiwan, 2006.
- [8] Li, C.H., Tsai, K.C. and Lin, C.H., "Cyclic Tests of Four Two-story Narrow Steel Plate Shear Walls", *The Proceedings of the 5th International Symposium on Steel Structures*, March 12-14, Seoul, Korea, 2009, pp. 237-245.
- [9] Guo, L.H., Ma, X.B., Zhang, S.M. and Guan N., "Experimental and Theoretical Analyses of Composite Shear Walls with Two-Side Connections", *The Proceedings of the 5th International Symposium on Steel Structures*, March 12-14, Seoul, Korea, 2009, pp. 710-716.
- [10] Gao, H., "Experimental and Theoretical Studies on Composite Steel Plate Shear Walls" (in Chinese), Dissertation submitted to Tongji University in Conformity with the Requirements for the Degree of Master, 2007.
- [11] Zhang, Y.C., Liu, Y.H., etc., "A Simplified Model for Static Analyses of Slit RC Shear Walls", *China Civil Engineering Journal*, 2006, Vol. 39, No. 9, pp. 62-68.
- [12] Wang, W.T., "Experimental and Theoretical Study on Buckling Restrained Steel Plate Shear Wall with Slits", Dissertation submitted to Tongji University in Conformity with the Requirements for the Degree of Master, 2008.
- [13] Lu, Y., "Research on the Steel Frame of Bound-Column System with Buckling Restrained Steel Plate Shear Wall in Large Aspect Ratio", Dissertation submitted to Tongji University in Conformity with the Requirements for the Degree of PHD, 2009.

# RANDOM EQUIVALENT INITIAL BOW AND TILT IN STEEL FRAME

A. Machowski<sup>1</sup> and I. Tylek<sup>2,\*</sup>

<sup>1</sup>Assoc. Prof. D. Sc. Ph. D., Faculty of Civil Engineering,  
Cracow University of Technology, ul. Warszawska 24, 31-155 Cracow, Poland,

<sup>2</sup>Assist. Prof. Ph. D., Faculty of Civil Engineering,  
Cracow University of Technology, ul. Warszawska 24, 31-155 Cracow, Poland

\*(Corresponding author: E-mail: ik2@poczta.fm)

Received: 3 September 2011; Revised: 26 September 2011; Accepted: 30 September 2011

---

**ABSTRACT:** Probabilistic models of equivalent geometrical imperfections suitable to analysis of steel buildings frames are under consideration. Statistically based models of equivalent imperfections, besides of application in structural reliability analysis, should be taken as basis of verification of equivalent imperfection formulas and rules of introducing imperfections into frame calculations proposed in different Standards. Column random equivalent initial bow was obtained in this paper utilizing randomization of buckling coefficient in well-known deterministic formula of equivalent initial bow. Problem of random equivalent initial tilt of frame was considered for spatial mechanical model of skeletal structure, braced by rigid floor disks, using results of existing buildings geodesic measurements statistical analysis. In the paper assessment of random initial tilts and initial bows joint effect is commented.

**Keywords:** Multistory steel frame, Random equivalent geometrical imperfection, Eurocode 3

---

## 1. INTRODUCTION

Carrying capacity of steel frames significantly depends on imperfections (Table 1(a)): single column; residual stresses and axes misalignments as well as bar system imperfections; column out-of-plumbs, eccentricity in column field joints, assembly stresses, random joint rigidity.

In traditional approach (Chen and Toma [1], Narayanan [2]) imperfections are modeled by linear combination of buckling modes (simplifying – only dominant buckling mode) which correspond to solution of bifurcation problem using linearized model of perfect system elastic stability. In this approach real structure imperfections are taking into consideration only indirectly – by using standard buckling curves. Column out-of-plumbs and other important imperfections, arising during assembly, are passed over in traditional approach.

Contemporary standard approach depends on taking into account of two equivalent geometrical imperfections (Table 1(b)): equivalent initial column bow  $e_0$  (column misalignment and column residual stresses) and equivalent initial frame tilt  $\phi_0$  (column out-of-plumbs, eccentricity in column field joints, assembly stresses, randomness of beam-column joints rigidity).

Standard approach approximately takes into consideration steel skeleton fabrication conditions, in particular (Figure 1): columns division on assembly parts and its assembly with random out-of-plumbs – causing significant changes of moment values in equilibrium equations – because of large vertical forces occurrence.

Table 1. Conceptions of Equivalent Geometric Imperfections

(a) Imperfections of compressed bar and frame				
compressed bar		frame		
residual stresses	misalignment	column out-of-plumb	joints eccentricity	joints stiffness randomness
(b) Equivalent geometric imperfections				
compressed bar		frame		

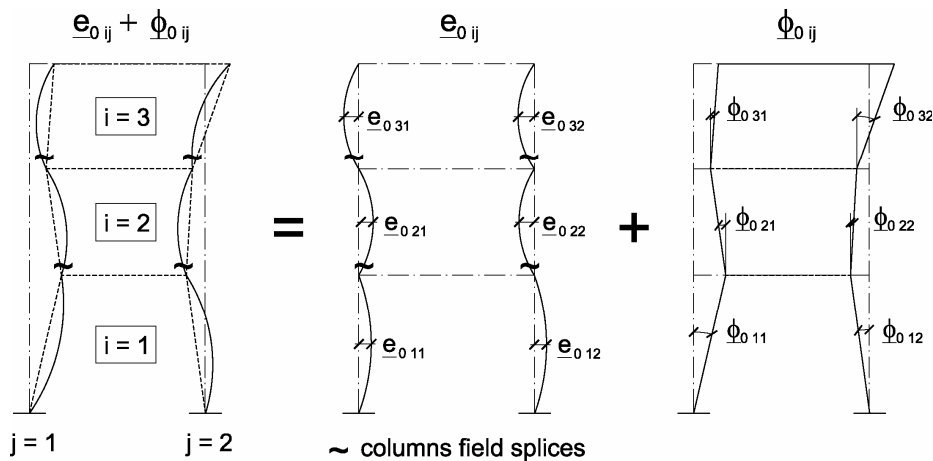


Figure 1. Columns Random Initial Bows and Initial Tilts

Issues connected with research and modeling of equivalent geometrical imperfections  $e_0$  and  $\phi_0$  are discussed in chapters 2 to 4 of this paper.

## 2. RANDOM EQUIVALENT INITIAL BOW OF COLUMN

Random equivalent initial bow of column is obtained as function of random buckling coefficient  $\underline{\varphi}$  (random values are underlined).

Random buckling coefficient was determined in papers (Machowski, A. [3]) utilizing Fukumoto and Itoh statistical data (Fukumoto, Y. and Itoh, Y. [4]) and applying randomization of axially compressed steel bar flexural buckling resistance standard formula

$$\underline{N}_{b,R} = \underline{\varphi} \cdot \underline{N}_{pl} \tag{1}$$

It was assumed that random flexural buckling resistance of compressed steel bar  $\underline{N}_{b,R}$  and bar cross-section random plastic resistance  $\underline{N}_{pl}$  have logarithmic-normal distribution<sup>(\*)</sup> – stable (invariant) with respect to multiplication and defined only for positive values of  $\underline{N}_{b,R}$  and  $\underline{N}_{pl}$ .

It follows that stochastically independent (originally) from  $\underline{N}_{pl}$  buckling coefficient  $\underline{\varphi}$  has also logarithmic-normal distribution. Flexural buckling resistance  $\underline{N}_{b,R}$  has median equal to product of medians  $\check{N}_{b,R} = \check{\varphi} \cdot \check{N}_{pl}$  and logarithmic coefficient of variation equal to vector sum of logarithmic coefficients of variation  $v_{N_{b,R}} = \sqrt{v_{\varphi}^2 + v_{N_{pl}}^2}$ .

Appropriate sets of data have been statistically processed with a mean-square approximation of experimental values of medians  $\check{\varphi}(\Lambda)$  and logarithmic coefficients of variation  $\check{v}_{\varphi}(\Lambda)$ , where

$\Lambda = \sqrt{\check{N}_{pl} / \check{N}_E}$  - relative slenderness ( $\check{N}_E$  - median of bar Euler's resistance) and application of formulas:

$$\check{\varphi}(\Lambda) = (1 + \Lambda^{2n})^{-\frac{1}{n}}, \quad \check{v}_{\varphi}(\Lambda) = v_m \cdot \left( \frac{2 \cdot l \cdot \Lambda}{1 + (l \cdot \Lambda)^2} \right)^2 \tag{2}$$

Empirical parameters (Machowski, A. [3]):  $n$ ,  $v_m$ , and  $l$  for buckling curves: “a”, “b” and “c” (CEN [5], PKNMiJ [6]) are presented in Table 2.

Table 2. Empirical parameters for formula (2)

	Buckling curve		
	a	b	c
$n$	3,0	2,6	2,2
$v_m$	0,10	0,11	0,13
$l$	0,8	0,9	1,0

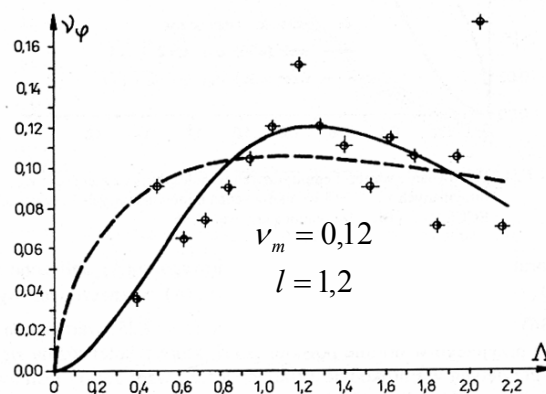


Figure 2. The Example of Values  $v_{\varphi}(\Lambda)$  Approximation for  $N = 1251$  Column Research Council Test Results (Machowski [3])

<sup>(\*)</sup> parameters of logarithmic-normal variable  $X > 0$  with probability density function  $f(x) = \frac{1}{\sqrt{2\pi} \cdot v_X \cdot X} \cdot \exp(-\ln^2(X/\check{X})/(2 \cdot v_X^2))$ ; mean value  $\check{X} = E\{X\}$  and coefficient of variation  $v_X$  are related as follows:  $\check{X} = \bar{X} / \sqrt{1 + v_X^2}$ ,  $v_X = \sqrt{\ln(1 + v_X^2)}$ .

An example of experimental coefficients of variation approximation by means of function  $\nu_\varphi(\Lambda)$  according to Eq. 2 is shown in Figure 2; single points represent empirical mean values of  $\nu_\varphi^*(\Lambda)$  connected with individual slenderness  $\Lambda$ . Form of function (2) refers to earlier proposals connected with stability coefficients (PKNMiJ [6], Allen [7], Rondal and Maquoi [8]).

For logarithmic-normal distribution parameters:  $\check{\varphi}$ ,  $\nu_\varphi$  and design value  $\varphi_d$  of buckling coefficient  $\varphi$  are related as follows

$$\begin{aligned} \varphi_d &\stackrel{df}{=} N_{b,Rd} / N_{pl,d} = \check{N}_{b,R} \cdot \exp(-\beta_R \cdot \sqrt{\nu_\varphi^2 + \nu_R^2}) / (\check{N}_{pl} \cdot \exp(-\beta_R \cdot \nu_R)) = \\ &= \check{\varphi} \cdot \exp(\beta_R \cdot (\nu_R - \sqrt{\nu_\varphi^2 + \nu_R^2})). \end{aligned} \quad (3)$$

Introducing into Eq. 3 values according formula (2) and Table 2,  $\nu_R = 0,10$  (according to (Murzewski [9])) for random plastic resistance of steel  $\underline{R} \equiv \underline{f}$  ( $\underline{R} = \underline{N}_{pl} / \underline{A}$ ) corrected for random deviation of bar cross-section area  $A$  and partial reliability index  $\beta_R = 3,0$  relationship  $\varphi_d(\Lambda)$  was received. This relationship was compared (for buckling curve "b") in Figure 3 with other curves characterizing buckling coefficient.

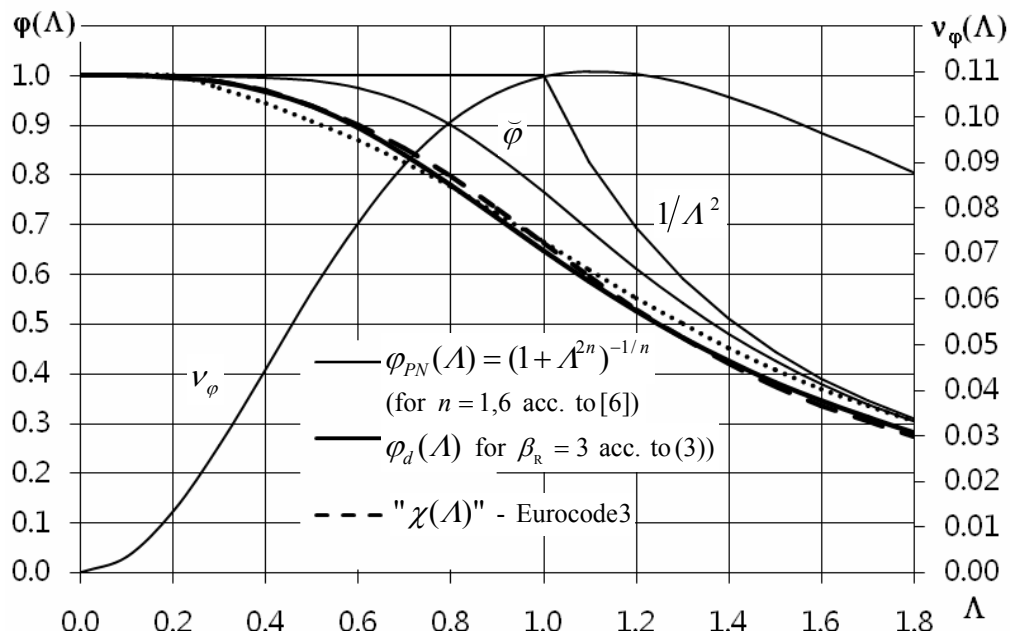


Figure 3. Parameters  $\check{\varphi}$  and  $\nu_\varphi$  and Different Relationships  $\varphi_d(\Lambda)$  for Buckling Curve "b"

Design values of  $\varphi_d$  obtained from Eq. 3 for  $\beta_R = 3,0$  and parameters according to Table 2 are very close to standard values of  $\varphi_{PN}(\Lambda)$  from Polish Standard [6] and values of  $\chi(\Lambda)$  from Eurocode [5] (it was shown in Figure 3 – for buckling curve "b") if following relationship will be used

$$\Lambda = 1,1178 \cdot \bar{\lambda} \cong 1,12 \cdot \bar{\lambda}. \quad (4)$$

Relationship (4) may be obtained by assuming in general formula for relative slenderness

$$\lambda_r \stackrel{df}{=} \sqrt{N_{pl} / N_E} \cong \lambda / (\pi \cdot \sqrt{E / R_{pl}}) = \lambda / \lambda_1, \quad (5)$$

medians:  $E = \bar{E} = 205$  GPa and  $R_{pl} = \bar{f} = 290$  MPa (hence  $\lambda_1^{PN} = 84$ ) – as it was made in Polish Standard [6] for low-carbon steel or values:  $E = 210$  GPa and  $R_{pl} = f_y = 235$  MPa (hence  $\lambda_1^{EC} = 93,9$ ) – according to Eurocode [5].

To determinate column random equivalent initial bow we use well-known formula of dimensionless equivalent initial deflection  $\varepsilon_0$  (Rondal And Maquoi [8], ECCS [10]) of hinged bar with sinusoidal initial bow (the formula is based on bar resistance conservation criterion)

$$\varepsilon_{0e} = e_{0e} / r = (\varphi^{-1} - 1) \cdot (1 - \varphi \cdot \Lambda^2) = \varphi^{-1} + \varphi \cdot \Lambda^2 - (1 + \Lambda^2), \quad (6)$$

where:  $e_{0e}$  - bar equivalent initial bow,

$r \equiv W / A$  - radius of cross-section core.

Random imperfection  $\varepsilon_{0e} = e_{0e} / r$  is obtained utilizing randomization of Eq. 6 by introducing in place of  $\varphi$  random bucking coefficient  $\underline{\varphi}$  with logarithmic-normal distribution and parameters according to formulas (2) and Table 2. It follows that we have to determinate  $\varepsilon_{0e}$  probability distribution as a known deterministic function  $\varepsilon_{0e}(\underline{\varphi})$  of the known random variable  $\underline{\varphi}$ .

According to mechanical interpretation and property of logarithmic-normal distribution quantity  $\varepsilon_{0e} = e_{0e} / r$ , similarly as other quantities in Eq. 6, are treated as non-negative (or positive) what follows that function  $\varepsilon_{0e}(\varphi)$  is determined for  $\varphi \in (0, \min(1, 1/\Lambda^2)]$ . In this range of  $\varphi$  values function  $\varepsilon_{0e}(\varphi)$  is monotonically decreasing (Figure 4(a)) and probability density function  $g(\varepsilon_{0e})$  amounts to transformation type (Papoulis [11]):

$$g(y) = f(u^{-1}(y)) \cdot \left| \frac{du^{-1}(y)}{dy} \right| \quad (7)$$

where:  $f(x)$  - known probability density function of random variable  $\underline{x}$ ,

$u^{-1}(y_x)$  - inverse function of given function  $y = u(x)$  - strictly monotonic,

$g(y)$  - inquired probability density function of random variable  $\underline{y} = u(\underline{x})$ .

Logarithmic-normal distribution, rational in case of coefficient  $\varphi$  (definite for  $\varphi > 0$  and stable in relation to multiplication) does not fulfil yet condition  $\varphi \leq \varphi_{\max} = \min(1, 1/\Lambda^2)$ . To calculate density function  $g(\varepsilon_{0e})$  we introduce corrected (cut off) distribution  $\underline{\varphi}$  with density  $c \cdot f(\varphi)$ , where:  $c = 1/(1 - \omega_m)$  - normalizing factor,  $\omega_m = \text{Prob.}\{\varphi \geq \varphi_{\max}\}$  (Figure 4(a)). This adoption we propose for skeleton column slenderness  $\Lambda \leq \sim 1,4$  (that is  $\lambda < \sim 120$ ). For slenderness values distant from 1 coefficient  $c$  increases significantly.

After introducing into Eq. 7 function  $\varepsilon_{0e}(\varphi; \Lambda)$  and corrected logarithmic-normal probability density function  $f(\varphi; \Lambda)$  with parameters  $\varphi(\Lambda)$  and  $v_\varphi(\Lambda)$  we obtain density function of random variable  $\varepsilon_{0e}$  in the form of:

$$g(\varepsilon_{0e}; \Lambda) = \frac{c}{\sqrt{2\pi} \cdot v_\varphi \cdot \varphi(\varepsilon_{0e})} \cdot \exp\left\{-\frac{\ln^2(\varphi(\varepsilon_{0e})/\bar{\varphi})}{2 \cdot v_\varphi^2}\right\} \cdot \left|\frac{d\varphi(\varepsilon_{0e})}{d\varepsilon_{0e}}\right|, \tag{8}$$

where:  $\varphi(\varepsilon_{0e}) = (a - b)/(2 \cdot \Lambda^2)$ ,  $d\varphi/d\varepsilon_{0e} = (1 - a/b)/(2 \cdot \Lambda^2)$ ,  $a = a(\varepsilon_{0e}; \Lambda) = \varepsilon_{0e} + \Lambda^2 + 1$ ,  
 $b = b(\varepsilon_{0e}; \Lambda) = \varepsilon_{0e}^2 + 2 \cdot \varepsilon_{0e} \cdot (1 + \Lambda^2) + (1 - \Lambda^2)^2$ .

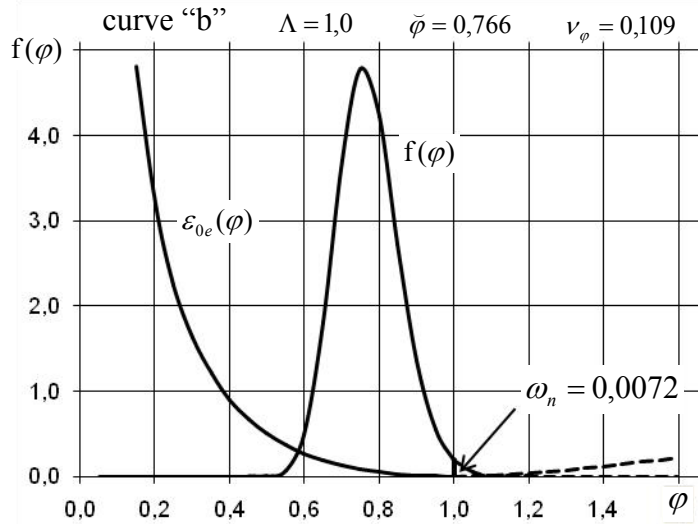


Figure 4(a). The Example of  $\varepsilon_{0e}(\varphi)$  and  $f(\varphi)$  Relationship

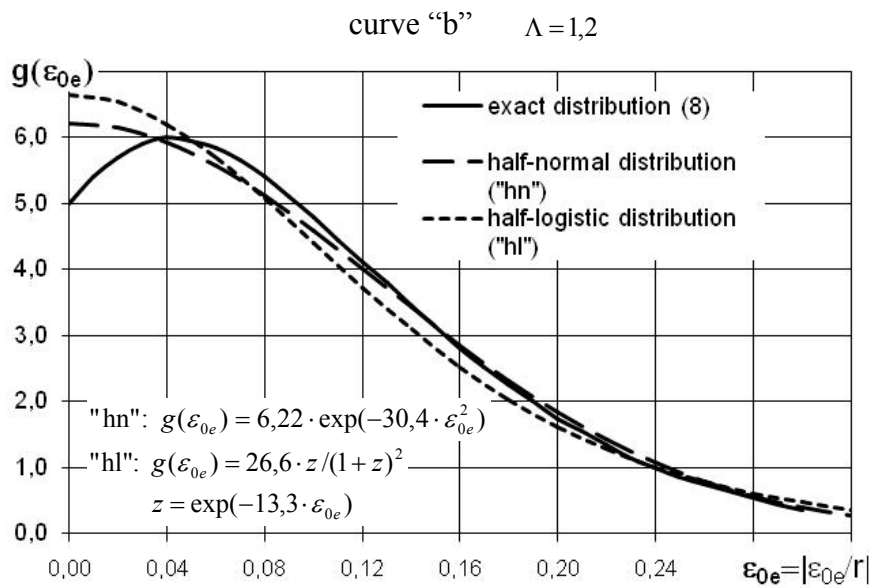


Figure 4(b). The Example of Probability Density Function  $g(\varepsilon_{0e})$

Example results of calculation according to Eq. 8, for bucking curve “b” and  $\Lambda = 1,2$ , were shown in Figure 4(b). Density of “exact” distribution (“8”) according to Eq. 8 shows (beside of close surroundings of  $\varepsilon_{0e} = 0$  point) very good compatibility with density of half-normal distribution (“hn”) and good compatibility with density of half-logistic distribution (“hl”). One-parameter half distributions mentioned above were matched according to mean values conformity criterion:  $\bar{X}_e = \bar{X}_{hn} = \bar{X}_{hl}$  (where  $\bar{X} \equiv \bar{\varepsilon}_{0e}$ ).

Mean values  $\bar{\varepsilon}_{0e}$  and standard deviations  $\mu_{\varepsilon_{0e}}$ , determined from numerical integration of Eq. 8, for appropriate half-normal distributions  $\underline{\varepsilon}_{0e}$ , are related to  $\Lambda$  almost linearly (Figure 5(a))

$$\bar{\varepsilon}_{0e} = C_{\bar{\varepsilon}} \cdot \Lambda, \quad \mu_{\varepsilon_{0e}} = C_{\mu\varepsilon} \cdot \Lambda, \tag{9}$$

with direction coefficients  $C_{\bar{\varepsilon}}$  and  $C_{\mu\varepsilon}$  given in Table 3.

Value of coefficient  $C_{\mu\varepsilon}^*$  (for relationship  $\mu_{\varepsilon_{0e}}^* = C_{\mu\varepsilon}^* \cdot \Lambda$ ) corresponding to normal distribution  $\underline{\varepsilon}_{0e}^*$  with changeable signs and mean value  $\bar{\varepsilon}_{0e}^* = 0$  is obtained (Table 3) from relationship  $C_{\mu\varepsilon}^* = C_{\mu\varepsilon} / \sqrt{1 - 2/\pi}$  (Machowski [3]).

In Figure 5(b) values of  $\varepsilon_{0e}(\Lambda)$ , obtained from half-normal distribution  $\varepsilon_{0e}$  with parameters according to Table 3, were compared, for bucking curve “b”, with values from Standard Recommendations and values from formula (6). Straight lines “1” and “2” are obtained for assumed probability  $\omega$  of exceeding  $\varepsilon_{0e}$  value (top quantiles) in half-normal distribution. Straight line “2” corresponding to value  $\omega = 2\%$  turns out very close to straight line “3” characterized by equation  $\varepsilon_{0z} = 0,3 \cdot \lambda / 100 = 0,3 \cdot \Lambda \cdot \lambda_1 / 100$  (for  $\lambda_1 = 0,84$ ) – representing traditional British Recommendations (BS 449). Broken line “4”, according to Eurocode 3 – with equation:  $\varepsilon_{0z} = 0,34 \cdot (\bar{\lambda} - 0,2)$  - for  $\bar{\lambda} > 0,2$  and  $\varepsilon_{0z} = 0$  - for  $\bar{\lambda} \leq 0,2$ , (taking relationship  $\Lambda = 1,12 \cdot \bar{\lambda}$  into consideration) shows good compatibility with curve “5” obtained from (6) substituting  $\chi(\bar{\lambda})$  in place of  $\varphi(\lambda)$  and  $\bar{\lambda}$  in place of  $\Lambda$ .

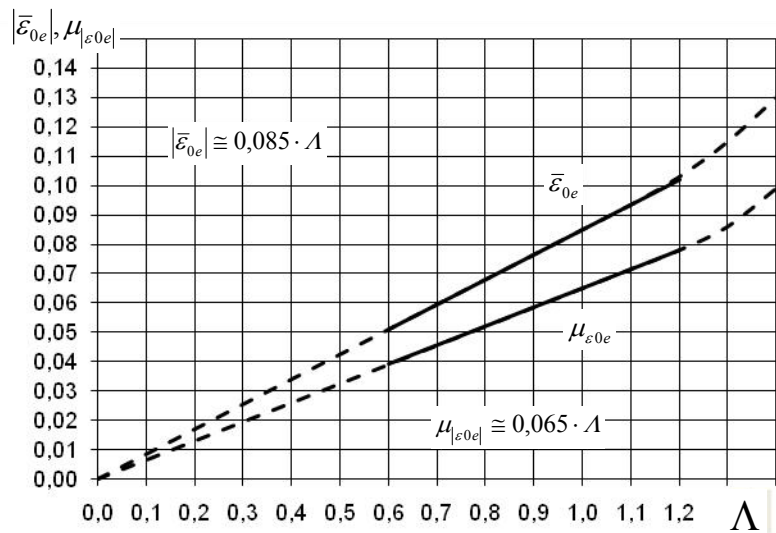


Figure 5(a). Examples of Relation  $\bar{\varepsilon}_{0e}(\Lambda)$  and  $\mu_{\varepsilon_{0e}}(\Lambda)$  for Curve “b”

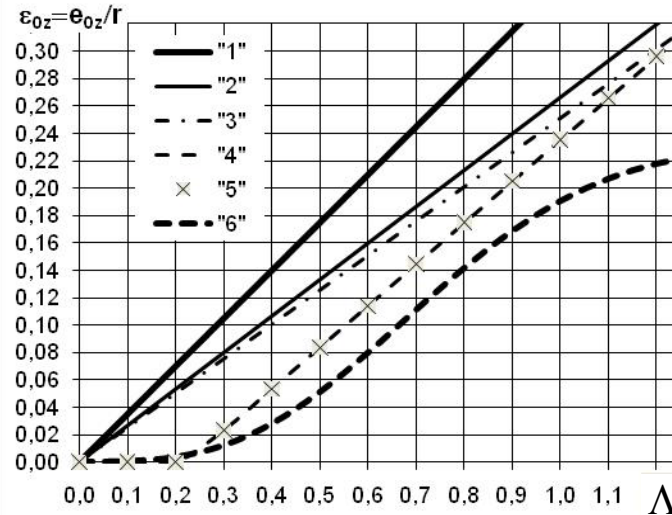


Figure 5(b). Comparison of relation  $\varepsilon_{0e}(\Lambda)$  according to different formulas (“1” – random for  $\omega = 1,35\%$ , “2” – random for  $\omega = 2\%$ , “3” – “ $0,3\lambda/100$ ”, “4” – “ $0,34(\bar{\lambda} - 0,2)$ ”, “5” – acc. to Eq. 6 for  $\bar{\lambda}$  and  $\chi(\bar{\lambda})$ , “6” – acc. to Eq. 6 for  $\Lambda$  and  $\varphi(\Lambda)$ )

Table 3. Coefficients values for formula (9)

buckling curve	$C_{\varepsilon}$	$C_{\mu\varepsilon}$	$C_{\mu\varepsilon}^*$
a	0,065	0,045	0,075
b	0,085	0,065	0,110
c	0,120	0,085	0,140

Occurrence of  $\varphi$  and  $\Lambda$  quantities in non-linear form in Eq. (6) cause significant mutual discrepancy between curves “5” and “6” (Figure 5(b)) despite of affirmed earlier good compatibility of buckling curves (Figure 3).

### 3. RANDOM EQUIVALENT INITIAL TILT OF FRAME

Mathematical model of column single story initial tilt was determined on the basis of column out-of-plumbs post-fabrication measurements, carried out after all frames erection and after construction of all floors.

Most extensive statistical analysis of measurements mentioned above was conducted in (Machowski [3, 12]) which also includes results obtained earlier by Beaulieu (Beaulieu and Adams [13]) and Lindner (Lindner and Gietzelt [14]).

Conducted analysis showed that that mathematical model of stationary gaussian random noise  $\phi_{ijk}^x$  and  $\phi_{ijk}^y$  (stationary random series with mean value  $\bar{\phi} = 0$  and constant variance  $D_{\phi} = \mu_{\phi}^2 = \text{const.}$ ) is justified if empirical variance fulfils a constraint

$$\mu_{\phi}^2 \leq 3 (\text{‰})^2, \tag{10}$$

what agrees with keeping initial tilt standard tolerance.

The second conclusion was that only exist weak autocorrelation dependence between tilts of columns in the same vertical planar frames and lack of correlation between any other initial tilts.

For design purposes it is very convenient to assume one random value of equivalent initial tilt for frame as a whole  $\underline{\phi}^{EFF}$  instead of column initial tilts random sequences  $\underline{\phi}_{ip}$ .

Post-fabrication column out-of-plumbs cause additional bending moments from vertical load for frame as vertical cantilever (Machowski, A. [3, 12]).

For bar-disk analytical scheme of multistory skeletal structure with rigid floor-disks effective initial random tilt for  $i$ -th story of building  $\underline{\phi}_i^{eff}$  may follow from conservation of global moment increment condition (if torsional effect for building as vertical cantilever is neglected)

$$\Delta \underline{M}_i^\phi = \sum_{p=1}^s P_{ip} \cdot h_i \cdot \underline{\phi}_{ip} = P_i \cdot h_i \cdot \underline{\phi}_i^{eff}, \quad (11)$$

where:  $P_i = \sum P_{ip}$ , ( $p = 1 \dots s$ ) - sum of all vertical loads acting on building above  $i$ -th story,  
 $P_{ip}$  (for  $s$  columns  $i = 1, 2, \dots, s$ . on  $i$ -th story of building) – sum of vertical loads above  $i$ -th story in  $p$ -th column,

hence  $i$ -th story equivalent initial tilt

$$\underline{\phi}_i^{eff} = \sum_{p=1}^s w_{ip} \cdot \underline{\phi}_{ip} = \mathbf{w}_i \boldsymbol{\phi}_i^T, \quad (12)$$

Story random initial tilt  $\underline{\phi}_i^{eff}$  is normal random variable with parameters (Machowski [3, 12]):

$$E\{\underline{\phi}_i^{eff}\} = 0, \quad \mu_{\phi_i}^2 = k_{c,i}^2 \cdot \mu_{\phi}^2, \quad (13)$$

where

$$k_{c,i}^2 = \mathbf{w}_i \boldsymbol{\rho}_s \mathbf{w}_i^T = \sum_{p=1}^s w_{ip} \cdot \sum_{q=1}^s w_{iq} \cdot \rho_{pq} \quad (14)$$

is positively defined quadratic form of  $s$ -variables:  $w_{i1}, \dots, w_{ip}, \dots, w_{is}$ . with symmetric matrix of coefficients  $\boldsymbol{\rho}_s$  equal to normalized correlation matrix  $\boldsymbol{\rho}_s$  of random vector  $\boldsymbol{\phi}_i$ .

Values of reduction coefficient  $k_{c,i}$  according to Eq. 14 have been analysed in detail in (Machowski [3, 12]). Conducted analysis showed that among standard formulas closest to obtained result is that in Polish Standard [6], on condition that only columns with vertical load (above  $i$ -th story) arrangement parameter  $c \geq 0,5$  are taken into account.

Safe approximation of effective random initial tilt for frame as a whole may be defined as follows

$$\underline{\phi}^{EFF} = \max_{i=1}^n \left| \underline{\phi}_i^{EFF} \right| = \max_{i=1}^n \left| \sum_{t=i}^n V_t \cdot \sum_{q=i}^t h_q \cdot \underline{\phi}_q^{eff} \cdot \left( \sum_{t=i}^n V_t \cdot \sum_{q=i}^t h_q \right)^{-1} \right|, \quad (15)$$

$\underline{\phi}_i^{EFF}$  – effective random initial tilt for frame as a whole, which guarantee safe estimation of additional bending moment for  $i$ -th story of frame as vertical cantilever,

$\underline{\phi}_i^{eff}$  – according to Eq. 12,

$V_t$  – sum of vertical loads imposed immediately to  $t$ -th story.

Analyses conducted in (Machowski [3, 12]) showed that within confines of discussed conception reduction of initial tilt standard deviation and characteristic value depending on story number is unfounded. According to extensive analyses presented in (Rondal and Maquoi [8], Machowski and Tylek [15]) this reduction is justified only in special cases, e.g. with reference to frames fulfilled “strong columns” condition (columns remain elastic up to plastic mechanism formation).

#### 4. JOINT EFFECT OF EQUIVALENT INITIAL TILT AND INITIAL BOW

Statistically based models of equivalent imperfections  $\underline{e}_{0e}$  and  $\underline{\phi}_{0e}$ , according to chapters 2 and 3, first of all may be used to verify Standard conceptions of steel skeletons calculation. This verification may apply, among others things, to often criticized effective length conception for sway frames and described in p. 6.3.4 Eurocode 3 [5] so called “general method” depending on reduction of resistance coefficient  $\alpha_{ult,k}$  by means of factor  $\chi_{op}$  determined as Standard flexural buckling coefficient  $\chi$  or Standard lateral-torsional buckling coefficient  $\chi_{LT}$  - calculated for “global non-dimensional slenderness”  $\bar{\lambda}_{op}$ , connected with out-of-plane buckling of a structural component. Analysis of Standard conceptions mentioned above with application of proposed models of  $\underline{e}_{0e}$  and  $\underline{\phi}_{0e}$  would require, as it seems, separate extensive study.

Another important problem that will be consider farther in this article, is influence of both random equivalent imperfections on total imperfections effect. In this case random variability of  $\underline{e}_{0e}$  sign (direction) in column assembly elements may be important. Taking into account of this last effect requires, even in the simplest cases, to consider examples of multistory steel frames.

Joint effect of random equivalent initial tilt  $\underline{\phi}_{0e}$  and random equivalent initial bow  $\underline{e}_{0e}$  in “advanced analysis” was considered on the example of 5-story steel skeleton (Figure 6). Vertical loads from floors, roof and walls of the building are carried by floor beams on five transversal rigid frames located in axes 1-1 to 5-5 of building horizontal projection. Skeleton bracing system, carrying horizontal load, is made up, among transversal frames mentioned above, three equal two-bay rigid frames located in axes: A-A, B-B and C-C (see horizontal projection in Figure 6). Skeleton filling consist of floors and flat roof with reinforced concrete supporting structure, (rigid in own plane and nonflexibly connected with beams) and light-weight partition and curtain walls. It should be noticed that plane of every longitudinal frame agrees with column minor stiffness plane (Figures 6 and 7).

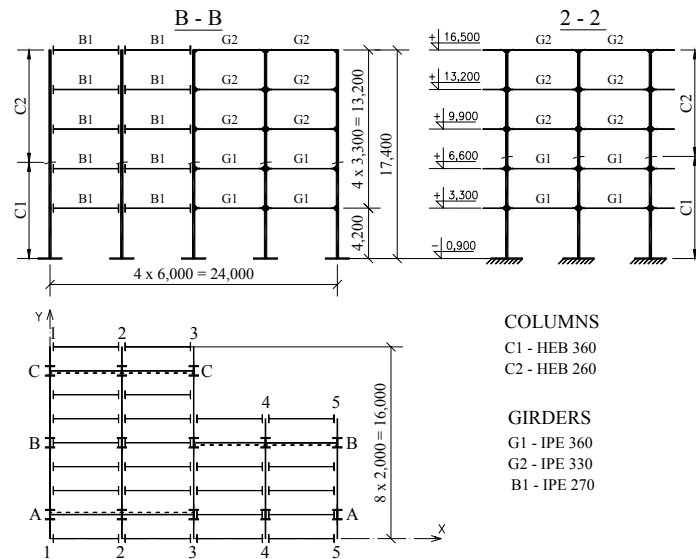


Figure 6. Analysed Skeletal Framed Steel Structure

Considering vertical planar frame of longitudinal bracing system (e.g. C-C) acc. to Figure 6 and neglecting torsional effects for building as vertical cantilever substitute static system of planar frame (Figure 7) was assumed. This system was loaded by realistic vertical loads in the form of concentrated forces  $Q_{11}^C$  to  $Q_{n3}^C$  – putted in nodes and fictitious imperfectional load uniformly distributed on columns:  $q_{11} \dots q_{n3}$  (as in [5]) – balanced by reactions  $R_{11} \dots R_{n3}$ .

Influence of column initial tilts of skeleton braced in longitudinal direction by three identical frames, joined by rigid floor disks, was taken into consideration by adding to planar frame fictitious system (Figure 7) consisted of bars ideally rigid, connected by hinges with each other and with frame. To the nodes of system mentioned above following loads were applied: vertical loads  $V_1 \dots V_n$  equal to 1/3 of sum of  $Q_i$  vertical loads on  $i$ -th skeleton floor and couples of forces  $P_i \phi_{0i}$  ( $i = 1, 2, \dots, n$ ) representing equivalent imperfectional load from initial tilts.

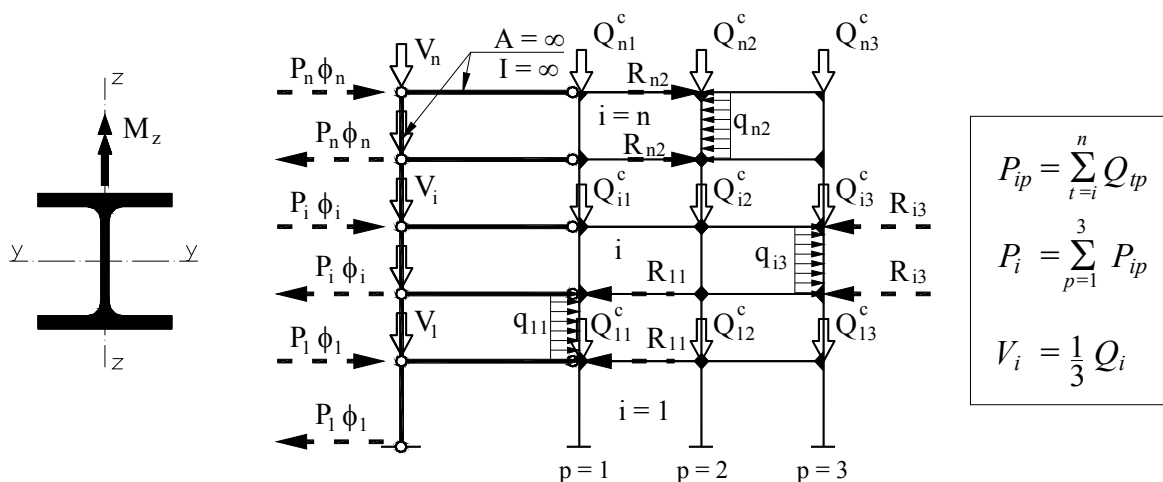


Figure 7. Substitute Static System of Analyzed Planar Bracing System of 5-story Skeletal Steel Structure ( $Q_{ip}$  – Total Vertical Load of Building as a Whole  $i$ -th story)

Random sequences of story initial tilts were computer generated in the form of vector  $\underline{\phi}^{eff} = \{\phi_i^{eff}\}$  which elements were normal variable with parameters according to Eq. 13. Week correlation between initial tilts in vertical sequences was neglected.

Mathematical model of column random equivalent initial bow was product of random initial bow and random binary sequence (with elements 1 and -1). Value of column random initial bow was determined on the basis of knowledge of probability density function and characteristics of random dimensionless column bow distribution (according to p.2). Normal distribution with parameters  $\{\bar{\varepsilon}_{0e}^* = 0, \mu_{\varepsilon 0e}^* = C_{\mu\varepsilon}^* \cdot \Lambda\}$  ( $C_{\mu\varepsilon}^*$  according to Table 3) was assumed. It was also assumed that column splices are located on every story (above bottom node of column) so there is no correlation between initial bows of individual columns.

Additional effect of column equivalent initial bows on frame carrying capacity (associated with limit point on frame equilibrium path) was determined by comparison of frame initial tilt  $\phi^{EFF}(\phi_{0e})$  (substitutes for random sequence of story initial tilts only – Figure 8a) standard deviation with frame initial tilt  $\phi^{EFF}(\phi_{0e}, \varepsilon_{0e})$  (substitutes for story random initial tilts and column random initial bows – Figure 8b) standard deviation values. In both cases the same sequences of story random initial tilts were considered.

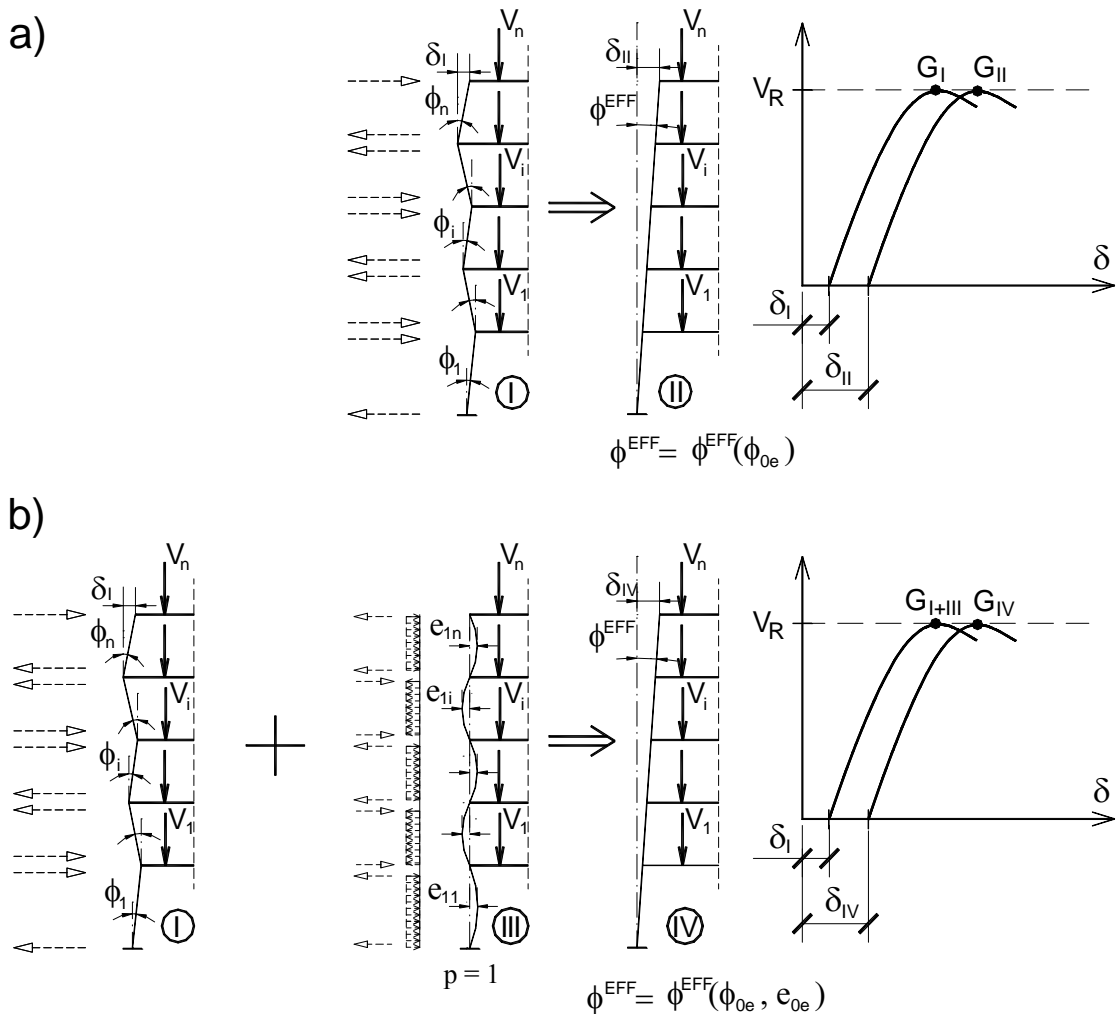


Figure 8. Random Sequence of Story Initial Tilts, Random Set of Column  $p = 1$  Initial Bows and Its Equivalent Forces; Equivalent Tilts of Frame as a Whole and Corresponding Paths of Equilibrium

According to applied simulation procedure, for every realization of equivalent imperfection loads set (Figure 7) respective frame equilibrium path and frame carrying capacity were determined. Next the effective initial tilt of frame as a whole  $\underline{\phi}^{EFF}$  was chosen in agreement with condition of frame limit carrying capacity conservation (Figure 8). Equivalent random initial tilt of plane frame as a whole  $\underline{\phi}^{EFF}$  was determined on the basis of conservation of carrying capacity associated with limit point on frame equilibrium path criterion. Calculations were conducted for 700 elements population.

In order to obtain frame equilibrium path and frame limit carrying capacities computer program ANSYS, based Finite Element Method, were utilized. Two-dimensional bar structure model with regular mesh and elastic-plastic (bilinear) model of material was assumed. Description of the material model was based on Huber-Mises-Hencky plasticity criterion, associative flow rule and rule of kinematic hardening. Development of plastic zones (in cross section and along length of element) and large displacements (translations and rotations) with small deflections were take into consideration.

Difference between standard deviations of frame initial tilt  $\underline{\phi}^{EFF}(\underline{\phi}_{0e})$  and frame initial tilt  $\underline{\phi}^{EFF}(\underline{\phi}_{0e}, \underline{e}_{0e})$  obtained from conducted analysis is lower than 2% and indicates that additional influence of column random equivalent initial bows on frame carrying capacity in advanced analysis may be neglected.

Results of earlier works (De Luca and Mele [17]) indicated that interaction of global (tilts) and local (bows) geometric imperfections causes reduction of frame carrying capacity by 10%, but authors [17] assumed deterministic (instead of random) values of equivalent imperfections and selected some combinations of global and local equivalent geometric imperfections, compatible with first buckling eigenvector of ideal elastic frame and combinations of initial bows acceptable for the sake of columns splices (Figure 9).

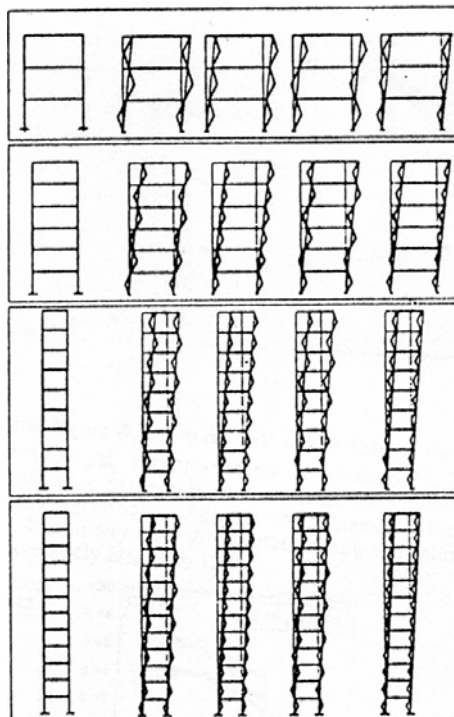


Figure 9. Set of Local and Global Geometrical Imperfections Combination Analyzed in [17]

## 5. CONCLUSIONS

Verification of Standard recommendations of steel skeletons design with equivalent geometrical imperfections (column initial tilt  $\phi_0$  and bow  $e_0$ ) should base on probabilistic models of these imperfections and takes into account its interaction. Application of random models and imperfections acting together should lead to taking into consideration of favourable effects – similar to these which we deal with in case of random load combinations.

Possibility of applying approach mentioned above offers this work model of equivalent random initial bow of compressed bar  $e_0$ . It is obtained out of randomization of buckling coefficient in well-known deterministic formula of equivalent initial bow. This model together with known from earlier works, e.g. authors' works [3, 12, 15, 16], model of equivalent random initial tilt  $\phi_0$ , allows analyses of mentioned above Standard recommendations.

In the paper effects of column initial tilts and initial bows interaction were investigated using probabilistic approach, introducing into calculations, in elastic-plastic structure behaviour, statistically based models of equivalent imperfections.

Analysis of 2-bay 5-story frame planar bracing system with random sequences of story initial tilts and random sets of column initial bows showed slight influence of column random initial bows on frame carrying capacity and equivalent initial tilt of frame as a whole  $\phi^{EFF}$ . Influence of interaction of global and local imperfections on frame carrying capacity was lower than 2%.

Results of conducted analysis justify passing over of local geometric imperfections influence in planar frames advanced analysis. It also shows that Eurocode 3 procedure of steel frame design, recommending to introduce in stage on static calculations only frame equivalent initial tilt while influence of column equivalent initial bows is taking into account in beam-column design formulas.

## ACKNOWLEDGEMENT

Scientific research has been carried out as a part of the Project “Innovative resources and effective methods of safety improvement and durability of buildings and transport infrastructure in the sustainable development” financed by European Union from the European Fund of Regional Development based on the Operational Program of the Innovative Economy.

## REFERENCES

- [1] Chen, W.F. and Toma, S., “Advanced Analysis of Steel Frames”, London-Tokyo: CRC Press, 1994.
- [2] Narayanan, R. ed, “Steel Framed Structures, Stability and Strength”, Elsevier Science, 1985.
- [3] Machowski, A., “Problems of Limit States and Reliability of Steel Multistory Building Frames”, Monograph No. 262, Cracow University of Technology, 1999 [in Polish].
- [4] Fukumoto, Y. and Itoh, Y., “Multiple Buckling Curves Based on Experimental Data”, Construction Métallique, 1984, Vol. 3 [in French].
- [5] CEN “EN 1993-1-1. Eurocode 3, Design of Steel Structures, Part 1.1: General Rules and Rules for Buildings”.
- [6] PKNMiJ, “PN-90/B-03200, Steel Structures, Design Rules” [in Polish].

- [7] Allen, D., “Merchant-Rankine Approach to Member Stability”, *Journal of the Structural Division*, 1978, 104 (ST.12), pp. 1909-1914.
- [8] Rondal, J. and Maquoi, R., “The Ayrton-Perry Formulation for Buckling of Metallic Bars”, *Construction Métallique*, 1979, 4, pp. 41-53 [in French].
- [9] Murzewski, J., “Design of Steel Structures for Differentiated Reliability Levels”, *Archives of Civil Engineering*, 2008, LIV(1), pp. 209-237.
- [10] ECCS, “European Specifications for Steel Structures”, 1-st ed; 1974.
- [11] Papoulis, A., “Probability, Random Variables and Stochastic Processes”, McGraw-Hill Inc, 1965.
- [12] Machowski, A., “Initial Random Out-of-plumbs of Steel Frame Columns”, *Archives of Civil Engineering*, 2002, XLVIII(2), pp. 207-226.
- [13] Beaulieu, D. and Adams, P.F., “The Results of a Survey on Structural Out-of-plumbs”, *Canadian Journal of Civil Engineering*, 1978, Vol. 5, pp. 642-470.
- [14] Lindner, J. and Gietzelt, R., “Evaluation of Imperfections of Support – Elements”, *Stahlbau*, 1984, Vol. 4, pp. 97-98 [in German].
- [15] Machowski, A. and Tylek, I., “Conceptions of Equivalent Imperfections in Analysis of Steel Frames”, *The International Journal of Advanced Steel Construction*, 2008, Vol. 4, No. 1, pp. 13-25.
- [16] Tylek, I., “Equivalent Geometrical Imperfections of Multistory Steel Building Frames”, *Doctoral Thesis*, Cracow University of Technology, 2007 [in Polish].
- [17] De Luca A. and Mele, E., “Analysis of Steel Frames in the Light of Eurocode 3 and New Research Results”, In: White, D.W. and Chen, W.F. ed., “Plastic Hinge Based Methods for Advanced Analysis and Design of Steel Frames”, SSRC, Lehigh Univ., 1993, pp. 97-152.

# THE EFFECTS OF FRAME DEFORMATION ON WELDED GUSSET PLATES FOR DIAGONAL BRACING ELEMENTS LOADED IN TENSION

J. Kent Hsiao<sup>1,\*</sup>, Donald W. Tempinson<sup>2</sup> and Jianming Li<sup>3</sup>

<sup>1</sup>Associate Professor, Department of Civil and Environmental Engineering,  
Southern Illinois University Carbondale, Carbondale, IL, USA

<sup>2</sup>Former Graduate Student, Department of Civil and Environmental Engineering,  
Southern Illinois University Carbondale, Carbondale, IL, USA

<sup>3</sup>Graduate Student, Department of Civil and Environmental Engineering,  
Southern Illinois University Carbondale, Carbondale, IL, USA

\*(Corresponding author: E-mail: hsiao@engr.siu.edu)

Received: 10 February 2012; Revised: 17 April 2012; Accepted: 27 April 2012

---

**ABSTRACT:** The effects of frame deformation on a gusset plate in a braced frame can be defined as the increases in stress in the gusset plate caused by the deformations of the beams and the columns of the braced frame. The hand-calculated approach for the design of gusset plates for diagonal bracing elements loaded in tension has traditionally neglected the frame deformation effects. A design example for a brace-beam-column gusset plate connection using the traditional hand-calculated approach is given in this paper. Two finite element approaches (one neglects the effects of frame deformation on the gusset plate while the other one considers the effects) are used to investigate the adequacy of the gusset plate designed by the hand-calculated approach. This study concludes that frame deformation effects have caused the increases in the von Mises and the first-principal stresses located at the Whitmore section of the gusset plate, as well as the increase in the combined effects of the factored tension and shear forces at the gusset edges. The traditional hand-calculated approach which neglects the frame deformation effects, therefore, may result in an under-design of the gusset plate.

**Keywords:** Finite element method, Nonlinear analysis, Rigid frames, Stress concentration, Tensile strength, Welded connections, Yield stress

---

## 1. INTRODUCTION

Gusset plates are used to transmit the applied forces from main elements (beams and columns) to bracing elements and vice versa. Figures 1 and 2 illustrate examples of gusset plate connections for an eccentrically braced frame and a special concentrically braced frame [1]. Many research papers have addressed the analyses and designs of gusset plate connections [2, 3, 4]. The stresses distributed along the edges and/or at the Whitmore effective sections of the gusset plates were the major topics discussed in these papers.

When a bracing member is subjected to a compressive force, the gusset plate, which is connected to the bracing member, will be stressed in compression and shear. However, since the vertical main member is deflecting away from the bracing member (refer to the lower left-hand quarter portion of the braced frame shown in Figures 3(a) & (b)), the angle between the vertical main member and the horizontal main member is enlarged. As a result, tensile stresses are also introduced to the gusset plate.

The effects of frame deformation on gusset plates for diagonal bracing elements loaded in compression were investigated by Cheng, Grondin, and Yam [5] using full-scale tests. Their tests found that the capacity of the gusset plate was reduced due to the effects of frame deformation on the gusset plate.

Similarly, for a reverse condition, when a bracing member is subjected to a tensile force, the gusset plate, which is connected to the bracing member, will be stressed in tension and shear. However, since the vertical main member is deflecting toward the bracing member (refer to the lower left-hand quarter portion of the braced frame shown in Figures 3(c) & (d)), the angle between the vertical main member and the horizontal main member is reduced. As a result, compressive stresses are also introduced to the gusset plate.

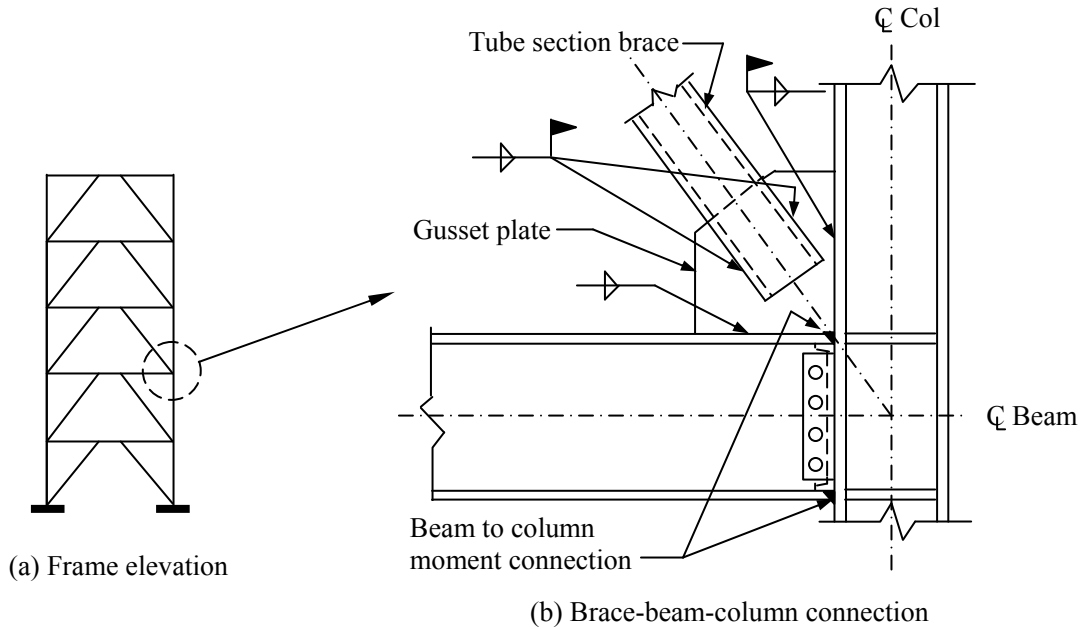


Figure 1. Gusset Plate Connection Example for an Eccentrically Braced Frame

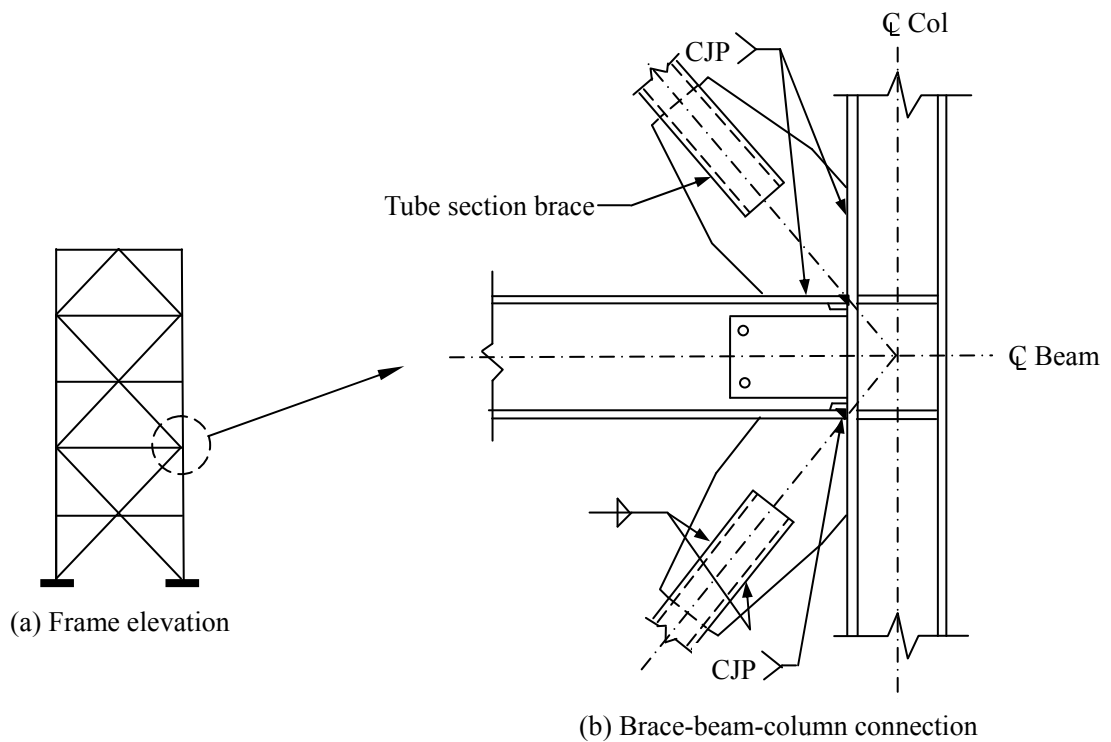


Figure 2. Gusset Plate Connection Example for a Special Concentrically Braced Frame

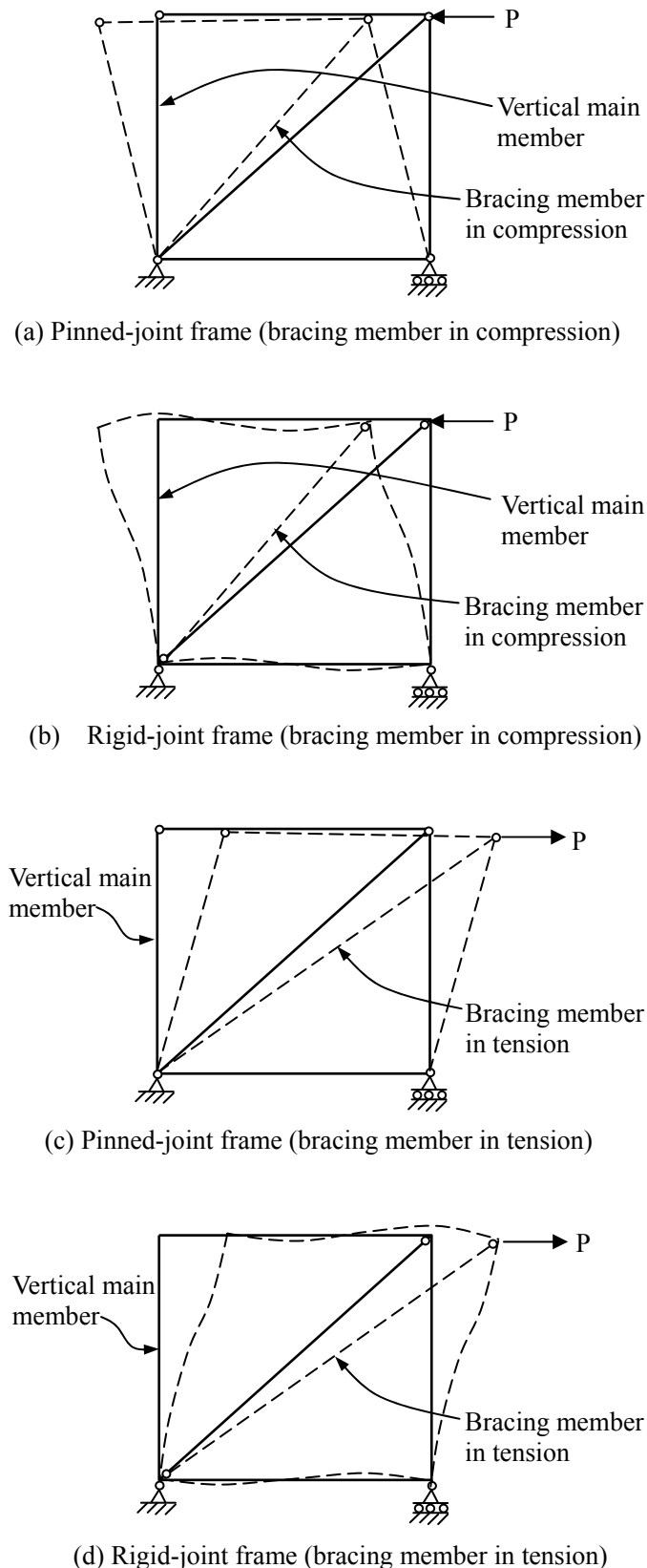


Figure 3. Deformations of Laterally Loaded Braced Frames

The effects of frame deformations on a welded gusset plate for a diagonal bracing element loaded in tension are investigated and the results are presented in this paper. This study is limited to the following conditions: (1) the gusset plate, the web of the beam (the horizontal member) and the

web of the column (the vertical member) are in the same plane; (2) as shown in Figures 1 and 2, the beam (the horizontal member) is rigidly connected to the column (the vertical member); (3) the bracing element is welded to the gusset plates and is loaded in tension; and (4) fillet welds are used for the gusset-to-bracing element, gusset-to-beam, and gusset-to-column connections.

## 2. DESIGN EXAMPLE OF A GUSSET PLATE CONNECTION FOR A DIAGONAL BRACING ELEMENT LOADED IN TENSION

The following is a design example of a gusset plate connection for a diagonal bracing element loaded in tension. Two C3×6 channels are used as the diagonal bracing element in a rigid frame as shown in Figure 4. ASTM A36 steel is used for the columns, beams, bracing member, and the gusset plates. Note that in the U.S., A992 steel is the preferred material for W shapes, while the availability of A36 should be confirmed prior to the use of it. Also, E70XX electrodes having a minimum tensile strength of 483 MPa (70 ksi) are used for the fillet weld made by shielded metal arc welding (SMAW). Assume that the factored tensile force,  $P_u$ , applied to the bracing element is 507 kN (114 kips).

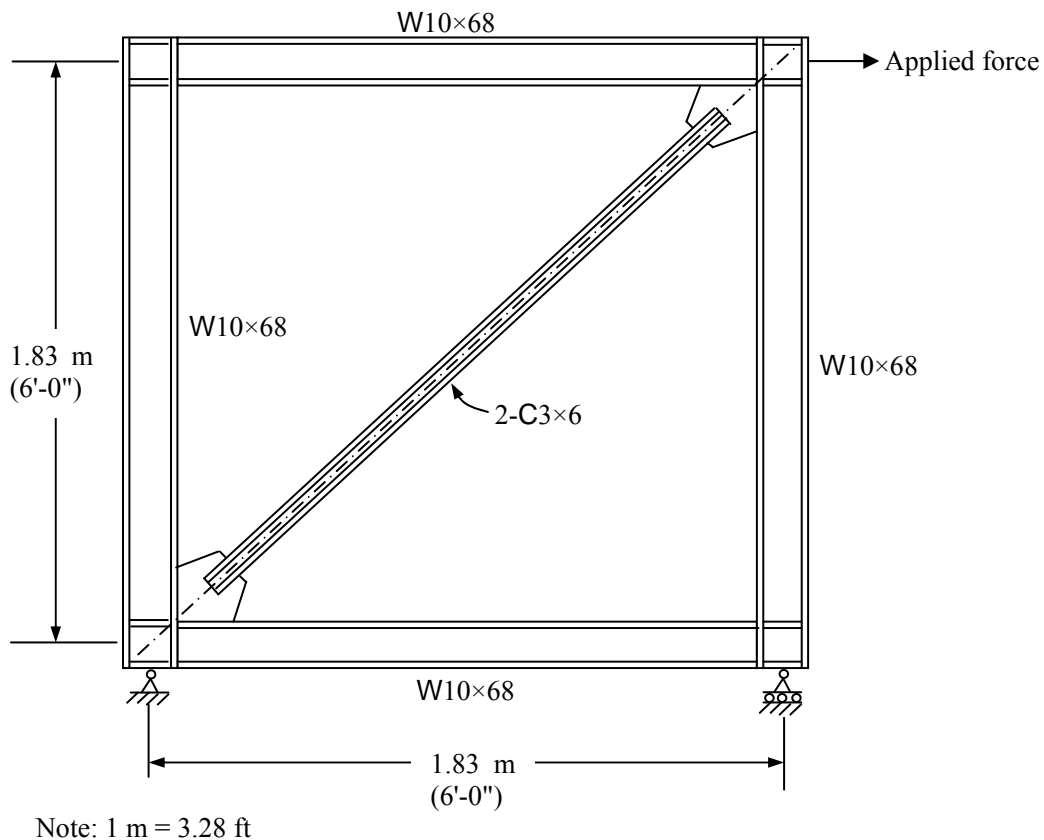


Figure 4. Braced Frame Elevation

### *Design of a gusset plate connection using the hand-calculated approach*

The following hand-calculated approach illustrates the use of the Whitmore section [6, 7] and the Uniform Force Method [1, 7, 8, 9] for the design of the gusset plate connection for the diagonal bracing element loaded in tension.

1. Compute the design tensile strength of the bracing member [7]:

(a) For tensile yielding in the gross section:

$$\phi_t P_n = \phi_t F_y A_g = 0.9 (248 \text{ MPa}) (2270 \text{ mm}^2) = 507 \text{ kN} (114 \text{ kips}) \geq P_u \quad \mathbf{o.k.}$$

where  $\phi_t P_n$  = design tensile strength;  $F_y$  = specified minimum yield stress of the type of steel being used [ $F_y = 248 \text{ MPa}$  (36 ksi) for A36 steel]; and  $A_g$  = gross area of the bracing member [ $A_g = 2270 \text{ mm}^2$  (3.52 in<sup>2</sup>) for 2-C3×6].

(b) For tensile rupture in the net section:

$$U = 1 - \frac{\bar{x}}{l} = 1 - \left( \frac{11.6}{200} \right) = 0.942$$

$$\phi_t P_n = \phi_t F_u A_n U = 0.75 (400 \text{ MPa}) (2270 \text{ mm}^2) (0.942) = 642 \text{ kN} (144 \text{ kips}) \geq P_u \quad \mathbf{o.k.}$$

where  $U$  = reduction coefficient, used in calculating effective net area;  $\bar{x}$  = horizontal distance from the outer edge of a channel web to its centroid;  $l$  = length of the weld (assume that each weld length for the bracing element-to-gusset plate connection is 200 mm (8 in.); the assumed length will be verified in the following step);  $\phi_t P_n$  = design tensile strength;  $F_u$  = specified minimum tensile strength of the type of steel being used [ $F_u = 400 \text{ MPa}$  (58 ksi) for A36 steel]; and  $A_n$  = net area.

2. Design the fillet weld for the bracing element-to-gusset plate connection:

In order to avoid brittle failure of connections, the capacity of the welded connection is recommended to be at least equal to or greater than the axial tension yield capacity of the bracing member determined using a conservative expected yield stress of  $1.1 R_y F_y$  [4]. Therefore, the axial tension yield capacity of the bracing member (2-C3×6) can be computed as follows:

$$1.1 R_y F_y A_g = 1.1 (1.5) (248 \text{ MPa}) (2270 \text{ mm}^2) = 929 \text{ kN} (209 \text{ kips})$$

where  $R_y$  = ratio of the expected yield strength to the specified minimum yield strength of the grade of steel to be used ( $R_y = 1.5$  for ASTM A36 steel channels [10]).

Using an 8 mm (<sup>5</sup>/<sub>16</sub> in.) fillet weld, the effective throat of the 8mm (<sup>5</sup>/<sub>16</sub> in.) fillet weld is  $t_e = (8 \text{ mm}) (0.707) = 5.66 \text{ mm}$  (0.22 in.)

Therefore, the capacity of weld per inch can be computed as follows:

$$0.75 t_e (0.60 F_{EXX}) = 0.75 (5.66 \text{ mm}) (0.60) (483 \text{ MPa}) = 1.23 \text{ kN/mm} (7.0 \text{ kips/in.})$$

Using a length of 200 mm (8 in.) for each fillet weld, since there are a total of four (4) 200 mm-long welds for the bracing element-to-gusset plate connection, the total welding capacity is 984 kN (222 kips) ( $= 4 \times 1.23 \text{ kN/mm} \times 200 \text{ mm}$ ), which is larger than 929 kN (209 kips) (the axial tension yield capacity of the bracing member). Therefore, the capacity of the fillet weld for the bracing element-to-gusset plate connection is adequate. Figure 5 illustrates the fillet weld for the bracing element-to-gusset plate connection.

3. Determine the thickness of the gusset plate using the Whitmore section:  
In order to increase global ductility of a braced frame, yielding of the bracing member shall occur before the yielding of the gusset plate [4]. Therefore, the following equation is suggested for the determination of the gusset plate thickness:

$$R_y F_y A_g \leq F_y A_e \quad (1)$$

where  $R_y = 1.5$  for ASTM A36 steel;  $F_y = 248$  MPa (36 ksi) for ASTM A36 steel;  $A_g$  = cross area of steel channels (bracing member); and  $A_e$  = area of the Whitmore effective section of the gusset plate.

Referring to Figures 5 and 6, the Whitmore effective width [7] of the plate is:

$$l_w = 2 (200 \text{ mm})(\tan 30^\circ) + 76 \text{ mm} = 307 \text{ mm} (12.2 \text{ in.})$$

Note that 76 mm (3 in.) is the depth of the C3×6 channels. Therefore, the area of the Whitmore effective section can be computed as follows:

$$A_e = (l_w)(t) = 307t \text{ mm}^2 (12.2t \text{ in.}^2)$$

Note that  $t$  is the thickness of the gusset plate. From Eq. 1, one has

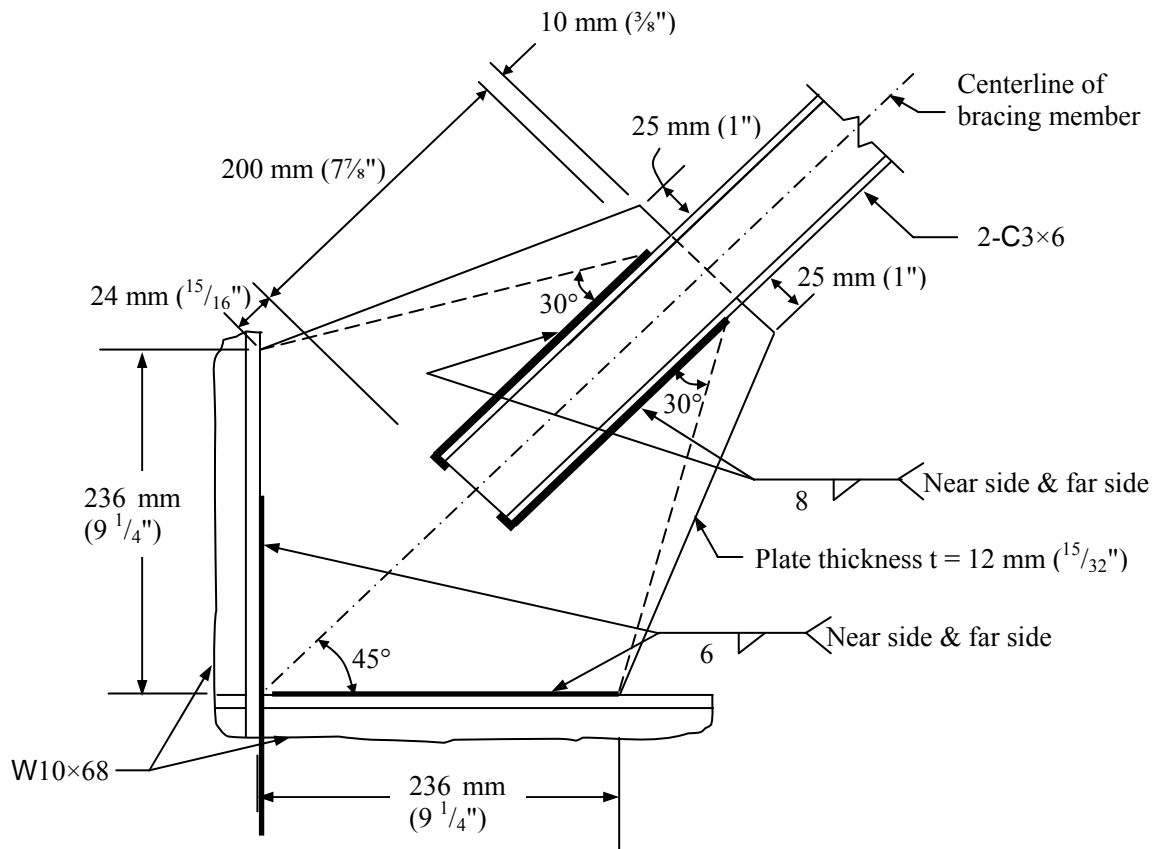
$$1.5 (248 \text{ MPa}) (2270 \text{ mm}^2) \leq 248 \text{ MPa} (307t \text{ mm}^2)$$

$$[1.5 (36 \text{ ksi}) (3.52 \text{ in.}^2) \leq 36 \text{ ksi} (12.2t \text{ in.}^2)]$$

From which, the minimum required thickness  $t = 11.1$  mm (0.43 in.). Therefore, 12 mm ( $^{15}/_{32}$  in.) is used for the thickness of the gusset plate.

4. Determine the configuration of the gusset plate:

The configuration of the gusset plate shown in Figure 5 was determined based on the following criteria: (1) A minimum length of 25 mm (1 in.) is provided on each side of the bracing element along the gusset plate edge, which is perpendicular to the diagonal bracing element. (2) Weld is terminated not less than one weld size from edge of the gusset plate. Since the weld size is 8 mm ( $^{5}/_{16}$  in.), 10 mm ( $^{3}/_{8}$  in.) is provided for the required distance as shown in Figure 5. (3) The re-entrant corner of the gusset plate is located at the intersection of the face of the column (or the face of the beam) and the 30° line as shown in Figures 5 and 6). (4) The distance from the end of the bracing element to the line that connects the two re-entrant corners is not less than two times the thickness of the gusset plate in order to ensure that the gusset plate can freely rotate when the bracing element is subjected to a compression force [4]. Since the thickness of the gusset plate is 12 mm ( $^{15}/_{32}$  in.), 24 mm ( $^{15}/_{16}$  in.) is provided for the required distance as shown in Figure 5.



Note: 1 mm = 0.0394 in.

Figure 5. Gusset Plate Connection for a Diagonal Bracing Element

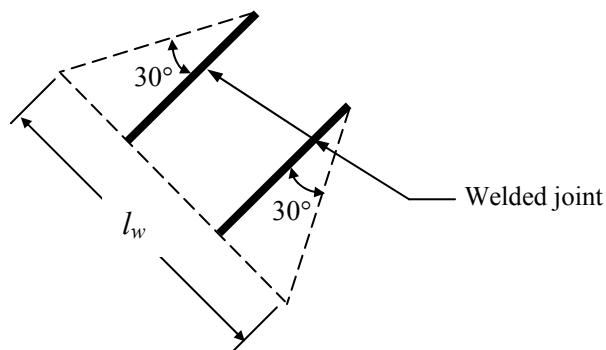


Figure 6. The Effective Width of the Whitmore Section for a Welded Joint

- Determine the adequacy of the thickness of the gusset plate using the Uniform Force Method: Using the connection geometry shown in Figures 5 and 7, five geometric parameters  $e_b$ ,  $e_c$ ,  $\alpha$ ,  $\beta$ , and  $r$  can be determined as:

One-half the depth of the beam (the horizontal element W10x68),  $e_b = d_b/2 = (264 \text{ mm})/2 = 132 \text{ mm}$  (5.2 in.).

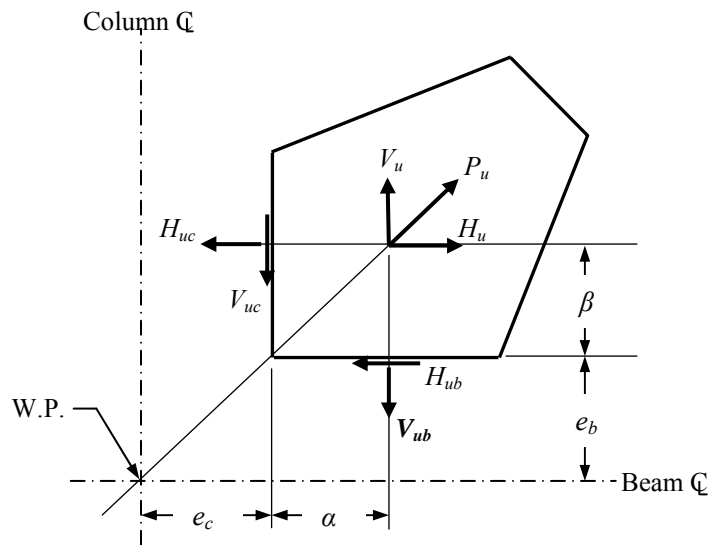


Figure 7. Gusset Plate Free-body Diagram

One-half the depth of the column (the vertical element W10×68),  $e_c = d_c/2 = (264 \text{ mm})/2 = 132 \text{ mm}$  (5.2 in.).

The distance from the face of the column flange to the centroid of the gusset-to-beam connection,  $\alpha = 118 \text{ mm}$  (4.6 in.).

The distance from the face of the beam flange to the centroid of the gusset-to-column connection,  $\beta = 118 \text{ mm}$  (4.6 in.).

The distance from the working point (as shown in Figure 7) to the centroid of the gusset plate connection,

$$r = \sqrt{(\alpha + e_c)^2 + (\beta + e_b)^2} = \sqrt{(118 \text{ mm} + 132 \text{ mm})^2 + (118 \text{ mm} + 132 \text{ mm})^2} \\ = 354 \text{ mm} (13.9 \text{ in.})$$

Therefore, the factored shear force at the gusset-to-column connection,

$$V_{uc} = \frac{\beta}{r} P_u = \frac{118 \text{ mm}}{354 \text{ mm}} (507 \text{ kN}) = 169 \text{ kN} (38.0 \text{ kips})$$

The factored axial force at the gusset-to-column connection,

$$H_{uc} = \frac{e_c}{r} P_u = \frac{132 \text{ mm}}{354 \text{ mm}} (507 \text{ kN}) = 189 \text{ kN} (42.5 \text{ kips})$$

The factored axial force at the gusset-to-beam connection,

$$V_{ub} = \frac{e_b}{r} P_u = \frac{132 \text{ mm}}{354 \text{ mm}} (507 \text{ kN}) = 189 \text{ kN} (42.5 \text{ kips})$$

The factored shear force at the gusset-to-beam connection,

$$H_{ub} = \frac{\alpha}{r} P_u = \frac{118 \text{ mm}}{354 \text{ mm}} (507 \text{ kN}) = 169 \text{ kN (38.0 kips)}$$

The next step is to check the design strength at the horizontal and vertical edges of the gusset plate against the combined effects of the factored tension and shear forces using the von Mises yield criterion [1].

The combined effects of the factored tension and shear forces at the vertical edge of the gusset plate can be computed as follows:

$$P_u = \sqrt{H_{uc}^2 + 3V_{uc}^2} = \sqrt{(189 \text{ kN})^2 + 3(169 \text{ kN})^2} = 348 \text{ kN (78.2 kips)}$$

The design strength at the vertical edge of the gusset plate is

$$\phi P_n = \phi(2\beta)tF_y = 0.9(2 \times 118 \text{ mm})(12 \text{ mm})(248 \text{ MPa}) = 632 \text{ kN (142.1 kips)}$$

Therefore, the design strength at the vertical edge is larger than the combined effects of the factored tension and shear forces.

The result at the horizontal edge of the gusset plate will be the same as that at the vertical edge of the gusset plate since the horizontal and vertical edges are symmetric about the diagonal bracing element.

The results shown above indicate that the thickness of the gusset plate is adequate.

- Design the fillet weld for the gusset-to-W10×68 flange connection using the Uniform Force Method:

Since  $H_{ub} = 169 \text{ kN (38.0 kips)}$ , the shear force along the gusset-to-beam interface can be computed as follows:

$$f_v = \frac{169 \text{ kN}}{236 \text{ mm}} = 0.716 \text{ kN/mm (4.09 kips/in.)}$$

Also, since  $V_{ub} = 189 \text{ kN}$ , the tension force along the gusset-to-beam interface can be computed as follows:

$$f_a = \frac{189 \text{ kN}}{236 \text{ mm}} = 0.801 \text{ kN/mm (4.57 kips/in.)}$$

Furthermore, since there is no in-plane bending stress along the gusset-to-beam interface,  $f_b = 0 \text{ KN/mm}$ . Therefore, the peak and average forces at the gusset-to-beam interface [9] can be computed as follows:

$$f_{peak} = \sqrt{f_v^2 + (f_a + f_b)^2} = \sqrt{f_v^2 + f_a^2} = 1.074 \text{ kN/mm (6.13 kips/in.)}$$

$$f_{avg} = (1/2) \left( f_{peak} + \sqrt{f_v^2 + (f_a - f_b)^2} \right) = \sqrt{f_v^2 + f_a^2} = 1.074 \text{ kN/mm (6.13 kips/in.)}$$

Note that when the gusset is directly welded to the beam or column, the connection should be designed for the larger of the peak stress and 1.25 times the average stress, but the weld size need not be larger than that required to develop the strength of the gusset [9]. Therefore, the connection should be designed for the stress of 1.343 kN/mm (7.67 kips/in.) ( $= 1.25 \times 1.074$  kN/mm), but need not be larger than 2.678 kN/mm (15.2 kips/in.). Note that  $\phi t F_y = 0.9$  (12 mm) (248 MPa) = 2.678 kN/mm ( $\phi t F_y = 0.9$  (0.47 in.) (36 ksi) = 15.2 kips/in.).

Using a 6 mm fillet weld, the design strength of the fillet weld for the gusset-to-beam (W10×68) flange connection can be computed as follows:

$$\phi R_n = 2 \times 0.75(0.6 F_{EXX} t_e) = 2 \times 0.75 \left[ 0.6 \times 0.483 \times \frac{\sqrt{2}}{2} \times 6 \right] = 1.844 \text{ kN/mm} \quad (10.53 \text{ kips/in.})$$

Since the design strength is larger than the required strength of 1.343 kN/mm (7.67 kips/in.), the horizontal fillet weld for the gusset-to-beam flange connection is adequate. The same approach can be repeated to determine the adequacy of the vertical fillet weld for the gusset-to-column flange connection.

Figure 5 summarizes the results of the above hand-calculated approach. Note that the hand-calculated approach neglects the effects of frame deformation on the gusset plate.

### 3. INVESTIGATION OF GUSSET PLATE CONNECTION USING FINITE ELEMENT METHOD

The following investigation procedure illustrates the use of the finite element method for the determination of the adequacy of the gusset plate connection, which was designed using the hand-calculated approach presented above. Nonlinear static analyses have been conducted using the computer software NISA/DISPLAY [11] for the finite element approaches. The elastic, linear hardening stress-strain curve (derived from Salmon et al. [12]), with  $F_y = 248$  MPa (36 ksi), corresponding to a strain of 0.00124 mm/mm (in./in.) and  $F_u = 400$  MPa (58 ksi), corresponding to a strain of 0.185 mm/mm (in./in.), has been used as the material property for the A36 steel. Assuming that the E7018 electrode was used for the fillet weld, the elastic, linear hardening stress-strain curve (derived from the Lincoln Electric Company [13]), with  $F_y = 448$  MPa (65 ksi), corresponding to a strain of 0.00224 mm/mm (in./in.) and  $F_u = 510$  MPa (74 ksi), corresponding to a strain of 0.15 mm/mm (in./in.), has been used as the material property for the fillet weld. In the strain-hardening range, the stress again increases and continues up to the tensile strength. In this paper, the elastic, linear hardening stress-strain curves were used in order to conduct the nonlinear static finite element analyses, as well as to determine the actual location of the maximum first-principal stress (which is related to the occurrence of fracture if the stress reaches the tensile strength, the limiting value in tension) in the gusset plate. Two approaches have been used for the investigation; one neglects the effects of frame deformation on the gusset plate while the other one considers the effects.

*Finite element approach I - neglecting the effects of frame deformation on the gusset plate:*

The lower left-hand quarter portion of the braced frame shown in Figure 4 was used for the development of the finite element model as shown in Figure 8. The model was made of 3-D solid elements. A pinned condition was used at the free end of the beam and column as well as at the base of the gusset-beam-column connection. In this model, an additional plate was added to the base of the gusset-beam-column connection in order to mitigate the stress concentration caused by the pinned support [Figure 8(a)].

A load increment was applied at the end of the bracing element. As the load gradually increased, the stress concentration gradually accumulated at the end of the welded joint, as well as at the start of the welded joint (Figures 9, 10, and 11). When the load applied to the bracing element reached 507 kN (114 kips), as shown in Figure 8(b), the von Mises stress reached 215 MPa (31.2 ksi) and 286 MPa (41.5 ksi) at the end of the welded joint and the start of the welded joint, respectively, as shown in Figure 10. Meanwhile, the first-principal stress reached 223 MPa (32.3 ksi) and 219 MPa (31.8 ksi) at the end of the welded joint and the start of the welded joint, respectively, as shown in Figure 11.

The above results indicate that when the load applied to the bracing element reaches 507 kN (114 kips), the maximum von Mises stress located at the start of the welded joint reaches 286 MPa (41.5 ksi), which is larger than 248 MPa (36 ksi) (the specified minimum yield stress of the A36 steel). Therefore, yielding is expected to initiate at the start of the welded joint. However, since the maximum first-principal stress, 223 MPa (32.3 ksi), located at the end of the welded joint is less than 400 MPa (= 58 ksi, the specified minimum tensile strength of the A36 steel), fracturing is not expected to happen in the gusset plate.

Moreover, when the load applied to the bracing element reaches 507 kN (114 kips), the shear stress ( $S_{xy}$ ) distributions along the gusset edges are shown in Figure 12, the normal stress ( $S_{xx}$ ) distribution along the vertical gusset edge is shown in Figure 13, and the normal stress ( $S_{yy}$ ) distribution along the horizontal gusset edge is shown in Figure 14. The resultant forces for the shear and tensile stresses are shown in Figure 15.

Figure 15 indicates that the resultant shear force acting along the horizontal and vertical gusset edges is 177 kN (39.8 kips), which is about 5% larger than that obtained from the hand-calculated approach (169 kN (38.0 kips)), as shown in the design example. Also, the resultant tensile force acting on the horizontal and vertical edges is 181 kN (40.7 kips), which is about 4% less than that obtained from the hand-calculated approach (189 kN (42.5 kips)), as shown in the design example.

Figure 15 also indicates that the resultant tensile force acting on the horizontal gusset edge is located outside the distance ' $\alpha$ ' (the distance from the face of the column flange to the centroid of the gusset-to-beam connection) and the resultant tensile force acting on the vertical gusset edge is located outside the distance ' $\beta$ ' (the distance from the face of the beam flange to the centroid of the gusset-to-column connection). Note that as shown in Figure 7, the hand-calculated approach assumes that the resultant tensile force ( $V_{ub}$ ) acting on the horizontal gusset edge is located at the centroid of the gusset-to-beam connection, while the resultant tensile force ( $H_{uc}$ ) acting on the vertical gusset edge is located at the centroid of the gusset-to-column connection.

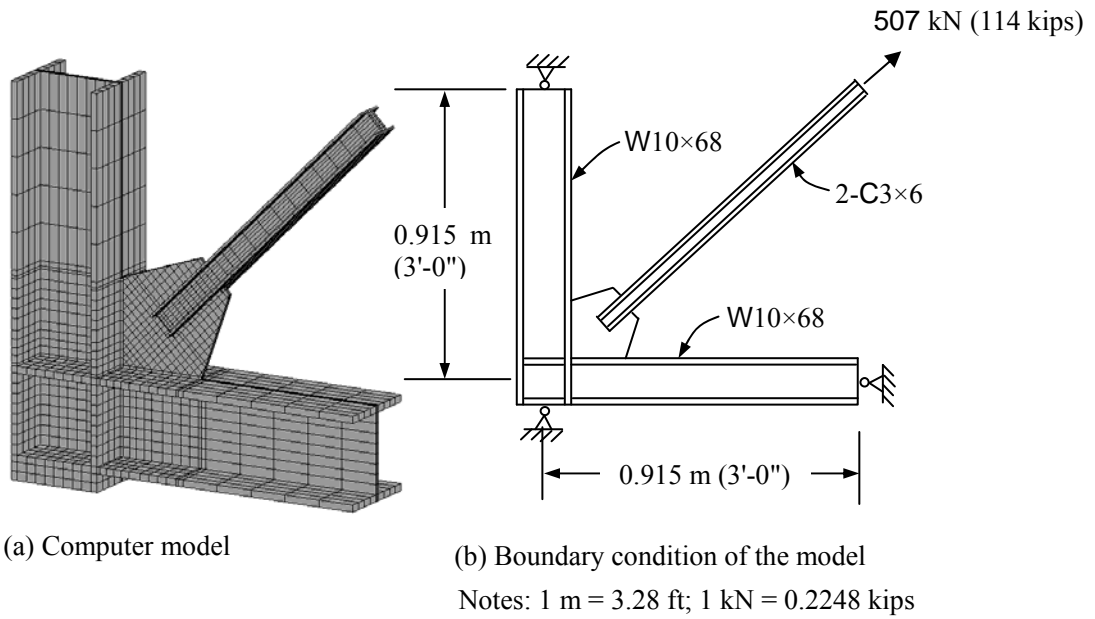


Figure 8. Finite Element Model Neglecting Frame Deformation Effects

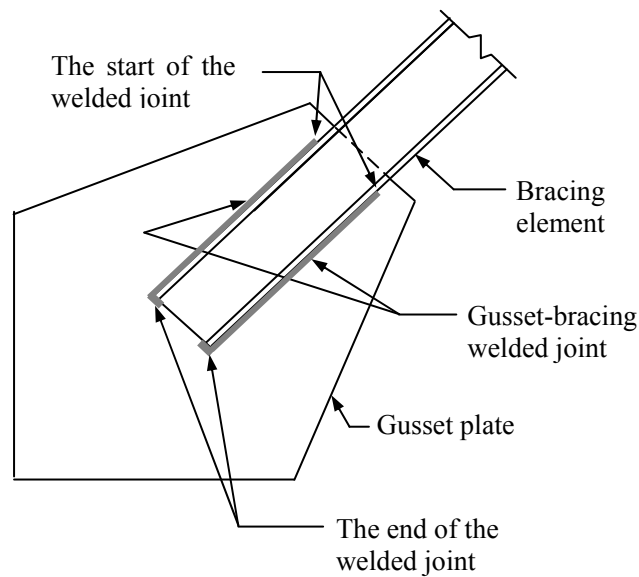


Figure 9. Gusset Plate-bracing Element Welded Joint

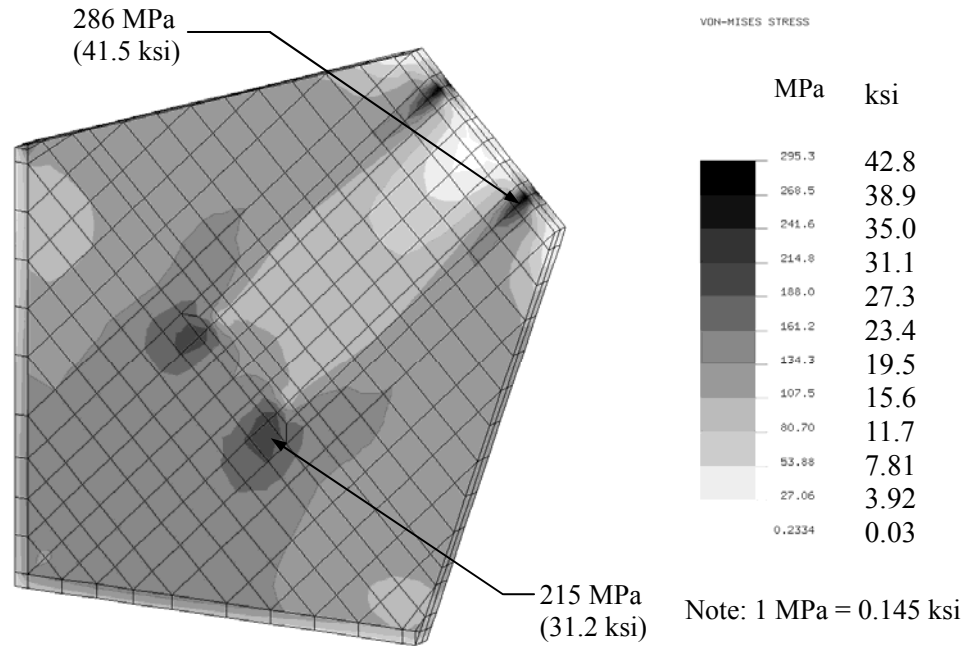


Figure 10. Von Mises Stress Distribution on Gusset Plate Neglecting Frame Deformation Effects

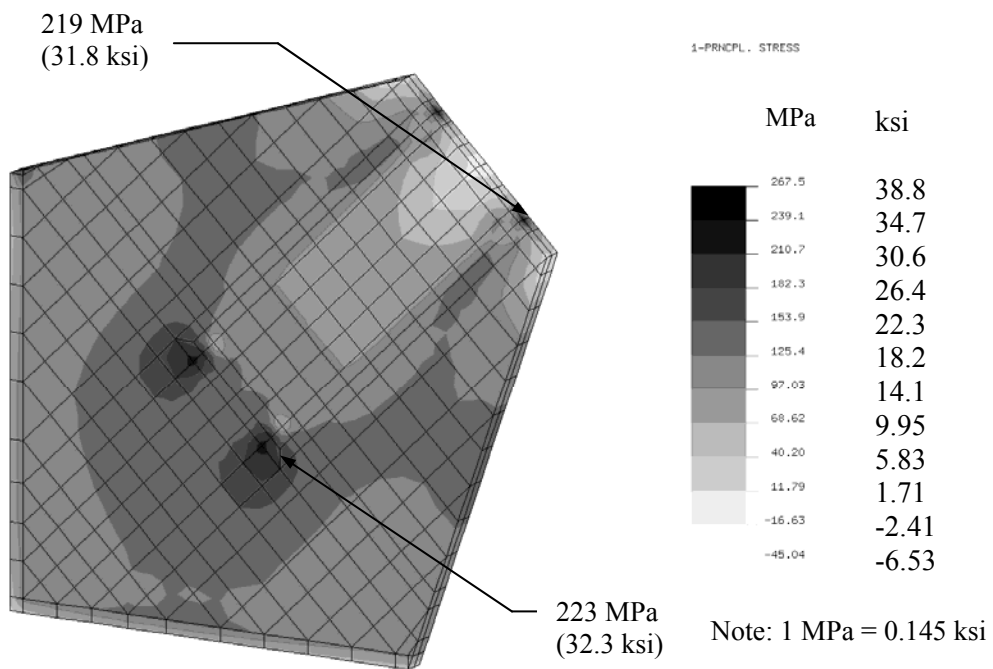


Figure 11. First-principal Stress Distribution on Gusset Plate Neglecting Frame Deformation Effects

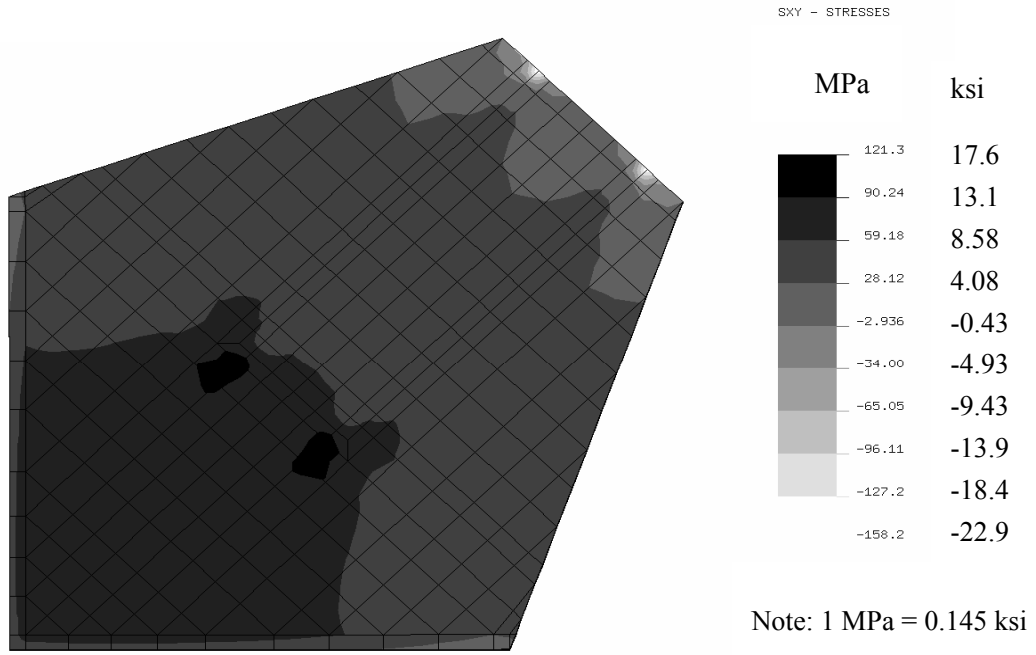


Figure 12. Shear Stress Distributions on Gusset Edges Neglecting Frame Deformation Effects

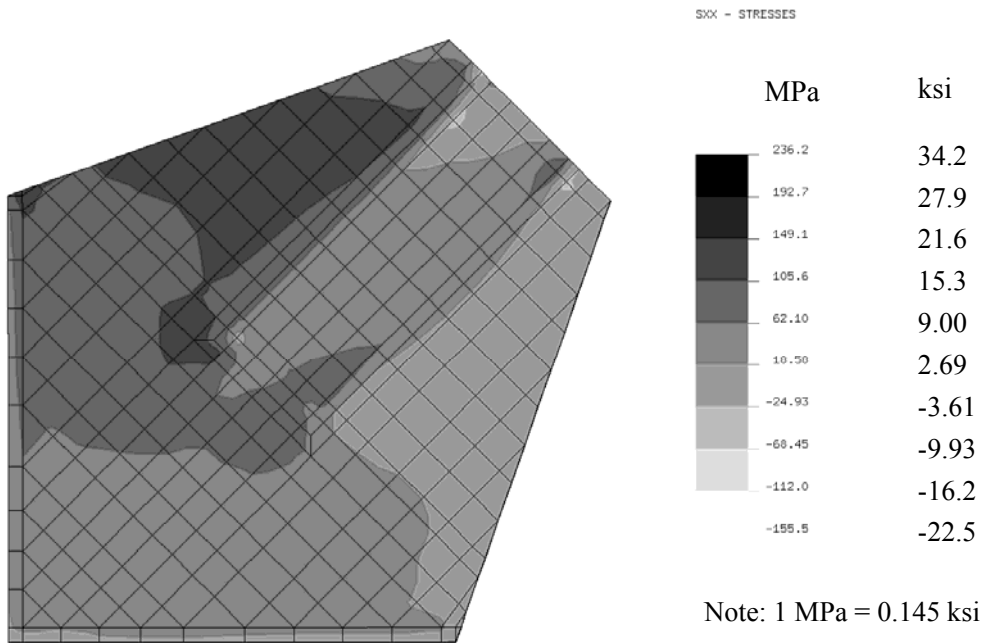


Figure 13. Normal Stress Distribution on Vertical Gusset Edge Neglecting Frame Deformation Effects

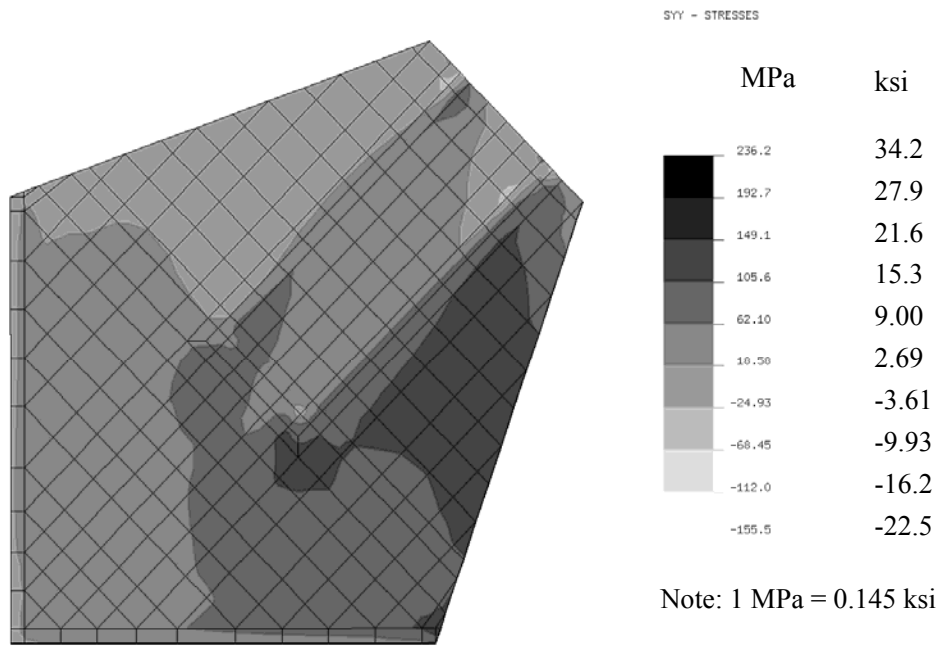


Figure 14. Normal Stress Distribution on Horizontal Gusset Edge Neglecting Frame Deformation Effects

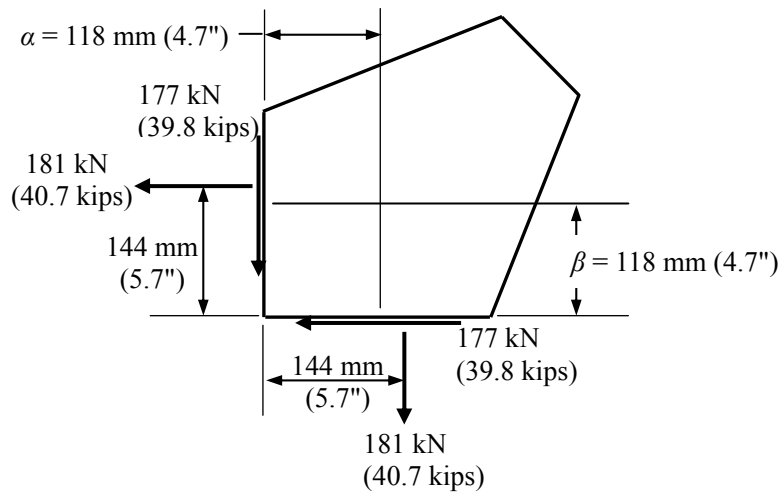


Figure 15. Resultant Shear and Tensile Forces Acting on Gusset Edges Neglecting Frame Deformation Effects

*Finite element approach II - considering the effects of frame deformation on the gusset plate:*

The entire braced frame shown in Figure 4 was used for the development of the finite element model as shown in Figure 16(a). A pinned condition was used at the base of the gusset-beam-column connection, as well as at the base of the beam-column connection. In this model, an additional plate was added to each of the bases in order to mitigate the stress concentrations caused by the pinned supports.

A load increment was applied horizontally at the upper right-hand corner of the frame as shown in Figures 4 and 16(b). When the applied load reached 485 kN (109 kips), the tensile force in the bracing element reached 507 kN (114 kips). Meanwhile, the shear forces in the columns (the vertical elements) and beams (the horizontal elements) were developed. Note that these shear forces caused deformations of the column and the beam which in turn produced compressive stresses in the gusset plate. The model shown in Figure 16(a), therefore, considers the frame deformation effects on the gusset plate. The frame deformation effects on the gusset plate can be illustrated using the free-body diagram as shown in Figure 16(c). The applied shear force in the column and the reaction shear force in the beam cause the deflections of the column and the beam, which in turn produce compressive stresses in the gusset plate.

The von Mises stress distribution in the gusset plate obtained from this approach is shown in Figure 17. The maximum von Mises stress located at the start of the welded joint and the end of the welded joint reached 295 MPa (42.8 ksi) and 266 MPa (38.6 ksi), respectively. Since both of them are larger than 248 MPa (36 ksi), yielding is expected to initiate at the start of the welded joint and the end of the welded joint. Meanwhile, as shown in Figure 18, the maximum first-principal stress, 251 MPa (36.4 ksi), located at the end of the welded joint is less than 400 MPa (58 ksi), fracturing is not expected to happen in the gusset plate.

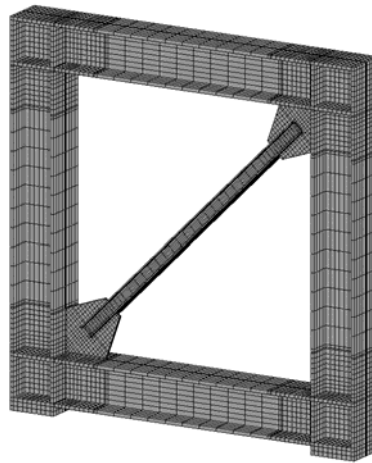
The above finite element approaches conclude that the maximum von Mises stress obtained from Approach II is about 24% more than that obtained from Approach I for the location at the end of the welded joint. Also, the maximum first-principal stress obtained from Approach II is about 13% more than that obtained from Approach I. The increases in stress were caused by the effects of frame deformation on the gusset plate.

Moreover, when the load applied to the bracing element reaches 507 kN (114 kips), the shear stress ( $S_{xy}$ ) distributions along the gusset edges are shown in Figure 19, the normal stress ( $S_{xx}$ ) distribution along the vertical gusset edge is shown in Figure 20, and the normal stress ( $S_{yy}$ ) distribution along the horizontal gusset edge is shown in Figure 21. The resultant forces for the shear and tensile stresses are shown in Figure 22.

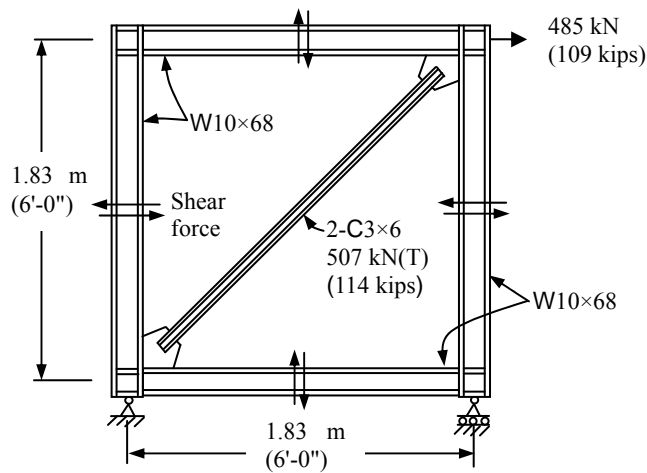
Figure 22 indicates that the resultant shear force acting along the horizontal and vertical gusset edges is 284 kN (63.8 kips), which is about 68% larger than that obtained from the hand-calculated approach (169 kN (38.0 kips)), as shown in the design example. Also, the resultant tensile force acting on the horizontal and vertical edges is 74 kN (16.6 kips), which is about 61% less than that obtained from the hand-calculated approach (189 kN (42.5 kips)), as shown in the design example.

Figure 22 also indicates that the resultant tensile force acting on the horizontal gusset edge is located inside the distance ' $\alpha$ ' (the distance from the face of the column flange to the centroid of the gusset-to-beam connection) and the resultant tensile force acting on the vertical gusset edge is located inside the distance ' $\beta$ ' (the distance from the face of the beam flange to the centroid of the gusset-to-column connection).

Also, referring to Figure 22, the combined effects of the factored tension and shear forces at the vertical and horizontal gusset edges can be computed (using the von Mises yield criterion [1]) as  $P_u = \sqrt{(74 \text{ kN})^2 + 3(284 \text{ kN})^2} = 497 \text{ kN}$  (112 kips), which is about 43% more than that obtained from hand-calculated approach (348 kN (78 kips)), which neglected the effects of frame deformation, as shown in the design example. Therefore, the above finite element approaches also conclude that neglecting the effects of frame deformation may result in significant underestimation of the combined effects of the factored tension and shear forces at the gusset edges.

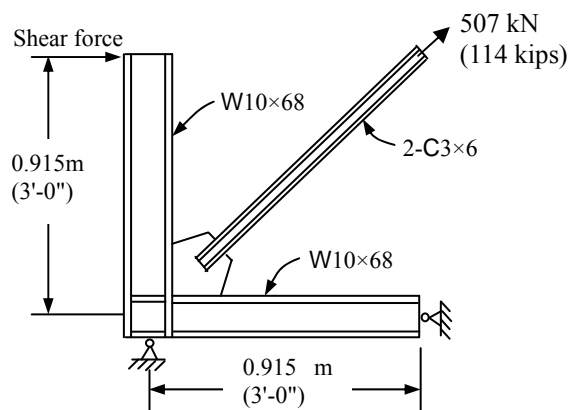


(a) Computer model



Notes: 1 m = 3.28 ft; 1 kN = 0.2248 kips

(b) Applied load



Notes: 1 m = 3.28 ft; 1 kN = 0.2248 kips

(c) Free body diagram of the model

Figure 16. Finite Element Model Considering Frame Deformation Effects

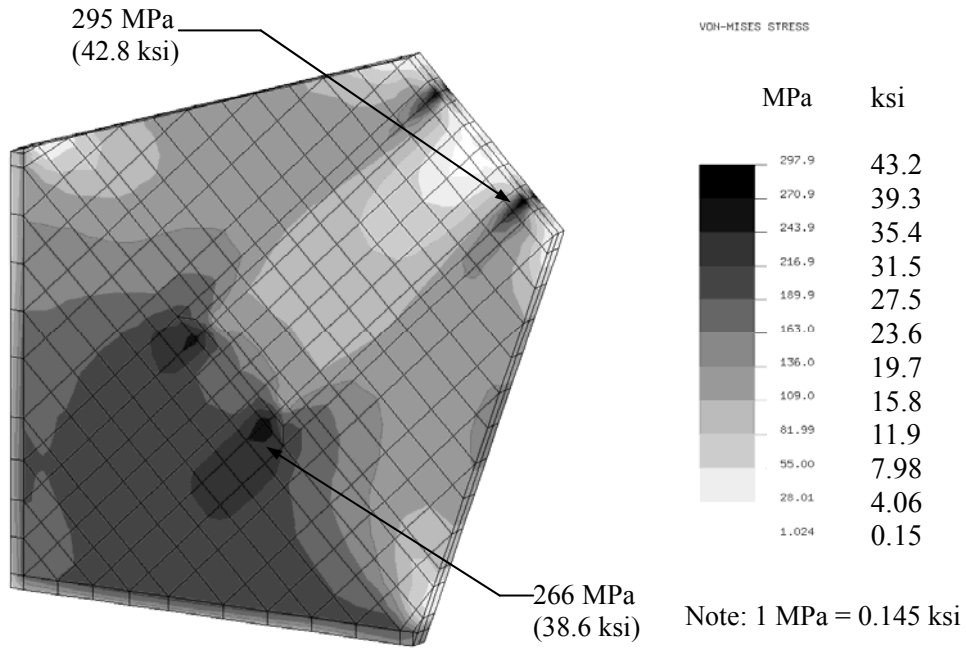


Figure 17. Von Mises Stress Distribution on Gusset Plate Considering Frame Deformation Effects

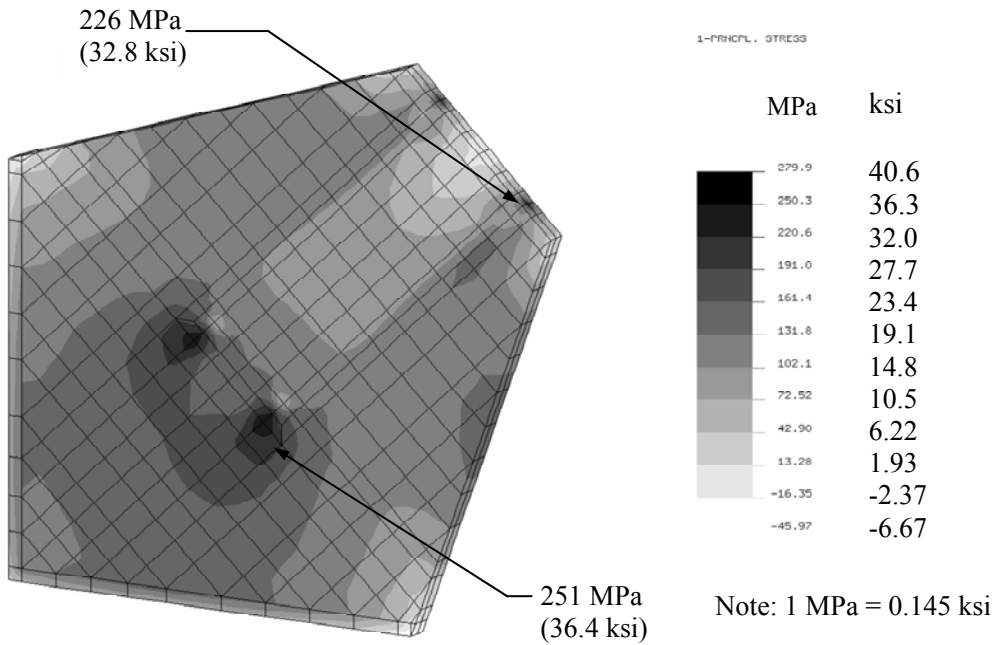


Figure 18. First-principal Stress Distribution on Gusset Plate Considering Frame Deformation Effects

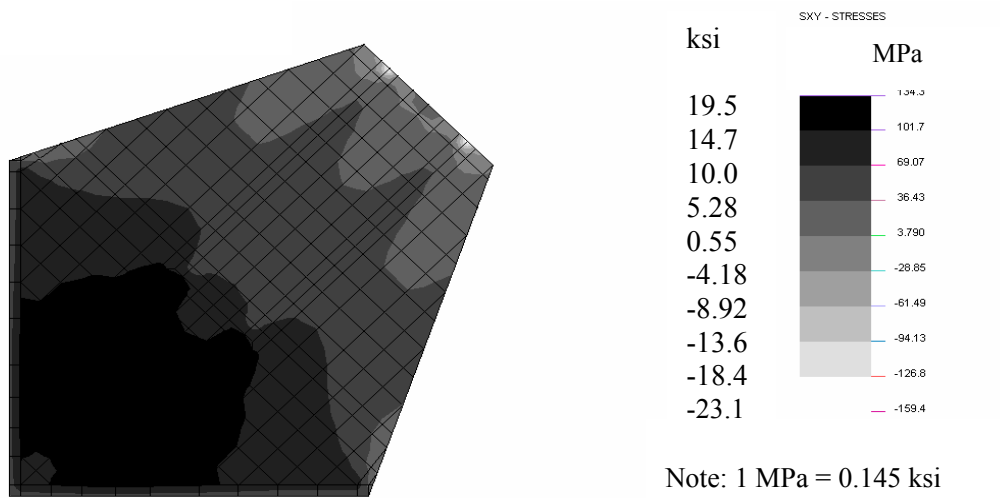


Figure 19. Shear Stress Distributions on Gusset Edges Considering Frame Deformation Effects

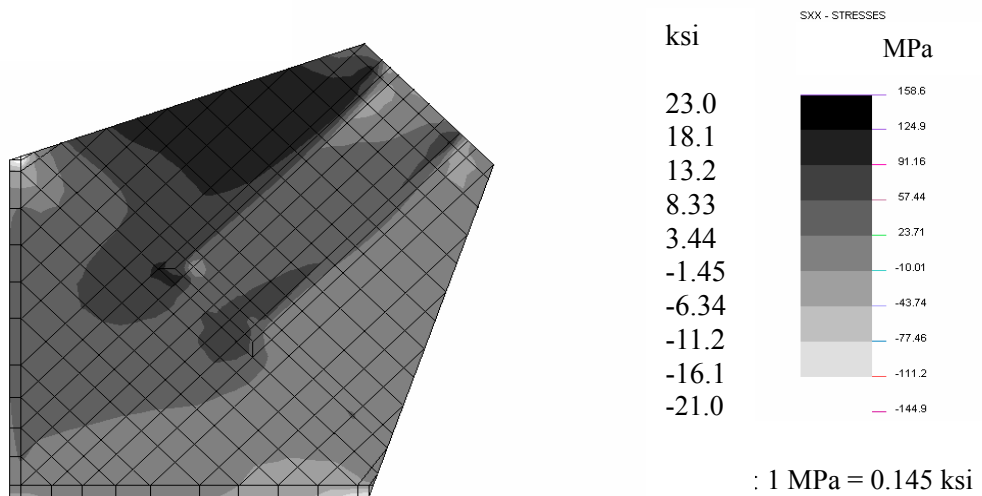


Figure 20. Normal Stress Distribution on Vertical Gusset Edge Considering Frame Deformation Effects

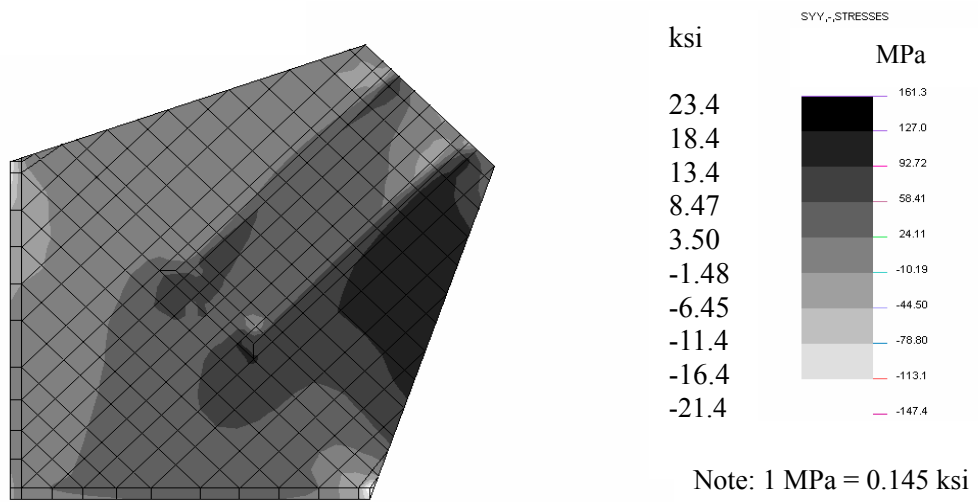


Figure 21. Normal Stress Distribution on Horizontal Gusset Edge Considering Frame Deformation Effects

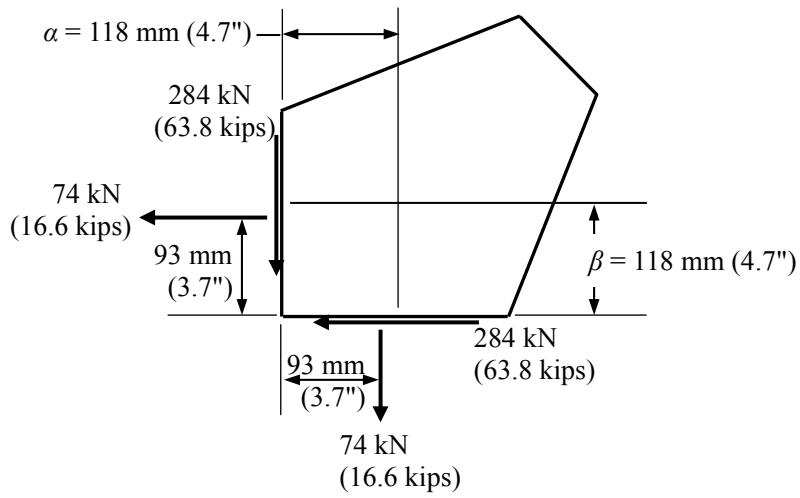


Figure 22. Resultant Shear and Tensile Forces Acting on Gusset Edges Considering Frame Deformation Effects

#### 4. DISCUSSION OF THE RESULTS

The results obtained from above indicate that significant increases in stress occurred at the end of the welded joint caused by the frame deformation effects on the gusset plate. Therefore, the hand-calculated approach, which neglects the frame deformation effects, may result in an under-design of the gusset plate connection. The following illustrates an under designed example caused by neglecting the deformation effects on the gusset plate:

Assume that ASTM A572 Grade 50 steel [ $F_y = 345$  MPa (50 ksi);  $F_u = 448$  MPa (65 ksi)] is used for the steel elements and the gusset plates as shown in Figure 4. Also assume that the factored tensile force,  $P_u$ , applied to the bracing element, is 705 kN (158 kips) (note that the factored tensile force applied to the bracing element using A36 steel was 507 kN (114 kips)). The required thickness of the gusset plate can be determined to be 9 mm ( $^{11}/_{32}$  in.) (note that the thickness for the gusset plate using A36 steel was determined to be 12 mm ( $^{15}/_{32}$  in.)) using Eq. 1 (note that  $R_y = 1.1$  for ASTM A572 Grade 50 steel [10]) of the hand-calculated approach, which neglected the frame deformation effects.

The maximum first-principal stress located at the end of the welded joint of the A572, Grade 50 gusset plate, therefore, can be estimated to be about 413 MPa (59.9 ksi) [= 223 MPa  $\times$  (12 mm / 9 mm)  $\times$  (705 kN / 507 kN)] using the finite element approach I which neglects the effects of frame deformation. Note that the 223 MPa (32.3 ksi) is the maximum first-principal stress at the end of the welded joint of the A36 gusset plate, as shown in Figure 11, which neglected frame deformation effects. Also, the maximum first-principal stress located at the end of the welded joint of the A572 Grade 50 gusset plate, therefore, can be estimated to be about 465 MPa (67.4 ksi) [= 251 MPa  $\times$  (12 mm / 9 mm)  $\times$  (705 kN / 507 kN)] using the finite element approach II which considers the effects of frame deformation. Note that the 251 MPa (36.4 ksi) is the maximum first-principal stress at the end of the welded joint of the A36 gusset plate, as shown in Figure 18, which considered frame deformation effects. Since 465 MPa (67.4 ksi) is larger than 448 MPa (65.0 ksi) (the specified minimum tensile strength of the ASTM A572, Grade 50 steel), fracturing may occur at the end of the weld joint of the A572, Grade 50 gusset plate. The above example indicates that the hand-calculated approach, which neglects the effects of frame deformation, may result in an under-design of the gusset plate.

Note that if A992 steel (instead of A36 steel) is used for the beam and column shown in Figure 16, the effects of frame deformation on the stress distribution in gusset plates will not change since the maximum von Mises stress in the column and beam caused by the applied force (485 kN (109 kips)) is below 248 MPa (36 ksi, the yielding stress of A36 steel).

In order to validate the finite element procedure presented in this paper, the following investigation has been conducted:

First, a compressive load increment was applied at the end of the bracing element as shown in Figure 8(a). As the load gradually increased, the stress concentration gradually accumulated at the end of the welded joint. When the load applied to the bracing element reached 198 kN (44.5 kips) (the approximate ultimate compressive capacity of the bracing element), the von Mises stress reached 84 MPa (12.2 ksi) at the end of the welded joint. Note that there is no frame deformation effect on the gusset plate in this case.

Second, a load increment was applied horizontally toward the upper right-hand corner of the frame as shown in Figure 16(a). When the applied load reached 189 kN (42.5 kips), the compressive force in the bracing element reached 198 kN (44.5 kips). Meanwhile, the von Mises stress reached 103

MPa (14.9 ksi) at the end of the welded joint. Note that the increase in von Mises stress at the end of the welded joint was caused by the effects of frame deformation on the gusset plate.

The compressive capacity of the gusset plate decreased due to the increase in von Mises stress at the end of the connected joint caused by the effects of frame deformation on the gusset plate. This result agrees with that of the full-scale tests conducted by Cheng, Grondin, and Yam [5].

## 5. CONCLUSIONS

This paper has focused on the effects of the frame deformation on welded gusset plates for diagonal bracing elements loaded in tension. A design example for a brace-beam-column gusset plate connection using the traditional hand-calculated approach, which neglects the frame deformation effects, has been given in this paper. Also, two finite element approaches have been used to investigate the adequacy of the gusset plate designed by using the hand-calculated approach. The first approach has neglected the frame deformation effects while the second approach has considered the effects.

The following conclusions are inferred from this study: (1) When a diagonal bracing member is subjected to a tensile force, the gusset plate will be stressed in tension, shear, and compression; the tension and shear stresses in the gusset plate are caused by the tensile force in the bracing member, while the compression stress in the gusset plate is caused by the deflections of the beam and column of the braced frame. (2) When the effects of frame deformation are considered, the resultant shear forces acting along the horizontal and vertical gusset edges will be increased while the resultant tensile forces acting on the horizontal and vertical gusset edges will be decreased. As a result, the combined effects of the factored tension and shear forces at the gusset edges will be increased. (3) Both the von Mises and first-principal stresses located at the end of the welded joint (which is in the Whitmore section) will be increased when the effects of the frame deformation are considered. Therefore, the traditional hand-calculated approach illustrated in this paper, which neglected the frame deformation effects, may result in an under-design of the gusset plate. (4) The increases in stress at the end of the weld joint caused by the frame deformation effects vary widely in magnitude and depend on the following factors: (a) the relative stiffness between the beam (bending stiffness), the column (bending stiffness), and the bracing element (axial deformation stiffness), (b) the configuration of the gusset plate, and (c) the degree of angle between the center line of the column and the center line of the bracing element (or the degree of angle between the center line of the beam and the center line of the bracing element).

All possible conditions of the relative stiffness, the gusset plate configuration, and the slope of the bracing element, therefore, need to be statistically studied in order to determine the maximum possible increases in stress caused by the frame deformation effects.

Due to the frame deformation effects, a rigid frame with brace-beam-column connections is highly indeterminate. Any simplifying hand-calculated approaches could be too approximate to be used for the final design of the gusset plate. The finite element analysis considering frame deformation effects, therefore, is recommended for the design of gusset plates for brace-beam-column connections. Also, this paper concludes that higher ductile structural steel (for example, A36 steel) can mitigate the frame deformation effects better than A572 Grade 50 steel.

## NOTATION

The following symbols are used in this paper:

$A_e$	=	area of the Whitmore effective section of a gusset plate
$A_g$	=	gross area
$A_n$	=	net area
$e_b$	=	one-half the depth of the beam being used
$e_c$	=	one-half the depth of the column being used
$F_{EXX}$	=	weld metal tensile strength
$F_u$	=	specified minimum tensile strength of the type of steel being used
$F_y$	=	specified minimum yield stress of the type of steel being used
$f_a$	=	tension force along the gusset-to-beam (or column) interface
$f_{avg}$	=	average force at the gusset-to-beam (or column) interface
$f_b$	=	in-plane bending stress along the gusset-to-beam (or column) interface
$f_{peak}$	=	peak force at the gusset-to-beam (or column) interface
$f_v$	=	shear force along the gusset-to-beam (or column) interface
$H_{ub}$	=	factored shear force at the gusset-to-beam connection
$H_{uc}$	=	factored axial force at the gusset-to-column connection
$l$	=	length of weld
$l_w$	=	Whitmore effective width of a plate
$P_u$	=	factored load
$R_y$	=	ratio of the expected yield strength to the specified minimum yield strength of the grade of steel to be used
$t$	=	thickness of a gusset plate
$t_e$	=	effective throat of fillet weld
$U$	=	reduction coefficient, used in calculating effective net area
$V_{ub}$	=	factored axial force at the gusset-to-beam connection
$V_{uc}$	=	factored shear force at the gusset-to-column connection
$\bar{x}$	=	horizontal distance from the outer edge of a channel web to its centroid
$\alpha$	=	distance from the face of the column flange to the centroid of the gusset-to-beam connection
$\beta$	=	distance from the face of the beam flange to the centroid of the gusset-to-column connection
$r$	=	distance from the working point to the centroid of the gusset plate connection
$\phi P_n$	=	design strength
$\phi_t P_n$	=	design tensile strength
$\phi R_n$	=	design strength of the fillet weld for the gusset-to-beam (or column) flange connection

## REFERENCES

- [1] SEAOC, "2006 IBC Structural/Seismic Design Manual, Building Design Examples for Steel and Concrete", Structural Engineers Association of California, Sacramento, Calif., 2006.
- [2] Thornton, W.A., "Bracing Connections for Heavy Construction", Engineering Journal, American Institute of Steel Construction, 3<sup>rd</sup> Quarter, 1984, Vol. 21, No. 3, pp. 139-148.
- [3] Richard, R., "Analysis of Large Bracing Connection Designs for Heavy Construction", Proceedings of the 1986 National Engineering Conference, AISC, Nashville, June 12-14, 1986.

- [4] Astaneh-Asl, A., "Seismic Behavior and Design of Gusset Plates", Steel Tips Report, Structural Steel Educational Council, Moraga, Calif., 1998.
- [5] Cheng, J.J.R., Grondin, G.Y. and Yam, M.C.H., "Design and Behavior of Gusset Plate Connections", Steel Connection IV Workshop, Roanoke, VA., 2000.
- [6] Whitmore, R.E., "Experimental Investigation of Stresses in Gusset Plates", Bulletin No. 16, Engineering Experiment Station, Univ. of Tennessee, TN., 1952.
- [7] AISC, "Steel Construction Manual", 14<sup>th</sup> Edition, American Institute of Steel Construction, Inc., Chicago, IL., 2011.
- [8] Thornton, W.A., "On the Analysis and Design of Bracing Connections", National Steel Construction Conference Proceedings, AISC, Chicago, IL., 1991, pp. 26.1-26.33.
- [9] AISC and SSEC, "Seismic Design Manual", American Institute of Steel Construction, Inc., Chicago, IL., 2006.
- [10] AISC, "Seismic Provisions for Structural Steel Buildings", American Institute of Steel Construction, Inc., Chicago, IL., 2005.
- [11] NISA, "NISA User's Manual", Engineering Mechanics Research Corporation, Troy, Michigan, 1998.
- [12] Salmon, C.G., Johnson, J.E. and Malhas F.A., "Steel structures, design and behavior", 5<sup>th</sup> Ed., Pearson Prentice Hall, Upper Saddle River, N.J., 2009.
- [13] The Lincoln Electric Company, "The Procedure Handbook of Arc Welding", 13<sup>th</sup> Ed., The Lincoln Electric Company, Cleveland, Ohio., 1994.

# VISCOUS DISSIPATIVE, DUCTILITY-BASED AND ELASTIC BRACING DESIGN SOLUTIONS FOR AN INDOOR SPORTS STEEL BUILDING

Stefano Sorace<sup>1,\*</sup>, Gloria Terenzi<sup>2</sup> and Gianluca Bertino<sup>1</sup>

<sup>1</sup> *Department of Civil Engineering and Architecture, University of Udine  
Via delle Scienze 208, 33100 Udine, Italy*

<sup>2</sup> *Department of Civil and Environmental Engineering, University of Florence  
Via S. Marta 3, 50139 Florence, Italy*

*\*(Corresponding author: E-mail: stefano.sorace@uniud.it)*

*Received: 21 December 2011; Revised: 28 June 2012; Accepted: 31 July 2012*

---

**ABSTRACT:** Three bracing solutions are developed for an indoor sports facility representative of the most recent architectural design trends for recreational and commercial steel buildings. A viscous-dissipative bracing system incorporating pressurized fluid viscous spring-dampers is assumed as anti-seismic technology for the first solution. Thanks to the protective capacities of this technology, non-structural and structural operational performance levels are pursued for the building up to the maximum considered design earthquake level. A traditional concentric X-shaped configuration is selected for the second and third solution, which differ from each other in the design strategy adopted. In the first case, a ductility-based solution is chosen, by adopting a basic behaviour factor equal to 4, reduced by 20% to take into account the structural irregularity caused by the eccentric position of the intermediate floor of the building. In the second case, the same performance objectives as originally formulated for the viscous-dissipative design hypothesis are assumed, fixing the behaviour factor at 1. The resulting dimensions of the members, and the total weight and cost of the steel structure are compared for the three layouts. A substantially higher seismic performance at all normative design levels at a comparable cost; and a cut in the cost by about 50%, with an improved look of the structure due to the remarkably greater slenderness of the constituting members, come out for the viscous-dissipative bracing design as compared to the ductility-based and elastic X-bracing solutions, respectively.

**Keywords:** Steel structures, Seismic protection, Fluid viscous dissipative bracing, Damping, Concentric bracing, Ductility-based design, Elastic design

---

## 1. INTRODUCTION

The most recent trends in the design of steel buildings favour transparency, lightness and aerial effects, which are obtained by including large glazed façades, by increasing the free spans of floors and roofs, and by implementing innovative architectural shapes and finishes. These emerging trends compel structural designers to reduce further the architectural impact of load-bearing systems, while at the same time meeting the high performance levels required by the latest generation of Technical and Seismic Standards on steel construction.

A satisfactory balance between the issues of high structural performance and limited architectural impact is a very demanding challenge for structural engineers, especially for buildings situated in medium-to-high seismicity zones. The normative solution to this problem was traditionally represented by the design of dissipative structures, i.e. structures that are able to dissipate energy by means of their ductile hysteretic (plastic) behaviour. According to this ductility-based design approach, the seismic forces for the verifications at the ultimate limit states (i.e. Life Safety — LS and Collapse Prevention — CP performance levels) are computed by scaling relevant pseudo-acceleration response spectra by behaviour factors proportional to the ductility resources of the structural systems. This allows keeping the size of structural members within acceptably small limits, while at the same time planning the plasticization, and thus significant damage, of their

critical (dissipative) zones under the highest earthquake levels considered in the design process. This implies that considerable repair costs after medium-intensity seismic events, and in many cases the complete demolition and rebuilding of the structure after severe seismic events, must be accepted.

Over the past two decades, this traditional approach has been revised for strategic buildings, where appreciable damage even at the highest design earthquake levels must be avoided. This class of buildings includes hospitals, barracks, fire-stations, civil protection headquarters, airports, railway stations, industrial plants, broadcasting facilities, etc. Recently, the concept of “strategic” has also been extended to various types of public and private buildings that, whatever their specific function, are likely to play an important role in the immediate post-earthquake emergency phases, e.g. shelter to injured people, and temporary headquarters for the coordination of rescue, assistance and recognition activities. These buildings, which include schools, indoor sports facilities, gyms, exhibition halls, etc., continue to be designed for their normative nominal structural life and their specific use (with coefficients of use greater than the ones assigned to ordinary buildings, but lower than the ones of strategic buildings), but with a shift towards higher performance levels, as compared to the seismic response capacities required by the traditional ductility-based design approaches.

New solutions to the combined issues of enhanced seismic performance and reduced dimensional impact for contemporary steel buildings are now offered by advanced seismic protection technologies. Among these technologies, viscous dissipative bracing (VDB) systems — which dissipate seismic energy by means of viscous dampers mounted on the supporting braces, rather than by plasticization of the constituting structural members — generally provide the most viable solutions for steel buildings, as they visually resemble the bracing elements traditionally incorporated in steel structural skeletons to absorb seismic and wind loads. This allows keeping the traditional setup of steel structures substantially unchanged, while reducing, for a predetermined set of performance objectives, the member sections and/or the number of locations where braces are placed, as a consequence of a remarkable reduction in seismic effects produced by the dampers.

Within the wide class of VDB technologies [1-3], a special system incorporating pressurized fluid viscous (FV) devices has been studied for several years by the first two authors of this paper, also in the frame of international research projects. In particular, numerical and analytical modelling; experimental characterization and verification; definition of design procedures; and technical implementation of the protective system have been carried out within these activities [4-8]. Pilot applications have also been developed, with special reference to the seismic retrofit of steel school buildings [9-10].

The study of a novel application, concerning a steel fitness and indoor sports facility in Italy, well representative of the most recent architectural design trends, is presented in this paper. The building constitutes a detailed prototype case study developed within a National Research Project funded by the Italian Department of Civil Protection and dedicated to the advanced seismic protection of structures, with the aim of establishing a benchmark for scholars and designers interested in similar studies and of implementing real applications in the near future. The building is characterized by a single-span roof, open space interiors, continuous floor-to-roof glazed façades, and a perimeter arcade. The architectural design also imposes the smallest possible structural member sizes and the introduction of the lowest possible number of vertical bracing alignments, in order to limit the visual obstruction of the glass façades.

The seismic design hypothesis based on the installation of the VDB system is compared to two X-shaped (concentric) bracing solutions, carried out by following the standard normative ductility-based approach (DBXB hypothesis), and by pursuing an elastic response up to the maximum input earthquake level (EXB hypothesis), respectively. The DBXB solution makes a basis for comparison in terms of performance capacities starting from similar structural member sizes and costs, as determined by a reduction in seismic effects owed to the protective action of the FV dampers, for the VDB design, and by adopting the normative value of the behaviour factor, for the traditional ductility-based design. On the other hand, the EXB hypothesis is developed to compare sizes and costs with the VDB solution, by postulating identical structural and non-structural performance objectives and by pursuing them without scaling dynamic response, i.e. by assuming a behaviour factor equal to 1, in both cases.

The general characteristics of the case study building, the earthquake and performance levels assumed, their relevant limitations, and a synthesis and comparison of sizes, dynamic response and costs of the three design solutions, are presented in the following sections.

## 2. GENERAL CHARACTERISTICS OF THE CASE STUDY BUILDING

The external dimensions of the building are 60 m × 30 m in plan, with a height of 18 m. The arcade is 3 m-wide, which determines net internal dimensions of 54 m × 24 m. An intermediate floor is situated at a height of 6 m on one side, covering a smaller area in plan, equal to 20 m × 24 m. The structural plans of the roof and the floor are shown in Figures 1 and 2. The elevation views in the longitudinal (parallel to y axis in plan) and transversal directions are drawn in Figures 3 and 4. The A-A cross section traced out in Figures 1 and 2 is displayed in Figure 5. Two architectural renderings of the whole building, and three views of the interiors, are reproduced in Figures 6 and 7, respectively. These images show how the structure would look with the X-bracing solutions. Views of a typical internal joint of the roof trusses, identical to the corresponding joint of the floor trusses, and a truss/column/longitudinal beam/arcade beam connection on the roof, are displayed in Figure 8. The latter connection too is identical to the one at the floor level, except for the absence of the arcade beam joining the top of the arcade columns.

The shapes and dimensions of the beams (HEA 180 Italian profiles — roof, HEB 200 — floor), trusses (all tubular sections, sized 244.5 mm — diameter × 8 mm — thickness, for the upper and lower horizontal profiles, and 139.7 mm × 8 mm for the diagonal profiles — roof; 244.5 mm × 10 mm for the upper and lower horizontal profiles, and 139.7 mm × 10 mm for the diagonal profiles — floor), horizontal braces (168.3 mm × 10 mm — roof, 139.7 mm × 12.5 mm — floor), and stairs (columns in 219.1 mm × 5 mm tubular sections, beams in HEA 300 profiles), are identical for the three structural solutions. Indeed, their design is essentially governed by gravity loads, equal to 2.8 kN/m<sup>2</sup> (roof), 3.6 kN/m<sup>2</sup> (floor) and 2 kN/m<sup>2</sup> (stairs) — for dead loads, and 1.1 kN/m<sup>2</sup> (roof) and 5 kN/m<sup>2</sup> (floor and stairs) — for live loads. The arcade columns are not designed for seismic action, which is completely absorbed by the bracing systems, and thus their section (219.1 mm × 5 mm tubular profile) is equal for the three design hypotheses too. Second order effects are computed in the design of these slender columns.

The glazed façades are supported by vertical aluminium trusses, whose base is fixed to the foundation and whose top is hinged to the perimeter beams of the roof structure. The glass panes have 4 fixing points, and are joined each other by “spider”-type connections.

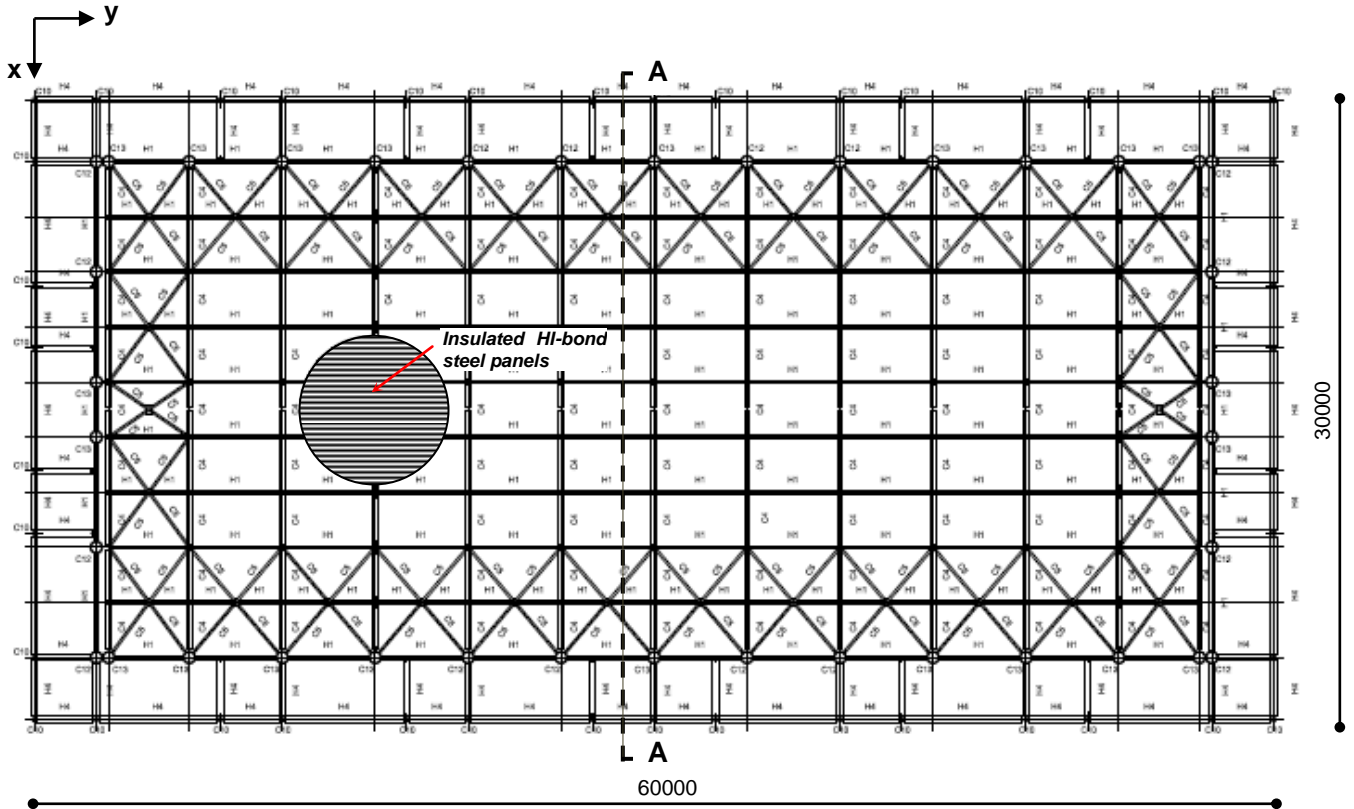


Figure 1. Structural Plan of the Roof

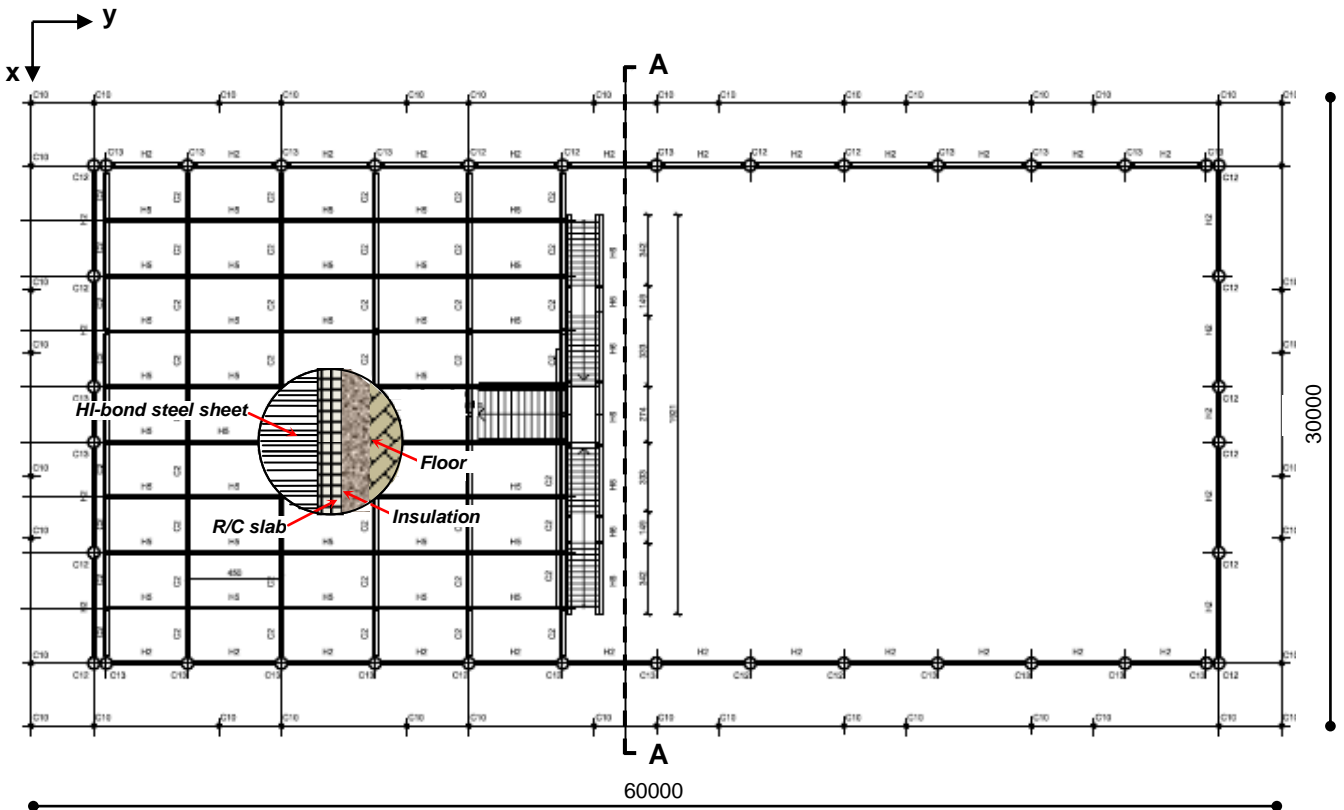


Figure 2. Structural Plan of the Floor

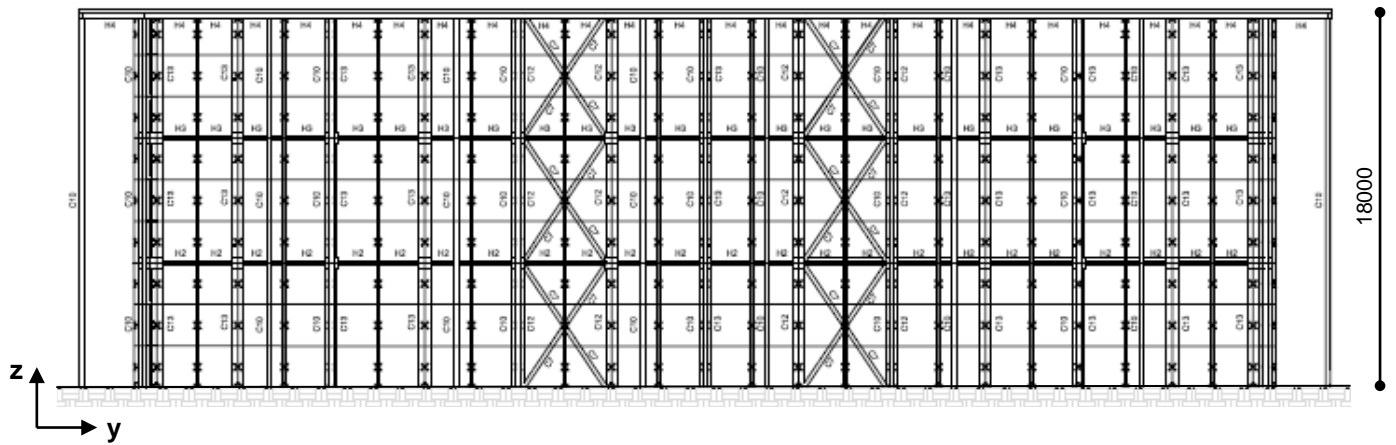


Figure 3. Longitudinal Elevation View (X-bracing)

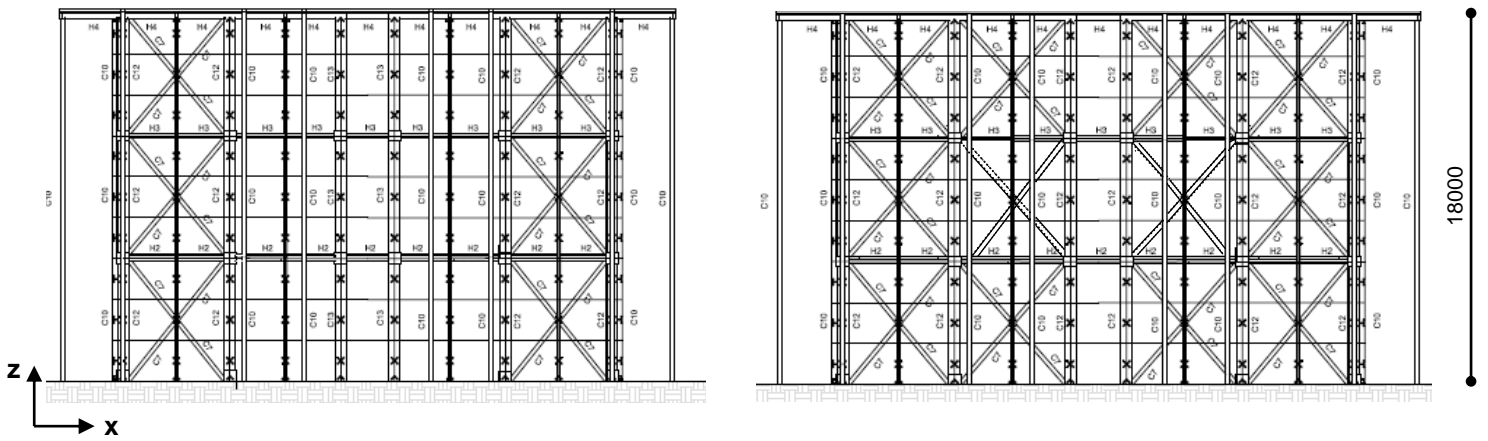


Figure 4. Transversal Elevation Views (X-bracing) – Left: Floor Side; Right: Opposite Side

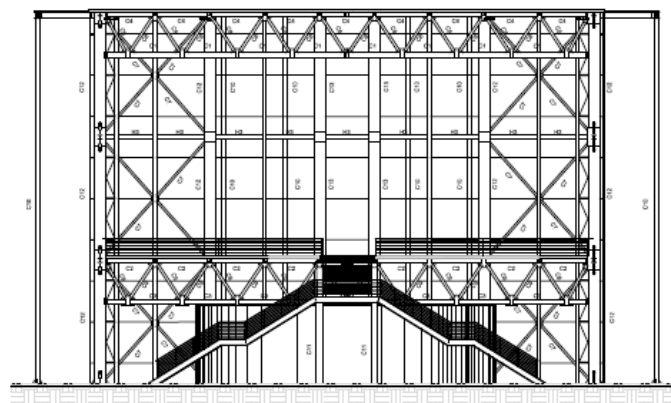


Figure 5. A-A Cross Section in Figures 1 and 2 (X-bracing)

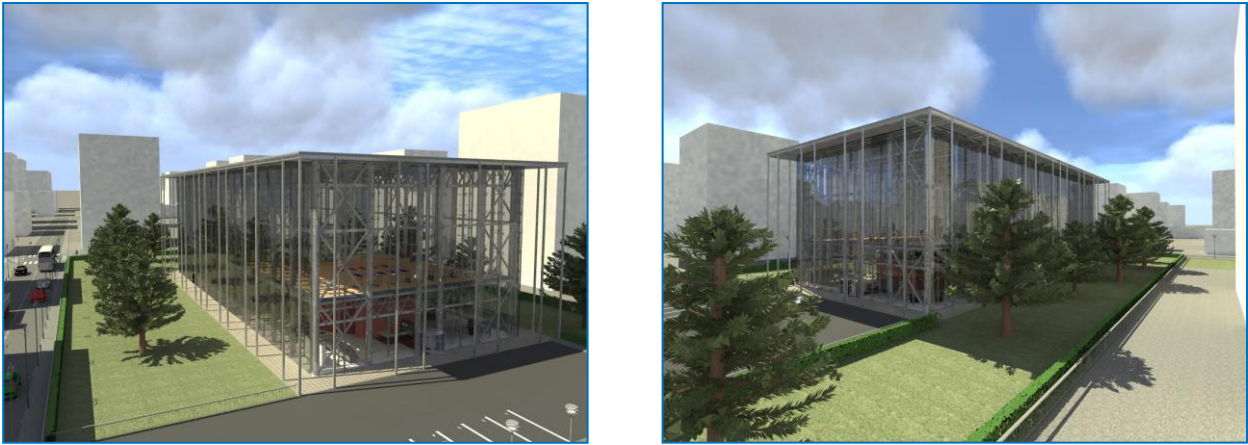


Figure 6. External Renderings of the Building on the Floor Side

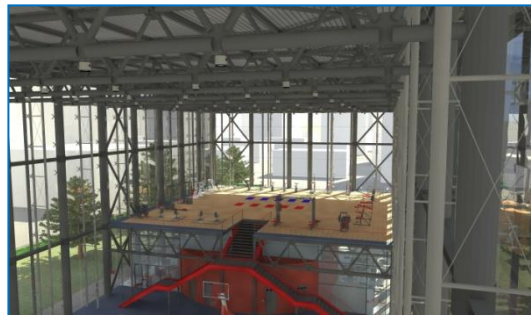
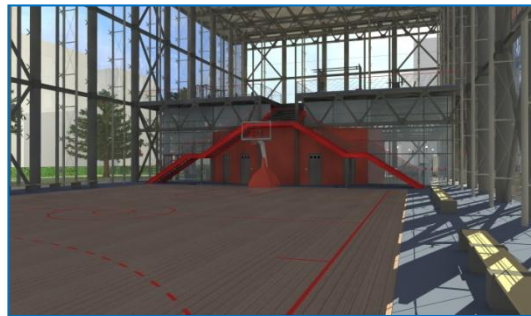


Figure 7. Internal Renderings of the Building

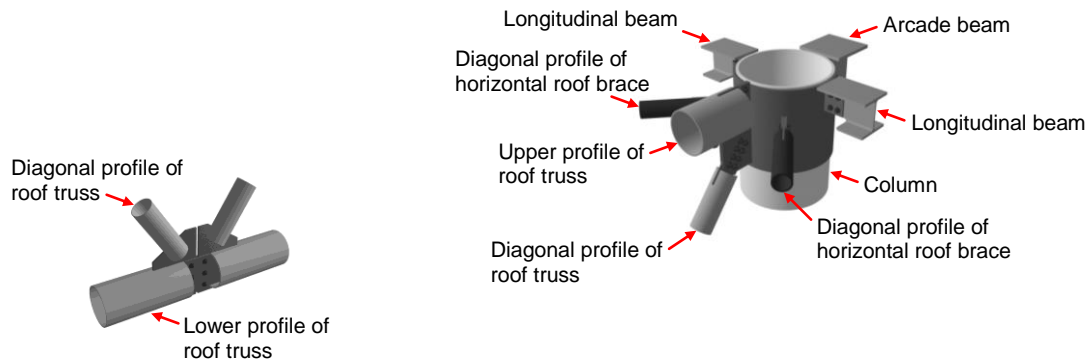


Figure 8. Views of an Intermediate Joint of Roof Trusses, and a Truss-column-beams Connection at the Roof Level

### 3. DESIGN EARTHQUAKE LEVELS

The building is designed to be located in the town of Udine, Friuli region, Italy, to which a medium-high seismicity level, according to the site-dependent seismic classification of the new Italian Technical Standards [11], is assigned. The pseudo-acceleration elastic response spectra scaled at the amplitudes of the frequent design earthquake (FDE, with a 81% probability of being exceeded over the reference time period  $V_R$ , calculated as:  $V_R = V_N \cdot C_U$ , where  $V_N$ ,  $C_U$  mean nominal life, and coefficient of use of the building, respectively); the serviceability design earthquake (SDE, with a 50%/ $V_R$  probability); the basic design earthquake (BDE, with a 10%/ $V_R$  probability); and the maximum considered earthquake (MCE, with a 5%/ $V_R$  probability), are displayed in Figure 9. The spectra are computed for the following parameters:  $V_N=50$  years,  $C_U=1.5$  (class of use III, corresponding to buildings with potential crowds), topographic category T1 (flat surface of the building site), and B-type soil (deposits of very thick sand, gravel, or very stiff clay, several dozens of meters thick). As anticipated in the introduction, the design analyses were developed in the DBXB design hypothesis by scaling the spectra referred to the BDE and the MCE by a behaviour factor  $q=4 \times 0.8=3.2$ , where a 0.8 penalty coefficient is assumed so as to take into account the structural irregularity caused by the eccentric position of the floor. The same spectra were not scaled ( $q=1$ ) for the EXB and VDB solutions. The FDE and SDE-related elastic response spectra were mutually assumed for the three design hypotheses. The verifications of the structural members were carried out according to the very similar requirements of the Italian Standards [11] and Eurocode 3 [12].

By applying the mutual prescriptions of Standards [11] and Eurocode 1 [13], the wind action for the site of the building (altitude of 113 m above ground, and terrain category IV, corresponding to an area where at least 15% of the surface is covered with buildings whose average height exceeds 15 m) is quantified by a peak velocity pressure  $q_p = q_b \cdot c_e(z) = 0.69 \text{ kN/m}^2$ , where  $q_b = 0.39 \text{ kN/m}^2$  is the basic velocity pressure, calculated as follows:  $q_b = \rho \cdot v_b^2$ , with  $\rho = \text{air density} = 1.25 \text{ kg/m}^3$  and  $v_b = \text{basic wind velocity} = 25 \text{ m/s}$ , and  $c_e(z) = 1.76$  is the exposure factor, computed for the  $z$  height above ground of the building, equal to 18 m. Based on the geometric and structural characteristics of the edifice, the size factor  $c_s$  and the dynamic factor  $c_d$  (and thus their product, i.e. the structural factor  $c_s \cdot c_d$ , as defined in [13]) are fixed at 1. The most demanding combination of wind forces — represented by the external pressure-related force,  $F_{w,e}$ , the internal pressure-related force,  $F_{w,i}$ , and the friction-related force associated to the wind action parallel to the external surfaces,  $F_{fr}$  — is obtained for the  $x$  direction in plan. This combination is determined by the following parameters:

external pressure coefficient  $c_{pe}=-0.8$ ; internal pressure coefficient  $c_{pi}=-0.5$ , which generates suction forces on the façades with the same sign as the external pressure-induced forces; and friction coefficient  $c_{fr}=0.4$ . This gives rise to a total wind force on the building (equal to the maximum wind-induced base shear)  $F_w=998$  kN, which is lower than the minimum earthquake-induced base shear, equal to 1140 kN, computed for the lowest earthquake level (FDE) and the VDB solution (greater minimum earthquake-induced base shear values are obtained for the DBXB and EXB design hypotheses). Therefore, the horizontal load-related design of the bracing systems is governed by seismic action.

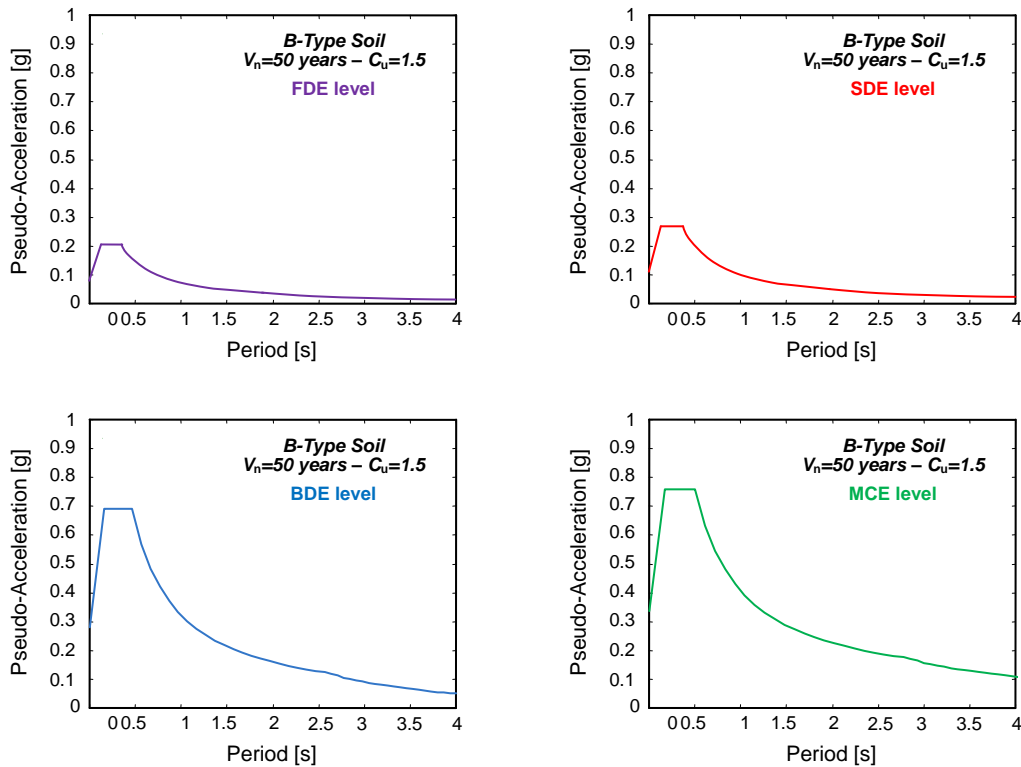


Figure 9. FDE, SDE, BDE and MCE-scaled Elastic Response Spectra

#### 4. SEISMIC PERFORMANCE LEVELS AND LIMITATIONS

The response limits related to the highest seismic performance levels (Operational — OP, and Immediate Occupancy — IO) are generally calibrated with the presence of damageable non-structural elements and finishes directly interacting with the structural skeleton or, in any case, of displacement-sensitive components. The 4 point-fixed glass panes wrapping the building are among the most sensitive non-structural elements to in-plane and out-of-plane displacements. Manufacturers of glass panes installed with spider-type or similar joints suggest that, in order to avoid local damage to glass and connectors, the maximum relative in-plane and out-of-plane horizontal displacements between the lower fitting points of the two upper connectors and the upper fitting points of the two lower connectors be constrained within 5‰ of their mutual distance  $D$  (i.e. 9.3 mm for the 2 m high panes considered in this design, where  $D$  is equal to 1.85 m). Therefore, the  $0.005D$  threshold can be fixed as the relative displacement limit associated to the non-structural OP performance level,  $rd_{NS,OP}$ , which also allows matching the slightly less prudential value suggested by the recently released Technical Recommendations on glass elements [14], equal to  $D/175$  ( $0.0057D$ ) for any type of 4-edge supported pane. Beyond this level of

deformation, a first series of hairline cracks appears, normally confined at glass-connector interfaces, and repairable without interrupting the use of the building until the relative displacement of the pane approximates  $0.01D$ . Therefore, this value can be adopted as the limit for the non-structural IO performance level,  $rd_{NS,IO}$ . Clearly visible and irreparable cracks are observed on the surface of the panes in the  $0.01\text{--}0.015D$  range of relative displacement, and cracks extended to the entire surface, although at no risk of detachment, in the  $0.015\text{--}0.02D$  range, with  $0.02D$  marking the acceptable boundary for the LS performance level,  $rd_{NS,LS}$ . The glass panes become fallout-prone for relative displacements around  $0.03D$ , which can be fixed as the upper limit for the CP performance level,  $rd_{NS,CP}$ .

Concerning structural performance, the limitations on deformations are implicitly dictated by the compliance with the ones postulated for non-structural levels. Moreover, response is assessed in terms of plasticization levels of the main members constituting the steel structure. For all design solutions, no plasticization is admitted for the structural OP and IO limit states. This requirement is extended to the LS and CP levels for the EXB and VDB design hypotheses. In the case of the DBXB solution, considerable buckling effects are expected in several braces at the LS limit state. Indeed, according to the design philosophy of Standards [11] and Eurocode 8 [15], as well as of any damage control-based approach to the seismic design of steel structures [16], plastic activity must be primarily concentrated in the bracing members, with a smaller involvement of columns and beams, so as to facilitate the possible post-earthquake repair and/or substitution of damaged members. The level of plasticization must be compatible with the preservation of the original strength and stiffness of the structural system against vertical loads, as well as of a residual horizontal stiffness equal to about 50% of the original elastic stiffness. The CP-related requirements consist in keeping the vertical load-bearing capacity of the structural system, though under severely damaged conditions of the bracing members and moderate-to-medium damage of columns and beams; and an approximately 25% residual fraction of the original horizontal stiffness, with very low safety margins from collapse against seismic forces. For all design hypotheses and performance levels, no damage to foundations is allowed.

## 5. DESIGN CONCEPTION OF THE VERTICAL STRUCTURAL SYSTEM

The classical design of the vertical structures of steel buildings tends to separate the role of standard columns (the gravity load-bearing system) from the role of bracings (the seismic and wind load-resisting system). In the examined case study, this design conception is regularly applied to the VDB and DBXB design solutions, as an acceptably small number of vertical bracing alignments results to be necessary in both cases (2 on both building sides along  $x$  as well as  $y$ , for a total of 8 — VDB; 2 on the floor side and 4 on the opposite side along  $x$ , and 2 on both sides along  $y$ , for a total of 10 — DBXB), as illustrated in the next sections. This allows meeting the basic architectural requirement of limiting the visual impact of bracings on the glazed façades, mentioned in the introduction. On the other hand, this objective cannot be met for the EXB solution if the same clear distinction between gravity and seismic/wind load resisting functions is considered in this case too. Indeed, in this hypothesis, the incorporation of bracings should be necessarily extended to all vertical alignments along  $x$ , and to at least 6 out of the 12 alignments along  $y$ , as a consequence of the highly demanding approach followed in this special design ( $q=1$ ). In this configuration, maximum 8 standard gravity-only load bearing columns would be kept, while the remaining 30 out of 38 would be involved in the bracing system. This poorly balanced proportion, along with the drastically prevailing sizes of the 30 columns belonging to the bracing alignments over the sizes of the 8 residual standard columns, would significantly impair the aesthetic quality of the building. Therefore, for the EXB design hypothesis the columns not incorporated in the bracing system were preferably involved in the absorption of the horizontal loads. This was obtained by designing

semi-rigid connections, rather than hinged joints, for these columns. This way, braces could be placed exactly in the same alignments as selected for the DBXB solution. As a consequence, not only all architectural restraints were met, but also the structural design was balanced properly. Moreover, the cost of the building resulted to be lower, as detailed in section 8.3.

It should be remarked that this necessarily different conception of the vertical structures does not affect the comparisons between the EXB design hypothesis and the other two solutions. Indeed, according to the objectives of the study formulated in the introduction, the comparisons are carried out in terms of performance for similar costs (VDB vs DBXB), or of costs for similar performance (VDB vs EXB), for the global structural solutions adopted in the three design hypotheses, rather than specifically in terms of response of the three bracing systems.

## 6. VDB DESIGN SOLUTION

The FV spring-dampers incorporated in the VDB system, detailed in [17-22], produce their damping action by a compressible silicone fluid flowing through the thin annular space found between the piston head and the internal casing (Figure 10). The inherent re-centering capacity of the devices is ensured by the pressurization of the fluid imposed upon manufacturing by means of a static pre-load force. The  $F_d(t)$  damping and  $F_{ne}(t)$  non-linear elastic reaction forces corresponding to the damper and spring functions of the devices are effectively simulated by the following analytical expressions [17], [23]:

$$F_d(t) = c \operatorname{sgn}(\dot{x}(t)) |\dot{x}(t)|^\alpha \quad (1)$$

$$F_{ne}(t) = k_2 x(t) + \frac{(k_1 - k_2) x(t)}{\left[ 1 + \left| \frac{k_1 x(t)}{F_0} \right|^5 \right]^{1/5}} \quad (2)$$

where  $c$ =damping coefficient;  $\operatorname{sgn}(\cdot)$ =signum function;  $|\cdot|$ =absolute value;  $\alpha$ =fractional exponent, ranging from 0.1 to 0.2 [17];  $F_0$ =static pre-load force;  $k_1, k_2$ =stiffness of the response branches situated below and beyond  $F_0$ .

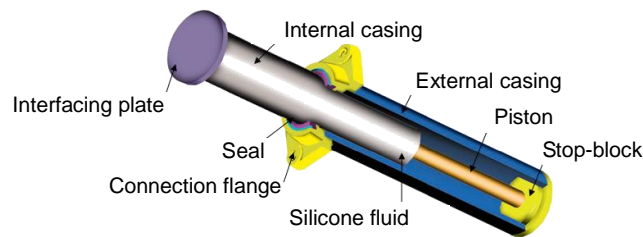


Figure 10. Cross Section of a Pressurized FV Spring-damper

The basic layout of the VDB system, illustrated in Figure 11, consists in a pair of interfaced FV spring-dampers installed in parallel with the floor-beam axis, at the tip of each couple of supporting steel braces. A half-stroke initial position is imposed on site to the pistons of both dissipaters by means of the connecting threaded steel bars, so as to obtain symmetrical tension-compression response cycles, starting from a compressive-only response of the single devices [17], [20]. Renderings of the installation details in the case study building are shown in Figure 12.

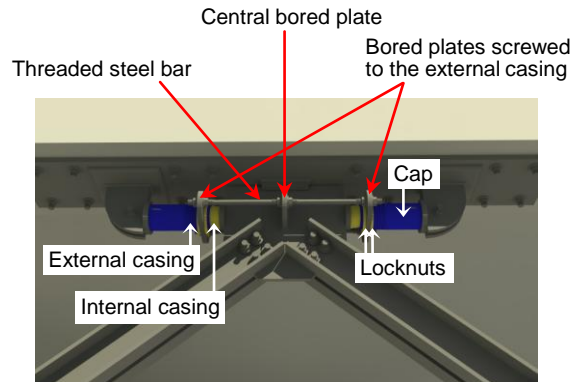


Figure 11. Typical Installation Layout of FV Spring-dampers in the VDB System

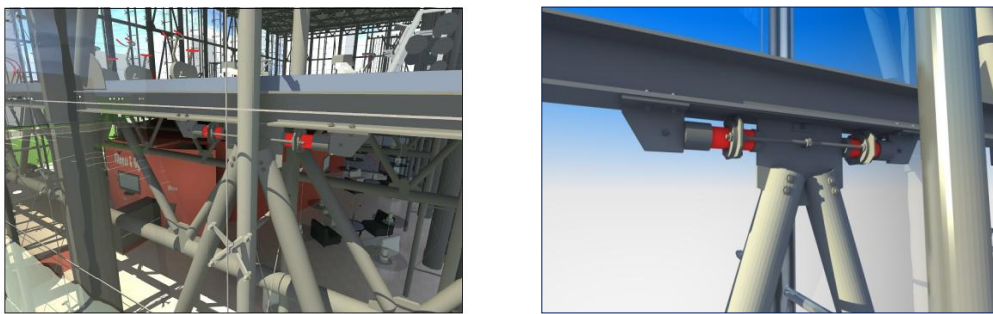


Figure 12. Renderings of the Installation of FV Spring-dampers in the VDB System of the Case Study Building

A preliminary design of the dissipative bracing system was developed by the general criterion formulated for applications to frame structures in [6], which consists in assigning the set of FV devices to be installed on a building story the capability of dissipating a prefixed fraction of the maximum seismic input energy computed by the numerical model of the structure on that story. By adapting the criterion to the special configuration of the building, which does not include whole intermediate floors, the energy balance was computed for the overall structure, rather than story by story, by assigning 90% of the total seismic input energy to the whole set of dampers to be incorporated in the system, along both x and y. Two types of spring-dampers were adopted, namely BC1FN and BC1GN type, selected from the manufacturer's basic catalogue [24]. The values of the mechanical parameters included in Equations (1) and (2) for these devices are:  $c=6.2 \text{ kN}\cdot(\text{s}/\text{mm})^\alpha$  (BC1FN),  $c=13.8 \text{ kN}\cdot(\text{s}/\text{mm})^\alpha$  (BC1GN);  $\alpha=0.15$  (BC1FN and BC1GN);  $k_2=1 \text{ kN}/\text{mm}$  (BC1FN),  $k_2=1.25 \text{ kN}/\text{mm}$  (BC1GN);  $k_1=20 k_2$  (BC1FN and BC1GN); and  $F_0=90 \text{ kN}$  (BC1FN),  $150 \text{ kN}$  (BC1GN). Further mechanical characteristics are: nominal energy dissipation capacity  $E_n=6 \text{ kJ}$  (BC1FN),  $12 \text{ kJ}$  (BC1GN); maximum reaction force  $R_{\max}=150 \text{ kN}$  (BC1FN),  $230 \text{ kN}$  (BC1GN); and stroke  $d_{\max}=65 \text{ mm}$  (BC1FN),  $80 \text{ mm}$  (BC1GN). As anticipated in section 5, the devices were placed over eight symmetrical vertical alignments, sketched in Figure 13, each being subdivided in three levels, determined by the geometry of the braces along the height. These levels correspond to 1/3 of the building height (6 m, coinciding with the floor height), 2/3 (12 m), and the top (18 m). The torsional response effects caused by the eccentric position of the floor with respect to the x axis were compensated by incorporating at the first level of the alignments parallel to this axis the smallest (BC1FN) devices, on the floor side, and the biggest (BC1GN) devices, on the opposite side. BC1FN dissipaters were introduced at the second and third level on both sides, and BC1GN dissipaters were placed at all levels along y, for a total of 24 pairs of devices (10 pairs of BC1FN and 14 pairs of BC1GN elements).

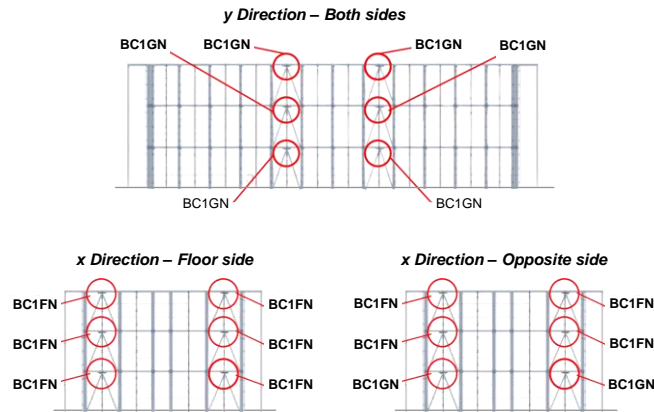


Figure 13. VDB Design Solution: System Alignments and FV Spring-damper Types

Table 1. VDB Design Solution: Profiles of the Main Structural Members

Tubular profiles (diameter×thickness) – (mm×mm)	
Standard columns	219.1×8
Columns included in bracing alignments	355.6×20
Braces	168.3×10
Italian H-shaped profiles	
Perimeter beams	HEB 160

The profiles adopted for the main members of the vertical structure are summarized in Table 1. These members include the internal columns, either of standard type or belonging to the vertical bracing alignments, the perimeter beams situated at the three levels of the same alignments, and the diagonal braces. As observed in section 2, all the other members, i.e. beams, trusses and horizontal braces of the floor and the roof, columns and beams of the stairs, and columns of the arcade, are equal for the three design solutions.

The modal parameters of the VDB-protected structure result as follows. The first mode is purely translational along  $y$ , with vibration period  $T_1$  equal to 0.88 s and effective modal mass (EMM) equal to 77.3% of the total seismic mass of the building. The second mode is mainly translational along  $x$ , with a relatively low contribution of the rotation around the vertical axis  $z$ . The vibration period  $T_2$  is equal to 0.72 s and the EMM is equal to 75.6% along  $x$  and 9.5% around  $z$ . The third mode is purely rotational around  $z$ , with  $T_3=0.45$  s and EMM=38.1%. The fourth mode is again purely translational along  $y$ , and is sufficient to obtain a summed effective modal mass (SEMM) greater than 90% along the same axis. Indeed, this mode shows 18.9% EMM, along  $y$ , giving rise to 96.2% SEMM. At the same time, the third translational mode is needed, in addition to the second one, to reach a SEMM greater than 90% in the  $x$  direction (attaining a total value of 93.2%). Concerning the calculation of modal parameters, it should be noted that the spring-dampers respond with their second branch stiffness  $k_2$  beginning from very low input seismic actions (i.e. with amplitudes just capable of overcoming the static pre-load  $F_0$ ). Therefore, in order to compute the actual dynamic parameters characterizing the seismic response of the VDB-protected structure, the first branch of the spring component of the devices was removed from the finite element model of the structure when the modal analysis was carried out, so that the devices may respond with  $k_2$  only [6-9]. As a consequence, due to the in-series connection of the spring-dampers to the supporting steel braces, the stiffening

effects of the VDB system on the modal behaviour of the structure result to be very little, as  $k_2$  is very low in comparison to the stiffness of the supporting braces (the modal parameters are nearly the same as the unbraced structure). This explains why the vibration periods are considerably higher than those calculated for the DBXB hypothesis, reported in the next section, although the sizes of the bracing system of this design solution are not much greater than the sizes selected for the VDB-protected structure.

## 7. DBXB AND EXB DESIGN SOLUTIONS

The profiles adopted for the main members of the vertical structure in the DBXB and EXB hypotheses are listed in Tables 2 and 3. As mentioned in section 5, the torsional effects were offset in these cases by doubling the bracing alignments along  $x$  on the opposite side of the floor (passing from two to four). This design choice helps to obtain a satisfactory modal behaviour, although not characterized by purely translational modes along  $x$  (similarly to the VDB solution), which could be reached by increasing further the number and/or the size of braces on the opposite side of the floor, but with negligible additional benefits on the modal response in plan and a considerable increase in costs.

Table 2. DBXB Design Solution: Profiles of the Main Structural Members

Tubular profiles (diameter×thickness) – (mm×mm)	
Standard columns	219.1×8
Columns included in bracing alignments	406.4×25
Braces	193.7×14.2
Italian H-shaped profiles	
Perimeter beams	HEB 200

Table 3. EXB Design Solution: Profiles of the Main Structural Members

Tubular profiles (diameter×thickness) – (mm×mm)	
Standard columns	508×40
Columns included in bracing alignments	610×40
Braces	273×20
Italian H-shaped profiles	
Perimeter beams	HEB 320

Based on these assumptions, for both design hypotheses the first mode results to be purely translational along  $y$ , with vibration period  $T_1$  equal to 0.71 s (DBXB) and 0.52 s (EXB), and EMM equal to 74.2% (DBXB) and 76.2% (EXB) of the total seismic mass. Similarly to the VDB solution, the second mode is mainly translational along  $x$ , with  $T_2$  equal to 0.48 s (DBXB) and 0.37 s (EXB), and EMM equal to 73.4% along  $x$  and 15.6% around  $z$  (DBXB), and 73.3% along  $x$  and 15.1% around  $z$  (EXB). The third mode is purely rotational around  $z$ , with  $T_3=0.35$  s and EMM=33.5% (DBXB), and  $T_3=0.28$  s and EMM=28.7% (EXB). The fourth mode is again purely translational along  $y$ , with EMM of 22.6% (DBXB) and 17.1% (EXB), which produces a SEMM of 96.8% (DBXB) and 93.9% (EXB) along the same axis, in combination with the first mode. In these two

design hypotheses too, the third translational mode in x direction is required to reach a SEMM greater than 90%, with total values of 93.8% and 94.2%, for DBXB and EXB, respectively.

## 8. SYNTHESIS OF DYNAMIC ANALYSES, PERFORMANCE EVALUATIONS AND COST ESTIMATES

The finite element models used to carry out the dynamic time-history design analyses of the structure for the three bracing solutions were elaborated with the SAP2000NL commercial analysis program [25]. One of the three models (VDB configuration) is demonstratively shown in Figure 14. Four sets of seven artificial accelerograms, generated from the FDE, SDE, BDE and MCE-scaled response spectra in Figure 9, were assumed as inputs for the analyses. A schematic roof plan and the positions of the upper joints of the two most distant internal columns (denoted by letters A and B), which were selected as control points for the evaluation of the global response of the building, are sketched in Figure 15.

The evaluation of the performance of the glazed façades was developed by separate finite element models, which included all the constituting panes (reproduced by shell elements), the spider connections and the supporting aluminium trusses (simulated by frame elements). The maximum displacements of the upper ends of the trusses (hinged to the perimeter beams of the roof, as mentioned in section 2) deduced from the time-history analyses of the structure for the various earthquake levels were imposed to the corresponding top joints of the façade models. This allowed precisely computing the displacements of each pane, and comparing these values with the non-structural performance limitations assumed. A view of the model of a longitudinal glazed façade, and a demonstrative out-of-plane deformed shape resulting from one of the analyses carried out, are displayed in Figure 16.

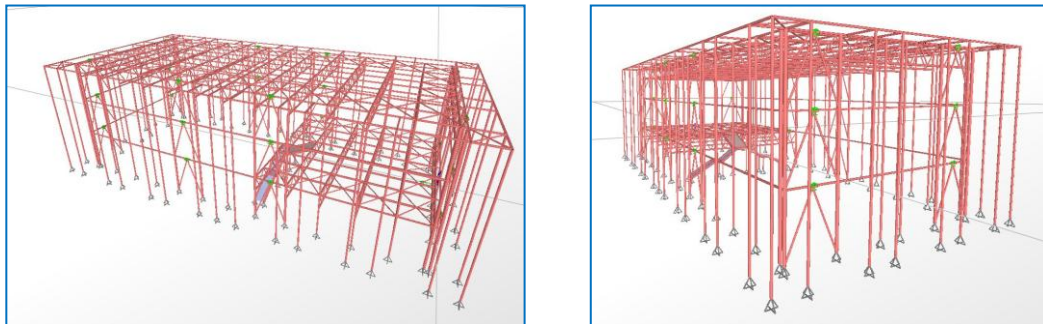


Figure 14. VDB Design Solution: Views of the Finite Element Model

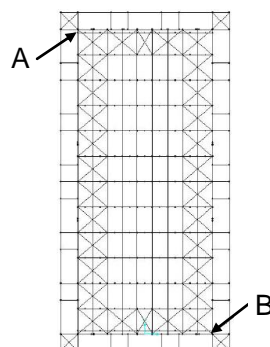


Figure 15. Reference Joints A and B

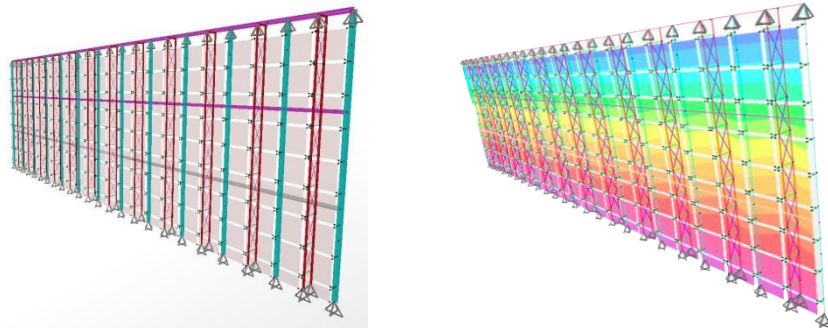


Figure 16. Finite Element Model of the Longitudinal Glazed Façades and Demonstrative Out-of-plane Deformed Shape Derived from Computation

### 8.1 Response and Performance of VDB Design Solution

As an example of the analyses developed on the structure protected by the VDB system, results extracted from the response to the most demanding of the seven input accelerograms scaled at the BDE level of the input action are reported in Figures 17 through 19. The former illustrates the displacement time-histories of control joints A and B in x and y direction. Differences no greater than 10% are observed in the peak values, which highlight the remarkable constraint of torsional components obtained with this design solution. The response cycles of a pair of BC1FN (floor side) and BC1GN (opposite side) devices situated at the first level of one of the two alignments parallel to x, displayed in Figure 18, exhibit peak displacements no greater than 20 mm. At the MCE level, the maximum displacements are again very low, as they do not exceed 27 mm. Similar data come out for the dissipaters placed on the second and third level along x, as well as for the most stressed devices incorporated in the alignments parallel to y. The energy time-histories plotted in Figure 19 show that around 90% of the total input energy is absorbed by the dissipaters (90.3% in x direction, and 91.5% in y), as targeted in the design of the system.

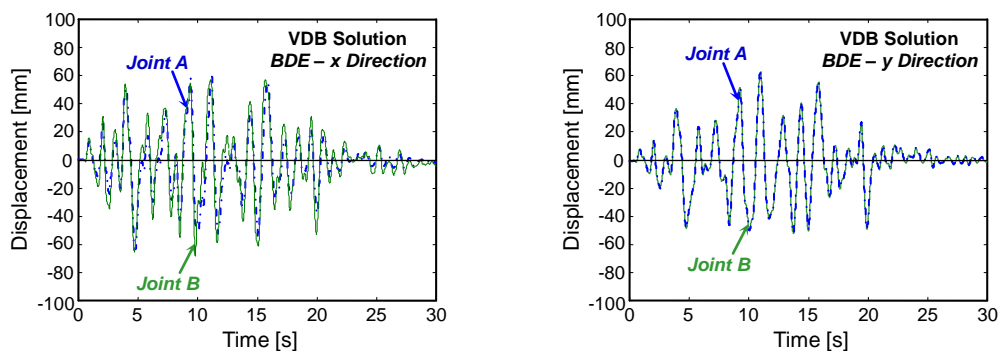


Figure 17. VDB Design Solution: Displacement Time-histories of Reference Joints A and B obtained from the Most Demanding BDE-scaled Accelerogram

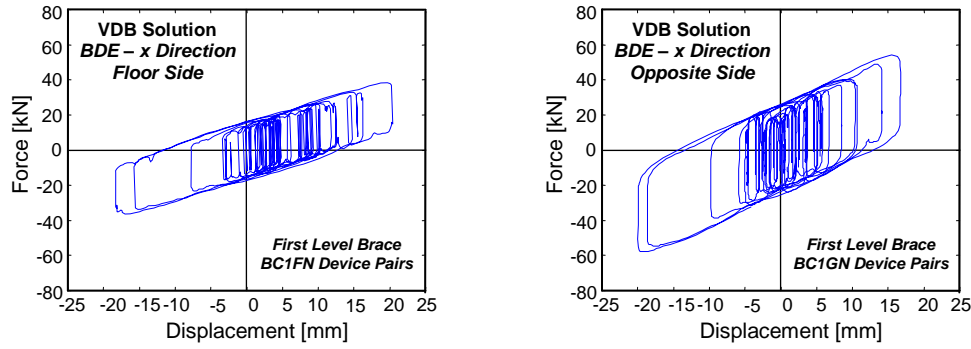


Figure 18. VDB Design Solution: Response Cycles of a Pair of BC1FN and a Pair of BC1GN Devices Situated at the First Level along x obtained from the Most Demanding BDE-scaled Accelerogram

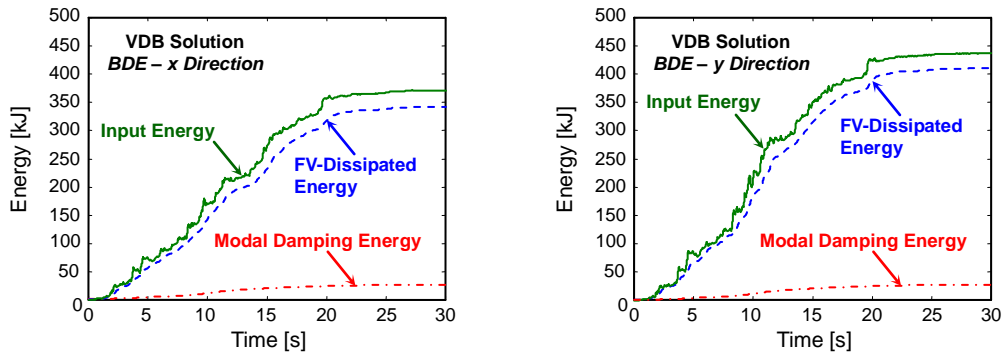


Figure 19. VDB Design Solution: Energy Time-histories of the Structure obtained from the Most Demanding BDE-scaled Accelerogram

The total percent equivalent linear viscous damping coefficient of the structure estimated from the response to the BDE and MCE-scaled levels of seismic action is equal to about 27% and 33%, respectively, with the DB system accounting for 25% — BDE and 30.5% — MCE, and the modal contribution of the steel skeleton accounting for 2% — BDE and 2.5% — MCE. As a consequence of these remarkably damped response conditions, the maximum base shear is limited below 20% — BDE and 24% — MCE of the total weight of the building.

The non-structural performance of the building deduced from the results of the dynamic analyses is summarized in the first column of Table 4, where the mean maximum relative displacements of the glass panes computed over the response to the seven input accelerograms scaled at the four earthquake level amplitudes —  $rd_{FDE,max}$ ,  $rd_{SDE,max}$ ,  $rd_{BDE,max}$ , and  $rd_{MCE,max}$  — are compared with the admissible relative displacement thresholds formulated in section 4 for the four reference non-structural limit states —  $rd_{NS,OP}$ ,  $rd_{NS,IO}$ ,  $rd_{NS,LS}$ , and  $rd_{NS,CP}$ . The data in Table 4 underline a very high performance of the VDB system, which allows meeting the strict OP-related limitation of  $0.005D$  up to the MCE-scaled seismic action.

Table 4. Maximum Relative Displacements of Glass Panes and Comparisons with Performance Limitations

Maximum $rd$ values	Design solution		
	VDB	DBXB	EXB
$rd_{FDE,max}$	0.0012 $D$ < $rd_{NS,OP}$	0.0035 $D$ < $rd_{NS,OP}$	0.0011 $D$ < $rd_{NS,OP}$
$rd_{SDE,max}$	0.0016 $D$ < $rd_{NS,OP}$	0.0046 $D$ < $rd_{NS,OP}$	0.0014 $D$ < $rd_{NS,OP}$
$rd_{BDE,max}$	0.0042 $D$ < $rd_{NS,OP}$	0.0148 $D$ < $rd_{NS,LS}$	0.0036 $D$ < $rd_{NS,OP}$
$rd_{MCE,max}$	0.0048 $D$ < $rd_{NS,OP}$	0.0211 $D$ < $rd_{NS,CP}$	0.0044 $D$ < $rd_{NS,OP}$

The structural performance of the building is qualified by the absence of plasticization in all members, which satisfies the basic requirement for the structural OP level up to the MCE amplitude too. By combining the results of non-structural and structural dynamic assessment analyses, the formal evaluation summarized in the four leftmost columns of Table 5 is obtained for the VDB-protected building, which corresponds to the highest attainable performance objective in the seismic design of a new structure.

Table 5. Assessment of Non-structural (NS) and Structural (S) Building Performance

	Design solution											
	VDB				DBXB				EXB			
	OP	IO	LS	CP	OP	IO	LS	CP	OP	IO	LS	CP
FDE	NS				NS				NS			
	S				S				S			
SDE	NS				NS				NS			
	S				S				S			
BDE	NS						NS		NS			
	S						S		S			
MCE	NS							NS	NS			
	S							S	S			

## 8.2 Response and Performance of DBXB and EXB Design Solutions

The performance of the two X-bracing design solutions is summarized in Tables 4 and 5 as well. The mean maximum relative displacements of the glass panes for the EXB hypothesis are very similar to the ones of the VDB-protected structure (Table 4), and no plasticization of steel members is observed again. Therefore, the resulting non-structural and structural performances coincide for the two designs. The quality of response is very similar too, with differences in the peak displacements of control joints A and B below 10%, like in the VDB case. The maximum base

shear is equal to about 61% — BDE and 73% — MCE of the total weight of the building, as a consequence of its totally elastic response at all earthquake levels. These high base shear values confirm, under a different viewpoint, the need for very massive dimensions of the structural members.

The DBXB-protected building meets the non-structural OP limitation of  $0.005D$  for the FDE and SDE-scaled amplitudes. At these earthquake levels, the response is totally elastic, and characterized by very little torsional effects, again with differences lower than 10% between the displacements of joints A and B. Buckling occurs in about 45% of braces (modelled in the non-linear field as trusses with elastic buckling in compression and bilinear elastic-plastic behaviour in tension) at the BDE, and in about 85% at the MCE, whereas relatively little plasticization is observed in about 30% of beams and 20% of columns (both schematized by a Giberson-type one-component model [26], with the end-section plastic hinges modelled by inelastic springs characterized by a Bouc/Wen-type [27] moment-rotation constitutive relationship). The total drifts computed at the roof level are equal to 229 mm (BDE) and 327 mm (MCE), corresponding to 1.27% (BDE) and 1.82% (MCE) of the building height. The residual (plastic) drifts are: 31 mm (0.17%) — BDE, and 129 mm (0.72%) — MCE. The residual horizontal stiffness of the structure is equal to 75% (BDE) and 46% (MCE) of the elastic stiffness, meeting the requirements of the structural LS and CP levels, respectively. The mean peak relative displacements of glass panes reach  $0.015D$  (BDE) and  $0.021D$  (MCE), which are below the non-structural LS limit of  $0.02D$ , and CP limit of  $0.03D$ , respectively. The resulting combined evaluation (NS-OP, S-OP — FDE; NS-OP, S-OP — SDE; NS-LS, S-LS — BDE; NS-CP, S-CP — MCE, where NS, S mean non-structural and structural) identifies the basic multi-level performance objective typically underlying the ductility-based design of braced steel structures, with the only exception of a slightly better performance at the SDE, for which the non-structural and structural IO levels are normally targeted, instead of the OP levels reached in this case. The maximum base shear is equal to about 15% — BDE and 18% — MCE. Both values are 25% lower than the corresponding values computed for the VDB solution, thanks to the relatively low ordinates of the design response spectra determined by the behaviour factor of 3.2.

### 8.3 Comparison of costs

The total weight of the structural members mutually adopted for the three solutions, described in section 2, is equal to about 142 tons, with a cost of 312,000 Euros, structural connections and installation expenses included. The weights and costs of the profiles in Tables 1, 2 and 3 are: 119 tons and 248,000 Euros, 190 tons and 398,000 Euros, and 496 tons and 1,090,000 Euros, respectively. Therefore, the total weights and costs of the steel structure are: 261 tons and 560,000 Euros (VDB), 337 tons and 710,000 Euros (DBXB), 638 tons and 1,402,000 Euros (EXB). For the VDB hypothesis, the cost of the spring-dampers must be added. This amounts to 128,000 Euros, given by the sum of 44,000 Euros for the set of 20 BC1FN devices (2,200 Euros per device) and 84,000 Euros for the set of 28 BC1GN devices (3,000 Euros per device). Therefore, the total cost of the steel structure for the VDB solution is equal to 688,000 Euros. The cost of the foundations amounts to 90,000 Euros (VDB), 120,000 Euros (DBXB), and 145,000 Euros (EXB), which determine the following total structural costs: 778,000 Euros (VDB), 830,000 Euros (DBXB), and 1,547,000 Euros (EXB).

These data show that the cost of the VDB-based design is slightly lower than the one of the DBXB solution (about 6%), and is about 50% lower than the cost of the EXB layout capable of producing the same overall performance. In addition to these remarkable economic advantages, the comparison between the VDB and EXB solutions show a considerably lower impact on the visual perception of the building for the viscous dissipative design, as a consequence of a drastic drop in member sections. This is visually highlighted by the renderings of a mesh of a bracing alignment

demonstratively displayed in Figure 20. The aesthetical benefits are evident, especially for columns, which are very massive in the case of the EXB design.

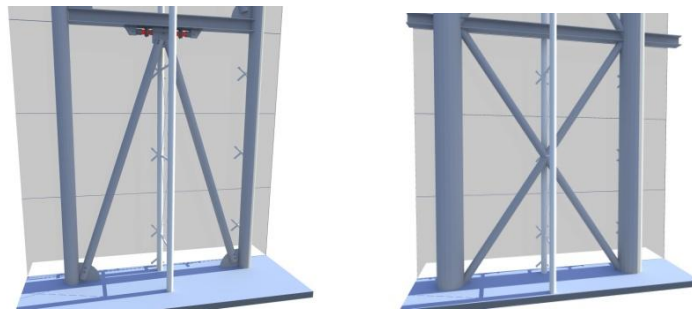


Figure 20. Rendering of a Mesh of Braces for the VDB and EXB Design Solutions

It can be noted that, should the EXB solution be designed by keeping the traditional separation between gravity load-bearing columns and bracing systems, the following tubular profiles would result: 219.1 mm × 8 mm, for the 8 standard columns (like for the VDB and DBXB hypotheses); 610 mm × 50 mm, for the 30 columns involved in the bracing system; and 323.9 mm × 25 mm, for diagonal braces. Apart from the negative effects on the building's aesthetic quality and the overall balance of structural proportions, commented in section 5, the cost of the steel structure in this case would be equal to 1,671,000 Euros, with an increase of 114,000 Euros (+7.4%) as compared to the basic EXB solution developed in this study.

The visual impact of the DBXB solution is similar to that of the VDB design, except for the layout of braces, a greater size of these members as well as of the columns involved in the bracing system, and the incorporation of two additional bracing alignments on the opposite side of the intermediate floor. The lower performance of the dissipative X-bracing hypothesis causes reparation costs of the structure and the glazed façades (all other finishes, plants and furniture excluded) estimated at 240,000 Euros for a seismic event comparable to the BDE, by amplitude and spectral composition. This amount is partly owed to the substitution of the damaged glass panes, and particularly of about 80% of their total number, which exceed the  $0.01D$  limit of visible and irreparable cracking, with a rounded cost of 100,000 Euros, as the total cost of glass panes is equal to about 130,000 Euros. The spider fittings and supporting aluminum trusses, whose total cost amounts to 150,000 Euros, remain practically undamaged at this input earthquake level, and they need no reparations. The remaining share of reparation costs, that is about 140,000 Euros, is related to structural damages, and namely to the substitution of the braces that are subject to buckling, and by the repair works required by the beams and columns that are subject to plastic rotation. The reparation costs increase to about 200,000 Euros, for the façades, and 270,000 Euros, for the structural elements, giving rise to a total amount of 470,000 Euros, for a seismic event comparable to MCE.

## 9. CONCLUSIONS

A novel application of the viscous-dissipative bracing system incorporating pressurized FV spring-dampers, originally conceived for installation in multi-story frame structures, was developed in this study with regards to an open-space, single-span steel indoor sports facility wrapped by continuous floor-to-roof glazed façades, the characteristics of which are typical of the most recent architectural design trends for recreational and commercial steel buildings. The performance offered by the system, and a comparison with the ductility-based and elastic X-bracing hypotheses carried out as alternative design solutions, prompts the remarks reported below.

- The high seismic protection capabilities of the system already evaluated in previous research activities dedicated to the analysis of new steel frame buildings, as well as to the retrofit of existing ones, were confirmed in the new design context demonstratively represented by the case study building. The limitations for the non-structural OP performance level originally formulated in this paper for the spider-joined panes constituting the glazed façades, fixed by collecting and elaborating requirements and suggestions from international seismic Standards, as well as from Technical and manufacturers' Recommendations specially dedicated to the design of glass members, were met up to the highest design earthquake intensity. Also, the basic requirement for the achievement of the structural OP level, i.e. no plasticization of the steel skeleton elements, was satisfied up to MCE, determining the highest attainable combined performance objective in the seismic design of a new structure.
- These high performance capabilities were reached with structural sizes of the bracing system of the VDB-protected structure notably smaller than the ones obtained for the ductility-based X-bracing solution, with the standard columns assumed with equal sections in the two cases. This further favours an effect of slenderness in the outer look of the building. The costs — spring-dampers and foundations included — are slightly lower (6%) for the VDB design.
- The performance capacities targeted for the DBXB system, consisting in the attainment of the basic multi-level objective identified by a “diagonal” correlation between performance levels and earthquake levels (OP–FDE, IO–SDE, LS–BDE, CP–MCE), were actually met, except for the improved “extra-diagonal” correlation between non-structural and structural OP levels and SDE obtained in this case. The reparation costs for a seismic event with amplitude and spectral characteristics comparable to BDE were estimated at about 240,000 Euros for the structure and the façades, i.e. about 24% of the original construction cost of 990,000 Euros (710,000 Euros — structure, plus 280,000 Euros — façades). The reparation costs increase to about 470,000 Euros, i.e. about 47% of the construction cost, for a seismic event comparable to MCE.
- The elastic X-bracing solution designed for the same performance objectives as the VDB one shows a total weight of the structure about 2.5 times greater, and a cost 2 times greater. The outer look of the EXB-protected steel skeleton results to be inevitably massive. Nonetheless, a worsened architectural and structural look, and a further 7% increase in costs, would derive in the hypothesis of basing the EXB design on the classical separation between gravity load-bearing columns and bracing systems, which was satisfactorily adopted, instead, for the VDB and DBXB hypotheses.

The study highlights the advantages offered by the viscous-dissipative bracing system, and potentially by any other supplemental damping-based protection technology, in a different field of application, poorly explored as yet. The system, in fact, offers a convincing solution to the combined issues of enhanced seismic performance and reduced dimensional impact required by the latest generation of steel buildings.

## ACKNOWLEDGEMENTS

The study reported in this paper was sponsored by the Italian Department of Civil Protection within the Reluis-DPC Project 2010/2013. The authors gratefully acknowledge this financial support.

**REFERENCES**

- [1] Constantinou, M.C., Soong, T.T., and Dargush, G.F., “Passive Energy Dissipation Systems for Structural Design and Retrofit”, Monograph Series No. 1, MCEER–Multidisciplinary Center for Earthquake Engineering, Buffalo, NY, 1998.
- [2] Hanson, R.D., and Soong, T.T., “Seismic Design with Supplemental Energy Dissipation Devices”, Publication MNO-8, EERI–Earthquake Engineering Research Institute, Oakland, CA, 2001.
- [3] Christopoulos, C., and Filiatrault, A., “Principles of Passive Supplemental Damping and Seismic Isolation”, IUSS Press, Pavia, Italy, 2006.
- [4] Sorace, S., and Terenzi, G., “Large-scale Experimental Validation of a Design Procedure for Damped Braced Steel Structures”, Proceedings of STESSA 2003 – 4<sup>th</sup> International Conference on the Behaviour of Steel Structures in Seismic Areas, Naples, Italy, 2003, pp. 657-662.
- [5] Molina, F.J., Sorace, S., Terenzi, G., Magonette, G., and Viacoz, B., “Seismic Tests on Reinforced Concrete and Steel Frames Retrofitted with Dissipative Braces”, Earthquake Engineering and Structural Dynamics, 2004, Vol. 33, No. 12, pp. 1373-1394.
- [6] Sorace, S., and Terenzi, G., “Seismic Protection of Frame Structures by Fluid Viscous Damped Braces”, Journal of Structural Engineering, ASCE, 2008, Vol. 134, No. 1, pp. 45-55.
- [7] Sorace, S., and Terenzi, G., “Advanced seismic retrofit of a low-rise R/C building”, Advanced Materials Research, 2012 (in press).
- [8] Sorace, S., and Terenzi, G., “Shaking Table and Numerical Seismic Performance Evaluation of a Fluid Viscous-dissipative Bracing System”, Earthquake Spectra, 2012 (in press).
- [9] Sorace, S., and Terenzi, G., “Fluid Viscous Damped-based Seismic Retrofit Strategies of Steel Structures: General Concepts and Design Applications”, Advanced Steel Construction, 2009, Vol. 5, No. 3, pp. 322-339.
- [10] Sorace, S., and Terenzi, G., “New Design and Seismic Retrofit Applications of Fluid Viscous-damped Bracing Systems”, Proceedings of Eurodyn 2011 – 8<sup>th</sup> International Conference on Structural Dynamics, Leuven, Belgium, 2011, Paper No. 562, CD-ROM.
- [11] Italian Council of Public Works, “Technical Standards on Constructions” [in Italian], Rome, Italy, 2008.
- [12] European Committee for Standardization, “Eurocode 3 – Design of Steel Structures. Part 1-1: General Rules and Rules for Buildings”, EN 1993-1-1, Bruxelles, Belgium, 2005.
- [13] European Committee for Standardization, “Eurocode 1 – Actions on Structures. Part 1-4: General Actions – Wind Actions”, EN 1991-1-4, Bruxelles, Belgium, 2005.
- [14] American Society for Testing and Materials, “ASTM E1300-04 – Standard Practice for Determining Load Resistance of Glass in Buildings”, West Conshohocken, USA, 2004.
- [15] European Committee for Standardization, “Eurocode 8 – Design of Structures for Earthquake Resistance. Part 1: General Rules, Seismic Actions and Rules for Buildings”, EN 1998-1, Bruxelles, Belgium, 2004.
- [16] Sorace, S., “Seismic Damage Assessment of Steel Frames”, Journal of Structural Engineering, ASCE, 1998, Vol. 124, No. 5, pp. 567-576.
- [17] Sorace, S., and Terenzi, G., “Non-linear Dynamic Modelling and Design Procedure of FV Spring-dampers for Base Isolation”, Engineering Structures, 2001, Vol. 23, No. 12, pp. 1556-1567.
- [18] Sorace, S., and Terenzi, G., “Non-linear Dynamic Design Procedure of FV Spring-dampers for Base Isolation — Frame Building Applications”, Engineering Structures, 2001, Vol. 23, No. 12, pp. 1568-1576.

- [19] Sorace, S., Terenzi, G., Magonette, G., and Molina, F.J., “Experimental Investigation on a Base Isolation System Incorporating Steel-Teflon Sliders and Pressurized Fluid Viscous Spring Dampers”, *Earthquake Engineering and Structural Dynamics*, 2008, Vol. 34, No. 2, pp. 225-242.
- [20] Sorace, S., and Terenzi, G., “Analysis and Demonstrative Application of a Base Isolation/Supplemental Damping Technology”, *Earthquake Spectra*, 2008, Vol. 24, No. 3, pp. 775-793.
- [21] Sorace, S., and Terenzi, G., “The Damped Cable System for Seismic Protection of Frame Structures — Part I: General concepts, Testing and Modelling”, *Earthquake Engineering and Structural Dynamics*, 2012, Vol. 41, No. 5, pp. 915-928.
- [22] Sorace, S., and Terenzi, G., “The Damped Cable System for Seismic Protection of Frame Structures — Part II: Design and Application”, *Earthquake Engineering and Structural Dynamics*, 2012, Vol. 41, No. 5, pp. 929-947.
- [23] Pekcan, G., Mander, J.B., and Chen, S.S., “The Seismic Response of a 1:3 Scale Model R.C. Structure with Elastomeric Spring Dampers”, *Earthquake Spectra*, 1995, Vol. 11, No. 2, pp. 249-267.
- [24] Jarret SL, “Shock-control Technologies”, URL <http://www.introini.info>, 2012.
- [25] Computers & Structures Inc., “SAP2000NL. Structural Analysis Programs – Theoretical and Users Manual”, Release No. 14.03, Berkeley, CA, 2011.
- [26] Giberson, M.F., “The Response of Nonlinear Multi-story Structures Subjected to Earthquake Excitation”, Doctoral Dissertation, California Institute of Technology, Pasadena, USA, 1967.
- [27] Wen, Y., “Method for Random Vibration of Hysteretic Systems”, *Journal of the Engineering Mechanics Division, ASCE*, 1976, Vol. 102, No. 2, pp. 249-263.